Stability of Periodically Modulated Rotating Disk Boundary Layers

Scott Morgan

Cardiff University

Submitted for the degree of Doctor of Philosophy

August 2018

Declaration

This work has not been submitted in substance for any other degree or award at this or any other university or place of learning, nor is being submitted concurrently in candidature for any degree or other award.

Signed ..... (candidate) Date .....

STATEMENT 1

This thesis is being submitted in partial fulfilment of the requirements for the degree of PhD.

Signed ..... (candidate) Date .....

STATEMENT 2

This thesis is the result of my own independent work/investigation, except where otherwise stated. Other sources are acknowledged by explicit references. The views expressed are my own.

Signed ..... (candidate) Date .....

STATEMENT 3

I hereby give consent for my thesis, if accepted, to be available for photocopying and for inter-library loan, and for the title and summary to be made available to outside organisations.

Signed ..... (candidate) Date .....

Abstract

The linear stability properties of the boundary layer generated above a disk of infinite extent which rotates around its azimuth are explored for a novel configuration. The rotation rate is taken to be temporally periodic, motivated by findings from Thomas et. al. (Proc. Royal Soc. A, 2011) that the addition of an oscillatory component to an otherwise steady flow has stabilising effects.

The vorticity-based methods that were first adopted by Davies & Carpenter (J. Comput. Phys., 2001) are utilised in a novel way for the solution of steady and temporally periodic eigenvalue dispersion relations. Validation of this method is provided by archetypal flow configurations such as the steady Blasius boundary layer and the temporally periodic Stokes layer, where Floquet theory is incorporated.

Floquet stability theory is applied to the periodically modulated rotating disk for fixed wavenumber and fixed frequency disturbances, where it is shown that the addition of a modulated rotation rate has a stabilising effect on the boundary layer across a range of modulation frequencies. Confirmation is provided by frozen profile analyses and direct numerical simulations of the subsequent flow development. An energy analysis of the perturbation quantities is conducted to provide insights into the physical mechanisms for the stabilisation.

The flow response to impulsive excitations in the periodically modulated rotating disk boundary layer is explored. Direct numerical simulations of radially homogeneous and inhomogeneous configurations are conducted and global stability behaviour is investigated.

Acknowledgements

The acknowledgements of any thesis are amongst my favourite parts to read, providing the author with a rare opportunity to express deserving gratitude and invariably lending some humanity to what is otherwise an impersonal scientific document. Throughout the research which has led to the creation of this thesis, there have been a great many family, friends and colleagues who have contributed either directly or indirectly and I express my warmest thanks to everyone who has had even a small part to play. There are, however, several people who I will take this opportunity to personally acknowledge, without whom this thesis would simply not exist.

Firstly, I would like to thank the Cardiff School of Mathematics and its staff for accommodating me throughout the project and the EPSRC for funding this research.

My deepest gratitude goes to my supervisor, my friend and mentor Dr. Christopher Davies, whose guidance and support throughout this project has been outstanding. I cannot express enough how much appreciation I have for your advice and direction through the last four years. I have thoroughly enjoyed our conversations.

Secondly, to the friends and colleagues who I have had the pleasure of working alongside throughout my time at Cardiff School of Mathematics. To Alex, for all of your support and for being my right-hand-man. To my academic sister Martina, for your invaluable advice and for the endless entertainment both at work and outside. To James, for some great conversations and distractions through squash. To Danny, for your help and support during events, conferences and academic travelling.

I would like to express my heartfelt thanks and appreciation to Claire George, whose commitment and determination in all walks of life is inspiring. I would not be where I am today without your support.

For her phenomenal company in the final stages of this research, I will be eternally grateful to Chelsea. You have an unnatural ability to distract me and make me laugh, even when the pressures of writing a thesis are greatest. Your passion is inspirational and thank you for everything.

Finally, for all of her support throughout my life, I thank my Mum. From revising with me through undergraduate studies to being a rock in my life through this research, I cannot express the gratitude I have towards you. Also to my wonderful sister Charlotte, who is simply the best person in the world.

Contents

Chapter 1

Linear Stability Analysis of Two-Dimensional Boundary Layers using a Velocity-Vorticity Formulation

1.1 Introduction

The following exposition broadly describes the study of instability mechanisms in flows of so-called Newtonian fluid. Stability theory is a large and important area of fluid dynamics, with the essential problems being recognised, among others, by Reynolds, Rayleigh, Kelvin and Helmholtz towards the end of the nineteenth century.

We will make reference to *stability* throughout and it will prove useful to have a concept of what it means for a flow to be *stable* or *unstable* from the outset. In what follows, we will take stability as an umbrella term for describing the subsequent behaviour of a fluid flow after having been subjected to a small perturbation or variation. James Clerk Maxwell, as explained in Drazin [32], described stability concisely in the late nineteenth century as

When...an infinitely small variation of the present state will alter only by an infinitely small quantity the state at some future time, the condition of the system, whether at rest or in motion, is said to be stable; but when an infinitely small variation in the present

state may bring about a finite difference in the state of the system in a finite time, the condition of the system is said to be unstable.

This explains that following some sort of disturbance, the flow is *unstable* if it never returns to its original state but *stable* if the disturbance decays over time. In almost all applications, stable flows are preferable and instabilities are usually associated with greater energy consumption, less efficiency and greater cost. Unstable flows can often evolve into a chaotic state of motion called *turbulence* which is extremely irregular and often undesirable. Turbulence is very poorly understood and in 2006, Richard Feynman [34] described it as *the most important unsolved problem of classical physics.*

For the last century or so, many mathematicians and physicists have attempted to understand the complexities of stability theory and turbulence. Osborne Reynolds' [62] famous series of experiments in 1883 studying the stability of fluid flow in a pipe were among the first of their kind, and still present one of the clearest ways of introducing stability theory.

Reynolds considered flow in three pipes at varying velocities, studying the behaviour of dye streaks in the liquid, and figure 1.1 shows the configuration where two distinct cases develop over time.

The first image shows the case of *laminar flow*, where the streak extends in a straight line through the tube. In the other case, the dye has mixed with the fluid and filled the tube with colour, indicating a *turbulent* situation. The third drawing shows the second case in more detail, illustrating the colour as a mass of curls and eddies during the transition to turbulence.

Reynolds proceeded to demonstrate that the different cases of smooth laminar flow and turbulence are dependent on the quantities V, the maximum velocity of the fluid in the pipe, a, the radius of the pipe and ν, the kinematic viscosity of the fluid. He noted that the laminar flow started to break down when the ratio $\frac{Va}{\nu}$ exceeded a certain value. This dimensionless quantity is now known as the *Reynolds number* and can be defined differently depending on the flow configuration. Throughout this report we will denote the Reynolds number by R. It should be noted however, that many texts and references cited herein use the notation Re instead, with no interesting distinction between the two.

This idea of a somewhat *critical* Reynolds number above which the flow is unstable is

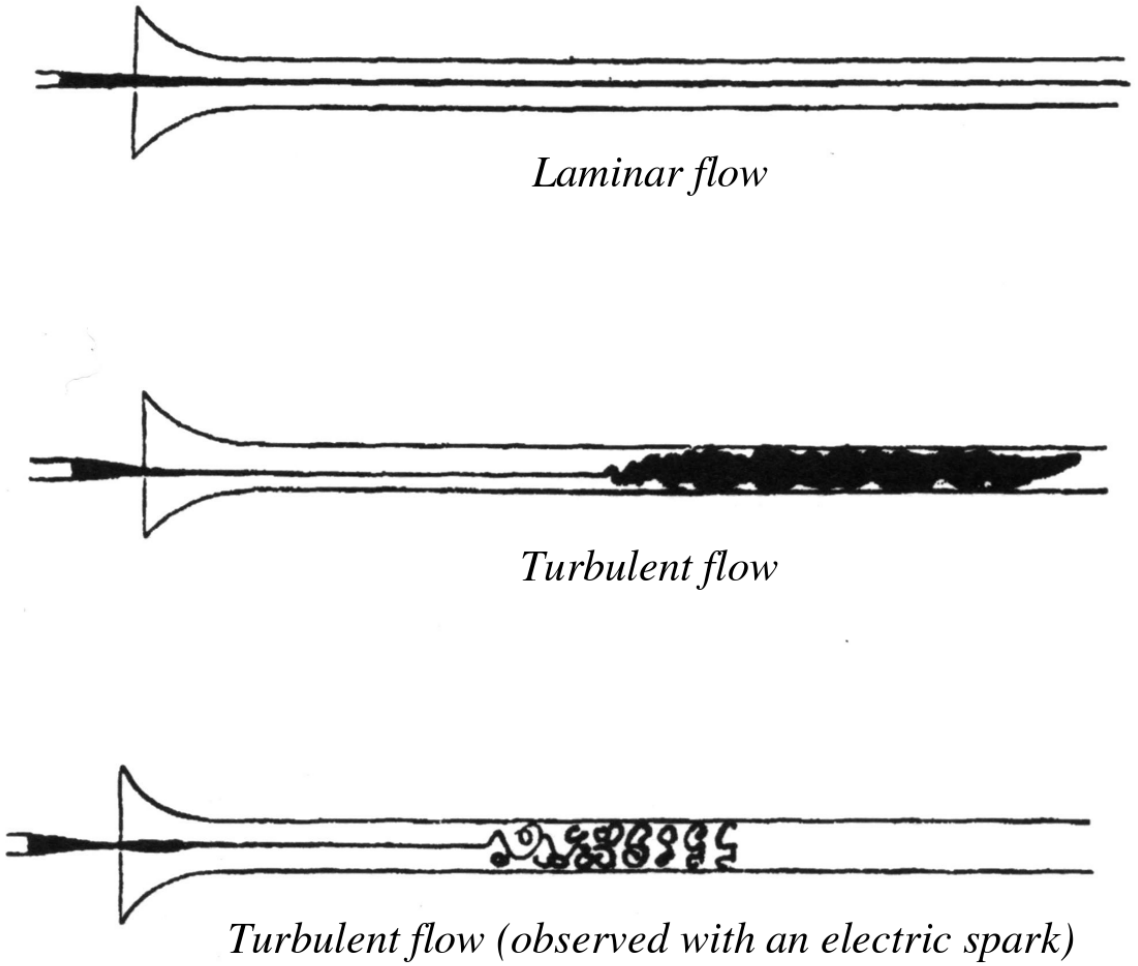

Figure 1.1: Reynolds' experiment of flow in a pipe, taken from Drazin [32].

in fact a general idea and can be applied to many flows. Typically, a fluid flow is stable if the Reynolds number R is small enough, although there might exist a critical value R_c such that the flow is unstable with respect to infinitesimal perturbations for $R > R_c$. Finding this critical value R_c is often a computationally difficult task and must be carried out numerically.

On the topic of computation, both experimental and analytic solution techniques have drawbacks, with experiments being almost always subject to disruption by noise in the system and analytical approaches being hindered by the complexity of the Navier-Stokes equations. These limitations have been somewhat alleviated in more recent times with the rapid development of technology and efficient numerical methods have been developed which can, in some cases, model even the fine complexities of turbulence with sufficient accuracy in a practical time frame.

There are several types of stability analysis that exist and these can be loosely categorised into *linear* or *non-linear analysis* and *local* or *global analysis* and all must be used in conjunction with each other if a flow configuration is to be fully understood.

Linear theory is usually employed as a first stage and will predict whether sufficiently small disturbances grow or remain bounded, although further investigation is often necessary to fully understand the outcome. There are famous examples of linearly stable flows that actually become turbulent such as Poiseuille pipe flow, largely due to the fact that as disturbances grow they become large enough to invalidate the linear theory. Weakly non-linear theories predict the next stages of disturbance evolution if growth rates are weak but not infinitesimal and in recent years, with an increase in computational power, it has been possible in some cases to conduct fully non-linear simulations.

Local analyses may be carried out by separating the disturbances into Fourier-type travelling wave modes, a superposition of which gives an idea of the stability properties. This is the background to the *Orr-Sommerfeld equation* and its relatives introduced in section 1.2 and discussed through chapters 2-3. Global analyses are typically conducted using time-dependent simulations of the Navier-Stokes equations, and offer deeper insights into the real-world flows. We will discuss a global approach to stability theory in chapter 4.

The classical, historical approach has been to study the local, linear development of infinitesimal disturbances to a known steady base flow field, and attempt to glean some understanding of the flow configuration as a whole. Under this theory, regions of a fluid flow domain may be categorised into one of three categories:

- Stable
- Convectively unstable
- Absolutely unstable

and an illustration of convective and absolute instabilities can be seen in figure 1.2. These schematic diagrams are taken with reference to x as the streamwise direction and the time t. If at all streamwise locations x, the disturbance decays with time, then the flow is said to be *stable*. In such flows all disturbances always decay with time. If a disturbance grows as it propagates upstream or downstream but is such that at any given x, the flow at that point eventually returns to the undisturbed basic state, the flow is said to

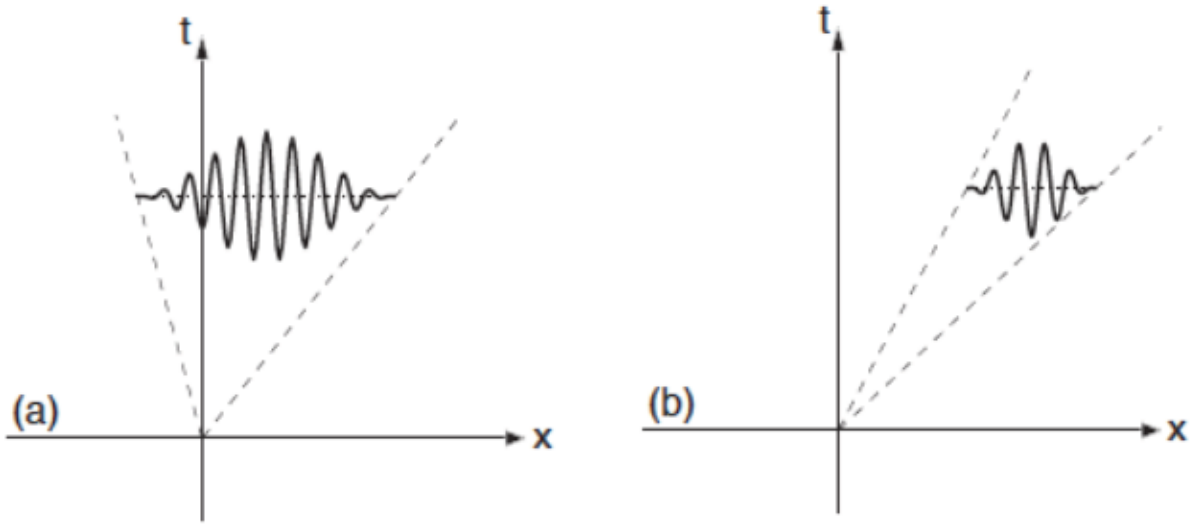

(a) Absolute instability (b) Convective instability

Figure 1.2: Schematic diagram of convective and absolute instabilities for illustration purposes.

be *convectively unstable*. On the other hand, if at that fixed streamwise location, the magnitude of the disturbance grows with time, it is said to be *absolutely unstable*. In such flows, the disturbance grows at all spatial locations and at all times.

1.1.1 About this Thesis

Throughout this presentation we detail the instability mechanisms for several flow configurations in a variety of situations. We discuss numerical techniques, some of which are novel, before setting the scene for a thorough examination of a particular three-dimensional temporally periodic boundary layer. This boundary layer is formed in a configuration which has not previously been studied, over a disk which rotates with a modulated rotation rate.

Prior to our examination of the local and global stability properties of such a configuration, chapter 1 provides a thorough introduction to stability theory and introduces the novel numerical methods in application to archetypal two-dimensional flow configurations. We present discussions of standard equations such as the Orr-Sommerfeld equation in section 1.2 and provide an overview of the numerical solution methods used throughout this thesis based on Chebyshev series and their corresponding integral operators.

Chapter 2 provides a comprehensive review of the local linear stability properties of the boundary layer formed over a disk which rotates with a constant rotation rate and applies the two-dimensional methods of chapter 1 to this three-dimensional scenario. This configuration was first studied by von Kármán [80] in 1921 due to its admission of an exact similarity solution to the Navier-Stokes equations and later by Gregory et al. [38] due to its similarities with fluid flow over swept-wings. Further interest in the configuration was generated by Lingwood [43] after her discovery of a local absolute instability in the flow and further still by Davies and Carpenter [27] upon their realisations that the local absolute instability did not generate a linearly unstable global mode, leading to the conclusion that convective instabilities persist at all Reynolds numbers, at least for the range of azimuthal mode numbers considered by Davies and Carpenter [27]. However, more recently, Thomas and Davies [75] have explored a higher range of azimuthal mode numbers than what was previously studied and have found evidence for global instability at these levels. Further work has been done on the non-linear behaviour of disturbances via direct numerical simulations in studies such as Appelquist et al. [4, 5, 6]. Research into the global stability properties of the steady rotating disk boundary layer is still highly active and Lingwood and Alfredsson [46] provide a thorough review of the field prior to 2015.

In chapter 3, we present a discussion of a novel flow configuration and analyse the stability properties of a disk of infinite extent which rotates with a periodically modulated angular velocity about the azimuth. The motivation for the addition of a modulated rotation rate originates with the Thomas et al. [76] study of an oscillatory Stokes layer added to a Poiseuille flow. The authors show that inducing this small amount of oscillation can have stabilising effects, complementing the work of Kelly and Cheers [42] and Von Kerczek [81] who studied modulation of plane Couette flow and also found stabilisation. Thomas et al. [76] found that the steady flow was stabilised for certain frequencies of the oscillation but destabilised for others. Wise and Ricco [82] also show that turbulent drag reduction may be achieved using oscillation of flat plates and rotating disks.

Chapter 4 extends the discussion of the local analysis of the periodically modulated rotating disk boundary layer to a global setting, and introduces techniques for direct numerical simulations of a response to an impulsive forcing. We briefly review the global behaviour in the steady case, before presenting archetypal results for the modulated con-

figuration. Some discussion is given to the aforementioned discovery by Davies and Carpenter [27] that the steady flow is linearly globally stable and some exploratory results are presented for the modulated case. However, a detailed examination of the subtleties involved in this configuration is reserved for future work.

Aside from stabilising the steady rotating disk boundary layer, the periodically modulated rotating disk is an interesting problem in its own right, and has applications in electrochemical engineering. As discussed in Bard and Faulkner [8], the steady rotating disk electrode provides a convenient configuration for conducting hydrodynamic voltammetry, where convection of an analyte controlled by the rotation is designed to increase the rate of controlled mass transport of ions at an electrode surface. This technique is commonly used for electroplating, and Schwartz et al. [66] discuss the effects of a periodically modulated rotation rate on the mass transfer. These concepts will be briefly discussed in the context of future work in chapter 5.

Also discussed in chapter 5 are the parallels and similarities between our proposed stabilising technique and periodically distributed surface roughness. Several recent studies such as Garrett et al. [36] and Cooper et al. [21] have investigated radially iso- and anisotropic roughness in the context of linear stability and found significant stabilising effects. The significance of our method in the context of theirs is discussed, and some advantages of our technique are presented.

The following sections are intended to be introductory, and provide an overview to the interested reader of the fundamental equations that underpin stability theory. Some of the derivations are standard and discussed in many introductory textbooks so we will omit the finer details for brevity. However, an overview will be presented at this stage thereby setting the scene for the forthcoming chapters.

1.2 The Orr-Sommerfeld Equation

Consider flows of an incompressible viscous fluid in a given domain Π. Let ρ be the density of the fluid, and ν the kinematic viscosity. Let also $\mathbf{u^*}$ and p^* be the dimensional velocity and pressure respectively of the fluid at a given point $\mathbf{x^*}$ and time t^*. Then the Navier-Stokes equations which govern the fluid motion in the absence of body forces are given by

$$\frac{\partial \mathbf{u*}}{\partial t^*} + (\mathbf{u*} \cdot \nabla^*)\mathbf{u*} = -\nabla^* p^* + \nu \nabla^{*2} \mathbf{u*} \tag{1.1a}$$

$$\nabla^* \cdot \mathbf{u*} = 0 \tag{1.1b}$$

Non-dimensionalisation is carried out by some characteristic velocity scale V and length scale L, to give the dimensionless quantities

$$\mathbf{x} = \frac{\mathbf{x*}}{L}, \quad \mathbf{u} = \frac{\mathbf{u*}}{V}, \quad t = \frac{Vt^*}{L}, \quad p = \frac{p^*}{\rho V^2} \tag{1.2}$$

Substitution of (1.2) into the equations (1.1) gives the familiar non-dimensional Navier-Stokes equations

$$\frac{\partial \mathbf{u}}{\partial t} + (\mathbf{u} \cdot \nabla)\mathbf{u} = -\nabla p + \frac{1}{R}\nabla^2 \mathbf{u} \tag{1.3a}$$

$$\nabla \cdot \mathbf{u} = 0 \tag{1.3b}$$

where R is the Reynolds number defined by $R = \frac{VL}{\nu}$. Equation (1.3a) is known as the *momentum equation*, while equation (1.3b) is known as the *continuity equation* and is equivalent to conservation of mass in the system. It is sometimes useful to interpret the Reynolds number as a measure of the inertial effects relative to the viscous effects of the fluid. If R is large, the viscous term is typically much smaller than the inertial term, indicating that it may be safe to treat the flow as essentially inviscid. Some care must be taken when doing this and conducting stability analyses however, as is highlighted in section 1.2.2.

To provide an illustration of common linear stability concepts, we consider a steady two-dimensional base flow of the form

$$\mathbf{U} = (U(z), 0, 0), \quad P = \text{constant} \quad \text{for} \quad z_1 \leq z \leq z_2$$

where $z_1,\ z_2 \in \mathbb{R} \cup \{\pm\infty\}$ bound the region of the flow. The analysis proceeds by introducing a small perturbation to the flow so that

$$\mathbf{u}(\mathbf{x}, t) = \mathbf{U}(z) + \epsilon \mathbf{u}'(\mathbf{x}, t), \quad p(\mathbf{x}, t) = P + \epsilon p'(\mathbf{x}, t)$$

where $\mathbf{x} = (x, y, z)$, the $'$ denotes the perturbation quantities and $\epsilon << 1$. After substituting these representations for $\mathbf{u}$ and p into the equations (1.3) and linearising by retaining

$\mathcal{O}(\epsilon)$ terms, we get

$$\frac{\partial \mathbf{u}'}{\partial t} + (\mathbf{U}\cdot\nabla)\mathbf{u}' + (\mathbf{u}'\cdot\nabla)\mathbf{U} = -\nabla p' + \frac{1}{R}\nabla^2\mathbf{u}' \tag{1.4a}$$

$$\nabla\cdot\mathbf{u}' = 0 \tag{1.4b}$$

which are often referred to as the *perturbation equations*. Indeed, the *perturbation equations* referred to throughout this document should be understood as the momentum and continuity equations for the perturbation quantities.

The following method relies on the base flow being *parallel*, which means that the velocity does not vary in the direction of the flow. This property is satisfied exactly for simple flows such as Poiseuille channel flow, but the method carries through for other flows provided we apply the so-called *parallel flow approximation*. This amounts to treating the streamlines as being approximately parallel and proceeding with the method anyway. Used with caution, non-parallel contributions can often be ignored in a system with few adverse effects, although this is not true for all flow configurations as will be discussed later in the context of the rotating disk boundary layer. Assuming for now that we are at liberty to apply it, the parallel flow approximation allows us to assume that the base flow is independent of x and y, thereby making the solution separable and enabling us to consider a normal mode solution in the form of a travelling wave given by

$$\mathbf{u}' = \hat{\mathbf{u}}(z)e^{i(\alpha x+\beta y-\omega t)}, \quad p' = \hat{p}e^{i(\alpha x+\beta y-\omega t)} \tag{1.5}$$

The parameters α, β and ω can be interpreted as the wavenumber in the x-direction, the wavenumber in the y-direction and the disturbance frequency respectively. The wavenumber is the spatial frequency of the travelling wave solution, and can be interpreted as the number of waves that exist over a specified distance. The full derivation of the Orr-Sommerfeld equation is standard and described thoroughly in many introductory texts to hydrodynamic stability so is omitted here, but the interested reader is referred to a very well presented derivation in [25]. Another standard result, Squire's theorem, which enables us to consider only two-dimensional disturbances when investigating the stability properties of a flow, is also stated, proven and described in reference [25]. Thus, we merely state here only the Orr-Sommerfeld equation for two-dimensional perturbations to the steady base flow $U(z)$ as

$$\left[(D^2-\alpha^2)^2 - iR\left((\alpha U-\omega)(D^2-\alpha^2) - \alpha U''\right)\right]\phi = 0 \tag{1.6}$$

where $D^2 = \frac{d^2}{dz^2}$ and the perturbation stream function ϕ is of the form

$$\hat{\phi}(x, z, t) = \phi(z)e^{i(\alpha x - \omega t)} \tag{1.7}$$

The boundary conditions that are imposed on ϕ are

$$\phi(z_1) = 0, \quad \phi(z_2) = 0, \quad \phi'(z_1) = 0, \quad \phi'(z_2) = 0 \tag{1.8}$$

where $z_1 \leq z_2$. Similar conditions hold for a semi-infinite or unbounded flow where either one or both of z_1 and z_2 are infinite.

1.2.1 Eigenvalue Solutions of the Orr-Sommerfeld Equation

The Orr-Sommerfeld equation (1.6) is a fourth order differential equation, which upon solving would admit four linearly independent solutions ϕ_1, ϕ_2, ϕ_3, ϕ_4 which could be written as

$$\phi = A_1\phi_1 + A_2\phi_2 + A_3\phi_3 + A_4\phi_4$$

subject to the boundary conditions (1.8). This can be recast in the usual way as a matrix problem

$$\begin{pmatrix} \phi_1(z_1) & \phi_2(z_1) & \phi_3(z_1) & \phi_4(z_1) \\ \phi_1(z_2) & \phi_2(z_2) & \phi_3(z_2) & \phi_4(z_2) \\ \phi_1'(z_1) & \phi_2'(z_1) & \phi_3'(z_1) & \phi_4'(z_1) \\ \phi_1'(z_2) & \phi_2'(z_2) & \phi_3'(z_2) & \phi_4'(z_2) \end{pmatrix} \begin{pmatrix} A_1 \\ A_2 \\ A_3 \\ A_4 \end{pmatrix} = \begin{pmatrix} 0 \\ 0 \\ 0 \\ 0 \end{pmatrix}$$

which has non-zero solutions if the determinant of the matrix on the left hand side is zero. Hence, the solution for the eigenvalues of the Orr-Sommerfeld equation (1.6) can be expressed in the form of the eigenvalue relation

$$\mathcal{D}(\omega, \alpha, Re) = 0 \tag{1.9}$$

This generalised eigenvalue problem (1.9) is called the *Orr-Sommerfeld problem* and is attributed independently to Orr [55] and Sommerfeld [68]. This equation is central to stability theory since the analysis of the eigenvalues of this equation for a fixed Reynolds number provides insight into the linear stability properties of flow configurations. There are two main types of stability analysis usually performed, *temporal* and *spatial*, which impose conditions on α and ω and are outlined below.

- If α is fixed real and ω the complex eigenvalue then the disturbances are periodic in x and grow or decay in time depending on the sign of the imaginary part of ω. In this analysis, the eigenvalue ω appears linearly in the stability equation. This is called *temporal* stability analysis.

- If ω is prescribed real and α the complex eigenvalue then the disturbances are periodic in time and grow or decay exponentially with x. This is termed *spatial* stability analysis and the corresponding disturbance growth may be observed in reality.

Inspection of the normal mode approximation (1.7) reveals that we can interpret the real and imaginary parts of α as the spatial frequencies and growth rates respectively, and similarly for ω. The original comparisons between experimental results and the growth rates predicted by linear theory were based on converting temporal growth rates into spatial growth rates using a downstream convection speed. However, as argued by Gaster [37], it is more physical to calculate the spatial growth rates directly and this is now computationally feasible. The difficulty with this approach is that the eigenvalue α appears non-linearly with a fourth power, forming a polynomial eigenvalue problem. A method for dealing with this issue is given by Bridges and Morris [14] which involves an indefinite integration of the Orr-Sommerfeld equation and the use of Chebyshev polynomials to solve the eigenvalue problem. Other methods of solving spatial eigenvalue problems exist, such as those based on a differential formulation, as seen in Trefethen [79] or on a system of first order equations, see Malik [50], but the integral formulation of Bridges and Morris [14] has some advantages over these other methods which will be discussed in section 1.3. This integral formulation provides the solution method for the majority of analyses conducted through this work and will be discussed at length throughout this thesis.

1.2.2 Inviscid Theory and Rayleigh's Equation

In the interest of completeness, we briefly consider the limit of inviscid flows and Rayleigh's equation, which is the counterpart of the Orr-Sommerfeld equation in this limit. Fixing z and α and letting $R \to \infty$, the Orr-Sommerfeld equation (1.6) becomes

$$(U - c)(D^2 - \alpha^2)\phi - U''\phi = 0 \tag{1.10}$$

which is known as Rayleigh's equation. Since this equation is only of second order, we only require the two boundary conditions

$$\phi(z_1) = 0, \quad \phi(z_2) = 0$$

This equation is important in the study of flows for which the use of an inviscid fluid gives a good approximation to the stability characteristics of a viscous fluid at large Reynolds numbers. Care must be taken however and in fact, viscosity, although it dissipates energy, may destabilise a flow which is stable for an inviscid fluid. Introducing viscosity introduces a viscous layer near the wall that brings this inviscid slip velocity down to zero at the wall in what is known as *boundary layer* behaviour. Prandtl [58] suspected that the inclusion of a viscous wall layer could be destabilizing and Tollmien [77] found asymptotic solutions to the Orr-Sommerfeld equation for profiles with no inflection point predicting instability but their counter-intuitive results were not widely accepted until this behaviour was verified in wind tunnel experiments on boundary layers in the 1940s. It had been previously assumed that the additional friction associated with viscosity would be stabilising, but this turned out not to be the case. Therefore, while inviscid theory can be used to investigate stability, it must be used with caution and indeed if it predicts stability then this may not give the correct behaviour once viscosity is incorporated. However in general, if the inviscid theory predicts instability then it will usually be correct with small viscous corrections.

1.3 Numerical Solutions of the Orr-Sommerfeld Equation using Chebyshev Series Expansions

This section turns attention back to the Orr-Sommerfeld equation (1.6) and discusses in detail the procedure taken to solve the resulting eigenvalue problem. A standard technique, detailed in Bridges and Morris [14], will be briefly discussed to provide context before we introduce a method based on a velocity-vorticity formulation of the Navier-Stokes equations which to the extent of our literature search has not been described previously. This approach will be described in detail for the standard Blasius flow configuration which will serve as an introduction to the added three-dimensional complexities later studied in the context of the linear stability of the rotating disk boundary layer. The solution procedure relies on expanding the disturbance functions in terms of Chebyshev

polynomials and a form of the Chebyshev-tau method. In the interest of concision we will assume throughout that the base flow and disturbance functions live in an appropriate functional space and can thus be expanded in terms of Chebyshev polynomials.

The Chebyshev polynomials T_n are defined in the standard way as

$$T_n(x) = \cos(n \arccos(x)), \quad x \in [-1, 1] \tag{1.11}$$

and using basic trigonometric identities, we can derive the recursion relations

$$T_0(x) = 1$$
$$T_1(x) = x$$
$$T_{k+1}(x) = 2xT_k(x) - T_{k-1}(x) \quad \text{for} \quad k \in \{1, 2, ...\}$$

These polynomials have many properties which have made them a favourable choice for spectral expansions in computational mathematics for many years. They are orthogonal functions in the domain $[-1, 1]$ with respect to their defining inner product and hence, in the appropriate space, any function can be expressed via the expansion

$$f(x) = \sum_{k=0}^{\infty} c_k T_k(x)$$

while the coefficients c_k are determined from some appropriate inner product relation. While not unique in their ability to do so, they also alleviate some of the computational phenomena associated with either interpolation by trigonometric polynomials or interpolation on equally spaced points.

The most important advantage of the Chebyshev series representations in terms of the work conducted for this report is their close links with Fourier series and the availability of a Fast Fourier Transform (FFT) for computationally transforming between physical space and Chebyshev space. The FFT has been discussed extensively by several authors including Boyd [13] and Trefethen [79] and so only the main points will be discussed here. In particular, since throughout this work we will work mainly with even and odd representations separately, we lean towards discussing these cases in what follows.

1.3.1 The Fast Fourier Transform for Chebyshev Series

We begin by introducing Fourier spectral methods in general, before moving towards describing the methods used in this report regarding Chebyshev expansions. It is well

known that the *Fourier transform* of a function $f(\theta)$ is the function $F(k)$ defined by

$$F(k) = \int_{-\infty}^{\infty} e^{-ik\theta} f(\theta) d\theta, \quad k \in \mathbb{R} \tag{1.12}$$

and we can interpret the transformed variable F as a decomposition of the physical variable f into sinusoids of different frequencies. Similarly, we can recover the physical variable f from F by way of the *inverse Fourier transform*

$$f(x) = \frac{1}{2\pi} \int_{-\infty}^{\infty} e^{ik\theta} F(k) dk, \quad \theta \in \mathbb{R} \tag{1.13}$$

As one might imagine, these transforms have discrete analogues which are appropriate for computational problems on discretised domains. If we consider a bounded, periodic interval $[0, 2\pi]$ and divide it into an equally spaced grid with N points, labelled θ_j and a grid spacing $h = \frac{2\pi}{N}$, then the *discrete Fourier transform* of a function $f(\theta)$ evaluated at the points θ_j is given by

$$c_k = h \sum_{j=1}^{N} e^{-ik\theta_j} f(\theta_j), \quad k = -\frac{N}{2} + 1, \ldots, \frac{N}{2} \tag{1.14}$$

while the *inverse discrete Fourier transform* is given by

$$f(\theta_j) = \frac{1}{2\pi} \sum_{k=-N/2+1}^{N/2} e^{ik\theta_j} c_k, \quad j = 1, \ldots, N \tag{1.15}$$

We have assumed here that N is even, as we will throughout, although similar results hold for odd N. The periodicity refers to the fact that any data on the grid points comes from evaluating a periodic function, while periods of lengths other than 2π are easily accommodated by some scaling factor. Of course, this periodic restriction is a serious one, and not all problems can be treated as such. If we were to periodically extend a smooth but inherently non-periodic function then the contamination caused by the discontinuities would be global if using equally spaced points as we have above. This is known as the Gibbs phenomenon and destroys the spectral accuracy of the scheme.

This problem can be alleviated by using *unevenly* spaced points in the periodic domain an example of which we illustrate by considering the domain $[-1, 1]$. Various different sets of points can be used, but they mainly share the common property that

$$\text{density} \approx \frac{N}{\pi\sqrt{1 - x^2}} \tag{1.16}$$

This has the effect of clustering the points near the boundaries, with the average grid spacing being $\mathcal{O}(N^{-2})$ for $x \approx \pm 1$ and $\mathcal{O}(N^{-1})$ away from the boundaries. Our example

of such points are the well-known *Chebyshev-Lobatto* or *Chebyshev-extreme* collocation points in $[-1, 1]$ given by

$$x_j = \cos\left(\frac{j\pi}{N}\right), \quad j = 0, \ldots, N \tag{1.17}$$

These points are naturally associated with the Chebyshev polynomials T_n, since they are the extreme values of T_n in $[-1, 1]$. If, as we will do often in what follows, we choose to work only with odd and even Chebyshev representations separately then we can define our collocation points on the half-grid $(0, 1]$ as

$$x_j = \cos\left(\frac{j\pi}{2N}\right), \quad j = 0, \ldots, N-1 \tag{1.18}$$

We can also derive direct relations between Fourier series and Chebyshev series by applying some transformations to the variable θ in equation (1.14). As we have seen, the Fourier transform is applicable on the domain $\mathbb{R}$ and so taking some $\theta \in \mathbb{R}$, we can recover the domain $x \in [-1, 1]$ by writing $x = \cos(\theta)$. Thus, combining this with equation (1.11), the Chebyshev polynomials on $[-1, 1]$ can be written as

$$T_n(x) = \cos(n\theta) \tag{1.19}$$

and it can be shown using trigonometric identities that T_n defines a polynomial of degree n and that T_n is odd when n is odd and even when n is even. Since T_n is exactly degree n for each n, any N degree polynomial can be written uniquely as a linear combination of Chebyshev polynomials. Thus, if we have a degree N polynomial p such that

$$p(x) = \sum_{n=0}^{N} p_n T_n(x), \quad x \in [-1, 1] \tag{1.20}$$

then there is the equivalent representation for the 2π-periodic even trigonometric polynomial P given by

$$P(\theta) = \sum_{n=0}^{N} p_n \cos(n\theta), \quad \theta \in \mathbb{R} \tag{1.21}$$

Hence, given an arbitrary function f defined on $[-1, 1]$, we can draw the comparison between the Chebyshev and Fourier series by saying that $P(\theta)$ interpolates f at the equispaced points θ_j while $p(x)$ interpolates f at the Chebyshev points x_j.

Similar ideas can be employed when considering odd and even Chebyshev representations separately. Any function $f(x)$ which is *symmetric* about 0 in x or about $\frac{\pi}{2}$ in θ can be written as

$$f(x) = \frac{f_0}{2} + \sum_{n=1}^{\infty} f_n T_{2n}(x), \quad x \in (0, 1] \tag{1.22}$$

since all even degree cosines have the same property. The halving of the first term in a Chebyshev expansion is standard practice, and helps with consistency for several identities. Similarly, a function $g(x)$ which is *anti-symmetric* about 0 in x or about $\frac{\pi}{2}$ in θ takes the form

$$g(x) = \sum_{n=1}^{\infty} a_n T_{2n-1}(x), \quad x \in (0, 1] \tag{1.23}$$

since all odd degree cosines have the same property. When talking about these representations throughout this report, we will describe them as *even* and *odd* representations respectively. The reader should be aware of a possible confusion. The labelling *even* and *odd* refers to the degree of the expansion polynomials, and thus to the representation in terms of $x \in (0, 1]$.

The transformations between physical space and Chebyshev space are necessary for many situations, including several outlined in this report. A solution method which travels back and forth between physical space and Chebyshev space is generally called a *pseudo-spectral* method, where the advantages of each space are exploited at each stage. For example, integration and differentiation are far easier and more accurate when performed in Chebyshev space, while products between functions are easiest performed in physical space. Since the Chebyshev series are so closely related to Fourier series, there is the availability of a highly efficient technique called the Fast Fourier Transform (FFT) for converting from physical space to Chebyshev space and vice-versa. This transform can be computed in $\mathcal{O}(N \log N)$ steps, as opposed to the $\mathcal{O}(N^2)$ required for a standard Fourier transform. The algorithm for the FFT is standard and largely irrelevant for the purpose of this report, since most numerical algorithms libraries such as NAG [53] and MATLAB have built in routines that carry out the transforms. The precise details of the algorithm are therefore omitted here for brevity, while the interested reader is directed to Boyd [13] or Trefethen [79] where a thorough introduction and explanation is given.

Given the parities which we are interested in utilising, we can adapt the FFT routine slightly and define the *discrete cosine transform* as

$$f_k = \frac{1}{2}x_0 + \sum_{j=1}^{n-1} x_j \cos\left(\frac{jk\pi}{n}\right) + \frac{1}{2}(-1)^k x_n, \quad k = 0, \ldots, n-1 \tag{1.24}$$

which is equivalent up to an overall scale factor of 2 to a discrete Fourier transform of length $2(N-1)$ with even symmetry. This is its own inverse, when multiplied by $2/(N-1)$. This routine can be used directly to calculate the even Chebyshev coefficients of a function

which can be approximated by a sum of even Chebyshev polynomials and likewise in the opposite direction. In practise, it is accomplished using the proprietary NAG [53] routine C06RBF or the open-source routine *dcost* from *dfftpack* [54].

The transformations for the odd representations are not so obvious, but can be achieved by way of the *discrete quarter-wave sine transform* which can be defined as

$$g_k = \sum_{j=1}^{n-1} x_j \sin\left(\frac{j(2k-1)\pi}{2n}\right) + \frac{1}{2}(-1)^{(k-1)}x_n, \quad k = 0, \ldots, n \tag{1.25}$$

with inverse

$$x_k = 2\sum_{j=1}^{n} g_j \sin\left(\frac{j(2k-1)\pi}{2n}\right) \quad k = 0, \ldots, n \tag{1.26}$$

Given a representation

$$g(x_j) = \sum_{n=1}^{\infty} g_n T_{2n-1}(x_j), \quad x \in (0, 1] \tag{1.27}$$

we can write

$$G(\theta_j) = \sum_{n=1}^{\infty} g_n \cos\left[\frac{(2n-1)j\pi}{2N}\right] \tag{1.28}$$

where the collocation points x_j are defined by equation (1.18). Using the trigonometric identity

$$\cos(\phi) = \sin\left(\phi + \frac{\pi}{2}\right) = -\sin\left(\phi - \frac{\pi}{2}\right) \tag{1.29}$$

and setting $h_n = (-1)^{n-1}g_n$ we get

$$G(\theta_{N-j}) = \sum_{n=1}^{\infty} h_n \sin\left[\frac{(2n-1)j\pi}{2N}\right] \tag{1.30}$$

which is in the correct form for a discrete quarter-wave sine transform. In practise, this transform is accomplished using the proprietary NAG routine C06RCF [53] or the open-source routine *dsinqt* from *dfftpack* [54].

1.3.2 Numerical Solution of the Orr-Sommerfeld Equation

There appear to be two standard methods for solving the temporal and spatial eigenvalue problems associated with the Orr-Sommerfeld equation. The first, based on derivatives of Chebyshev polynomials is discussed in many texts including Trefethen [79] and Schmid and Henningson [65] and utilises the identity

$$2T_k(x) = \frac{1}{k+1}T'_{k+1}(x) - \frac{1}{k-1}T'_{k-1}(x) \tag{1.31}$$

where $T_0'(x) = 0$ and $T_1'(x) = 1$ to derive the so-called *differentiation* matrices $D^k \approx \frac{d^k}{dx^k}$ which operate on the physical values of the function being differentiated. This approach is discussed in great detail by Trefethen [79] and has been formalised in a MATLAB library called *chebfun* [78].

While this approach is effective and has long been used for this type of problem, we will adopt an alternative technique, described in Bridges and Morris [14], in which the Orr-Sommerfeld equation is integrated indefinitely and solved using matrix representations of the integral operators. The integrated form of the Chebyshev polynomials takes a somewhat more convenient form than the differentiated form and so has been chosen as the solution method for all cases in this report. The main advantage of the integral operators is that they can be expressed as n-diagonal banded matrices, for relatively small n, as opposed to the fully populated ones present in the differential formulation. In time-dependent simulations, and in particular the ones carried out for the rotating disk in chapter 2, this allows for a modified Thomas algorithm to be implemented at each time step, rather than a full matrix inversion. The matrix representations of the operators in the differential formulation are fully populated and would thus greatly increase the computational cost. The same advantage is not present in the eigenvalue problem however, since products of the base flow profile with the disturbance variable lead to fully populated matrices, but the integral formulation is retained since the operator definitions are identical in both cases and thus only need to be derived once.

As an illustration of the banded representation, we can derive the following identity for the integration of Chebyshev polynomials from equation (1.31)

$$\int T_n(x)dx = \begin{cases} \frac{T_{n+1}(x)}{2(n+1)} - \frac{T_{n-1}(x)}{2(n-1)} & n \geq 2 \\ \frac{1}{4}[T_0(x) + T_2(x)] & n = 1 \\ T_1(x) & n = 0 \end{cases} \tag{1.32}$$

Considering the interpolating polynomial p to an arbitrary appropriate function f defined on $[-1, 1]$ with Chebyshev representation

$$p(x) = \sum_{n=0}^{N} p_n T_n(x)$$

we can write

$$\begin{aligned}\int f(x)dx &\approx \sum_{n=0}^{N} p_n \int T_n(x)dx \\ &= aT_0(x) + p_0T_1(x) + \frac{1}{4}[T_0(x) + T_2(x)]p_1 + \frac{1}{2}\sum_{n=2}^{N}\left(\frac{T_{n+1}(x)}{n+1} - \frac{T_{n-1}(x)}{n-1}\right)p_n \\ &= aT_0(x) + +p_0T_1(x) + \frac{1}{4}[T_0(x) + T_2(x)]p_1 + \frac{1}{2}\sum_{n=2}^{N}\frac{1}{n}(p_{n-1} - p_{n+1})T_n(x)\end{aligned}$$

where a is an arbitrary constant of integration. This results in a tridiagonal banded matrix representation for the integral operator $\mathbf{I}_1 := \int$.

1.4 Linear Stability of Two-Dimensional Parallel Flows using a Velocity-Vorticity Formulation

The method of Bridges and Morris [14] proceeds by indefinitely integrating Orr-Sommerfeld equation (1.6) four times with respect to the single flow coordinate variable and rearranging to give a polynomial eigenvalue equation in α given by

$$\begin{aligned}&\alpha^4 \iiiint \phi + \alpha^3\left(iR \iiiint U\phi\right) + \alpha^2\left(-2\iint \phi - i\omega R \iiiint \phi\right) + \\ &\alpha\left(2iR\iiint U'\phi - iR\iint U\phi\right) + \left(\phi + i\omega R\iint \phi\right) + \frac{b_1y^3}{6} + \frac{b_2y^2}{2} + b_3y + b_4 = 0\end{aligned} \tag{1.33}$$

where b_i, $i = 1, \ldots, 4$ denote constants of integration. We note that, throughout this thesis, repeated integrals are taken with respect to the same variable as the goal of the integration procedure is to eliminate higher order derivatives in the equations in preparation for the numerical solution method. This notation is standard in the literature, see Bridges and Morris [14] and Cooper and Carpenter [19]. Whilst no further mention of this exact solution method will be given in this report, many of the same ideas carry through to our new formulation which we present in detail. The results of Bridges and Morris [14] were used as a validation tool for the new method and are described in detail for the Poiseuille channel flow by the authors of [14]. The interested reader is referred to the references for further details.

1.4.1 The Velocity-Vorticity Formulation of the Navier-Stokes Equations

In 2001, Davies and Carpenter [26] developed a velocity-vorticity formulation of the unsteady, three-dimensional Navier-Stokes equations which is particularly suitable for simulating the evolution of disturbances in three-dimensional boundary layers.

Velocity-vorticity methods provide a convenient format for dealing with unsteady flow fields and have several advantages over traditional methods, a key one being that there are only three governing equations for three dependent variables, the so-called *primary* variables.

In this formulation, the dependent variables are perturbations to a known, undisturbed flow field where the three primary variables comprise two vorticity components and the wall normal velocity component. These are governed by two vorticity transport equations and a Poisson equation. The *secondary* variables consist of the remaining velocity and vorticity components and the pressure and can be determined explicitly from the primary variables by means of an integral. It is shown by Davies and Carpenter [26] that, subject to some fairly general conditions at infinity, the formulation is fully equivalent to the Navier-Stokes equations. It is also worth noting that the only fundamental boundary conditions are those that must be imposed on the velocity field, and in Davies and Carpenter's [26] formulation, no boundary conditions at the wall are needed for the vorticity. Instead, integral conditions can be derived from the definition of vorticity, which will be discussed later.

To introduce this method, we consider the velocity-vorticity formulation for the Blasius boundary layer. This flow is two-dimensional and has been included here to serve as a stepping-stone to the analysis of the three-dimensional rotating disk boundary layer. Although there is no necessity to use the velocity-vorticity formulation for the spatial stability analysis of this flow, there is a significant advantage to doing so. This is due to the fact that the perturbation equations are reduced to two second order equations, as opposed to one fourth order one, making the integral operator definitions much neater and more amenable to calculations. It should also be noted that the following derivation is base flow independent, provided the base flow in question is either steady or temporally periodic, two dimensional and parallel. Validation of this new approach was also carried out against the well-documented Poiseuille channel flow but these results are not presented

here.

Consider a base flow $\mathbf{U}_B = (U_B, V_B, W_B)$ with vorticity $\boldsymbol{\Xi} = \nabla \times \mathbf{U} = (\Xi_x, \Xi_y, \Xi_z)$. Let $\mathbf{u}$ denote the usual velocity perturbation components and $\boldsymbol{\xi}$ the vorticity perturbation. Then the velocity-vorticity formulation equations for the three primary variables $\{\xi_x, \xi_y, w\}$ take the form

$$\frac{\partial \xi_x}{\partial t} + \frac{\partial N_z}{\partial y} - \frac{\partial N_y}{\partial z} = \frac{1}{R}\nabla^2 \xi_x \tag{1.34a}$$

$$\frac{\partial \xi_y}{\partial t} + \frac{\partial N_x}{\partial z} - \frac{\partial N_z}{\partial x} = \frac{1}{R}\nabla^2 \xi_y \tag{1.34b}$$

$$\nabla^2 w = \frac{\partial \xi_x}{\partial y} - \frac{\partial \xi_y}{\partial x} \tag{1.34c}$$

where $\mathbf{N} = (N_x, N_y, N_z)$ is defined as

$$\mathbf{N} = \boldsymbol{\Xi} \times \mathbf{u} + \boldsymbol{\xi} \times \mathbf{U}_B + \boldsymbol{\xi} \times \mathbf{u} \tag{1.35}$$

Linearisation can be performed if necessary by dropping out the $\boldsymbol{\xi} \times \mathbf{u}$ term in $\mathbf{N}$.

The convective quantity $\mathbf{N}$ can only be evaluated if the secondary variables $\{u_x, u_y, \xi_z\}$ are known. Thus, we make the explicit definitions

$$u_x = -\int_z^\infty \left(\xi_y + \frac{\partial w}{\partial x}\right) dz \tag{1.36}$$

$$u_y = \int_z^\infty \left(\xi_x - \frac{\partial w}{\partial y}\right) dz \tag{1.37}$$

$$\xi_z = \int_z^\infty \left(\frac{\partial \xi_x}{\partial x} + \frac{\partial \xi_y}{\partial y}\right) dz \tag{1.38}$$

which are obtained by integrating the appropriate definitions of vorticity via the usual relation $\boldsymbol{\xi} = \nabla \times \mathbf{u}$.

Boundary Conditions

We will present here an overview of the imposed boundary conditions in the case of an unbounded flow contained by a stationary flat plate located at $z = 0$. The boundary conditions imposed on the system are derived from the no-penetration and no-slip conditions at the wall and the integral constraint imposed on the vorticity. Hence, at the stationary boundary wall $z = 0$, we immediately have the boundary conditions

$$u_x(0) = \int_0^\infty \left(\xi_y + \frac{\partial w}{\partial x}\right) dz = 0 \tag{1.39a}$$

$$u_y(0) = \int_0^\infty \left(\xi_x - \frac{\partial w}{\partial y}\right) dz = 0 \tag{1.39b}$$

$$w(0) = 0 \tag{1.39c}$$

As discussed in Davies and Carpenter [26], there are no issues in implementing the condition $w \to 0$ as $z \to \infty$ as the vanishing of w provides a boundary condition for the solution of the Poisson equation (1.42b). It remains to constrain the other two primary variables ξ_x and ξ_y in the far field, which is achieved in practise by enforcing vanishing conditions at infinity. The validity of this approach is explained in detail in Davies and Carpenter [26] and essentially reduces to the requirement that the z-derivatives of the three primary variables vanish for $z \to \infty$. In practise, it is possible to satisfy this condition by making use of the coordinate transformation

$$\eta = \frac{l}{z+l} \tag{1.40}$$

which maps the semi-infinite physical domain $z \in [0, \infty)$ to the computational domain $\eta \in (0, 1]$ for some stretching factor l. This mapping transforms the z-derivative operators to

$$\frac{\partial f}{\partial z} = -\frac{\eta^2}{l}\frac{\partial f}{\partial \eta} \tag{1.41}$$

and it is clear that the requirement that the z-derivatives of the primary variables vanish for $z \to \infty$ becomes a condition that the η-derivative remains bounded as η approaches zero. Further discussion about this condition is given by Davies and Carpenter [26] but for now we will assume it will be satisfied for our perturbation variables and proceed to derive the corresponding formulation for two dimensional flows.

Reduction of the Full System to Two Dimensions

In two dimensions, consider a parallel base flow $\mathbf{U}_B = U_B(z,t)$. If, as for the three-dimensional case, we let u and w denote the usual streamwise and wall-normal velocity perturbation components and ξ the vorticity perturbation then the velocity-vorticity formulation equations take the form

$$\frac{\partial \hat{\xi}}{\partial t} + U\frac{\partial \hat{\xi}}{\partial x} + \underbrace{\frac{\partial(\hat{u}\omega)}{\partial z} + \frac{\partial(\hat{w}\xi)}{\partial y}}_{non-linear} + wU'' = \frac{1}{R}\nabla^2\hat{\xi} + \underbrace{\frac{1}{R}U'''}_{non-parallel} \tag{1.42a}$$

$$\nabla^2\hat{w} = -\frac{\partial \hat{\xi}}{\partial x} \tag{1.42b}$$

where the single secondary variable $\hat{u}$ is given by

$$\hat{u} = -\int_z^\infty \left(\hat{\xi} + \frac{\partial \hat{w}}{\partial x}\right) dz$$

and we have written $U'(z) := \frac{\partial U}{\partial z}$. Linearisation can be obtained by dropping out the terms with underbraces in the first of the above equations, equivalent to the linearisation achieved by dropping the $\boldsymbol{\xi} \times \mathbf{u}$ in equation (1.35). The non-parallel term also indicated by underbraces is removed under the parallel flow approximation. Having done this, we arrive at the two-dimensional velocity-vorticity perturbation equations

$$\frac{\partial \hat{\xi}}{\partial t} + U\frac{\partial \hat{\xi}}{\partial x} + wU'' = \frac{1}{R}\nabla^2\hat{\xi} \tag{1.43a}$$

$$\nabla^2\hat{w} = -\frac{\partial \hat{\xi}}{\partial x} \tag{1.43b}$$

At this stage we divide our discussion into two parts to consider steady and temporally periodic two-dimensional base flows separately, beginning with the steady case.

1.4.2 Two-Dimensional Steady Base Flow

Considering the base flow in question to be steady, we may assume a separable form for the perturbation and, as usual, take a normal mode approximation of the form

$$\hat{w} = we^{i(\alpha x - \omega t)} \qquad \hat{\xi} = \xi e^{i(\alpha x - \omega t)}$$

where α and ω have the same interpretations as in section 1.2.1. Substitution into the perturbation equations (1.43) gives the system of two second order ordinary differential equations

$$-i\omega\xi + i\alpha U\xi + wU'' = \frac{1}{R}(D^2 - \alpha^2)\xi \tag{1.44}$$

$$(D^2 - \alpha^2)w = -i\alpha\xi \tag{1.45}$$

where $D^2 = \frac{d^2}{dz^2}$. Following a similar procedure to that described by Bridges and Morris [14], we integrate the equations twice indefinitely and rearrange to get the polynomial eigenvalue equations in α

$$\left[\alpha^2\left(\frac{1}{R}\iint \xi dz\right) + \alpha\left(i\iint U\xi dz\right) + \left(-i\omega\iint \xi dz - \frac{1}{R}\xi\right)\right] + \left[\iint U''w dz\right] + a_1x + a_0 = 0 \tag{1.46a}$$

$$\left[\alpha\left(i\iint \xi dz\right)\right] + \left[\alpha^2\left(-\iint w dz\right) + w\right] + b_1x + b_0 = 0 \tag{1.46b}$$

where a_0, a_1, b_0 and b_1 are arbitrary constants of integration.

Eigenvalue Solutions

Given a base flow $\mathbf{U}_B$, we are able to expand both the perturbation variables and the base flow profile in terms of Chebyshev polynomials and derive matrix representations of the operators

$$\iint f dz \quad \text{and} \quad \iint U f dz \tag{1.47}$$

where f is an arbitrary perturbation variable. The boundary conditions are included in the system by replacing the matrix rows that would otherwise determine the four constants a_0, a_1, b_0 and b_1. This can be interpreted as a form of the tau-method and a similar method is described in Bridges and Morris [14]. The boundary conditions along with the operator form of the velocity-vorticity perturbation equations thus give a system of $(2N \times 2N)$ equations of the form

$$\begin{pmatrix} \mathbf{A}_0\alpha^2 + \mathbf{A}_1\alpha + \mathbf{A}_2 & \mathbf{B}_0\alpha^2 + \mathbf{B}_1\alpha + \mathbf{B}_2 \\ \mathbf{C}_0\alpha^2 + \mathbf{C}_1\alpha + \mathbf{C}_2 & \mathbf{D}_0\alpha^2 + \mathbf{D}_1\alpha + \mathbf{D}_2 \end{pmatrix} \begin{pmatrix} \xi \\ w \end{pmatrix} = \begin{pmatrix} 0 \\ 0 \end{pmatrix}$$

where $\mathbf{A}$, $\mathbf{B}$, $\mathbf{C}$ and $\mathbf{D}$ should be clear from (1.46). Bridges and Morris [14] present two methods for solving this polynomial eigenvalue equation, namely the companion and the lambda matrix methods. Both of these are now largely obsolete and can be accomplished by a simple call of MATLAB's *polyeig* function.

Eigenvalue solution methods are often prone to *spurious* eigenvalues, those that are not true eigenvalues of the perturbation equations. These spurious eigenvalues may be attributed to the solution method of the problem and may be either stable or unstable. Stable spurious eigenvalues are of little importance because the stable eigenvalues are rarely of interest, however spurious unstable eigenvalues are highly undesirable since they could wrongly predict an instability. There are two types of spurious eigenvalues which *must* be distinguished in order to be sure of their accuracy. The first are *physically spurious* eigenvalues, which are numerically computed eigenvalues in error because of misapplication of boundary conditions or some other misrepresentation of the physics. Boyd [13, p. 139] presents an example of how these physically spurious eigenvalues can show up in a system and so the reader is referred to the references for details. The other type of spurious eigenvalue are those which are *numerically spurious*. These are poor approximations to exact eigenvalues because the mode may be oscillating too rapidly to be resolved using a given discretisation, and can always be computed accurately using a

sufficiently large degree Chebyshev approximation. The physically spurious eigenvalues can often be eliminated by using basic row and column operations on the matrix representations of the integral operators. If the four boundary conditions are confined to the top four rows of the matrix operators then we can apply row and column operations in the following way

$$\underbrace{\begin{pmatrix} a_0 & \cdots & a_{N-3} & a_{N-2} & a_{N-1} & a_N \\ b_0 & \cdots & b_{N-3} & b_{N-2} & b_{N-1} & b_N \\ c_0 & \cdots & c_{N-3} & c_{N-2} & c_{N-1} & c_N \\ d_0 & \cdots & d_{N-3} & d_{N-2} & d_{N-1} & d_N \\ \cdots & \cdots & \cdots & \cdots & & \end{pmatrix}}_{} = 0$$

$$\rightarrow \begin{pmatrix} 0 & \cdots & \tilde{a}_{N-3} & \tilde{a}_{N-2} & \tilde{a}_{N-1} & \tilde{a}_N \\ 0 & \cdots & 0 & \tilde{b}_{N-2} & \tilde{b}_{N-1} & \tilde{b}_N \\ 0 & \cdots & 0 & 0 & \tilde{c}_{N-1} & \tilde{c}_N \\ 0 & \cdots & 0 & 0 & 0 & \tilde{d}_N \\ \cdots & \cdots & \cdots & \cdots & \cdots & \cdots \end{pmatrix}$$

Neglecting these rows from consideration will give a non-singular matrix of order $2(N-1)\times 2(N-1)$ in the polynomial eigenvalue problem and is shown in Boyd [13] and Bridges and Morris [14] to eliminate physically spurious eigenvalues. The other variety, numerically spurious eigenvalues, have very large magnitudes compared with genuine modes and will usually scale like $\mathcal{O}(N^4)$ where N is the degree of the Chebyshev polynomial approximation. This makes them easily distinguishable in practise, and any extremely large magnitude eigenvalues are often irrelevant for stability calculations.

An alternative method of eliminating spurious eigenvalues is to use two different orders of polynomial expansion and compare the results. The genuine eigenvalues are usually picked up by both expansions provided the difference in discretisation order is large enough to achieve genuine convergence. Both types of spurious eigenvalue may be noticed and discarded in this case as they fail to converge as the orders of expansion are increased.

Local Eigenvalue Iteration

Given an appropriate initial guess α_k, a cubically convergent method described in Bridges and Morris [14] can be used to evaluate the eigenvalue α. We can iteratively improve the

guess by the formula

$$\alpha_{k+1} = \alpha_k - \frac{2f(\alpha_k)}{f(\alpha_k)^2 - f_1(\alpha_k)} \tag{1.48}$$

where

$$f(\alpha_k) = \mathrm{Tr}[\mathbf{D}^{-1}(\alpha_k)\mathbf{D}'(\alpha_k)]$$
$$f_1(\alpha_k) = \mathrm{Tr}\{\mathbf{D}^{-1}(\alpha_k)\mathbf{D}''(\alpha_k) - [\mathbf{D}^{-1}(\alpha_k)\mathbf{D}'(\alpha_k)]^2\}$$

and $\mathbf{D}'(\alpha)$ and $\mathbf{D}''(\alpha)$ are the derivatives of $\mathbf{D}$ with respect to α.

1.4.3 Application of Solution Method to the Blasius Boundary Layer

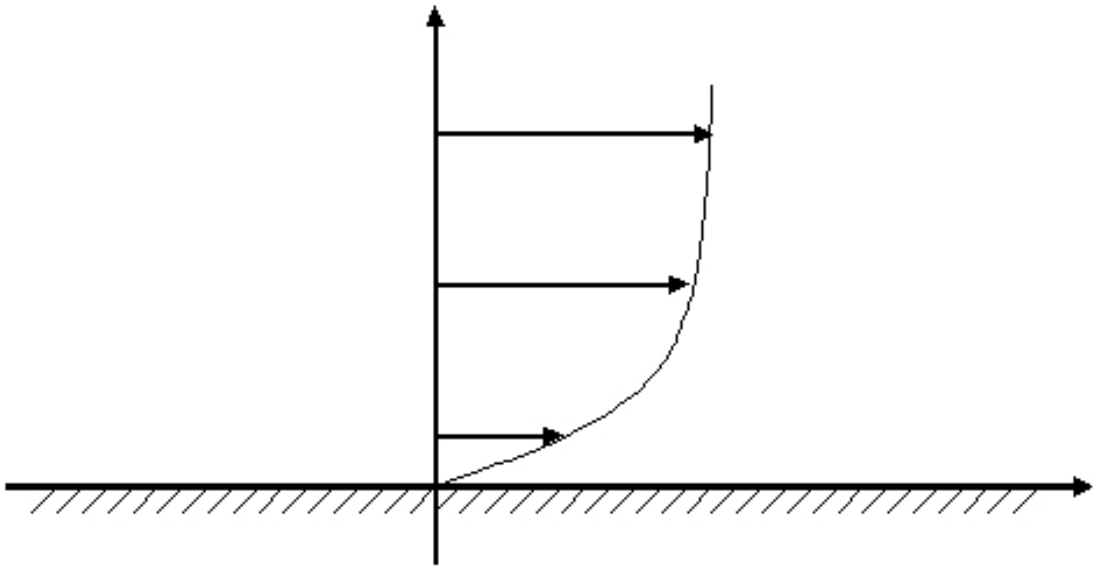

Figure 1.3: Schematic of Blasius boundary layer flow configuration.

In the interest of validation and to provide an exemplar application of the new method, we present now the solution procedure for the Blasius boundary layer configuration. This configuration has several features in common with the rotating disk which will be the main focus of this report. Since the formulation for the disk is particularly involved, this case will illustrate the methods while keeping the algebra relatively accessible. Assume we have a base flow $\mathbf{U}_B = (U_x, 0, U_z)$ which describes the steady flow over a semi-infinite plate, forming the standard two dimensional Blasius boundary layer at the plate, as seen

in figure 1.3. Assume the free-stream velocity of the fluid is U_∞. Then from a standard order of magnitude analysis, we can derive the boundary layer equations in dimensional form which are given by

$$\frac{\partial U_x}{\partial x} + \frac{\partial U_z}{\partial z} = 0$$
$$U_x \frac{\partial U_x}{\partial x} + U_z \frac{\partial U_x}{\partial z} = \nu \frac{\partial^2 U_x}{\partial z^2}$$

Defining a streamfunction ψ such that

$$U_x = \frac{\partial \psi}{\partial z}, \quad U_z = -\frac{\partial \psi}{\partial x}$$

and substituting into the boundary layer equations gives

$$\frac{\partial \psi}{\partial z}\frac{\partial^2 \psi}{\partial x \partial z} - \frac{\partial \psi}{\partial x}\frac{\partial^2 \psi}{\partial z^2} = \nu \frac{\partial^3 \psi}{\partial z^3}$$

Following the standard derivation, introducing a similarity variable ζ such that

$$\zeta = z\sqrt{\frac{U_\infty}{\nu x}}, \quad \psi = \sqrt{\nu U_\infty x} F(\zeta)$$

we arrive at the third order ordinary differential equation

$$F''' + \frac{1}{2} F F'' = 0 \tag{1.49}$$

subject to the boundary conditions arising from no slip and no penetration $F(0) = F'(0) = 0$ and $F \to 0$ as $\zeta \to \infty$, derived using the relationship between ψ and F.

Due to the relationship between ζ, z and x, we can see that the base flow, expressed in terms of the single similarity variable ζ, is $U_B = F'(\zeta)$ where we have set $U_\infty = 1$ and scaled the other variables accordingly.

Numerical Solution of the Base Flow Equations

For the stability analysis which follows in the subsequent sections based on the velocity-vorticity formulation described previously, we are required to calculate the coefficients of the base flow when expanded as a Chebyshev series. Thus, we require the solution of the base flow equation (1.49) evaluated at the Chebyshev collocation points in $(0, 1]$ given by equation (1.18). Since the Blasius configuration is naturally defined on the semi-infinite domain $[0, \infty)$, we must first map our equations to the computational domain $(0, 1]$ by means of the coordinate transformation (1.40).

This choice of domain is used primarily because of the symmetries enforced on the disturbance variables and the vanishing condition of the z-derivatives as discussed in section 1.4.1 and in Davies and Carpenter [26]. The standard Chebyshev domain $[-1, 1]$ could also be used, with the different mapping

$$\hat{\eta} = \frac{\zeta - l}{\zeta + l}$$

as discussed in references such as Cooper and Carpenter [19] but in the interest of consistency and the advantage of less explicitly imposed boundary conditions by splitting the odd and even cases separately we use only the mapping (1.40) for the remainder of this report.

The choice of l is facilitated by a wish to balance the degree of the Chebyshev approximation with computational time and achieve a high level of accuracy in the shortest time possible. It was found by Davies and Carpenter [26] that in the case of the time-dependent simulations of rotating disk, the variation of the primary perturbation variables across the boundary layer could be fully resolved using a Chebyshev expansion involving $N = 48$ polynomials. Although not explicitly mentioned in the reference, they also found that the most appropriate choice of l for computational efficiency was $l \approx 4$.

The base flow equations (1.49) can be solved fairly simply using MATLAB's *bvp4c* boundary value solver, and evaluated at the collocation points. It is worth noting that out-of-the-box, *bvp4c* has issues with directly solving the equation on a large physical domain. In fact, it is numerically unstable over $[0, a]$ for $a > 14$. This was circumvented by introducing an iterative scheme which used the solution over $[0, K]$ as an initial guess for the solution over $[0, K + 1]$ and proceeded for $K \geq 1$. The resulting base flow profile is shown in figure 1.4.

Boundary Layer Thickness

An additional scaling factor must be taken into account when calculating derivatives of the Blasius boundary layer base flow profile. Consider z^* to be the non-dimensional wall-distance in the Blasius configuration and the non-dimensional displacement thickness δ defined in the classical way as

$$\delta = \int_0^\infty \left(1 - \frac{U_B(\eta)}{U_\infty}\right) d\zeta$$

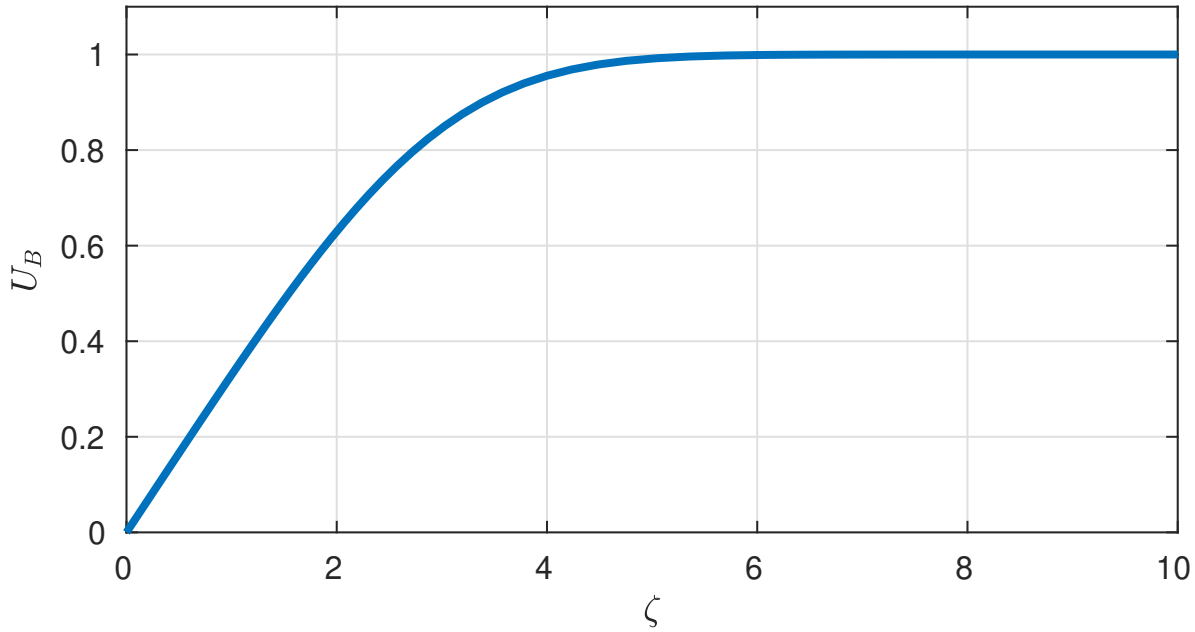

Figure 1.4: Blasius base flow profile U_B for $\zeta \in [0, 10]$.

Defining the dimensional displacement thickness as $\delta^* = \sqrt{\frac{\nu x}{U_\infty}}$, we get

$$z^* = \frac{z}{\delta} \implies \eta = \frac{z}{\delta^*} \quad \text{which gives} \quad \eta = \frac{\delta z}{\delta^*} = Cz \quad \text{for constant } C$$

Thus, since $U_B = F'$ and $U_\infty = 1$, we have

$$C = \frac{\delta}{\delta^*} = \int_0^\infty (1 - F')d\zeta$$

and by the chain rule

$$\frac{dU_B}{dz} = CF'', \qquad \frac{d^2U_B}{dz} = C^2F''' \tag{1.50}$$

Chebyshev Coefficients of the Base Flow

As will be the case for the rotating disk study of chapter 2, the base flow U_B and perturbation variables ξ and w are expanded in terms of either odd or even Chebyshev polynomials. It is acceptable to split the parities in this way since we are only working with half of the usual Chebyshev domain under the mapping (1.40). If an odd representation were to be used then it is assumed implicitly that the function decays at $\eta = 0$ since all odd Chebyshev polynomials have this property. This is equivalent to the condition that the flow profiles in physical space decay as $z \to \infty$. Since the base flow velocity U_B does not decay at infinity, it is sensible to use an even Chebyshev expansion for this variable and its second derivative. The Chebyshev coefficients of the base flow variable and its

derivatives can be calculated from the collocation values using the FFT method described in section 1.3.1.

Perturbation Equations

After applying the mapping (1.40), the derivative operators become

$$\frac{d}{dz} = \frac{-\eta^2}{l}\frac{d}{d\eta}, \quad \frac{d^2}{dz^2} = \frac{\eta^3}{l^2}\left(2\frac{d}{d\eta} + \eta\frac{d^2}{d\eta^2}\right)$$

and so the perturbation equations (1.44) after taking the usual normal mode approximation become

$$-i\omega\xi + i\alpha U\xi + wU'' = \frac{\eta^3}{Rl^2}\left(2\frac{d}{d\eta} + \eta\frac{d^2}{d\eta^2}\right)\xi - \alpha^2\xi \tag{1.51}$$

$$\frac{\eta^3}{l^2}\left(2\frac{d}{d\eta} + \eta\frac{d^2}{d\eta^2}\right)w - \alpha^2 w = -i\alpha\xi \tag{1.52}$$

while the integral definition of the secondary variable u becomes

$$u = l\int_0^\eta \left(\frac{\xi}{\tilde{\eta}^2} + i\alpha\frac{w}{\tilde{\eta}^2}\right)d\tilde{\eta}$$

Boundary Conditions

As described in section 1.4, the boundary conditions (1.39) imposed on the system are derived from the no-slip condition at the wall and the integral constraint imposed on the vorticity. Under the mapping given by equation (1.40), these become

$$w(1) = w(0) = \xi(0) = 0$$
$$\int_0^1 \left(\frac{\xi}{\eta^2} + \frac{1}{\eta^2}\frac{\partial w}{\partial x}\right)d\eta = 0$$

Since we are now working with the odd and even Chebyshev representations separately, the vanishing conditions as $z \to \infty$, or equivalently $\eta \to 0$, are assumed implicitly if we expand the perturbation variables in terms of odd Chebyshev polynomials. Thus, if we apply the normal mode approximation, the two remaining boundary conditions are

$$w(1) = 0$$
$$\int_0^1 \left(\frac{\xi}{\eta^2} + \frac{i\alpha w}{\eta^2}\right)d\eta = 0$$

The second boundary condition can be implemented by means of a tridiagonal matrix operation, details of which are given in the appendices of Davies and Carpenter [26] and

in Thomas [71]. However, we may simplify things slightly by dividing the perturbation equations by η^2, provided we take care when doing so. We could thus, in principle, work entirely with new variables defined by $\hat{f}(\eta) = \frac{f(\eta)}{\eta^2}$ for an arbitrary f, so that the integral condition becomes

$$\int_0^1 \left(\hat{\xi} + i\alpha\hat{w}\right) d\eta = 0$$

which is simple to implement numerically as it only involves the first integral of a Chebyshev representation. The apparent singularity at $\eta \to 0$ caused no problems in practise, and validation tests were carried out, both for the eigenvalue problem and the time-dependent simulations of later sections to ensure that this division did not alter any results. The expectation that this division is non-consequential may be justified by analysis of the perturbation quantities. Typically, for an arbitrary perturbation quantity f, we have $f \sim e^{-az}$ as $z \to \infty$. Thus, under the mapping (1.40), we have

$$\frac{f}{\eta^2} \sim \frac{1}{\eta^2} e^{\frac{-al}{\eta^2}} \quad \text{as} \quad \eta \to 0 \tag{1.53}$$

which decays to 0 as $\eta \to 0$ because of the dominance of the exponential. Thus, we should expect $\frac{f}{\eta^2}$ to be well behaved as η approaches zero, precisely what was observed in practise. Agreement was found between the divided and non-divided versions in all cases tested.

Thus, this division by η^2 in the perturbation equations and application of the mapped derivative operators gives

$$-i\omega\hat{\xi} + i\alpha U\hat{\xi} + U''\hat{w} - \frac{\eta}{Rl^2}\left(2\frac{\partial}{\partial\eta} + \eta\frac{\partial^2}{\partial\eta^2}\right)(\eta^2\hat{\xi}) + \alpha^2\hat{\xi} = 0 \tag{1.54}$$

$$\frac{\eta}{l^2}\left(2\frac{\partial}{\partial\eta} + \eta\frac{\partial^2}{\partial\eta^2}\right)(\eta^2\hat{w}) - \alpha^2\hat{w} + i\alpha\hat{\xi} = 0 \tag{1.55}$$

Following the same method as described in section 1.4 and integrating indefinitely with respect to the mapped variable η gives

$$\left[\alpha^2\left(\frac{1}{R}\mathbf{I}_2\right) + \alpha(i\mathbf{I}_2 U_B) + \left(-\frac{1}{l^2 R}\mathbf{J} - i\omega\mathbf{I}_2\right)\right]\hat{\xi} + [\mathbf{I}_2 U_B'']\hat{w} = 0 \tag{1.56}$$

$$[\alpha(i\mathbf{I}_2)]\hat{\xi} + \left[\alpha^2(-\mathbf{I}_2) + \left(\frac{1}{l^2}\mathbf{J}\right)\right]\hat{w} = 0 \tag{1.57}$$

where

$$\mathbf{I}_2 f := \iint f d\eta \quad \text{and} \quad \mathbf{J}f = \iint \frac{1}{\eta^2}\mathcal{D}^2(\eta^2 f(\eta)) d\eta \tag{1.58}$$

with $\mathcal{D}^2 := 6\eta^2 + 6\eta^3\frac{\partial}{\partial\eta} + \eta^4\frac{\partial^2}{\partial\eta^2}$. After integration by parts, we get

$$\mathbf{J}f = \eta^4 f - 2\int \eta^3 f d\eta \tag{1.59}$$

Operator Representations in Matrix Form

As mentioned previously, we will expand the perturbation variables in terms of odd Chebyshev polynomials, and using the matrix representation of $\int$, we can derive operators which approximate $\mathbf{I}_2$, $\mathbf{J}$ and $\iint U_B p$ for an arbitrary perturbation variable f. Thus, if

$$f = \sum_n f_n T_{2n-1}$$

then by the representation (1.32), we can integrate f twice and equate coefficients of T_{2n-1} to get

$$\mathbf{I}f = aT_0 + bT_1 + \frac{1}{8}\sum_n \left(\frac{f_{n-1}}{(2n-1)(n-1)} - \frac{f_n}{n(n-1)} + \frac{f_{n+1}}{n(2n-1)} \right) T_{2n-1}$$

where a and b are arbitrary constant of integration. Consider now the operator $\mathbf{J}$ given by equation (1.59). Expanding the multiplicative parts η^4 and η^3 in terms of the Chebyshev polynomial basis, we get

$$\eta^4 = \frac{1}{8}(T_4 + 4T_2 + 3T_0)$$
$$\eta^3 = \frac{1}{4}(T_3 + 3T_1)$$

which gives

$$\mathbf{J}f = \frac{1}{l^2}\left[\frac{1}{8}(T_4 + 4T_2 + 3T_0)\sum_n f_n T_{2n-1} - 2\int \frac{1}{4}(T_3 + T_1)\sum_n f_n T_{2n-1} \right]$$

Finally, making use of the identity

$$2T_m(\eta)T_n(\eta) = T_{m+n}(\eta) + T_{m-n}(\eta) \quad (m \geq n \in \mathbb{Z}) \tag{1.60}$$

we get

$$\mathbf{J}f = cT_0 + dT_1 + \sum_n \frac{1}{16}\left[\left(f_{k-2} + 4f_{k-1} + 6f_k + 4f_{k+1} + f_{k+2} \right) - \frac{2}{2k-1}\left(f_{k-2} + 2f_{k-1} - 2f_{k+1} - f_{k+2} \right) \right] T_{2k-1}$$

which is the pentadiagonal matrix form of the operator $\mathbf{J}$.

Thus, it remains to evaluate the product operators of the type

$$\iint U_B f d\eta \tag{1.61}$$

The method outlined below is discussed in Bridges and Morris [14] and can be applied to any base flow profile desired. The method is presented only for the case of no enforced parities, although similar formulae can be derived for the odd and even cases separately. Expanding some arbitrary base flow profile $U_B(\eta)$ and the disturbance variable $f(\eta)$ in terms of full Chebyshev representations gives

$$U_B(\eta) = \frac{U_0}{2} + \sum_{n=1}^{N} U_n T_n(\eta)$$

$$p(\eta) = \frac{f_0}{2} + \sum_{n=1}^{N} f_n T_n(\eta)$$

where the first term is halved for convenience as discussed previously. Thus, again using the identity (1.60), we can deduce that

$$U_B(\eta)p(\eta) = \frac{c_0}{2} + \sum_{n=1}^{N} c_n T_n(\eta)$$

where

$$c_n = \frac{f_n U_0}{2} + \frac{1}{2}\sum_{m=1}^{N}(f_{m+n} + f_{|m-n|})U_m, \quad n = 1, \ldots, N$$

This gives a matrix representation for the Chebyshev coefficients of the product $U_B p$ which may then be integrated by multiplication with the matrix integral operators defined previously.

Numerical Results

Having derived matrix operators for the constituent parts of the perturbation equations, we form a matrix dispersion relation

$$\mathcal{D}(R, \alpha, \omega) = 0 \tag{1.62}$$

which can be solved in either a spatial or temporal setting by prescribing either ω or α respectively, as described in section 1.2.1.

This dispersion relation is solved in MATLAB and the numerical eigenvalue spectrum for $R = 500$ and $\alpha = 0.2$ is plotted in figure 1.5. The order of Chebyshev discretisation was set to be $N = 64$ to ensure convergence and appendix A.1 shows the convergence properties for varying Chebyshev discretisation orders. The diagram shows the numerically spurious eigenvalues which are identifiable by their sensitivity to the order of discretisation and the genuine critical eigenvalue at $\omega_r \approx 0.0730$. This figure can be compared favourably with a similar one in Schmid and Henningson [65].

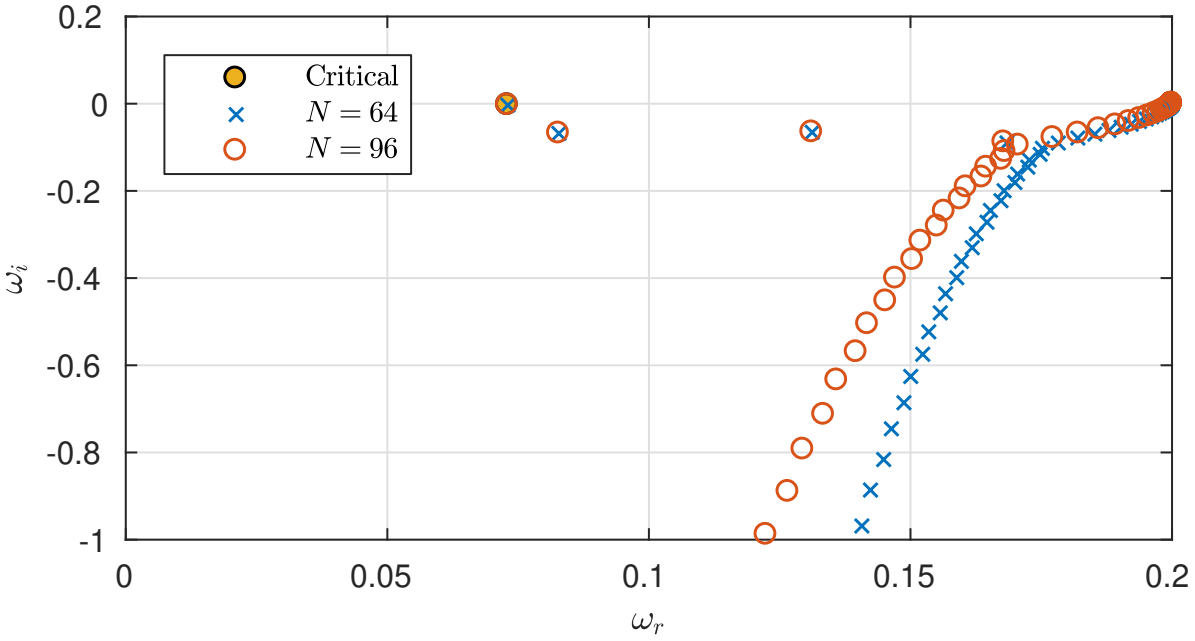

Figure 1.5: Discrete approximation to the continuous spectrum of the Blasius boundary layer dispersion relation for $R = 500$ and $\alpha = 0.2$. The critical eigenvalue is shown as a filled in circle, while the $\times$ and $\circ$ show the numerical spectra for $N = 64$ and $N = 96$ respectively.

1.4.4 Linear Stability of the Temporally Periodic Stokes Layer

Since the main part of the rotating disk study in chapter 3 of this thesis deals with undisturbed basic flow profiles with periodic time-dependencies, we present in this section an overview of the machinery required to deal with this modification. We will use the quintessential purely oscillatory flow that is generated when a flat plate oscillates in the plane beneath a semi-infinite expanse of fluid, namely the Stokes layer, to provide this illustration. Time-periodic oscillatory flows occur in many types of physical and physiological processes and in particular, Womersley [83] shows that high frequency oscillatory blood flow in an artery can be described by invoking a Stokes layer adjacent to the wall, along with a region of inviscid flow at the centre of the artery. The stability of the model plane Couette and plane Poiseuille problems for time-periodic flows has been thoroughly reviewed by Davis [29] in one of the earliest pieces of work on the subject, and several authors including Blennerhassett and Bassom [10], Blennerhassett and Bassom [11], Thomas et al. [76] and Ramage [59] have since extended the understanding of the stability of such flows. In order to introduce the methods employed in this report to analyse the stability

of the periodically modulated rotating disk boundary layer, we present first the derivation of the formulation applied to the semi-infinite flat Stokes layer, as previously studied by the aforementioned authors. While the flow configuration presented here is identical to previous work, the formulation which will be outlined in the following section is distinctly different from that which appears in previous literature and has not, to the best of my knowledge, been discussed previously. Since the basic flow under consideration is now time-dependent, we cannot use the eigenvalue methods employed thus far in this report, and so we begin with an overview of two different approaches for investigating the stability of time-periodic flows; the *instantaneous* or *frozen-flow* approximation and a method related to *Floquet theory*. In particular, given this time-dependence, we cannot readily utilise the standard normal mode form, and thus at this stage, a flow variable ϕ can only be decomposed as

$$\phi(x, z, t) = \hat{\phi}(z, t)e^{i\alpha x} \tag{1.63}$$

where the temporal dependence of the solution is still held in $\hat{\phi}$.

Stokes Layer Base Flow

Consider the Stokes layer that is generated by the motion of an infinitely long and flat rigid wall located at $z = 0$, which oscillates in its own plane with a velocity $U_0 \cos(\varphi t)$ beneath an unbounded body of viscous fluid that would otherwise remain stationary. The boundary layer thickness is described by $\delta = \sqrt{\frac{2\nu}{\varphi}}$ and we can define a Reynolds number associated with the flow as

$$R = \frac{U_0 \delta}{2\nu} = \frac{U_0}{\sqrt{2\nu\varphi}}$$

If all lengths are scaled on the boundary layer thickness $\delta = \sqrt{\frac{2\nu}{\varphi}}$ and we introduce a non-dimensional time $\tau = \varphi t$ then in the absence of disturbances, the basic Stokes flow is two-dimensional and given by

$$U_B(z, \tau) = e^{-z} \cos(\tau - z), \quad V_B(z, \tau) = 0$$

We can study the development of disturbances to the basic flow in the velocity-vorticity formulation described in section 1.4.3 by introducing, as usual, perturbations of the form

$$(U, V) = (U_B, 0) + (u, v), \quad \Xi = \Xi_B + \xi \tag{1.64}$$

where $\Xi_B = U_B'$ is the undisturbed vorticity field associated with the base flow U_B. Due to the chosen non-dimensionalisation, this gives the slightly different linearised velocity-vorticity formulation for this flow configuration as

$$\frac{1}{R}\frac{\partial \xi}{\partial \tau} + U_B\frac{\partial \xi}{\partial x} + U_B''w = \frac{1}{2R}\left(\frac{\partial^2}{\partial x^2} + \frac{\partial^2}{\partial z^2}\right)\xi \tag{1.65a}$$

$$\left(\frac{\partial^2}{\partial x^2} + \frac{\partial^2}{\partial z^2}\right)w = -\frac{\partial \xi}{\partial x} \tag{1.65b}$$

with the secondary variable u being defined by the integral relation

$$u = -\int_z^\infty \left(\xi + \frac{\partial w}{\partial x}\right)dz$$

Instantaneous Frozen-Flow Approximation

Instantaneous instability theory, as explained in Luo and Wu [48], can be characterised by *freezing* the base flow at a specific time instant and treating it as if it were steady. This allows for the time to be treated as a parameter, and has the advantage of allowing an Orr-Sommerfeld equation to be considered at each time instant. Using the Orr-Sommerfeld solutions at each time interval leads to a prediction of an instantaneous growth rate at each point in the cycle of the base flow. We can formalise this by considering a decomposition of (1.63) into the form

$$\phi(x, z, t) = \hat{\phi}(z; t)e^{i(\alpha x - \omega t)} \tag{1.66}$$

where $\hat{\phi}$ is a function which is slowly varying in time, allowing us to neglect the $\frac{\partial \hat{\phi}}{\partial t}$ term that arises in the perturbation equations after substitution.

While this is an attractive method, it must be used with caution as it can only be strictly justified in the limit $R \to \infty$ and may give misleading results when applied to the necessarily finite Reynolds numbers that we consider. The modal interaction which will be discussed in the forthcoming section is also not accounted for by this approach, and while the frozen-flow method is useful for tracking a single mode across a period, it cannot fully resolve the disturbance structure. Therefore a more appropriate and rigorous method for studying the stability of periodic time-dependent base flows is to be taken within the framework of Floquet theory. The study by Luo and Wu [48] attempted to explain the relationship between the results of an instantaneous approach and the more rigorous Floquet theory and found that for a given wavenumber, numerical simulation results from the instantaneous approach agreed well with those from Floquet theory over significant

parts of the cycle. However, there are certain intricacies in the stability properties that are not accounted for by these approaches and we leave our discussion of them for now in favour of formulating the Floquet analysis in detail. We will return to the instantaneous approach with our discussion of the modulated rotating disk, although the approaches of Luo and Wu [48] were used in preliminary work as a numerical validation of the code used in the rotating disk scenario.

Floquet Theory

In order to illustrate the concepts of Floquet theory in a general light, we first make some standard definitions relating to ordinary differential equations and provide a theoretical background to the methods involved. Since we are interested in general in the theory from the standpoint of hydrodynamic stability, we omit any laborious analytical detail in the derivations of theorems. However it should be noted that Floquet theory is a very well developed area of mathematics and extended details are available for the interested reader in Jordan and Smith [41].

From a very general standpoint, consider only the system of ordinary differential equations

$$\mathbf{u}'(t) = A(t)\mathbf{u}(t), \quad (t \in \mathbb{R})$$

for some matrix $A(t)$. Then we can define the *fundamental matrix* of the system as follows.

Definition. *(Fundamental Matrix) Take some $t_0 \in [a,b] \subseteq \mathbb{R}$ and let $A : [a,b] \to \mathbb{R}^{n,n}$ be continuous. Then the matrix-valued function $\mathbf{\Phi} : [a,b] \to \mathbb{R}^{n,n}$ such that*

$$\mathbf{\Phi}' = A\mathbf{\Phi}, \qquad \mathbf{\Phi}'(t_0) = \mathcal{I}$$

is called the t_0-canonical fundamental matrix of the ordinary differential equation $\boldsymbol{u}' = A\boldsymbol{u}$. Here, $\mathcal{I}$ represents the identity matrix.

Assume now that we impose an additional constraint on $A(t)$, and require that A is T-periodic. Then we have $A(t+T) = A(t)$ and it can be shown as in Jordan and Smith [41] that

$$\mathbf{\Phi}(t+T) = \mathbf{\Phi}(t)\mathbf{\Phi}(T)$$

The usefulness of this result can be seen in Floquet's theorem, which is stated below.

Theorem. *(Floquet's Theorem) The system* $\dot{\boldsymbol{u}} = \boldsymbol{A}(t)\boldsymbol{u}$*, where* $\boldsymbol{A}$ *is an* $n \times n$ *matrix-valued function with minimal period* T*, has at least one non-trivial solution* $\boldsymbol{u} = \boldsymbol{P}(t)$ *such that*

$$\boldsymbol{P}(t+T) = \lambda \boldsymbol{P}(t), \quad t \in \mathbb{R}$$

where λ *is a constant.*

The constants λ are eigenvalues of the matrix $\mathbf{M} = \mathbf{\Phi}^{-1}(t_0)\mathbf{\Phi}(t_0 + T)$ and are called the *Floquet multipliers* for the periodic linear system. The corresponding eigenvectors are called the *Floquet solutions*.

A final result can be shown which will provide a convenient format for our discussion of stability.

Theorem. *If* $\boldsymbol{M} = \mathbf{\Phi}^{-1}(t_0)\mathbf{\Phi}(t_0 + T)$ *has* N *distinct eigenvalues* μ_i*, then the system* $\boldsymbol{u}' = A(t)\boldsymbol{u}$ *admits* N *linearly independent solutions of the form*

$$\boldsymbol{u}_i(t) = \boldsymbol{p}_i(t)e^{\mu_i t}$$

where p_i *has minimal period* T *and we have set* $\lambda_i = e^{\mu_i t}$*. The constants* μ_i *are called the* ***Floquet exponents*** *of the system.*

This framework provides the most convenient format for the study of disturbances in time-periodic flows and since both the Stokes layer and the modulated rotating disk system are inherently periodic, we will utilise these ideas to attempt to provide an insight into the stability characteristics. As previously alluded to, several studies of the Floquet stability properties of the semi-infinite Stokes layer, such as Hall [39], Blennerhassett and Bassom [11, 10], Thomas and Davies [73] and Ramage [59] exist and the results presented in the following section are not intended to be novel. However, I am unaware of any Floquet eigenvalue solver which exists for the velocity-vorticity formulation of Davies and Carpenter [27] and in the interest of algebraic brevity and as numerical validation, we present the formulation of the Floquet problem in detail, and outline the methods used by previous authors for the Stokes layer study.

Derivation of the Floquet Stability Equations

To consider the development of small disturbances to the unsteady base flow $U_B = e^{-z}\cos(\tau - z)$, we introduce a perturbation and write

$$\mathbf{u}(\mathbf{x}, \tau) = \mathbf{U}^B(z, \tau) + \epsilon \mathbf{u}'(\mathbf{x}, \tau), \quad \xi(\mathbf{x}, \tau) = \Xi(z, \tau) + \epsilon \xi'(\mathbf{x}, \tau)$$

Following Hall [39], while making use of the theorems discussed previously, we can take a slightly different normal mode solution than that of the steady case to incorporate the temporal dependence. This normal mode solution is taken to be of the form

$$f(x,z,\tau) = \hat{f}(z,\tau)e^{\mu\tau}e^{i\alpha x} + c.c. \tag{1.67}$$

where $\hat{f}(z,\tau)$ is the now time-periodic primary variable with the same period as that of the wall oscillation. All exponential growth of $\hat{f}(z,\tau)$ is incorporated into the Floquet exponent $e^{\mu\tau}$ and the term *c.c.* denotes the complex conjugate, which is added to ensure that the disturbance is real. Clearly the quantities of interest here will be $\mathfrak{R}(\mu)$ and $\mathfrak{I}(\alpha)$ as these specify the temporal and spatial growth rates of the disturbance and whether or not we have temporal and spatial stability.

Substituting this normal mode approximation into (1.65a), multiplying through by R and rearranging gives

$$\left(\mu + i\alpha RU_B + \frac{\alpha^2}{2} - \frac{1}{2}\frac{\partial^2}{\partial z^2}\right)\xi + RU_B''w = 0 \tag{1.68a}$$

$$i\alpha\xi + \left(-\alpha^2 + \frac{\partial^2}{\partial z^2}\right)w = 0 \tag{1.68b}$$

The boundary conditions on the system, arising from no-slip and no-penetration are given by the representation of the secondary variable u and become

$$w(0) = 0, \qquad \int_0^\infty (\xi + i\alpha w)\, dz = 0 \tag{1.69}$$

Since these equations are now time dependent, the local ideas of stability analysis for the steady case are not strictly applicable and we must approach the problem from a slightly different angle. The following method was derived by Hall [39], and first successfully implemented by Blennerhassett and Bassom [11] for the Stokes layer and involves the decomposition of the perturbation variables into harmonics such that

$$\hat{f}(z,\tau) = \sum_{n=-\infty}^{\infty} f_n(z)e^{in\tau} \tag{1.70}$$

A representation for the time dependent part of the base flow is also required in a similar form, and this is given, by definition of cosine, by

$$U_B = e^{-z}\cos(\tau - z) = u_1 e^{i\tau} + u_2 e^{-i\tau} \tag{1.71}$$

where $u_1 = \frac{1}{2}e^{-(1+i)z}$ and $u_2 = \bar{u}_1$. To illustrate the method of Hall [39], we substitute (1.70) into (1.68) to get

$$\sum_{k=-\infty}^{\infty}\left[\left(\mu + ik + i\alpha R(u_1 e^{i\tau} + u_2 e^{-i\tau}) + \frac{\alpha^2}{2} - \frac{1}{2}\frac{\partial^2}{\partial z^2}\right)\xi_k + R(2iu_1 e^{i\tau} + 2iu_2 e^{-i\tau})w_k\right]e^{ik\tau} = 0$$

$$\sum_{k=-\infty}^{\infty}\left[i\alpha\xi_k + \left(-\alpha^2 + \frac{\partial^2}{\partial z^2}\right)w_k\right]e^{ik\tau} = 0$$

and comparing coefficients of $e^{ik\tau}$ for each k gives

$$\left(\mu + ik + \frac{\alpha^2}{2} - \frac{1}{2}\frac{\partial^2}{\partial z^2}\right)\xi_k + i\alpha R\left(u_1\xi_{k-1} + u_2\xi_{k+1}\right) + R\left(2iu_1 w_{k-1} + 2iu_2 w_{k+1}\right) = 0$$

$$i\alpha\xi_k + \left(-\alpha^2 + \frac{\partial^2}{\partial z^2}\right)w_k = 0$$

This gives a system of eigenvalue equations which can be solved in a similar way to the steady case. As has been done in previous sections, we introduce the mapping (1.40) to map the physical domain $[0,\infty)$ to the computational domain $(0,1]$, divide through by η^2 and integrate twice with respect to η to get

$$\mathcal{L}_1^k\hat{\xi}_k + \mathcal{M}\hat{\xi}_{k-1} - \bar{\mathcal{M}}\hat{\xi}_{k+1} + \mathcal{P}\hat{w}_{k-1} - \bar{\mathcal{P}}\hat{w}_{k+1} = -\mu\mathbf{I}_2\hat{\xi}_k \tag{1.72a}$$

$$i\alpha\mathbf{I}_2\hat{\xi}_k - \left(\alpha^2\mathbf{I}_2 + \mathbf{J}_2\right)\hat{w}_k = 0 \tag{1.72b}$$

where

$$\mathcal{L}_1^k = \frac{\alpha^2}{2}\mathbf{I}_2 - \frac{1}{2}\mathbf{J}_2 + ik\mathbf{I}_2, \quad \mathcal{M} = i\alpha R\mathbf{I}_2 u_1, \quad \mathcal{P} = 2iR\mathbf{I}_2 u_1 \tag{1.73}$$

For consistency with the odd Chebyshev expansions of the primary variables, the base flow profile and its second derivative are also represented in terms of odd polynomials, thereby implicitly, and physically appropriately, assuming decay as $z \to \infty$. Using the integral representation (1.32), we can create an infinite system of generalised matrix eigenvalue problems of the form

$$\mathcal{L}_k(\alpha, R)\hat{f}_k = -\mu\mathbf{I}_2\hat{f}_k \tag{1.74}$$

where the boundary conditions are included by replacing the rows which would otherwise determine the arbitrary constants of integration. Clearly, to enable a computational implementation of this method, we must truncate this system above and below by some M, giving a $(2MN+M)\times(2MN+M)$ where N is the degree of Chebyshev discretisation. This system is assembled and solved using MATLAB's sparse matrix routine *eigs*. As explained in Blennerhassett and Bassom [11], this formulation only determines μ_i modulo unity.

Thus, for each eigenvalue μ, we can expect $\mu \pm ik$ to also be an eigenvalue. Additionally, left and right propagating waves with the same growth rate are possible, implying the conjugate $\bar{\mu}$ should also be an eigenvalue. These symmetries allow us to restrict the search for the most unstable mode to the interval $\mu_i \in [0, \frac{1}{2}]$.

Thus, using the integral representation for Chebyshev polynomials as discussed in detail in section 1.3.2, the full matrix form of this equation becomes

$$\begin{pmatrix} \mathcal{L}_1^{-M} & -\bar{\mathcal{M}} & 0 & \cdots & \cdots & \cdots & \cdots & 0 \\ 0 & \mathcal{M} & \mathcal{L}_1^{-M} & -\bar{\mathcal{M}} & 0 & \cdots & \cdots & 0 \\ 0 & 0 & \ddots & \ddots & \ddots & 0 & \cdots & 0 \\ 0 & \cdots & \cdots & \cdots & \cdots & 0 & \mathcal{M} & \mathcal{L}_1^{M} \\ \mathbf{0} & -\bar{\mathcal{P}} & 0 & \cdots & \cdots & \cdots & \cdots & 0 \\ 0 & \mathcal{P} & \mathbf{0} & -\bar{\mathcal{P}} & 0 & \cdots & \cdots & 0 \\ 0 & 0 & \ddots & \ddots & \ddots & 0 & \cdots & 0 \\ 0 & \cdots & \cdots & \cdots & \cdots & 0 & \mathcal{P} & \mathbf{0} \end{pmatrix} \begin{pmatrix} \xi_{-M} \\ \vdots \\ \vdots \\ \xi_M \\ w_{-M} \\ \vdots \\ \vdots \\ w_M \end{pmatrix} = \mu \begin{pmatrix} \mathcal{R} \\ \vdots \\ \vdots \\ \mathcal{R} \\ \mathbf{0} \\ \vdots \\ \vdots \\ \mathbf{0} \end{pmatrix}$$

Results and Validation

Eigenvalue solutions for certain parameters examined in previous literature are summarised in table 1.1. In each case, μ is calculated from (1.74) for prescribed α. While in principle α can be calculated for prescribed μ, in practise the number of harmonics required led to prohibitive computational requirements at this time.

Evidently for the cases tested, the disparity between the results obtained via the method described above and those from previous studies is negligible. It should be noted that Blennerhassett and Bassom [10] and Ramage [59] were conducting their studies in a confined channel with a large width, so the small disparity between the truly semi-infinite case and theirs is expected. Table 1.2 shows the variation in μ depending on how many harmonics are taken in the truncation of the infinite series. As can be seen from the table, this method unfortunately does not improve on the bound set by Blennerhassett and Bassom [11] of $M \approx 0.8\alpha R$. Figures 1.6 and 1.7 show the temporal eigenvalue spectra for stable and unstable parameter choices, and also illustrate the symmetry properties in μ as discussed in the previous section.

R	α	Reference	μ
800	0.3	Blennerhassett and Bassom [11]	0.08174 + 0.35096i
		Blennerhassett and Bassom [10]	0.08238 + 0.34583i
		Ramage [59]	0.08238 + 0.34582i
		Current Work	**0.081743+0.35096i**
847.5	0.38	Blennerhassett and Bassom [11]	0.67594 + 0.14806i
		Blennerhassett and Bassom [10]	0.67616 + 0.14881i
		Ramage [59]	0.67620 + 0.14880i
		Current Work	**0.675937 + 0.148056i**

Table 1.1: Comparison between eigenvalues computed from the dispersion relation (1.74) for the semi-infinite Stokes layer in this study against identical parameter sets in the literature. Excellent agreement is found in all cases tested.

Variation of μ with Number of Harmonics M				
R	α	$0.8\alpha R$	M	μ
800	0.3	192	48	-0.045047-2.0829e-06i
			64	0.30537+0.49254i
			128	0.63373+0.1559i
			156	0.19995+0.47735i
			192	0.081743+0.35096i
			256	0.081743+0.35096i
847.5	0.38	257.64	64	0.19942+0.46809i
			128	1.2531-0.23944i
			156	1.2797-0.30737i
			192	1.0066-0.1865i
			256	0.675937 + 0.148056i
			300	0.675937 + 0.148056i

Table 1.2: Variation in the temporal eigenvalue μ calculated from the dispersion relation (1.74) for varying harmonics. Results agree well with the assertion by Blennerhassett and Bassom [11] that $M \gtrsim 0.8\alpha R$ for convergence.

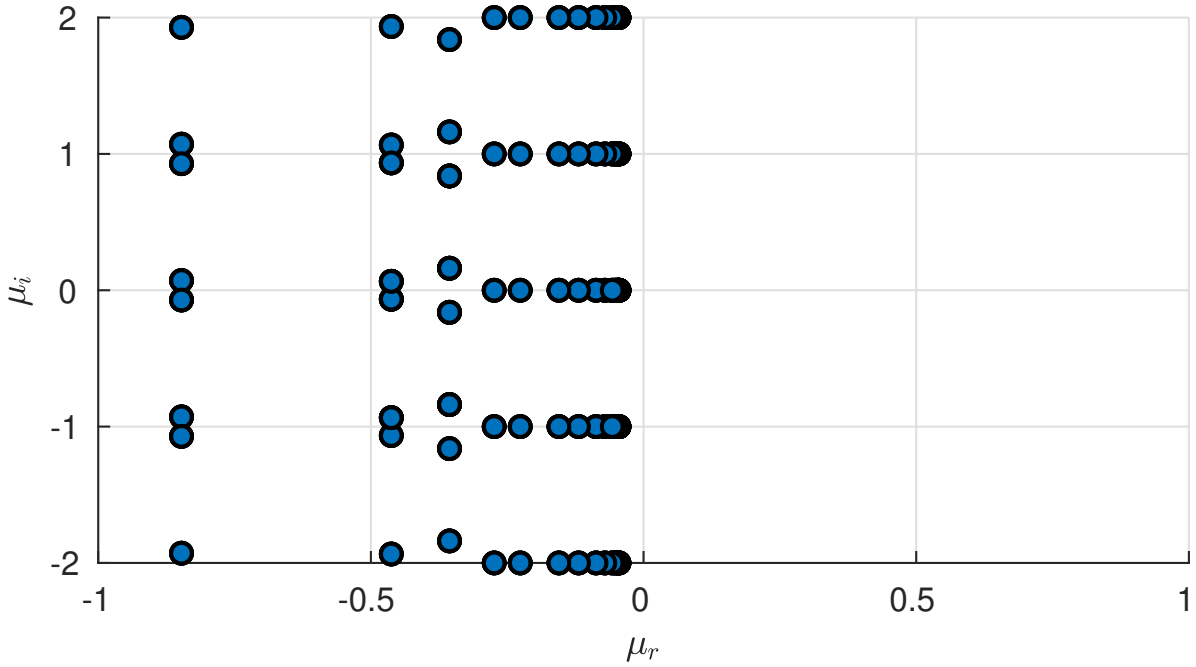

Figure 1.6: Eigenvalue spectra for the dispersion relation relating to the semi-infinite Stokes layer for a stable configuration with $R = 700$ and $\alpha = 0.3$.

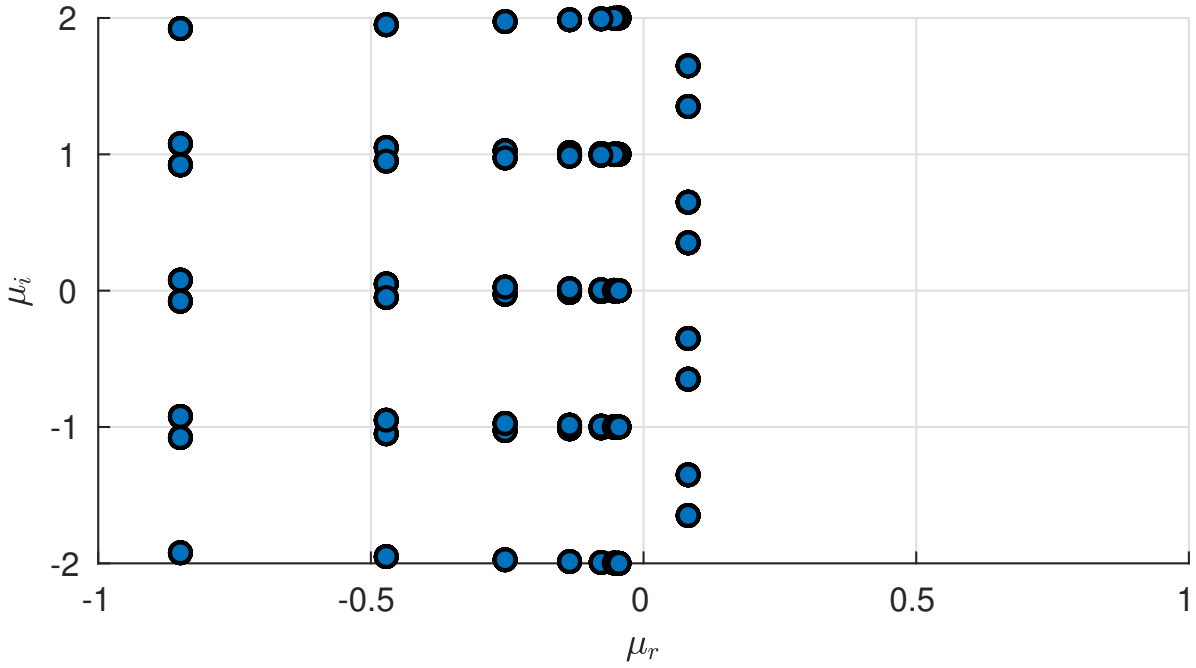

Figure 1.7: Eigenvalue spectra for the dispersion relation relating to the semi-infinite Stokes layer for an unstable configuration with $R = 800$ and $\alpha = 0.3$. The unstable eigenmodes are visible as those with $\mu_r > 0$.

1.5 The Neutral Stability Curve

Having read several introductory texts, lecture courses and articles relating to hydrodynamic stability theory, it is my belief that the fundamental concepts of the neutral stability curve are not particularly well documented in standard literature and I have been unable to find many formulaic approaches to calculating them. Although they appear in some form in most papers and articles, the method by which they are obtained is rarely, if ever, presented. The goal of the following section is to introduce an otherwise unfamiliar reader to this concept, and describe in detail the methods used in this report for calculating neutral stability curves. We will use the steady, two-dimensional case of section 1.4.3 for our exposition, although similar concepts apply to each scenario considered in this document.

The neutral curve is meant as a tool for quickly identifying linearly stable and unstable regions in the parameter space of a flow. They are usually displayed with the Reynolds number along the horizontal axis and the streamwise wavenumber α on the vertical. They can similarly be displayed showing the temporal frequency ω on the vertical although this is less common. The neutral curve for the Blasius flow configuration is shown in figure 1.8.

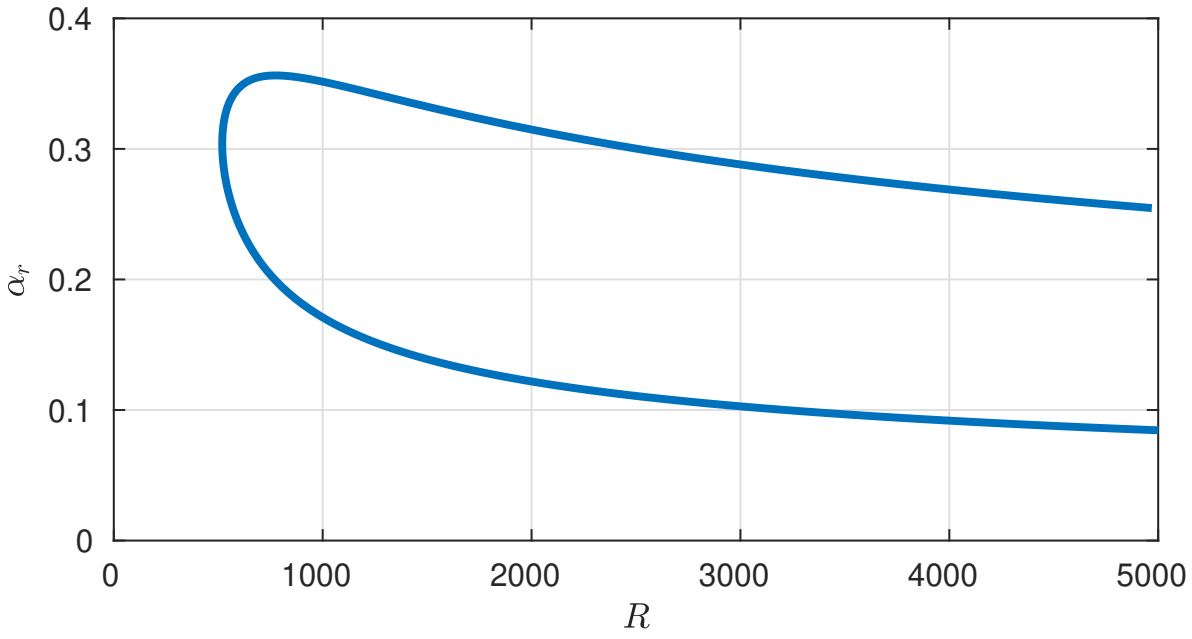

Figure 1.8: Neutral stability curve for the Blasius boundary layer.

This illustrates that *inside* the curve, the flow is linearly, convectively unstable with respect to infinitesimal perturbations. Similarly, *outside* the region, the flow is stable with

respect to infinitesimal perturbations. If the normal mode approximation were taken to be

$$\phi(x, z, t) = \hat{\phi}(z)e^{i(\alpha x - \omega t)}$$

where $\alpha = \alpha_r + i\alpha_i$, then the region inside the curve would correspond to $\alpha_i < 0$, while the region outside the curve would correspond to $\alpha_i > 0$. The curve itself is precisely the line of $\alpha_i = 0$. Similar concepts apply for the temporal curves, with the signs reversed due to the negative sign appearing in front of ω in the normal mode solution. Either way, regardless of whether a temporal or spatial analysis is conducted, the curve corresponds to $\alpha_i = \omega_i = 0$.

It remains to formulate an algorithm for recursively calculating points on the curve given an initial starting guess. A simple algorithm is described very briefly in Bridges and Morris [14] but for complex curves with many corners and turns, a more effective technique is required. For our purposes, this technique is a form of pseudo-arclength continuation similar to that described in Dickson et al. [31].

1.5.1 Arclength Continuation

Consider a parameter dependent non-linear equation of the form

$$F(\mathbf{u}, \lambda) = 0 \tag{1.75}$$

as λ varies. Assuming that we know the solution $\mathbf{u}_0$ for a particular value of λ_0, then simple parameter continuation [31] looks to solve the corresponding problem

$$F(\mathbf{u}_0, \lambda_0 + \delta\lambda) = 0 \tag{1.76}$$

using the known solution as an initial starting guess. We can interpret this for our case as knowing

$$\alpha_i(\omega_0, R) = 0 \tag{1.77}$$

and looking to solve the corresponding problem

$$\alpha_i(\omega_0, R_0 + \delta R) = 0 \tag{1.78}$$

having solved the global eigenvalue problem for some initial parameter pair (ω_0, R_0). The perturbed problem (1.78) can be solved using Newton iteration from the base problem (1.77) and taking δR sufficiently small can fully resolve a neutral curve *until a singularity*

is encountered. These singularities occur precisely when the Jacobian $F_{\mathbf{u}}$ is singular, or in our case when $\frac{\partial \alpha_i}{\partial \omega} = 0$. In practical terms, this occurs at a turning point of the neutral curve and unfortunately, this simple method cannot deal with the more complex neutral curves with many turns and corners without running into difficulty. This can be dealt with by a slightly more complex method described in Dickson et al. [31], termed *arclength continuation*. The major advantage of arclength continuation over simple parameter continuation is that the choice of δR is not a pre-defined input into the algorithm and so does not rely on any *a priori* idea about the curvature of the line. As explained in Dickson et al. [31], one way to remedy the failure of parameter continuation at singularities is to introduce an approximate arclength parameter s, so that both ω and R depend on s. This idea is known as pseudo-arclength continuation. We will present the method in our specific case for the neutral stability curve, although Dickson et al. [31] gives a more general approach involving arbitrary non-linear operators.

Assuming that both ω and R depend smoothly on s, we can differentiate $\alpha_i(\omega, R) = 0$ with respect to s to give

$$\frac{d\alpha_i(\omega(s), R(s))}{ds} = \left(\frac{\partial \alpha_i}{\partial \omega}\right)\dot{\omega} + \left(\frac{\partial \alpha_i}{\partial R}\right)\dot{R} = 0 \tag{1.79}$$

where the dot notation denotes differentiation with respect to s. Since s is the arclength, we must also have

$$||(\dot{\omega}, \dot{R})||^2 = |\dot{\omega}|^2 + |\dot{R}|^2 = 1 \tag{1.80}$$

which can serve as an extra equation to supplement the original equation $\alpha_i(\omega, R) = 0$ and fully specify the unknowns α_i and s. We can approximate condition (1.80) by introducing

$$N(\omega, R, s) = \begin{pmatrix} \dot{\omega}_0 \\ \dot{R}_0 \end{pmatrix} (\omega - \omega_0, R - R_0) - ds = 0 \tag{1.81}$$

which says that new point, (ω, R), on the path lies on a hyperplane orthogonal to the tangent vector through the current point (ω_0, R_0), and the intersection of that hyperplane with the tangent vector is a distance ds from (ω_0, R_0). We can thus extend the system (1.77) to

$$\begin{pmatrix} \alpha_i(\omega, R) \\ N(\omega, R, s) \end{pmatrix} = \begin{pmatrix} 0 \\ 0 \end{pmatrix} \tag{1.82}$$

which can be solved for the new point (ω, R) while specifying only the arclength ds. Note that this is not equivalent to specifying an increment in either ω or R and does not rely

on any pre-determined notion of the direction of the curve. Ramage [59] gives a thorough overview of this process.

In order to compute the N term given by equation (1.81), we require values of the derivatives $\dot{\omega}$ and $\dot{Re}$. These can be derived using a combination of the normalisation requirement (1.80) and the original dispersion relation

$$\mathcal{D}(\alpha;\omega,R)\phi = 0 \tag{1.83}$$

By equation (1.79), we see that

$$\dot{\omega} = \frac{-\frac{\partial\alpha}{\partial R}\dot{R}}{\frac{\partial\alpha}{\partial\omega}} \tag{1.84}$$

and since $|\dot{\omega}|^2 + |\dot{R}|^2 = 1$, we can thus specify R as $R = \pm\sqrt{1-|\dot{\omega}|^2}$. The sign of R determines which direction along the curve we are travelling using the method, either in the direction of increasing or decreasing R. Having derived these formulae, we may compute the remaining requirements $\frac{\partial\alpha}{\partial\omega}$ and $\frac{\partial\alpha}{\partial R}$ by making use of the dispersion relation (1.83). We present only the case for obtaining $\frac{\partial\alpha}{\partial\omega}$ but the other is essentially identical. Differentiating (1.83) with respect to ω gives

$$\frac{\partial\mathcal{D}}{\partial\omega}\phi + \mathcal{D}\frac{\partial\phi}{\partial\omega} = 0 \tag{1.85}$$

A similar dispersion relation must hold for a *left eigenvalue* $\varphi^\dagger$ such that

$$\varphi^\dagger\mathcal{D}(\alpha;\omega,R) = 0 \tag{1.86}$$

where $\dagger$ denotes the complex conjugate transpose. Multiplying through by $\varphi^\dagger$ in equation (1.85) eliminates the second term to give

$$\varphi^\dagger\frac{\partial\mathcal{D}}{\partial\omega}\phi = 0 \tag{1.87}$$

Finally, since $\varphi^\dagger\phi = \mathcal{I}$, we have

$$\frac{\partial\alpha}{\partial\omega} = \frac{\partial\alpha}{\partial\mathcal{D}}\frac{\partial\mathcal{D}}{\partial\omega} = \frac{\frac{\partial\mathcal{D}}{\partial\omega}}{\frac{\partial\mathcal{D}}{\partial\alpha}} \tag{1.88}$$

and

$$\frac{\partial\alpha}{\partial\omega} = \varphi^\dagger\frac{\partial\alpha}{\partial\omega}\phi = \frac{\varphi^\dagger\frac{\partial\mathcal{D}}{\partial\omega}\phi}{\varphi^\dagger\frac{\partial\mathcal{D}}{\partial\alpha}\phi} \tag{1.89}$$

The quantities $\frac{\partial\mathcal{D}}{\partial\omega}$ and $\frac{\partial\mathcal{D}}{\partial\alpha}$ are available directly from the perturbation equations, and the eigenvectors ϕ and $\varphi^\dagger$ are determined quickly in practise by recursive iteration from a non-zero guess.

Chapter 2

Local Linear Stability Analysis of the Steady Rotating Disk Boundary Layer

2.1 Introduction

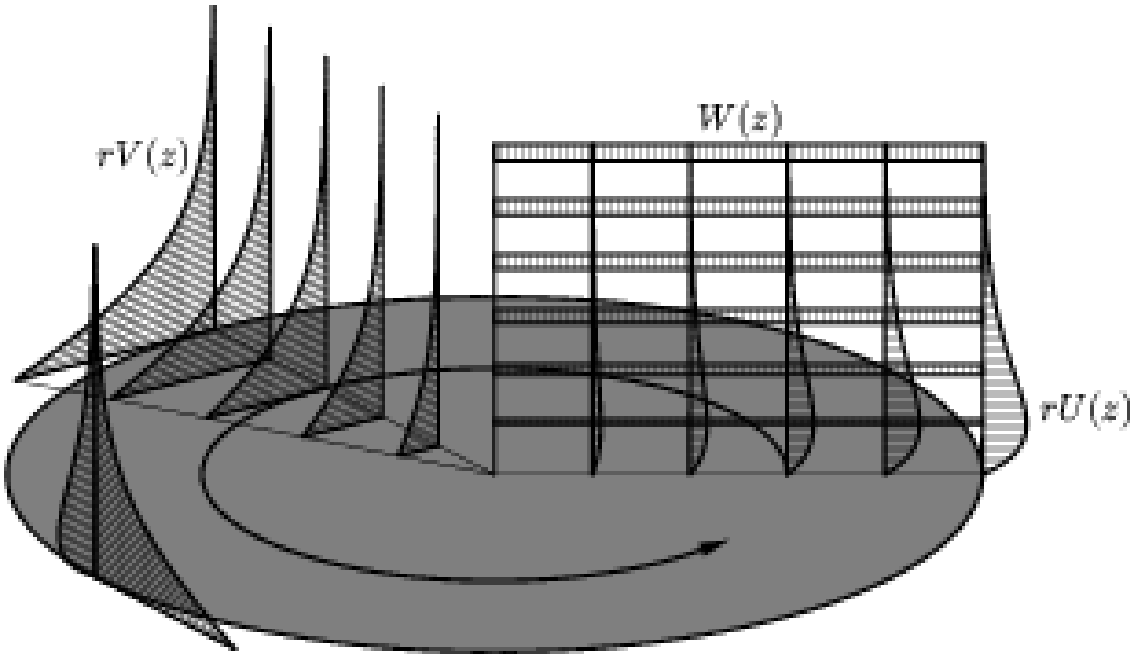

Figure 2.1: Rotating disk flow configuration.

This following chapter will detail the application of the numerical methods described in chapter 1 to a canonical three-dimensional steady boundary layer, and discuss the modifications to the techniques required therein. We begin by considering a disk of infinite extent rotating at a constant rate beneath an otherwise stationary fluid such as air or water. The motion of the disk creates a thin boundary layer on the surface where the flow is directly affected by the rotation. Viscous stresses act to drag the fluid near the disk in circular paths but the absence of a pressure gradient to hold fluid elements causes them to spiral outwards, to be replaced by an axial flow downwards towards the disk. The resulting flow has radial, azimuthal and vertical components and admits an exact similarity solution to the Navier-Stokes equations, first derived by von Kármán [80] in 1921.

For this reason, the flow as described over a rotating disk is often referred to as von Kármán flow, and provides a canonical example of a three-dimensional boundary layer. Boundary layers over swept wings also have flow components in two directions - along the span of the wing as well as in the direction of flight, and the crossflow inflexion point instability mechanism is common to both the rotating disk boundary layer and the flow over a swept wing. Thus the investigation of strategies for controlling the behaviour of disturbances that develop in the rotating disk flow may prove to be helpful for the identification and assessment of technologies that have the potential to maintain laminar flow over swept wings.

Additionally, the von Kármán problem has certain useful practical advantages over the swept wing configuration; it admits an exact similarity solution of the Navier-Stokes equations and is more amenable to experiments. However, it is important to note that there are differences between the two flow configurations. The boundary layer over a swept wing is not affected by Coriolis forces whereas the rotating disk layer is and the former does not include the azimuthal periodicity of the rotating disk configuration. We will review the implications of these differences later when discussing the stability properties of the rotating disk configuration.

As stated by Lingwood and Alfredsson [46], the rotating disk flow and its related flows are relevant not only to swept wing flows but to a wider range of complex three-dimensional configurations such as atmospheric and oceanic flows, rotating-cavity flows and computer storage devices. Additionally, in electrochemistry, the rotating disk elec-

trode is a common instrument utilised for performing a technique known as hydrodynamic voltammetry. In part, it is the simplicity of the base flow equations that has made the von Kármán flow an attractive candidate for studies of some of these more general three-dimensional boundary layers.

2.1.1 Numerical Solution of the Base Flow Equations

In 1921, Theodore von Kármán formulated the exact similarity solution to the Navier-Stokes equations for the steady laminar flow over a rotating disk of infinite radius. We will provide an overview of this solution method while adding the modifications required to deal with a non-constant rotation rate. Following von Kármán's method, let U^*, V^* and W^* denote the dimensional radial, azimuthal and axial similarity velocities respectively and r^* and z^* denote the dimensional radial position and wall-normal height. Let also ν^* denote the kinematic viscosity and Ω^* the angular velocity of the disk.

Thus, using the regular notation, the Navier-Stokes equations in cylindrical polar coordinates, with the absence of a θ-dependence due to inherent symmetry of the problem, reduce to

$$\begin{aligned}
\frac{\partial U^*}{\partial t^*} + \mathbf{U}^* \cdot \nabla U^* - \frac{V^{*2}}{r^*} - 2\Omega^* V^* - \Omega^{*2} r^* \\
= -\frac{1}{\rho}\frac{\partial P^*}{\partial r^*} + \nu\left(\nabla^2 U^* - \frac{U^*}{r^{*2}} - \frac{2}{r^{*2}}\frac{\partial V^*}{\partial \theta}\right) \\
\frac{\partial V^*}{\partial t^*} + \mathbf{U}^* \cdot \nabla V^* - \frac{U^* V^*}{r^*} + 2\Omega^* U^* \\
= -\frac{1}{r^*\rho}\frac{\partial P^*}{\partial \theta} + \nu\left(\nabla^2 V^* + \frac{2}{r^{*2}}\frac{\partial U^*}{\partial \theta} - \frac{V^*}{r^{*2}}\right) \\
\frac{\partial W^*}{\partial t^*} + \mathbf{U}^* \cdot \nabla W^* = -\frac{1}{\rho}\frac{\partial P^*}{\partial z^*} + \nu\nabla^2 W^* \\
\frac{\partial U^*}{\partial r^*} + \frac{U^*}{r^*} + \frac{1}{r^*}\frac{\partial V^*}{\partial \theta} + \frac{\partial W^*}{\partial z^*}
\end{aligned}$$

subject to the boundary conditions

$$U^*(0) = W^*(0) = 0, \;\; V^*(0) = 0; \quad U^* \to 0, V^* \to -\Omega^* r \;\; \text{as} \;\; z^* \to \infty$$

as a result of no-slip and no-penetration at the disk surface. In this formulation we have chosen to work in a frame of reference that is rotating with the disk, thereby requiring us to add Coriolis and streamwise curvature effects into the governing equations and alter the boundary conditions on the azimuthal base flow component. Most calculations and

simulations throughout this report will be conducted in this rotating frame, although one can switch between frames if necessary by removing appropriate terms and redefining the base flow boundary conditions accordingly.

In von Kármán's original derivation, the rotation rate of the disk, Ω^*, was considered constant, however for what follows we will assume that the disk rotates in the usual flow configuration at an arbitrary rotation rate $\Omega^*(t^*)$. If we let $\mathbf{U} = (U^*, V^*, W^*)$ denote the dimensional base flow then the boundary conditions associated with the system in a non-rotating frame of reference are given by

$$\begin{aligned} U^*(0,t^*) = W^*(0,t^*) = 0, \quad V^*(0,t^*) = r^*\Omega^*(t^*) \\ U^* \to 0 \quad V^* \to 0 \ \text{ as } \ z^* \to \infty \end{aligned}$$

Initially, von Kármán [80] scales out the radial dependence of the base flow and writes

$$f^*(z^*,t^*) = \frac{U^*(r^*,z^*,t^*)}{r^*}, \quad g^*(z^*,t^*) = \frac{V^*(r^*,z^*,t^*)}{r^*}, \quad h^*(z^*,t^*) = \frac{W^*(r^*,z^*,t^*)}{\delta^*} \tag{2.1}$$

where the lower case (f^*, g^*, h^*) now have the dimension of frequency, namely s^{-1}. Dropping the $*$ for notational simplicity gives the system of equations

$$\frac{\partial f}{\partial t} = g^2 - f^2 - h\frac{\partial f}{\partial z} + \nu\frac{\partial^2 f}{\partial z^2} \tag{2.2a}$$

$$\frac{\partial g}{\partial t} = -2fg - h\frac{\partial g}{\partial z} + \nu\frac{\partial^2 g}{\partial z^2} \tag{2.2b}$$

$$\frac{\partial h}{\partial z} = -2f \tag{2.2c}$$

with boundary conditions

$$\begin{aligned} f(0,t) = h(0,t) = 0, \quad g(0,t) = \Omega(t) \\ f \to 0 \quad g \to 0 \ \text{ as } \ z \to \infty \end{aligned}$$

The modulation we propose is of a periodic nature, similar to that of the Stokes layer discussed in section 1.4.4. In order to draw parallels between this work and that of Thomas et al. [76], the rotation rate is thus chosen to have the form

$$\Omega^*(t^*) = \Omega_0^* + \epsilon\phi^*\cos(\phi^* t^*) \tag{2.3}$$

where Ω_0^* may be thought of as analogous to the constant rotation rate in the steady case, while ϵ and ϕ^* denote the angular displacement and angular velocity of the modulation respectively. It should be noted that the steady system is recovered for $\epsilon = 0$. Depending

on the frequency of oscillation, the flow can be seen to evolve on two length scales; the boundary layer thicknesses based on the constant rotation rate Ω_0^* and on the modulation frequency ϕ^*. We will refer to these two length scales as the Kármán layer and the Stokes layer respectively, and they take the familiar forms

$$\delta_k^* = \sqrt{\frac{\nu^*}{\Omega_0^*}}, \qquad \delta_s^* = \sqrt{\frac{\nu^*}{\phi^*}} \tag{2.4}$$

There are also three temporal scales to consider, two associated with the local and global rotation rates of the disk and one pertaining to the modulation frequency. We can thus elect to non-dimensionalise the time-scale in either of the following ways

$$\tau_k^l = \frac{r_L^*}{\delta_k^*}\Omega_0^* t^*, \qquad \tau_k^g = \Omega_0^* t^*, \qquad \tau_s = \phi^* t^* \tag{2.5}$$

The differences incurred by the choice of scaling will be discussed later in chapter 4 in conjunction with the global stability but since we are only at this stage interested in dealing with the local stability analysis, we neglect the global time-scale τ_k^g. Thus, we are left with a choice of non-dimensionalisation based on either one of the scales

$$(\delta_k^*, \tau_k^l), \qquad (\delta_s^*, \tau_s) \tag{2.6}$$

Either scaling could equally be chosen without adverse effects, provided we are consistent in our solution method. However, since we are dealing primarily with a small-amplitude modulation of the otherwise steady system and with a necessity of validation in mind, we choose to non-dimensionalise on the Kármán scales (δ_k^*, τ_k^l) for the following procedure.

A local velocity scaling is obtained by using the circumferential disk velocity $r_L^*\Omega_0^*$ at some dimensional reference radius r_L^*, chosen over its global counterpart based on the boundary layer thickness, $\delta_k^*\Omega_0^*$. The local scaling gives a Reynolds number R, associated with the steady rotation of the disk as

$$R = \frac{r_L^*\Omega_0^*\delta_k^*}{\nu^*} = \frac{r_L^*}{\delta_k^*} = r_L \tag{2.7}$$

where we identify r_L as a local, non-dimensional radial position. We can also define a Reynolds number, R_s associated with the Stokes layer, in a similar manner to section 1.4.4 given by

$$R_s = \frac{r_L^*\epsilon\phi_0^*\delta_s^*}{\nu^*} = r_L\epsilon\sqrt{\frac{\phi^*}{\Omega_0^*}} = \epsilon\sqrt{\varphi}R \tag{2.8}$$

where we have defined $\varphi := \frac{\phi^*}{\Omega_0^*}$. We interpret φ as a non-dimensional frequency term, and identify it with the number of periods of modulation during one disk rotation. Scaling the velocities on the local scale $r_L^*\Omega_0^*$ gives

$$F(z,\tau) = \Omega_0^* f(z,\tau), \quad G(z,\tau) = \Omega_0^* g(z,\tau), \quad H(z,\tau) = \Omega_0^* h(z,\tau) \tag{2.9}$$

and results in the system of equations

$$\frac{\partial F}{\partial \tau} = \frac{1}{R}\left(G^2 - F^2 - H\frac{\partial F}{\partial z} + \frac{\partial^2 F}{\partial z^2}\right) \tag{2.10a}$$

$$\frac{\partial G}{\partial \tau} = \frac{1}{R}\left(-2FG - H\frac{\partial G}{\partial z} + \frac{\partial^2 G}{\partial z^2}\right) \tag{2.10b}$$

$$\frac{\partial H}{\partial z} = -2F \tag{2.10c}$$

with boundary conditions

$$F(0,\tau) = H(0,\tau) = 0, \quad G(0,\tau) = 1 + U_w \cos\left(\frac{\varphi}{R}\tau\right) \tag{2.11a}$$

$$F \to 0, \quad G \to 0 \quad \text{as} \quad z \to \infty \tag{2.11b}$$

where $U_w := \frac{R_s\sqrt{\varphi}}{R}$. Thus, we see that the flow properties are fully specified by the variation of the three parameters (R, U_w, φ), and that the steady case is recovered for $U_w = 0$. Keeping our laminar flow control motivation in mind, it is sensible to constrain the variation in the wall velocity to be relatively small with respect to the rotation rate, and so we impose the condition $U_w < 0.2$ for the remainder of this work. In turn, for sufficiently high φ and R in the region of interest, this keeps the Reynolds number associated with the Stokes layer, Rs, to be small compared with the Reynolds number associated with instability onset in the semi-infinite Stokes layer of Blennerhassett and Bassom [11], namely $Rs \approx 350$. We may, therefore, proceed with cautionary confidence that the introduction of the modulation will not introduce any additional modes of instability arising from the Stokes part of the flow, and will endeavour to ensure that this is indeed the case in the following solution procedures. Figure 2.2 shows the variation in Rs with φ for various wall modulation velocities U_w. For the majority of results discussed in chapter 3, we will use $U_w < 0.2$ and $\varphi > 1$ so as to appropriately constrain the value of R_s.

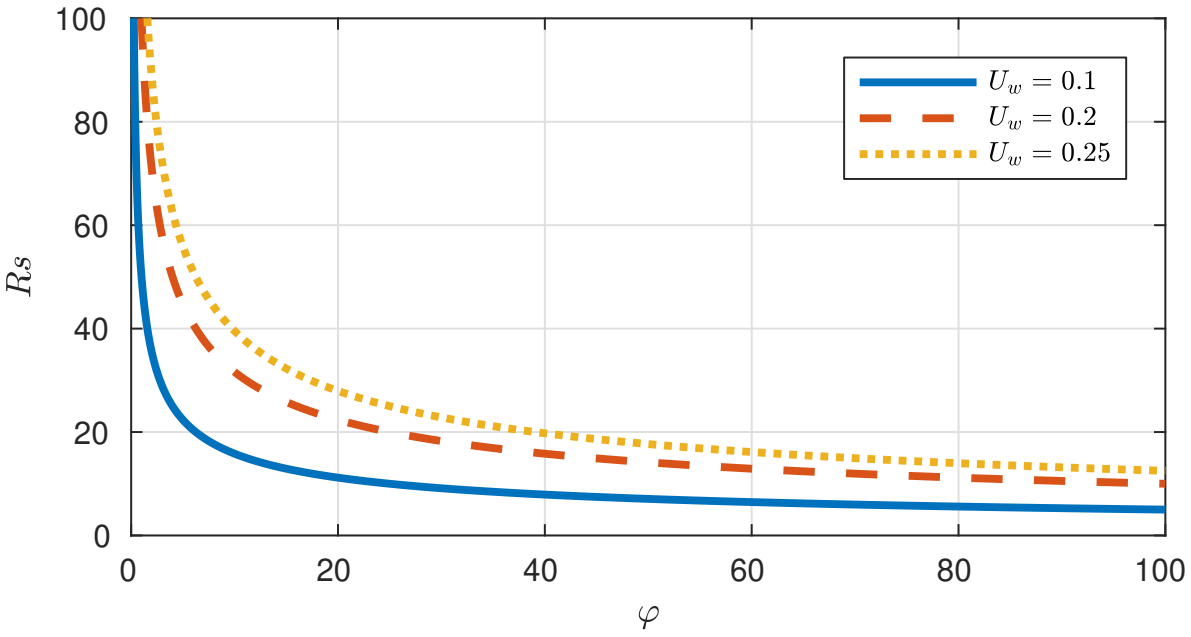

Figure 2.2: Variation in Rs with φ for wall modulation velocities $U_w = 0.1$ (-), $U_w = 0.2$ (- - -) and $U_w = 0.25$ ($\cdots$), for R fixed at $R = 500$.

Numerical Solution of the Base Flow Equations

In the steady case with $U_w = 0$, the system (2.10) reduces to the von Kármán system of ODEs

$$G^2 - F^2 - F'H + F'' = 0 \tag{2.12a}$$

$$-2FG - G'H + G'' = 0 \tag{2.12b}$$

$$H' = -2F \tag{2.12c}$$

Similarly to the Blasius configuration, this system can be solved with a relatively straightforward application of MATLAB's *bvp4c* solver, and evaluated at the collocation points. It is worth noting that out-of-the-box, *bvp4c* has issues with directly solving the equation on a large physical domain. In fact, it is numerically unstable over $[0, a]$ for $a > 12$. This was avoided by introducing an iterative scheme which used the solution over $[0, K]$ as an initial guess for the solution over $[0, K + 1]$ and proceeded for $K \geq 1$. The base flow profiles for the non-rotating frame are shown in figure 2.3.

To facilitate our aim of solving the full time-dependent equations (2.10), we use similar matrix operators to those already derived in section 1.4.3, and enforce similar parities on the base flow variables. Choosing to solve the equations in the non-rotating frame would ensure both F and G decay as $z \to \infty$ and allow these flow variables to be represented

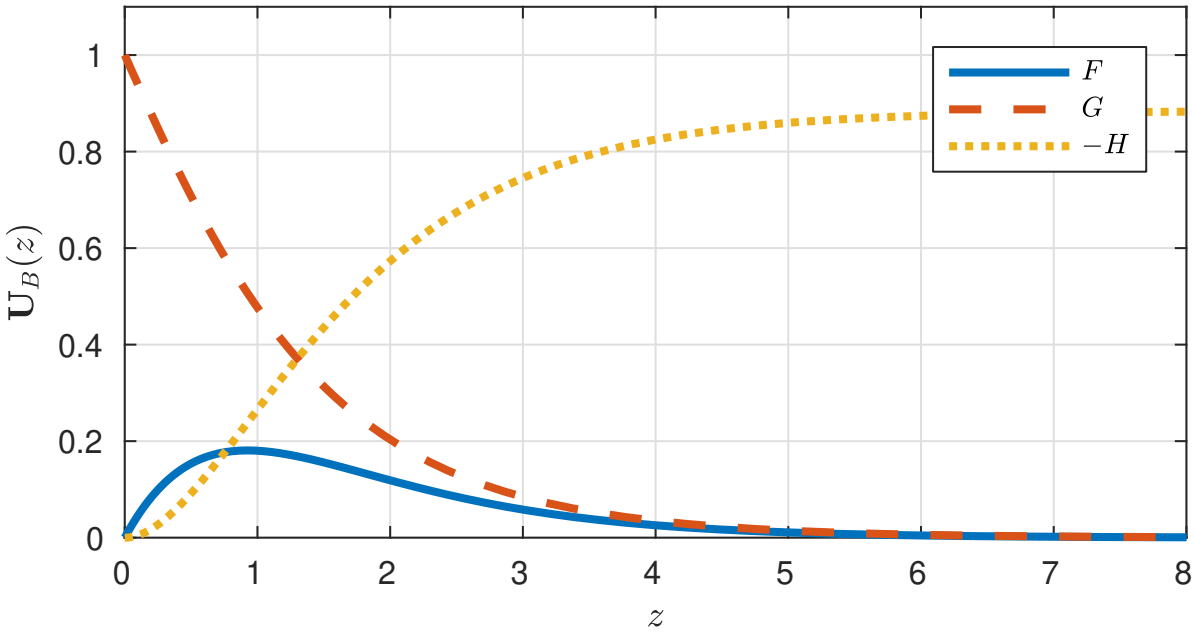

Figure 2.3: Steady rotating disk base flow velocity profiles F (-), G (- - -) and $-H$ ($\cdots$)

in terms of odd Chebyshev polynomials, while leaving H to be expressed as even since by definition it has opposite parity. Curtailing our discussion here and proceeding would give rise to a small problem, since we would require the value of H as $z \to \infty$ which is determined by the equations and not pre-specified. Fortunately this issue may be alleviated by the usual mapping (1.40), which gives, in the non-rotating frame,

$$\frac{\partial F}{\partial \tau} = \frac{1}{R}\left(G^2 - F^2 + \frac{1}{l}\left(\eta^2 H\right)\frac{\partial F}{\partial \eta} + \mathcal{D}^2 F\right) \tag{2.13a}$$

$$\frac{\partial G}{\partial \tau} = \frac{1}{R}\left(-2FG + \frac{1}{l}\left(\eta^2 H\right)\frac{\partial G}{\partial \eta} + \mathcal{D}^2 G\right) \tag{2.13b}$$

$$\frac{\partial H}{\partial \tau} = \frac{2l}{\eta^2}F \tag{2.13c}$$

with boundary conditions

$$F(1,\tau) = H(1,\tau) = 0, \quad G(1,\tau) = 1 + U_w \cos\left(\frac{\varphi}{R}\tau\right) \tag{2.14a}$$

$$F \to 0, \quad G \to 0 \quad \text{as} \quad \eta \to 0 \tag{2.14b}$$

where $\mathcal{D}^2 = \frac{\eta^2}{l}\left(2\eta\frac{\partial}{\partial\eta} + \eta^2\frac{\partial^2}{\partial\eta^2}\right)$.

Since the flow variable H only appears in the equations when multiplied by η^2, we may expand the modified variable $\tilde{H} := \eta^2 H$ in terms of even Chebyshev polynomials, thereby satisfying the required far-field decay. The continuity equation may be adapted

to take this into account by noticing that

$$\frac{\partial \tilde{H}}{\partial \eta} = \frac{2}{\eta}\tilde{H} + 2lF \tag{2.15}$$

which can be integrated analytically by means of an integrating factor to give the explicit definition

$$\tilde{H} = 2l\eta^2 \int_0^\eta \frac{F}{\eta^2} \tag{2.16}$$

In practise we are able to calculate $\tilde{H}$ given the Chebyshev coefficients of the expansion for $\hat{F} := \frac{F}{\eta^2}$. The multiplications and divisions by η^2 are performed in collocation space after a fast Fourier transform while the integration may be evaluated using the integral representations of the Chebyshev polynomials (1.32). Thus, we can write

$$\tilde{H}(\eta) = 2l\eta^2 \left[\left(\sum_{k=1}^{N} a_k \hat{f}_k \right) T_0(\zeta) + \frac{\hat{f}_1}{4} T_2(\eta) + \sum_{k=2}^{N} \frac{1}{4k} (\hat{f}_k - \hat{f}_{k+1}) T_{2k}(\eta) \right] \tag{2.17}$$

where

$$a_1 = 0, \quad a_k = \frac{(-1)^k (1-2k)}{4k(k-1)} \quad (k > 1) \tag{2.18}$$

and thus, $\tilde{H} = \mathbf{S}\hat{F}$ where $\mathbf{S}$ is the matrix form of (2.17).

The temporal integration is performed via a backward three-level scheme which takes the form

$$\left(\frac{\partial f}{\partial t} \right)^l = \frac{1}{2\Delta t} \left(3f^l - 4f^{l-1} + f^{l-2} \right) \tag{2.19}$$

where we have used the notation

$$f^l = f\Big|_{t=l\Delta t}$$

The majority of terms on the right hand side of (2.10) are treated explicitly via a predictor-corrector method in the temporal integration, although for numerical stability reasons the second z-derivative term is treated implicitly. The predictor step for the explicit terms is given by

$$(\mathcal{N}^l)_p = 2\mathcal{N}^{l-1} - \mathcal{N}^{l-2}$$

while the corrector step is defined by

$$(\mathcal{N}^l)_c = (\mathcal{N}^l)_p$$

where $(\mathcal{N}^l)_p$ denotes the velocity fields determined from the predictor stage.

We may simplify notation slightly by defining the operators $\mathcal{R}_F$ and $\mathcal{R}_G$ to be the right hand sides of the transport equations (2.13a) and (2.13b) without the second derivative terms, giving

$$\frac{\partial F}{\partial \tau} - \frac{1}{R}\mathcal{D}^2 F = \mathcal{R}_F$$
$$\frac{\partial G}{\partial \tau} - \frac{1}{R}\mathcal{D}^2 G = \mathcal{R}_G$$

while H is now defined in terms of F by (2.16). Discretising the time derivative using (2.19) and integrating the transport equations twice with respect to the mapped variable η gives

$$\left(\frac{3}{2\Delta\tau}\iint - \iint \mathcal{D}^2\right) F^{l+1} d\eta = \frac{2}{\Delta\tau}\iint F^l d\eta - \frac{1}{2\Delta\tau}\iint F^{l-1} d\eta + \iint \mathcal{R}_F^l d\eta \quad (2.20a)$$
$$\left(\frac{3}{2\Delta\tau}\iint - \iint \mathcal{D}^2\right) G^{l+1} d\eta = \frac{2}{\Delta\tau}\iint G^l d\eta - \frac{1}{2\Delta\tau}\iint G^{l-1} d\eta + \iint \mathcal{R}_G^l d\eta \quad (2.20b)$$

The Chebyshev polynomial representation allows the integrals to be expressed as matrix operators and the time-marching is achieved by means of matrix inversions and multiplications at each time-step.

The nonlinear product terms are treated with a pseudo-spectral scheme which uses a Fast Fourier Transform to convert between Chebyshev coefficients and collocation values. This method was explained in section 1.3.1 but essentially can be described by the following diagram:

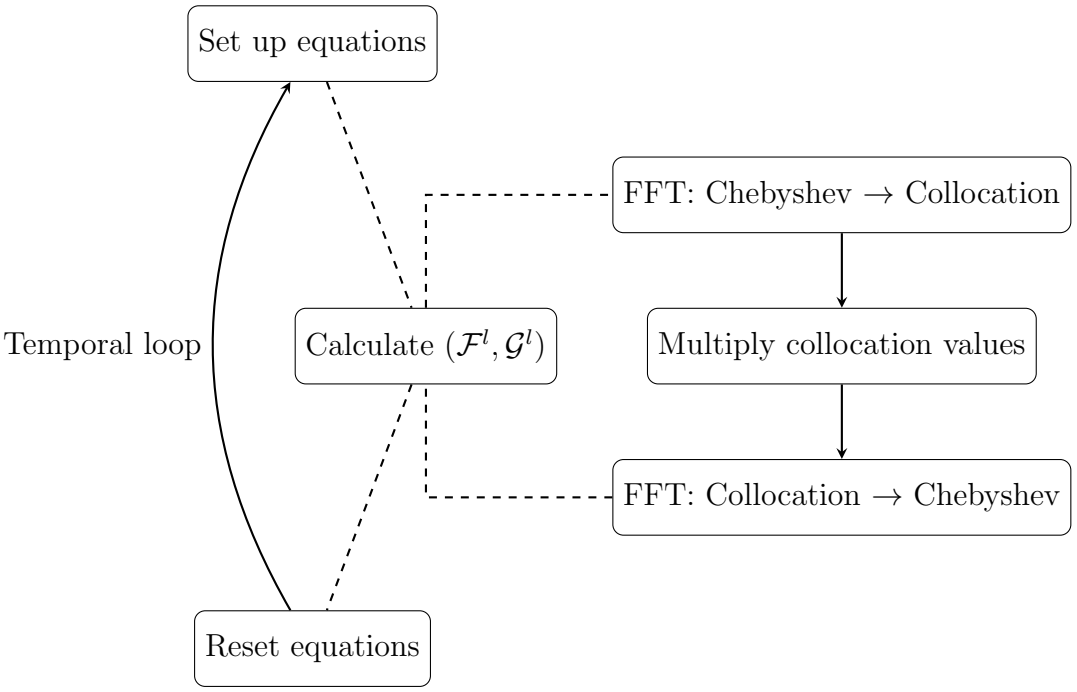

A similar idea is also employed to calculate the η-derivatives of F and G and is accomplished using the NAG library routines from the *C06* series or the open-source versions from *dfftpack* [54]. A slight gain in computational cost may be achieved by inverting the constant matrix on the left hand side once during initialisation of the method, and simply multiplying at each time-step.

Illustrative Results

Figure 2.4 shows a typical variation of the modulated base flow over one period of modulation. The profiles are shown for the non-rotating frame with boundary conditions on the azimuthal velocity field given by

$$G(z=0,\tau) = 1 + U_w \cos\left(\frac{\varphi}{R}\tau\right), \quad \text{where } R = 500,\ U_w = 0.2 \text{ and } \varphi = 10$$

Clearly there is much less variation in the radial and vertical flow components than in the azimuthal component. In fact it is shown in section 2.1.2 that the variation in F and H are of a lower order of oscillation magnitude than the variation in G.

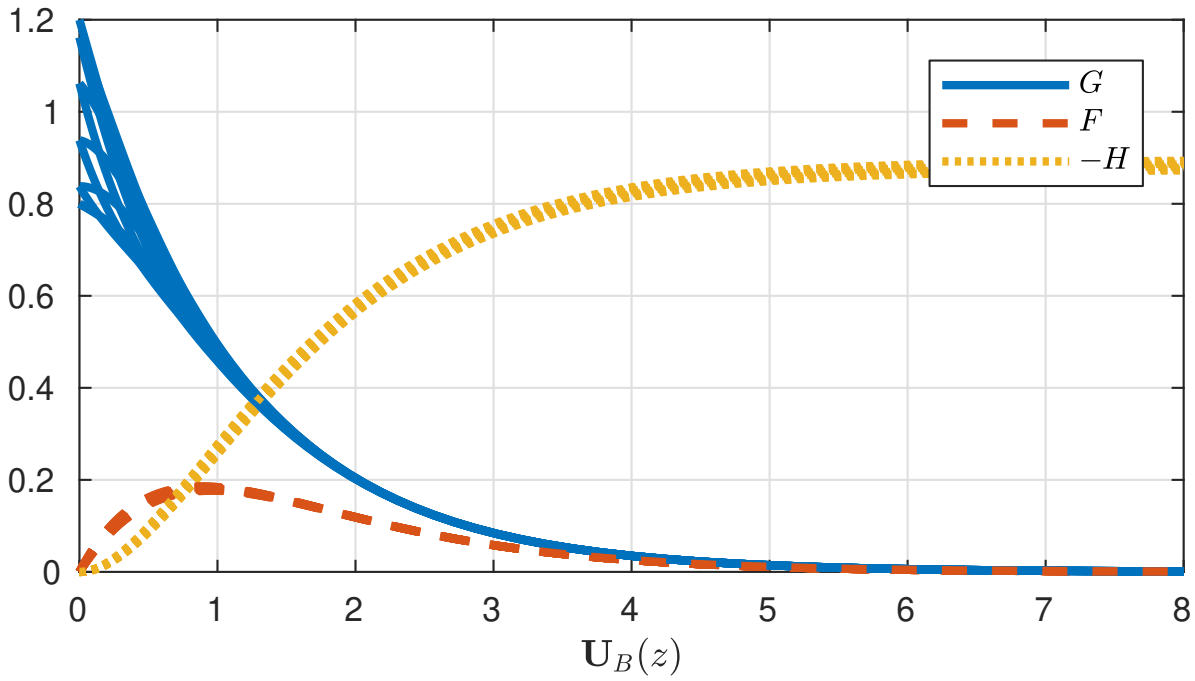

Figure 2.4: Typical variation of the modulated velocity profiles F (- - -), G (—), $-H$ ($\cdots$) with $R = 500$, $U_w = 0.2$ and $\varphi = 10$. Profiles have been sampled at 10 evenly spaced time locations over a period of modulation to demonstrate the variation in the three base flow components.

Figure 2.5 shows the temporal evolution of the base flow for vertical positions $z = 0$, $z = 0.1$ and $z = 0.25$ over one period of modulation with $R = 500$, $U_w = 0.2$ and $\varphi = 10$.

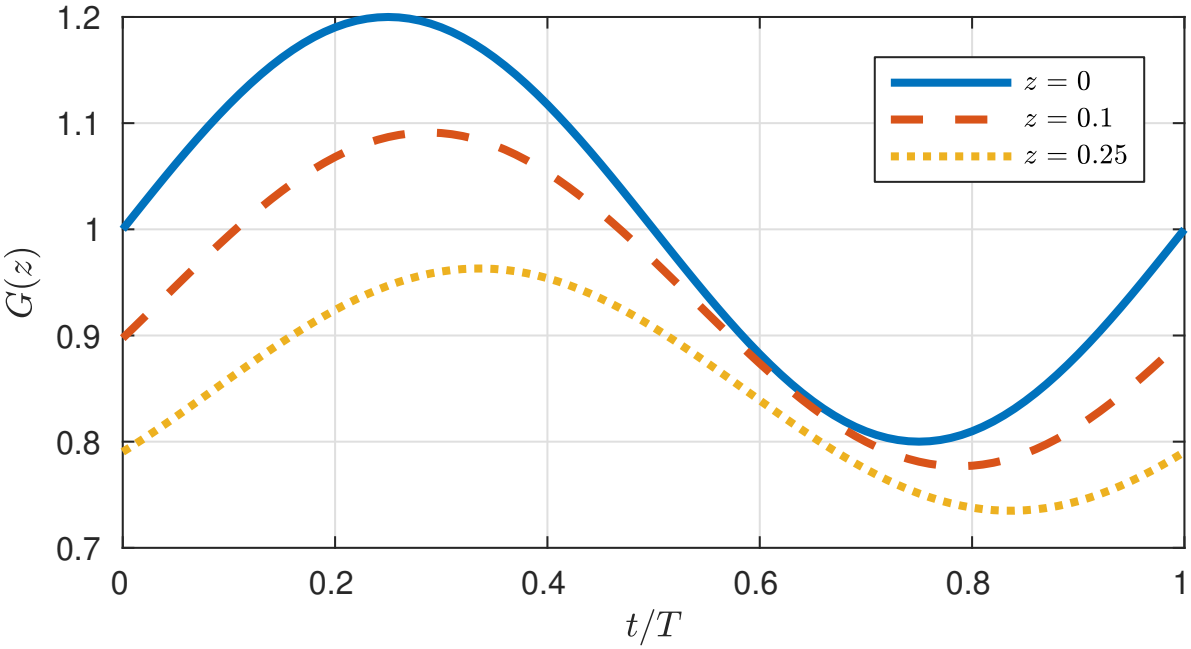

Figure 2.5: Temporal evolution of G for vertical positions $z = 0$ (-), $z = 0.1$ (- - -) and $z = 0.25$ ($\cdots$) over one period of modulation, with $R = 500$, $U_w = 0.2$ and $\varphi = 10$.

2.1.2 High Frequency Limit for Small Amplitude Modulation

To begin the exploration of alterations introduced by the modulation, it is informative to consider the base flow velocity fields in the high frequency limit. Throughout the following discussion in this section we will assume that the oscillations are of high frequency, $\varphi \gg 1$, and small amplitude so that $\hat{\epsilon} := \frac{R_s\sqrt{\varphi}}{R} \ll 1$, allowing for non-linear interactions in $\hat{\epsilon}$ to be neglected.

Consider the modulated equations in the non-rotating frame given by (2.10), with boundary conditions

$$F(0,\tau) = H(0,\tau) = 0, \quad G(0,\tau) = 1 + \hat{\epsilon}\cos\left(\frac{\varphi}{R}\tau\right)$$
$$F \to 0, \quad G \to 0 \quad \text{as} \quad z \to \infty$$

and small amplitude oscillations, $\hat{\epsilon} \ll 1$ with fixed R. We expand the flow variables in

terms of this small parameter $\hat{\epsilon}$ to give

$$F = F_0 + \hat{\epsilon} f_1 + \hat{\epsilon}^2 f_2 + \mathcal{O}(\hat{\epsilon}^3)$$
$$G = G_0 + \hat{\epsilon} g_1 + \hat{\epsilon}^2 g_2 + \mathcal{O}(\hat{\epsilon}^3)$$
$$H = H_0 + \hat{\epsilon} h_1 + \hat{\epsilon}^2 h_2 + \mathcal{O}(\hat{\epsilon}^3)$$

and derive the first and second order expansion equations to be

$$\frac{\partial f_1}{\partial \tau} = \frac{1}{R}\left[2\left(G_0 g_1 - F_0 f_1\right) - h_1 \frac{\partial F_0}{\partial z} - H_0 \frac{\partial f_1}{\partial z} + \frac{\partial^2 f_1}{\partial z^2}\right] \tag{2.21a}$$
$$\frac{\partial g_1}{\partial \tau} = \frac{1}{R}\left[-2\left(F_0 g_1 + G_0 f_1\right) - h_1 \frac{\partial G_0}{\partial z} - H_0 \frac{\partial g_1}{\partial z} + \frac{\partial^2 g_1}{\partial z^2}\right] \tag{2.21b}$$
$$\frac{\partial h_1}{\partial z} = -2 f_1 \tag{2.21c}$$

with boundary conditions

$$f_1(0,t) = h_1(0,t) = 0, \quad g_1(0,t) = \cos\left(\frac{\varphi}{R}\tau\right)$$
$$f_1 \to 0 \quad g_1 \to 0 \quad \text{as} \quad z \to \infty$$

and

$$\frac{\partial f_2}{\partial \tau} = \frac{1}{R}\left[2 g_2 G_0 + g_1^2 - 2 f_2 F_0 - f_1^2 + H_0 \frac{\partial f_2}{\partial z} + h_1 \frac{\partial f_1}{\partial z} + h_2 \frac{\partial F_0}{\partial z} + \frac{\partial^2 f_2}{\partial z^2}\right] \tag{2.22a}$$
$$\frac{\partial g_2}{\partial \tau} = \frac{1}{R}\left[f_2 G_0 + f_1 g_1 + F_0 g_2 + H_0 \frac{\partial g_2}{\partial z} + h_1 \frac{\partial g_1}{\partial z} + h_2 \frac{\partial G_0}{\partial z}\right] \tag{2.22b}$$
$$\frac{\partial h_2}{\partial z} = -2 f_2 \tag{2.22c}$$

with homogeneous boundary conditions on f_2, g_2 and h_2.

Since we are looking specifically at the high frequency limit, the primary lengthscale on which the flow will evolve will be the Stokes layer thickness δ_s. In the current non-dimensionalisation, this takes the form $\delta_s = \sqrt{\frac{2}{\varphi}}$ and we can scale

$$\tilde{z} = \frac{z}{\delta_s} \qquad \tilde{\tau} = \frac{\varphi}{R}\tau$$

to give

$$\frac{1}{R\delta^2}\frac{\partial f_1}{\partial \tilde{\tau}} = \frac{1}{R}\left[2\left(G_0 g_1 - F_0 f_1\right) - \frac{1}{\delta}\left(F_0' h_1 + H_0 f_1'\right) + \frac{1}{\delta^2} f_1''\right] \tag{2.23a}$$
$$\frac{1}{R\delta^2}\frac{\partial g_1}{\partial \tilde{\tau}} = \frac{1}{R}\left[-2\left(F_0 g_1 + G_0 f_1\right) - \frac{1}{\delta}\left(G_0' h_1 + H_0 g_1'\right) + \frac{1}{\delta^2} g_1''\right] \tag{2.23b}$$
$$h_1' = -2\delta f_1 \tag{2.23c}$$

where we have set $' = \frac{\partial}{\partial \tilde{z}}$ and dropped the subscript s from the definition of δ_s for notational simplicity. We have homogeneous boundary conditions on f_1 and h_1 together with

$$g_1(0,\tilde{\tau}) = \cos(\tilde{\tau}), \qquad g_1(\tilde{z}\to\infty,\tilde{\tau}) = 0 \tag{2.24}$$

At this stage, it is possible to develop an expansion for f_1, g_1 and h_1 in terms of the small parameter δ, so we set

$$\begin{aligned} f_1 &= f_1^0 + \delta f_1^1 + \delta^2 f_1^2 + \mathcal{O}(\delta^3) \\ g_1 &= g_1^0 + \delta g_1^1 + \delta^2 g_1^2 + \mathcal{O}(\delta^3) \\ h_1 &= h_1^0 + \delta h_1^1 + \delta^2 h_1^2 + \mathcal{O}(\delta^3) \end{aligned}$$

which, after substitution into (2.23), gives

$$\frac{\partial f_1^k}{\partial \tilde{\tau}} = 2\left(G_0 g_1^{k-2} - F_0 f_1^{k-2}\right) - F_0' h_1^{k-2} + H_0 \frac{\partial f_1^{k-1}}{\partial \tilde{z}} + \frac{\partial^2 f_1^k}{\partial \tilde{z}^2} \tag{2.25a}$$

$$\frac{\partial g_1^k}{\partial \tilde{\tau}} = -2\left(F_0 g_1^{k-2} + G_0 f_1^{k-2}\right) - G_0' h_1^{k-2} + H_0 \frac{\partial g_1^{k-1}}{\partial \tilde{z}} + \frac{\partial^2 g_1^k}{\partial \tilde{z}^2} \tag{2.25b}$$

$$\frac{\partial h_1^k}{\partial \tilde{z}} = -2 f_1^{k-1} \tag{2.25c}$$

for some integer k. Note that the superscript refers to the order in terms of the boundary layer thickness δ while the subscript refers to the order in terms of the modulation amplitude $\hat{\epsilon}$. If $k = 0$, this gives the dominant terms to first order in δ as

$$\frac{\partial f_1^0}{\partial \tilde{\tau}} = \frac{\partial^2 f_1^0}{\partial \tilde{z}^2} \tag{2.26a}$$

$$\frac{\partial g_1^0}{\partial \tilde{\tau}} = \frac{\partial^2 g_1^0}{\partial \tilde{z}^2} \tag{2.26b}$$

$$\frac{\partial h_1^0}{\partial \tilde{z}} = 0 \tag{2.26c}$$

which, subject to the boundary conditions (2.24), gives

$$f_1^0 = 0 \tag{2.27a}$$

$$g_1^0 = \exp(-\tilde{z})\cos(\tilde{\tau} - \tilde{z}) \tag{2.27b}$$

$$= e^{-(1+i)\tilde{z}} e^{i\tilde{\tau}} + e^{-(1-i)\tilde{z}} e^{-i\tilde{\tau}} \tag{2.27c}$$

$$h_1^0 = 0 \tag{2.27d}$$

If $k = 1$, the second order in δ equations reduce to

$$\frac{\partial f_1^1}{\partial \tilde{\tau}} = \frac{\partial^2 f_1^1}{\partial \tilde{z}^2} + \underbrace{H_0 \frac{\partial f_1^0}{\partial \tilde{z}}}_{=0} \tag{2.28a}$$

$$\frac{\partial g_1^1}{\partial \tilde{\tau}} = \frac{\partial^2 g_1^1}{\partial \tilde{z}^2} + H_0 \frac{\partial g_1^0}{\partial \tilde{z}} \tag{2.28b}$$

$$\frac{\partial h_1^1}{\partial \tilde{z}} = \underbrace{-2 f_1^0}_{=0} \tag{2.28c}$$

with homogeneous boundary conditions. This demonstrates that f_1 and h_1 are of at least an order of magnitude in δ smaller than g_1 in this limit. Equations (2.28) also provide the non-linear correction term g_1^1.

This process suggests that the dominant behaviour for small amplitude, high frequency modulations amounts to the addition of a Stokes layer to the steady rotating disk boundary layer in a similar fashion to Thomas et al. [76] for the channel flow scenario. Therefore, the configuration we are presenting throughout this report may be viewed as a combination of the archetypal two-dimensional oscillatory boundary layer, the Stokes layer, and one of the canonical three-dimensional boundary layer configurations, the steady rotating disk.

The results of the analysis may be confirmed numerically by solving the linearised system of equations (2.21) in a similar fashion to the solution of the basic state equations in section 2.1.1. Figure 2.6 shows a snapshot at a frozen time instant of the comparison between g_1^0 and the time-dependent part of the azimuthal component of the base flow, G_{osc}, calculated by the relation.

$$G_{\text{osc}} = G_{\text{total}} - G_{\text{steady}} \tag{2.29}$$

Figures 2.7 and 2.8 show a similar comparison across a single period of modulation at two values of z, namely $z = 0.1$ and $z = 0.25$. Figure 2.9 shows the maximum error

$$\max_{\tilde{\tau},\tilde{z}} |G_{\text{osc}} - g_1^0| \tag{2.30}$$

across the boundary layer and across a modulation period between the analytic Stokes layer contribution g_1^0 and the time-dependent part of the azimuthal component of the base flow G_{osc} for $\hat{\epsilon} = 0.1$ and $\hat{\epsilon} = 0.2$ across a range of values for φ. As would be expected, the maximum error is highest for low frequency modulations, although still relatively small

when compared against the modulation amplitude $\hat{\epsilon}$. Thus, it should be appropriate to utilise the approximation that

$$G(\tilde{z}, \tilde{\tau}) \sim G_0(\tilde{z}) + \exp(-\tilde{z}) \cos(\tilde{\tau} - \tilde{z}) \tag{2.31}$$

for any stability analyses conducted using the modulated rotating disk boundary layer, provided the oscillation amplitude and frequency are constrained appropriately. Throughout the stability analyses conducted in chapter 3, this approximation is not used, and the base flow is always computed numerically in full. However, for future studies that require a more restrictive computational load, the use of this approximation would aid in a reduction in computational cost and simplify the analysis. As will be explained in the forthcoming chapter, this approximation is in no way necessary for our analysis, and is intended only as an illustration of the dominant behaviour in the system.

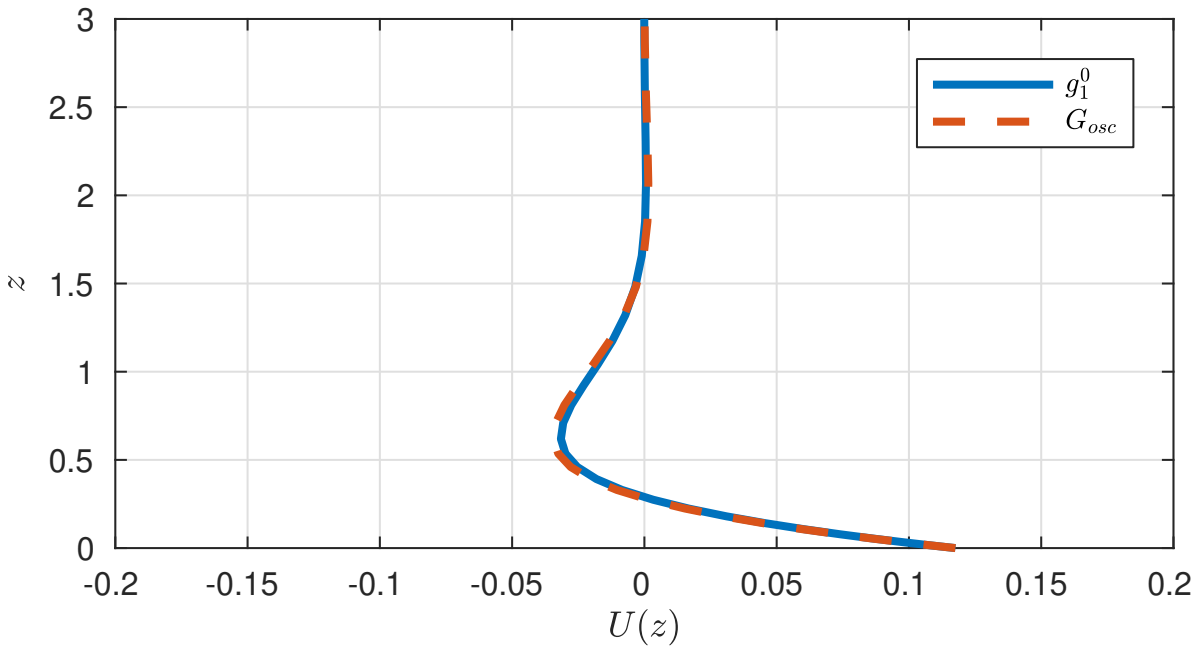

Figure 2.6: Comparison at frozen time instant between the Stokes layer contribution g_1^0 (—) and the time-dependent part of the azimuthal component of the base flow G_{osc} (- - -) for $\hat{\epsilon} = 0.2$ and $\varphi = 10$.

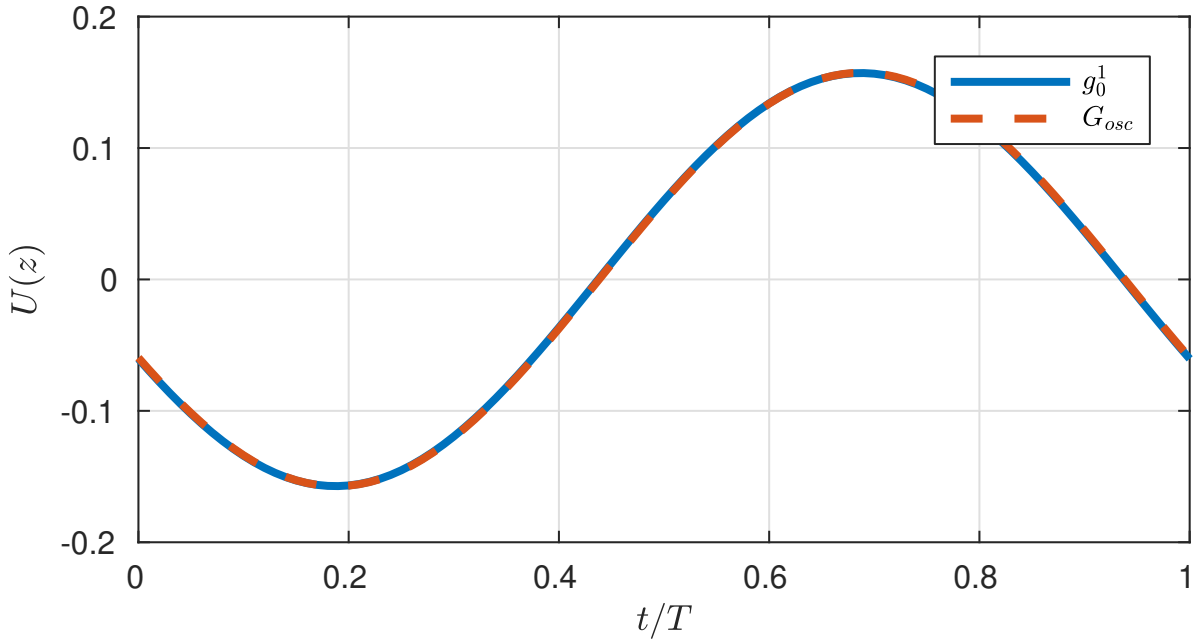

Figure 2.7: Comparison between the analytic Stokes layer contribution g_1^0 (—) and the time-dependent part of the azimuthal component of the base flow G_{osc} (- - -) for $\hat{\epsilon} = 0.2$ and $\varphi = 10$ at $z = 0.1$.

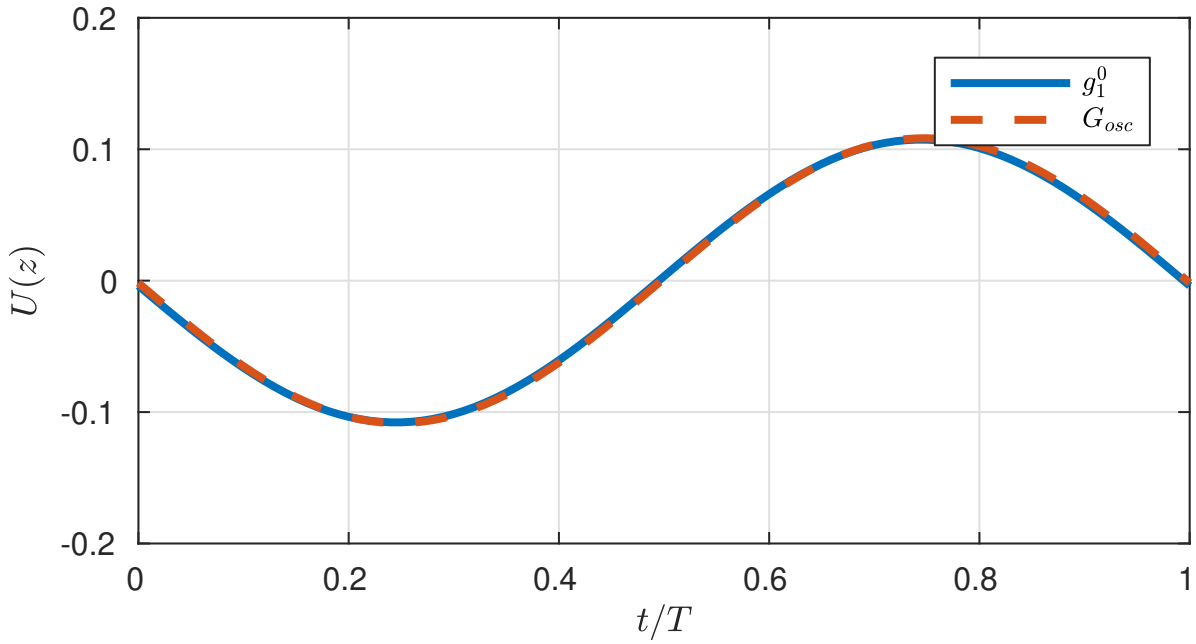

Figure 2.8: Comparison between the analytic Stokes layer contribution g_1^0 (—) and the time-dependent part of the azimuthal component of the base flow G_{osc} (- - -) for $\hat{\epsilon} = 0.2$ and $\varphi = 10$ at $z = 0.25$.

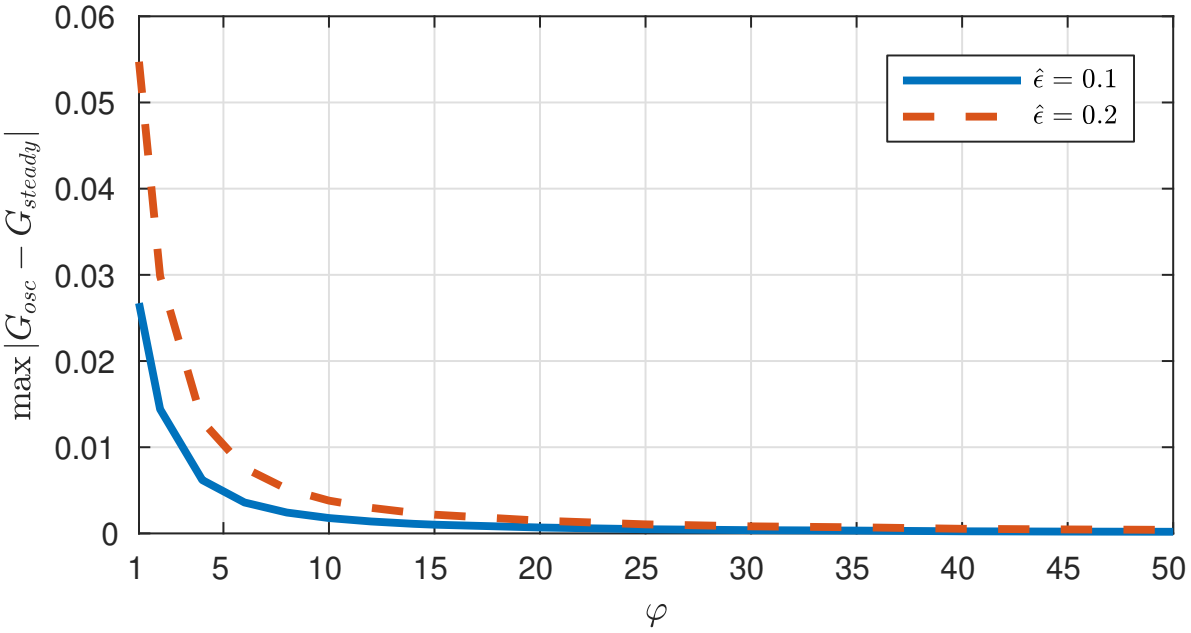

Figure 2.9: Maximum error $\max_{\tilde{\tau},\tilde{z}} |G_{\text{osc}} - g_1^0|$ across the boundary layer and across a modulation period between the analytic Stokes layer contribution g_1^0 and the time-dependent part of the azimuthal component of the base flow G_{osc} for $\hat{\epsilon} = 0.1$ (—) and $\hat{\epsilon} = 0.2$ (- - -) across a range of values for φ.

2.1.3 Average Deviation from the Basic State

An important feature of the modulated rotation rate when compared with other stabilising techniques such as the surface roughness imposed by Cooper et al. [21], Garrett et al. [36] is that there is no inherent average deviation from the base flow across a period. This may be checked by computing the average of a flow field over a period of modulation and comparing against the steady state solution. We compute the average using the expression

$$\bar{F}(z) = \frac{1}{T}\int_0^T F(z,t)dt$$

and figure 2.10 shows the maximum deviation between the averaged azimuthal flow component and the steady solution across a range of φ and U_w values. We can thus see that for small amplitude modulation, the deviation from the steady state is negligible, in contrast to other stabilising methods studied previously. We will revisit this averaging procedure of Garrett et al. [36] in our discussion of future directions in chapter 5.

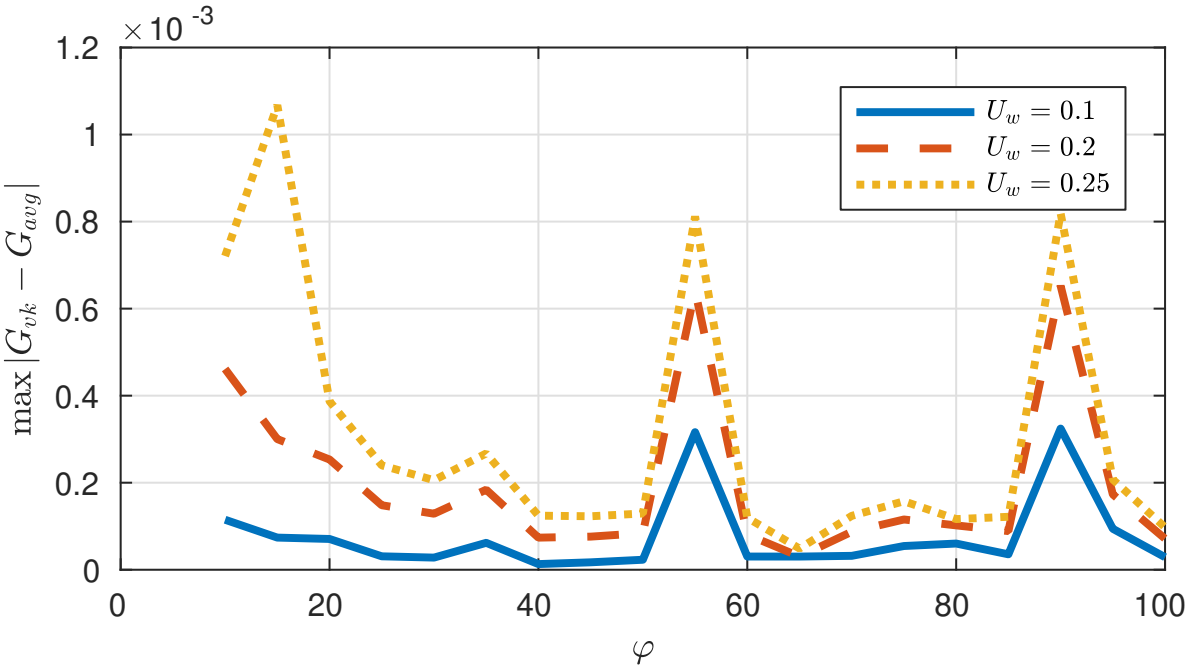

Figure 2.10: Maximum deviation of averaged modulated base flow profiles from the steady state solution for varying φ and $U_w = 0.1$ (-), $U_w = 0.2$ (- - -) and $U_w = 0.25$ ($\cdots$).

2.1.4 Review of the Local Stability Properties of Steady Rotating Disk Boundary Layers

The local linear stability of the steady rotating disk boundary layer was first studied by Gregory et al. [38] in 1955 with a view to approximating the flow over a swept wing, before Malik [50] and Mack [49] provided solutions to the eigenvalue dispersion relations and calculated neutral stability curves in the early 1980s. As discussed in section 2.1, both flow configurations are three-dimensional and have distinct flow components in two directions along the surface. The disk has flow components in the radial and azimuthal directions, while the swept wing configuration has flow components along the span of the wing and in the direction of flight. It was shown by Gregory et al. [38] that both configurations are also prone to *crossflow instabilities*, which give rise to crossflow vortices. For this reason, the rotating disk was classically studied as a canonical example for a three-dimensional flow and as an approximation to the flow over a swept wing. The facts that the rotating disk equations admit an exact similarity solution to the Navier-Stokes equations, and that the disk is easier to work with experimentally has inspired a great deal of stability studies over the past few decades.

There are three types of instability present in the rotating disk boundary layer. A crossflow instability or *type I mode* was originally discovered by Gregory et al. [38]. This instability is inviscid in nature, and similar mechanisms can be found on swept wings and other rotating objects. This is the *most unstable* of the three types of instability, in the sense that it occurs at the lowest Reynolds number for stationary disturbances. It was shown first by Malik [50], and then confirmed by Lingwood [44] and others such as Cooper and Carpenter [19], Thomas [71], Dhanak et al. [30], Garrett et al. [36] that the onset of this instability occurs around $R = 286$ for disturbances which are stationary with respect to the disk surface.

In addition to the crossflow instability, the boundary layer is convectively unstable to a second mode, *type II*, which is viscous in nature and caused by the streamwise curvature and Coriolis effects. In the neutral curves present in Malik [50], Lingwood [47] and this document, the type I and type II instabilities can be clearly seen as the upper and lower sections respectively. Mack [49] mentions a third mode, now known as the *type III* mode, which propels energy towards the disk centre, but is spatially damped. Travelling instabilities in the rotating disk configuration were discussed and

traced in detail by Balakumar and Malik [7] and their importance to the full spatio-temporal stability structure of the flow was realised with Lingwood's [43] discovery of an absolute instability present in the configuration. As explained in section 2.2.3, it is the coalescence of the type I and III modes which causes the absolute instability to arise.

As well as the convectively unstable type I and type II instabilities, where disturbances grow spatially as they convect radially outward, Lingwood [43] showed, using a local spatio-temporal linear stability analysis, that above a critical Reynolds number of approximately 507 the flow becomes absolutely unstable in the radial direction. Lingwood's [43] absolute instability was found using Briggs' method [15] and occurs for travelling, rather than stationary disturbances.

Given the similarities between the rotating disk and swept-wing boundary layers, it seems natural to consider whether such a mechanism exists for the latter. However, as discussed in Lingwood and Alfredsson [46], one major difference between the rotating disk and swept-wing flows lies with the inherent azimuthal periodicity. The possibility that disturbances can circulate in the azimuthal direction has significant implications for the long term behaviour. In order for there to exist a physically significant absolute instability in the swept-wing boundary layer, a wavepacket would need to grow in time simultaneously at fixed chordwise and spanwise locations. Lingwood and Alfredsson [46] mention the asymptotic studies of Lingwood [45], Ryzhov and Terent'ev [64] and Taylor and Peake [70] which demonstrate the possibility of chordwise, but not spanwise, absolute instability, and without spanwise periodicity analogous to the azimuthal periodicity of the rotating disk flow, chordwise absolute instability does not prevent disturbances convecting out of the domain of interest.

One of the original motivations for Lingwood's [43] spatio-temporal analysis was the relatively consistent experimental evidence of transition to turbulence around a Reynolds number of $R = 513 \pm 3\%$. The critical Reynolds number for the onset of absolute instability was found by Lingwood [43] to be $R = 507.3$ and she thus suggested that the absolute instability may be a cause for transition to turbulence. However, there are limitations as to what conclusions relating to the connection between absolute instability and transition can be drawn from this analysis, due to the fact that this analysis is purely linear and local in radius while experimental studies include non-linear effects and are spatially developing. In particular, Davies and Carpenter [27] showed, using linear DNS of impulsive

disturbances, that when the radial inhomogeneity of the flow is incorporated, disturbances do not grow in time at fixed radial locations above the critical Reynolds number for local absolute instability, at least for the azimuthal mode numbers in the range that Lingwood [43] focused upon. The conclusion drawn, therefore, was that the rotating disk boundary layer flow has no unstable linear global mode, and is linearly globally stable, even where the flow is locally absolutely unstable. This describes the first numerical global study of the flow and was contrary to what many others believed at the time. We will review the global stability results and present an explanation of the effects of incorporating radial inhomogeneity in chapter 4, but for now will concentrate on the local approximation in the context of establishing an eigenvalue dispersion relation analogous to equation (1.9).

2.1.5 Steady Local Eigenvalue Analysis Using a Primitive Variable Formulation

A brief account of the perturbation analysis undertaken by other authors such as Malik [50], Lingwood [47, 43] and Appelquist [3] will be given here, with the view of introducing the normal mode approximation taken, and the non-dimensionalisations that will be employed throughout the remainder of this chapter. Following the methods of these previous authors, we non-dimensionalise using the local radial position r_L, so that the timescale is non-dimensionalised by $\delta^*/(\Omega^* r_L^*)$ and the Reynolds number becomes

$$R = r_L \tag{2.32}$$

as described in section 2.1.1. This gives the mean flow in the non-dimensional form as

$$\mathbf{U}(r,z) = \left(\frac{r}{R}F(z), \frac{r}{R}G(z), \frac{1}{R}H(z)\right) \tag{2.33}$$

Under this scaling, the so-called parallel-flow approximation amounts to the replacement of the radial coordinate r by the constant r_L in the equations, which homogenises the mean flow along the radial direction. By selecting the mean flow at one given radial position and then artificially replicating it at all other radial locations, this parallel-flow approximation allows the disturbance to be separable along the radial direction and take a normal-mode form. As mentioned in Lingwood and Alfredsson [46], this is a useful and common approximation to make, and is known to give accurate results for the local analysis provided the disturbance wavelength is short compared to the scale the basic flow

varies on. However, on using this approach we must neglect terms which are the same order as others that are retained. In particular, some R^{-1} terms are kept because the no-slip boundary condition can create instability, whereas other R^{-1} terms are neglected because they would lead to a partial instead of an ordinary differential equation. While this approach has been shown by Balakumar and Malik [7], among others, to have little effect on the eigenvalue analysis, it is important to note that the inhomogeneity of the disk arising from including the non-parallel terms has a profound effect on the *global* stability of the flow. This will be revisited during the discussion of the global stability in chapter 4 but for the time being we will assume that the local effects of applying this approximation are negligible. The rotational symmetry of the mean flow, together with the inherent cylindrical geometry of the problem, ensures that the disturbance variation along the azimuthal direction can also be taken to have a normal-mode form. Similarly to usual stability analyses, we can decompose the total flow into mean and perturbation quantities

$$\begin{aligned} F(r,\theta,z,t) &= \frac{r}{R}F(z) + u(r,\theta,z,t) \\ G(r,\theta,z,t) &= \frac{r}{R}G(z) + v(r,\theta,z,t) \\ H(r,\theta,z,t) &= \frac{1}{R}H(z) + w(r,\theta,z,t) \\ P(r,\theta,z,t) &= \frac{1}{R^2}P(z) + p(r,\theta,z,t) \end{aligned}$$

and take a normal mode form of the disturbance to get

$$\mathbf{u} = \hat{\mathbf{u}}(z)e^{i(\alpha r+\beta R\theta-\omega t)}, \quad p = \hat{p}(z)e^{i(\alpha r+\beta R\theta-\omega t)} \tag{2.34}$$

where $\hat{\mathbf{u}} = (\hat{u}, \hat{v}, \hat{w})$ and $\hat{p}$ are the spectral representations of the perturbation fields. We interpret, as usual, ω as the frequency of the travelling wave disturbance and α, β as the radial and azimuthal wavenumbers respectively. The azimuthal mode number $n = \beta R$ can be identified as the integer number of complete cycles of the disturbance around the azimuth and can be compared experimentally with the number of spiral vortices around the disk surface. Although by definition n is integer-valued, for practical purposes we will do as others have done and treat β, and therefore n, as continuously varying. Substituting the normal mode solution (2.34) into the full perturbation equations and applying the

parallel-flow approximation by replacing r by R gives the perturbation equations

$$\left(i\alpha + \frac{1}{R}\right)\hat{u} + \left(\frac{i\beta}{R}\right)\hat{v} + \hat{w}' = 0$$

$$\left(i\alpha F + \frac{i\beta G}{R} + \frac{\alpha^2}{R} + \frac{\beta^2}{R^3} + \frac{F}{R}\right)\hat{u} + \frac{H}{R}\hat{u}' - \frac{1}{R}\hat{u}'' - \frac{2}{R}(1+G)\hat{v} + F'\hat{w} + i\alpha\hat{p} = i\hat{u}\omega$$

$$\frac{2}{R}(1+G)\hat{v} + \left(i\alpha F + \frac{i\beta G}{R} + \frac{\alpha^2}{R} + \frac{\beta^2}{R^3} + \frac{F}{R}\right)\hat{v} + \frac{H}{R}\hat{v}' - \frac{1}{R}\hat{v}'' + G'\hat{w} + \frac{i\beta}{R}\hat{p} = i\hat{v}\omega$$

$$\left(i\alpha F + \frac{i\beta G}{R} + \frac{\alpha^2}{R} + \frac{\beta^2}{R^3} + \frac{F}{R}\right)\hat{w} + \frac{H'}{R}\hat{w}' - \frac{1}{R}\hat{w}''\hat{p}' = i\hat{w}\omega$$

The stability properties of this flow have been studied using these equations in various works by Malik [50], Lingwood [47, 43] and Appelquist [3] and others and there is a wealth of literature describing their findings. Their solution method amounts to expressing these equations as an eigenvalue relation of the form

$$\mathcal{D}(\omega, \alpha, \beta, R) = 0 \tag{2.35}$$

and solving for α once ω, β and R are specified. We will not attempt to solve the eigenvalue equations in this form, but will instead make use of the velocity-vorticity ideas from chapter 1.

2.2 Local Stability of the Steady Rotating Disk Boundary Layer using a Velocity-Vorticity Formulation

The velocity-vorticity formulation of Davies and Carpenter [26] is discussed in section 1.4.1 for the general three-dimensional Cartesian case, and solved for a special two-dimensional case; the Blasius boundary layer. Since, in this section, we are interested in the rotating disk boundary layer, we will formulate the governing equations for this flow configuration and discuss the advantages over the methods of analysis based on the primitive variable perturbation equations. In previous studies, such as Davies and Carpenter [26, 27], Davies et al. [28] and Thomas and Davies [73], the velocity-vorticity formulation has been utilised to conduct direct numerical simulations (DNS) of the steady rotating disk boundary layer. The study described in the following section, however, marks the first linear normal mode analysis using said formulation. Direct numerical simulations are widely used in the fluid dynamics community to achieve numerical solutions of the Navier-Stokes equations which fully resolve the spatial and temporal evolution of velocity variables. These simulations

are often very computationally costly, and thus have become far more popular in recent years with the rapid advancement of computational power. Simulations that only in the last decade would have taken days on a departmental server can now be accomplished in a reasonable time frame on a personal workstation. This has led to many simulation based studies being carried out to understand the stability of the rotating disk boundary layer. Direct numerical simulations allow for a more complete understanding of the stability properties of a flow than eigenvalue-based approaches. One can view DNS as a stepping stone, bridging the gap between theory and experiment and indeed has allowed far more of an insight into spatially developing flows than was previously possible. A recent paper by Lingwood and Alfredsson [46] gives a review of the current state of the field and overviews are also given in section 2.1.4 and chapter 4. Some notable simulation studies are described in Davies and Carpenter [27], Davies et al. [28], Appelquist et al. [5, 6] and Appelquist et al. [4].

When considering the Blasius case, we used a Cartesian coordinate system to present the velocity-vorticity formulation. As stated in Davies and Carpenter [26], we can readily change to a cylindrical polar system and a non-inertial frame of reference which rotates at a constant angular velocity about the z-axis in conjunction with the disk. The Reynolds number R is given by (2.32), and under the scalings (2.6), the non-dimensional rotation rate is equal to $\Omega = \frac{1}{R}$.

In the same notation as section 2.1.5, let F, G and H denote the non-dimensional radial, azimuthal and axial similarity velocities respectively, so that the undisturbed base flow is given by (2.33). In the usual manner, perturbations to the velocity and vorticity fields are introduced, denoted by

$$\mathbf{u} = (u_r, u_\theta, w), \quad \boldsymbol{\xi} = (\xi_r, \xi_\theta, \xi_z)$$

If we define the *primary* variables as being (ξ_r, ξ_θ, w) then the following equations for the primary variables in the rotating frame of reference are fully equivalent to the Navier-Stokes equations

$$\frac{\partial \xi_r}{\partial t} + \frac{1}{r}\frac{\partial N_z}{\partial \theta} - \frac{\partial N_\theta}{\partial z} - \frac{2}{R}\left(\xi_\theta + \frac{\partial w}{\partial r}\right) = \frac{1}{R}\left[\left(\nabla^2 - \frac{1}{r^2}\right)\xi_r - \frac{2}{r^2}\frac{\partial \xi_\theta}{\partial \theta}\right] \tag{2.36a}$$

$$\frac{\partial \xi_\theta}{\partial t} + \frac{\partial N_r}{\partial z} - \frac{\partial N_z}{\partial r} + \frac{2}{R}\left(\xi_r - \frac{1}{r}\frac{\partial w}{\partial \theta}\right) = \frac{1}{R}\left[\left(\nabla^2 - \frac{1}{r^2}\right)\xi_\theta + \frac{2}{r^2}\frac{\partial \xi_r}{\partial \theta}\right] \tag{2.36b}$$

$$\nabla^2 w = \frac{1}{r}\left(\frac{\partial \xi_r}{\partial \theta} - \frac{\partial (r\xi_\theta)}{\partial r}\right) \tag{2.36c}$$

where

$$\mathbf{N} = (N_r, N_\theta, N_z) = (\nabla \times \mathbf{U}_B) \times \mathbf{u} + \boldsymbol{\xi} \times \mathbf{U}_B + \boldsymbol{\xi} \times \mathbf{u}$$

and

$$\nabla^2 = \frac{\partial^2}{\partial r^2} + \frac{1}{r}\frac{\partial}{\partial r} + \frac{1}{r^2}\frac{\partial^2}{\partial \theta^2} + \frac{\partial^2}{\partial z^2}$$

$$\nabla \times \mathbf{U}^B = \left(\frac{1}{r}\frac{\partial U_z^B}{\partial \theta} - \frac{\partial U_\theta^B}{\partial z}\right)\mathbf{e}_r + \left(\frac{\partial U_r^B}{\partial z} - \frac{\partial U_z^B}{\partial r}\right)\mathbf{e}_\theta + \frac{1}{r}\left[\frac{\partial}{\partial r}\left(rU_\theta^B\right) - \frac{\partial U_r^B}{\partial \theta}\right]\mathbf{e}_z$$

are the usual Laplacian and curl operators in cylindrical polar coordinates. Similarly to the Cartesian case, the *secondary* variables can be defined in terms of integrals of the primary variables as follows

$$u_r = -\int_z^\infty \left(\xi_\theta + \frac{\partial w}{\partial r}\right) dz \tag{2.37a}$$

$$u_\theta = \int_z^\infty \left(\xi_r - \frac{1}{r}\frac{\partial w}{\partial \theta}\right) dz \tag{2.37b}$$

$$\xi_z = \frac{1}{r}\int_z^\infty \left(\frac{\partial (r\xi_r)}{\partial r} + \frac{\partial \xi_\theta}{\partial \theta}\right) dz \tag{2.37c}$$

For the purposes of the present analysis, we linearise the governing perturbation equations by dropping the $\boldsymbol{\xi} \times \mathbf{u}$ term in the definition of $\mathbf{N}$, leaving

$$\mathbf{N} = (N_r, N_\theta, N_z) = (\nabla \times \mathbf{U}_B) \times \mathbf{u} + \boldsymbol{\xi} \times \mathbf{U}_B \tag{2.38}$$

and assume that we are dealing with a rigid disk. The linearised no-slip conditions on the perturbation variables thus become

$$u_r = u_\theta = w = 0 \quad \text{at} \quad z = 0$$

and substitution of these boundary conditions into the definitions of the secondary variables gives the following integral constraints on the primary variables

$$\int_0^\infty \left(\xi_\theta + \frac{\partial w}{\partial r}\right) dz = 0$$

$$\int_0^\infty \left(\xi_r - \frac{1}{r}\frac{\partial w}{\partial \theta}\right) dz = 0$$

The far-field vanishing conditions on the velocity and vorticity fields as $z \to \infty$ discussed for the Cartesian case in section 1.4 are satisfied for this configuration.

At this stage, we may proceed to gain insights into the stability of the flow configuration by solving the system (2.36) in one of three ways, each of which will be described in the following sections.

1. **Eigenvalue Analysis:** Firstly, as has been done in chapter 1, we may take a normal mode approximation of the form

$$\mathbf{u} = \hat{\mathbf{u}}(z)e^{i(\alpha r+\beta R\theta-\omega t)}, \quad \xi = \hat{\xi}(z)e^{i(\alpha r+\beta R\theta-\omega t)} \tag{2.39}$$

   and solve the resulting eigenvalue dispersion relation

$$\mathcal{D}(\omega, \alpha, \beta, R) = 0 \tag{2.40}$$

   for α or ω having specified the other parameters.

2. **Monochromatic DNS:** Secondly, we could retain the time dependence in the stability equations and only decompose the variables as

$$\mathbf{u} = \hat{\mathbf{u}}(z,t)e^{i(\alpha r+\beta R\theta)}, \quad \xi = \hat{\xi}(z,t)e^{i(\alpha r+\beta R\theta)} \tag{2.41}$$

   leaving a set of time-dependent ODEs to be solved in a similar manner to the base flow equations in section 2.1.1. This allows us to effectively calculate ω given a prescribed α and β.

3. **DNS with Radial Dependence:** Finally, we could genuinely include the radial dependence and decompose as

$$\mathbf{u} = \hat{\mathbf{u}}(z,t)e^{i\beta R\theta}, \quad \xi = \hat{\xi}(z,t)e^{i\beta R\theta} \tag{2.42}$$

   leaving us to discretise the system in the radial direction. The solution method for this scenario is described in detail in Davies and Carpenter [26] and will be discussed in this report in section 2.2.5. Removing the normal mode solution in the radial direction removes the necessity for the parallel flow approximation and allows an exploration of the effects of the true radial inhomogeneity of the flow. As briefly alluded to in section 2.1.5 and discussed in greater detail later in chapter 4, the inclusion of this inhomogeneity has profound effects on the global stability properties of the flow and the reader should be aware of the potential pitfalls of the parallel flow approximation throughout.

Each of these solution methods will be visited in turn throughout the following sections and we begin our discussion with the eigenvalue analysis.

2.2.1 Numerical Methods for Linear Stability - Eigenvalue Analysis

The following sections illustrate the attempt to extend the work of chapter 1 to the rotating disk configuration. We look to develop a temporal and spatial eigenvalue solver for the velocity-vorticity formulation of the perturbation equations discussed in section 2.2. While studies exist in which the eigenvalue stability problem has been solved using alternative methods to those presented in this work, no method for solving the velocity-vorticity formulation has yet been found in the available literature.

There appear to be three distinct approaches taken to solve the eigenvalue problem in the literature. Two of these, one based on a sixth order system of ODEs and one based on a collocation method, are outlined in Malik [50], Lingwood [43] and Appelquist [3] among other places and so the reader is referred to the references for details. The other is similar to methods already employed in this report which involves integral operators on the primitive variable formulation and is detailed in Cooper and Carpenter [19]. Due to the facts that we are working in a mapped domain and that the primitive formulation contains fourth order operators, this method leaves the operator definitions and the resulting equations inelegant and difficult to work with. Thus we turn to the velocity-vorticity formulation as a starting point for an eigenvalue solver since the operators in question take a much simpler form.

It is worth remarking that in deriving the velocity-vorticity formulation perturbation equations, we apply the parallel-flow approximation at a different stage of the formulation to other authors such as Malik [50], Lingwood [43] and Cooper and Carpenter [19], and thus retain some terms that are not present in the standard analysis due to derivatives taken with respect to the radial coordinate r. A study by Dhanak et al. [30] uses a different vorticity formulation to study effects of uniform suction at the surface, and the discrepancy between his and Malik's [50] formulations is discussed in Lingwood [44]. It has also been shown by Balakumar and Malik [7] that the additional terms arising from the radial inhomogeneity have little effect on the local stability characteristics. Thus, if we convince ourselves that we are at liberty to, we make the parallel flow approximation as usual, replace r by R and take a normal mode approximation of the form

$$\mathbf{u} = \hat{\mathbf{u}}(z)e^{i(\alpha r+\beta R\theta-\omega t)}, \quad \xi = \hat{\xi}(z)e^{i(\alpha r+\beta R\theta-\omega t)} \tag{2.43}$$

After neglecting the non-parallel $\mathcal{O}\left(\frac{1}{R^2}\right)$ terms, as per the previous literature and for consistency with validation, we get

$$-i\omega\xi_r + i\beta N_z - \frac{\partial N_\theta}{\partial z} - \frac{2}{R}\left(\xi_\theta + i\alpha w\right) = \frac{1}{R}\left(-\alpha^2 - \beta^2 + \frac{\partial^2}{\partial z^2}\right)\xi_r \tag{2.44a}$$

$$-i\omega\xi_\theta + \frac{\partial N_r}{\partial z} - \frac{\partial N_z}{\partial r} + \frac{2}{R}\left(\xi_r - i\beta w\right) = \frac{1}{R}\left(-\alpha^2 - \beta^2 + \frac{\partial^2}{\partial z^2}\right)\xi_\theta \tag{2.44b}$$

$$\left(\hat{\nabla}^2 + \frac{\partial^2}{\partial z^2}\right)w = i\beta\xi_r - i\alpha\xi_\theta - \frac{\xi_\theta}{R} \tag{2.44c}$$

with conditions

$$w(0) = 0 \tag{2.45}$$

$$\int_0^\infty \left(\xi_\theta + i\alpha w\right) dz = 0 \tag{2.46}$$

$$\int_0^\infty \left(\xi_r - i\beta w\right) dz = 0 \tag{2.47}$$

Treating the Convective Terms

The main difference between this formulation and the two-dimensional version discussed for the Blasius configuration in section 1.4 is the inclusion of all six flow variables in the convective terms. In order to create a well-posed eigenvalue problem we must eliminate the *secondary* variables $\{u_r, u_\theta, \xi_z\}$ from consideration by expressing them in terms of the *primary* variables $\{\xi_r, \xi_\theta, w\}$. This is done in a similar fashion to the method for the implementation of the boundary conditions in section 1.4 and utilises the mapping

$$\eta = \frac{l}{z + l} \tag{2.48}$$

where l is the scaling factor discussed in section 1.4. We can write an arbitrary secondary variable s in terms of an arbitrary primary variable f as

$$s(z) = \int_z^\infty f(\tilde{z}) d\tilde{z}$$

Transforming this integral to the computational domain under the mapping (2.48), we get

$$s(\eta) = l\int_0^\eta \frac{f(\tilde{\eta})}{\tilde{\eta}^2} d\tilde{\eta}$$

and if we divide through our perturbation equations by η^2 as we did for the Blasius case in section 1.4, then we can define $\hat{f}(\eta) = \frac{f(\eta)}{\eta^2}$ and thus get

$$s(\eta) = l\int_0^\eta \hat{f}(\tilde{\eta}) d\tilde{\eta} \tag{2.49}$$

The definitions of the secondary variables in terms of the primary variables are given by equations (2.37) and on introducing the mapping (2.48) become

$$u_r = -l \int_0^\eta \left(\hat{\xi}_\theta + i\alpha\hat{w} \right) d\tilde{\eta} \tag{2.50a}$$

$$u_\theta = l \int_0^\eta \left(\hat{\xi}_r - i\beta\hat{w} \right) d\tilde{\eta} \tag{2.50b}$$

$$\xi_z = l \int_0^\eta \left(\frac{1}{R}\hat{\xi}_r + i\alpha\hat{\xi}_r + i\beta\hat{\xi}_\theta \right) d\tilde{eta} \tag{2.50c}$$

To implement the solution method, we split the convective terms (2.38) into components and write

$$N_r = \frac{1}{R}\left(rF'w - 2Gu_\theta + H\xi_\theta - rG\xi_z\right)$$
$$N_\theta = \frac{1}{R}\left(rG'w + 2Gu_r - H\xi_r + rF\xi_z\right)$$
$$N_z = \frac{r}{R}\left(G\xi_r - G'u_\theta - F'u_r - F\xi_\theta\right)$$

By inspection of the equations and with the aid of hindsight, we can see that we will also require the r-derivative of N_z, given by

$$\frac{\partial N_z}{\partial r} = \frac{r}{R}\left(G\frac{\partial \xi_r}{\partial r} - G'\frac{\partial u_\theta}{\partial r} - F'\frac{\partial u_r}{\partial r} - F\frac{\partial \xi_\theta}{\partial r}\right) + \frac{1}{R}\left(G\xi_r - G'u_\theta - F'u_r - F\xi_\theta\right)$$

Since there are no other r-derivatives of the convective terms present in the stability equations, we can at this stage apply the parallel-flow approximation and replace r by R in our definitions of $\mathbf{N}$, leaving

$$N_r = F'w - \frac{2}{R}Gu_\theta + \frac{1}{R}H\xi_\theta - G\xi_z \tag{2.51a}$$

$$N_\theta = G'w + \frac{2}{R}Gu_r - \frac{1}{R}H\xi_r + F\xi_z \tag{2.51b}$$

$$N_z = G\xi_r - G'u_\theta - F'u_r - F\xi_\theta \tag{2.51c}$$

$$\frac{\partial N_z}{\partial r} = i\alpha(G\xi_r - G'u_\theta - F'u_r - F\xi_\theta) + \frac{1}{R}\left(G\xi_r - G'u_\theta - F'u_r - F\xi_\theta\right) \tag{2.51d}$$

Substitution of (2.50) into equations (2.51) gives

$$
\begin{aligned}
N_r &= F'w - \frac{2lG}{R}\int_0^\eta \left(\hat{\xi}_r - i\beta\hat{w}\right)d\tilde{\eta} + \frac{1}{R}H\xi_\theta - lG\int_0^\eta \left(\frac{1}{R}\hat{\xi}_r + i\alpha\hat{\xi}_r + i\beta\hat{\xi}_\theta\right)d\tilde{\eta} \\
N_\theta &= G'w - \frac{2lG}{R}l\int_0^\eta \left(\hat{\xi}_\theta + i\alpha\hat{w}\right)d\tilde{\eta} - \frac{1}{R}H\xi_r + lF\int_0^\eta \left(\frac{1}{R}\hat{\xi}_r + i\alpha\hat{\xi}_r + i\beta\hat{\xi}_\theta\right)d\tilde{\eta} \\
N_z &= G\xi_r - lG'\int_0^\eta \left(\hat{\xi}_r - i\beta\hat{w}\right)d\tilde{\eta} + lF'\int_0^\eta \left(\hat{\xi}_\theta + i\alpha\hat{w}\right)d\tilde{\eta} - F\xi_\theta \\
\frac{\partial N_z}{\partial r} &= i\alpha\left(G\xi_r - lG'\int_0^\eta \left(\hat{\xi}_r - i\beta\hat{w}\right)d\tilde{\eta} + lF'\int_0^\eta \left(\hat{\xi}_\theta + i\alpha\hat{w}\right)d\tilde{\eta} - F\xi_\theta\right) \\
&\quad + \frac{1}{R}\left(G\xi_r - lG'\int_0^\eta \left(\hat{\xi}_r - i\beta\hat{w}\right)d\tilde{\eta} + lF'\int_0^\eta \left(\hat{\xi}_\theta + i\alpha\hat{w}\right)d\tilde{\eta} - F\xi_\theta\right)
\end{aligned}
$$

The integral operator (2.49) maybe transformed to a matrix operator if we expand the primary variables $\hat{f}$ in terms of Chebyshev polynomials. As for the Blasius case, we use an odd representation for the primary variables and an even representation for the secondary variables. This parity choice implicitly assumes that the primary variables and all of their even order derivatives vanish as $\eta \to 0$, or equivalently, $z \to \infty$ in the physical domain. As discussed in section 1.4, it is reasonable to assume that this property holds for both velocity and vorticity variables and so we proceed to expand as described. It should be noted that a reverse parity can similarly be chosen, with an even representation for the primary variables and an odd representation for the secondary ones. However, the first case is subtly simpler as there is no halving of the first term, making the integral operators slightly more straightforward and easier to deal with. Truncating the expansion to finite order, we have, for an arbitrary primary variable $\hat{f}$,

$$\hat{f}(\eta) = \sum_{k=1}^{N} \hat{f}_k T_{2k-1}(\eta)$$

so that

$$
\begin{aligned}
s &= l\sum_{k=1}^{N}\hat{f}_k\int_0^\eta T_{2k-1}(\tilde{\eta})d\tilde{\eta} \\
&= \frac{l}{4}(T_0(\eta) + T_2(\eta) - T_0(0) - T_2(0))\hat{f}_1 + \frac{l}{4}\sum_{k=2}^{N}\hat{f}_k\left[\frac{T_{2k}(\eta)}{k} - \frac{T_{2k-2}(\eta)}{k-1} - \frac{T_{2k}(0)}{k} + \frac{T_{2k-2}(0)}{k-1}\right] \\
&= \left\{-\frac{l}{4}\sum_{k=2}^{N}\hat{f}_k\left[\frac{T_{2k}(0)}{k} - \frac{T_{2k-2}(0)}{k-1}\right]\right\}T_0(\eta) + \frac{l\hat{f}_1}{4}T_2(\eta) + \sum_{k=2}^{N}\frac{l}{4k}(\hat{f}_k - \hat{f}_{k+1})T_{2k}(\eta) \\
&= \left(\sum_{k=1}^{N}a_k\hat{f}_k\right)T_0(\zeta) + \frac{l\hat{f}_1}{4}T_2(\eta) + \sum_{k=2}^{N}\frac{l}{4k}(\hat{f}_k - \hat{f}_{k+1})T_{2k}(\eta)
\end{aligned}
$$

where

$$a_1 = 0, \quad a_k = -\frac{l}{4}\left[\frac{T_{2k}(0)}{k} - \frac{T_{2k-2}(0)}{k-1}\right] = \frac{(-1)^k l(1-2k)}{4k(k-1)} \quad (k>1)$$

In practise, for the computational implementation of the routine, since integration increases the order of the polynomial approximation, the highest order term is set equal to zero. The requirement that there is exponential decay of the disturbance variables is sufficient to ensure that the coefficients of the Chebyshev expansion converge to zero faster than any inverse power of their order, referenced to Canuto et. al. [12] in Davies and Carpenter [26]. Thus, taking a large enough N should make the effect of the truncation negligible. In computational tests, it was found that the eigenvalues could be fully resolved when using a discretisation of order $N = 64$. As for the Blasius case, tables of convergence are given in appendix A.3.

Solving the Eigenvalue Problem

To illustrate the process of dividing through by η^2 and subsequently solving the dispersion relation, we present the solution procedure only for the vorticity transport equation of the radial component. Dividing through by η^2 and applying the mapping to equation (2.44b) gives

$$-i\omega\hat{\xi}_r + i\beta\left(\frac{1}{\eta^2}N_z\right) - \left(\frac{1}{\eta^2}\right)\left(-\frac{\eta^2}{l}\frac{\partial N_\theta}{\partial \eta}\right) - \frac{2}{R}\left(\hat{\xi}_\theta + i\alpha\hat{w}\right) - \frac{1}{R}\left(-\alpha^2-\beta^2\right)\hat{\xi}_r - \frac{1}{l^2}\underbrace{\left(2\eta\frac{d}{d\eta} + \eta^2\frac{d^2}{d\eta^2}\right)\left(\eta^2\hat{\xi}_r\right)}_{=\left(6\eta^2+6\eta^3\frac{\partial}{\partial\eta}+\eta^4\frac{\partial^2}{\partial\eta^2}\right)\hat{\xi}_r} = 0$$

which can be condensed to

$$-i\omega\hat{\xi}_r + i\beta\hat{N}_z + \frac{1}{l}\frac{\partial N_\theta}{\partial \eta} - \frac{2}{R}\left(\hat{\xi}_\theta + i\alpha\hat{w}\right) + \frac{1}{R}\left(\alpha^2+\beta^2\right)\hat{\xi}_r - \frac{1}{l^2}\mathcal{D}^2\hat{\xi}_r = 0 \tag{2.52}$$

where

$$\mathcal{D}^2 = 6\eta^2 + 6\eta^3\frac{\partial}{\partial\eta} + \eta^4\frac{\partial^2}{\partial\eta^2} \quad \text{and} \quad \hat{N}_z = \frac{1}{\eta^2}N_z$$

The $\hat{N}_z$ and $\frac{\partial\hat{N}_z}{\partial r}$ terms are calculated in practise by incorporating the division by η^2 directly into the collocation values for the base flow profiles. Thus,

$$\hat{N}_z = G\hat{\xi}_r - l\hat{G}'\int_0^\eta\left(\hat{\xi}_r - i\beta\hat{w}\right)d\tilde{\eta} + l\hat{F}'\int_0^\eta\left(\hat{\xi}_\theta + i\alpha\hat{w}\right)d\tilde{\eta} - F\hat{\xi}_\theta$$

where $\hat{F}$ and $\hat{G}$ represent the divided mean flow quantities. The procedure for the $\frac{\partial\hat{N}_z}{\partial r}$ term is similar, and likewise, a similar procedure is employed for the multiplications by η^2 that occur in N_r and N_θ due to the single integral operator. Following the same method

as for the two-dimensional configuration in section 1.4, we integrate the perturbation equations (2.44) twice with respect to η to give

$$\mathbf{I}_2\left[-i\omega\hat{\xi}_r + i\beta\hat{N}_z - \frac{2}{R}\left(\hat{\xi}_\theta + i\alpha\hat{w}\right) + \frac{1}{R}\left(\alpha^2+\beta^2\right)\hat{\xi}_r\right] + \frac{1}{l}\mathbf{I}_1 N_\theta - \frac{1}{Rl^2}\mathbf{J}\hat{\xi}_r = 0$$

$$\mathbf{I}_2\left[-i\omega\hat{\xi}_\theta - \frac{\partial\hat{N}_z}{\partial r} + \frac{2}{R}\left(\hat{\xi}_r - i\beta\hat{w}\right) + \frac{1}{R}\left(\alpha^2+\beta^2\right)\hat{\xi}_\theta\right] - \frac{1}{l}\mathbf{I}_1 N_r - \frac{1}{Rl^2}\mathbf{J}\hat{\xi}_\theta = 0$$

$$\mathbf{I}_2\left(\frac{i\alpha}{R} - \alpha^2 - \beta^2 - i\beta\hat{\xi}_r + i\alpha\hat{\xi}_\theta + \frac{\hat{\xi}_\theta}{R}\right) + \frac{1}{l^2}\mathbf{J}\hat{w} = 0$$

where, similarly to equations (1.58) and (1.59), the operators $\mathbf{I}_1 f$, $\mathbf{I}_2 f$ and $\mathbf{J}f$ are defined as

$$\mathbf{I}_1 f = \int f$$

$$\mathbf{I}_2 f = \iint f$$

$$\mathbf{J}f = \eta^4 f - 2\int \eta^3 f$$

and the boundary conditions (2.45) transform under the division by η^2 to

$$\hat{w}(1) = 0$$

$$\int_0^1 \left(\hat{\xi}_\theta + i\alpha\hat{w}\right) d\eta = 0$$

$$\int_0^1 \left(\hat{\xi}_r - i\beta\hat{w}\right) d\eta = 0$$

We can write this system as a polynomial eigenvalue problem in α as

$$\begin{pmatrix} \alpha^2 F_0 + \alpha F_1 + F_2 \\ \alpha^2 S_0 + \alpha S_1 + S_2 \\ \alpha^2 T_0 + \alpha T_1 + T_2 \end{pmatrix} \begin{pmatrix} \hat{\xi}_r \\ \hat{\xi}_\theta \\ \hat{w} \end{pmatrix} = 0 \tag{2.53}$$

where $\{\mathbf{F}, \mathbf{S}, \mathbf{T}\}_k$, $(k = 1, \ldots, 3)$ are $(N \times N)$ matrices corresponding to the first, second and third equations respectively and N is the order of the Chebyshev discretisation. The solution method is identical to that discussed in section 1.4.3 and a discussion of spurious eigenvalues and local eigenvalue iteration is given there.

2.2.2 Results and Validation for the Steady Case

In the interest of validation of the results of the velocity-vorticity formulation, we present some established results and compare them against the new method. For the validation

procedure, we will concentrate mainly on the *spatial* setting, where wavenumbers α are calculated from a prescribed real ω. In the alternative scenario, the so called *temporal* analysis, the dispersion relation (2.53) is simplified to a generalised linear eigenvalue problem and becomes

$$\begin{pmatrix} \omega\hat{F}_1 + \hat{F}_2 \\ \omega\hat{S}_1 + \hat{S}_2 \\ \omega\hat{T}_1 + \hat{T}_2 \end{pmatrix} \begin{pmatrix} \xi_r \\ \xi_\theta \\ w \end{pmatrix} = 0 \tag{2.54}$$

We will use this solution method in section 2.2.4 when talking about monochromatic DNS, although presently, the following section will describe the careful numerical validation of the new formulation in the spatial setting.

Direct Eigenvalue Comparisons

Figure 2.11 shows the global spectrum of radial eigenvalues for stationary disturbances with $R = 286$ and $\beta = 0.077$. These parameters were chosen to exactly match a similar diagram in Thomas [71], but are important in their own right as they are the close to the critical parameters for the onset of convective instability. The numerical eigenvalues can be identified as those which differ for the two discretisation orders $N = 96$ and $N = 128$, while the genuine eigenvalues are shown on the figure as filled-in circles. This diagram shows excellent agreement with Thomas [71].

Table 2.1 gives an overview of previously published eigenvalue results relating to the critical parameters for the onset of both type I and type II instabilities and comparison of these with the current work. Some small discrepancies are clearly visible between several of the results, which could be due to several factors relating to the difference in formulations or numerical methods by different authors, or to the fact that some authors round up or down to use only physical integer values of azimuthal mode number n, while some treat β, and therefore n, as continuously varying. Garrett et al. [36] provide a relatively up-to-date discussion of these inconsistencies in their appendix. As mentioned in section 2.2.1, in deriving the velocity-vorticity formulation perturbation equations, we apply the parallel-flow approximation at a different stage to other authors, and as a result should expect some small deviation in our results than those in the literature. The non-parallel correction to the local, eigenvalue analysis is shown by Malik and Balakumar [51] not to be significant, and in practise the deviations between our formulation and that of others

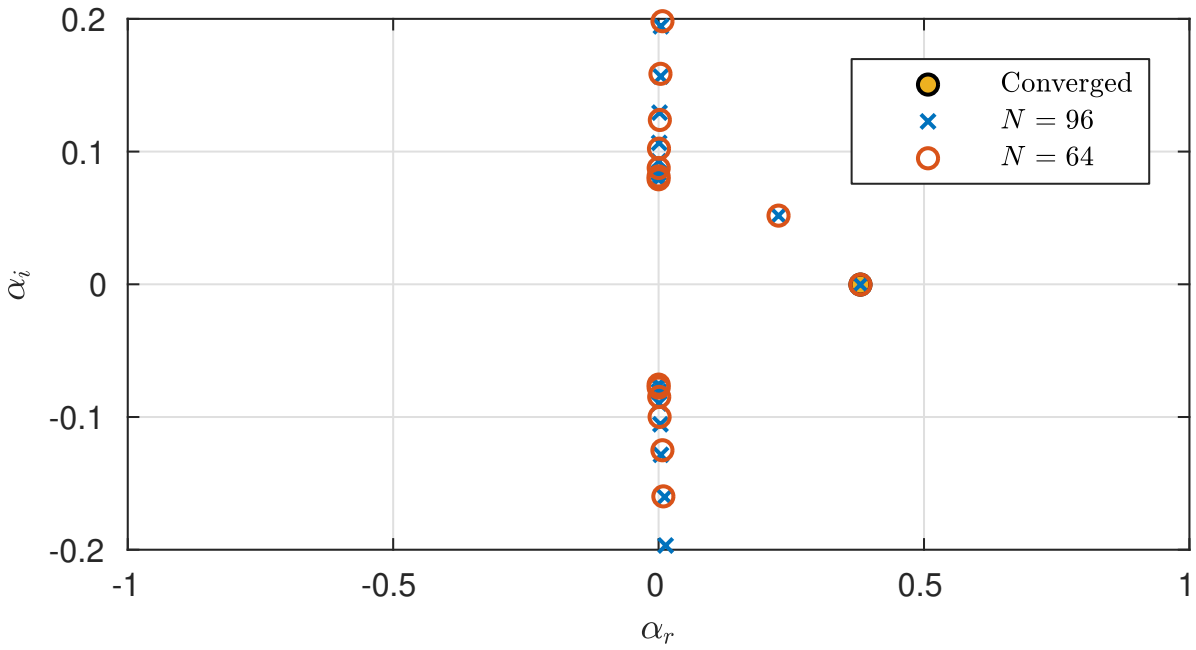

Figure 2.11: Radial wavenumber spectrum for $R = 286$, $\beta = 0.077$ and $\omega = 0$. The most unstable eigenvalue is shown as a filled in circle, while the $\circ$ and $\times$ correspond to the Chebyshev discretisation orders $N = 64$ and $N = 96$ respectively.

have turned out to be small. One would expect the correction to be $\mathcal{O}\left(\frac{1}{R}\right)$, and this is certainly apparent in our results, as larger discrepancies are seen when R is smaller in magnitude. In each case presented below, the temporal frequency ω was prescribed while neutral values of α, β and R were calculated using the arclength continuation method described in section 1.5.1. For the non-stationary ($\omega \neq 0$) disturbance validation, the parameter ω was selected to be identical to that in Thomas [71], to give appropriate comparisons.

Eigenvalue Validation against Literature					
Mode	Reference	ω	R_c	β_c	α_c
Type I	Malik [50]	0	285.36	0.07759	0.38402
	Cooper & Carpenter [19]	0	285.36	0.0776	0.38451
	Thomas [71]	0	290	0.077	0.3779
	Garrett et. al. [36]	0	286.05	0.0775	0.38419
	Appelquist [3]	0	286.05	0.0776	0.38338
	Current Work	**0**	**285.55**	**0.0772**	**0.3818**
Type II	Malik [50]	0	440.88	0.04672	0.13228
	Cooper & Carpenter [19]	0	440.87	0.0466	0.13159
	Thomas [71]	0	451	0.04641	0.1336
	Garrett et. al. [36]	0	450.95	0.04634	0.13067
	Appelquist [3]	0	452.97	0.0468	0.13227
	Current Work	**0**	**439.95**	**0.0468**	**0.13186**
Type I	Thomas [71]	-0.01023	284	0.09379	0.36064
	Current Work	**-0.01023**	**282.49**	**0.0949**	**0.37277**
Type II	Lingwood [43]	0.1225	64.4	-0.106	0.276
	Thomas [71]	0.1225	65	-0.106	0.2661
	Current Work	**0.1225**	**71.958**	**-0.1047**	**0.2940**

Table 2.1: The temporal frequencies ω for this data are prescribed while neutral values of α, β and R were calculated using the arclength continuation method described in section 1.5.1. For the non-stationary ($\omega \neq 0$) disturbance validation, the parameter ω was selected to be identical to that in Thomas [71], to give appropriate comparisons.

Neutral Curve

The algorithm for calculating the neutral curve for the rotating disk configuration is identical in most respects to that for the Blasius configuration described in section 1.5. The only notable difference is the inclusion of the azimuthal mode number β, but the algorithm can be applied analogously with ω replaced everywhere by β, provided we impose some additional constraint on ω. In practise this additional constraint is to specify ω as the desired temporal frequency of the disturbance, with the stationary case corresponding to

$\omega = 0$. The radial and azimuthal wavenumber neutral curves for stationary disturbances are shown in figures 2.12 and 2.13.

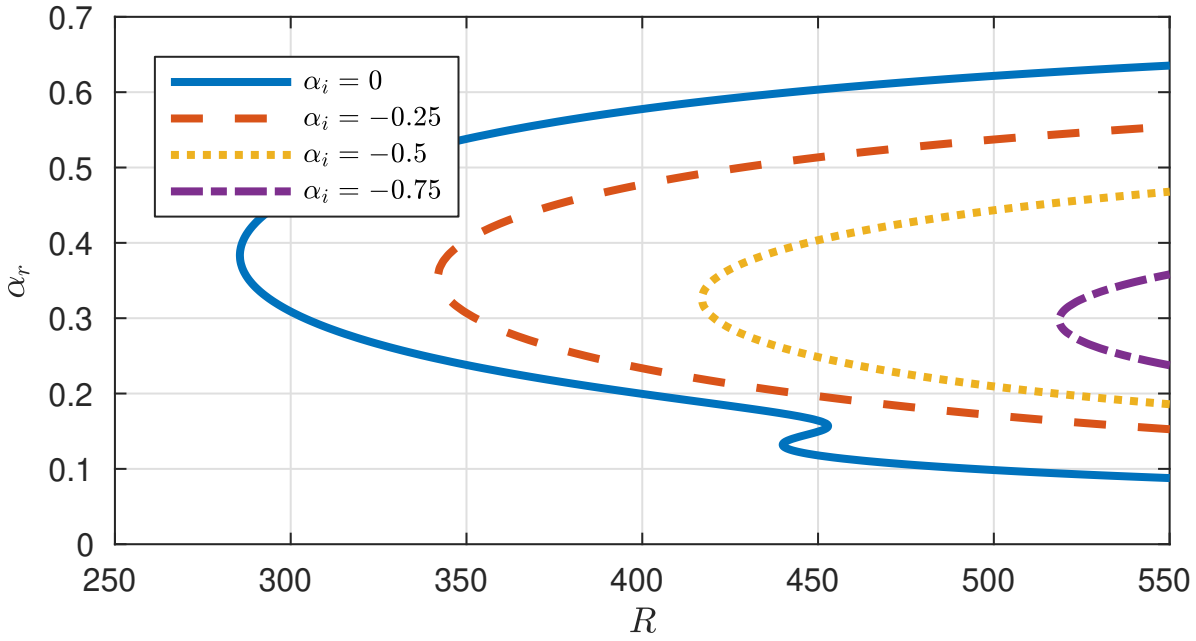

Figure 2.12: Radial growth rate contours for stationary disturbances, with the neutral curve $\alpha_i = 0$ (—) and $\alpha_i = -0.25$ (- - -), $\alpha_i = -0.5$ ($\cdots$), $\alpha_i = -0.75$ ($\circ$–).

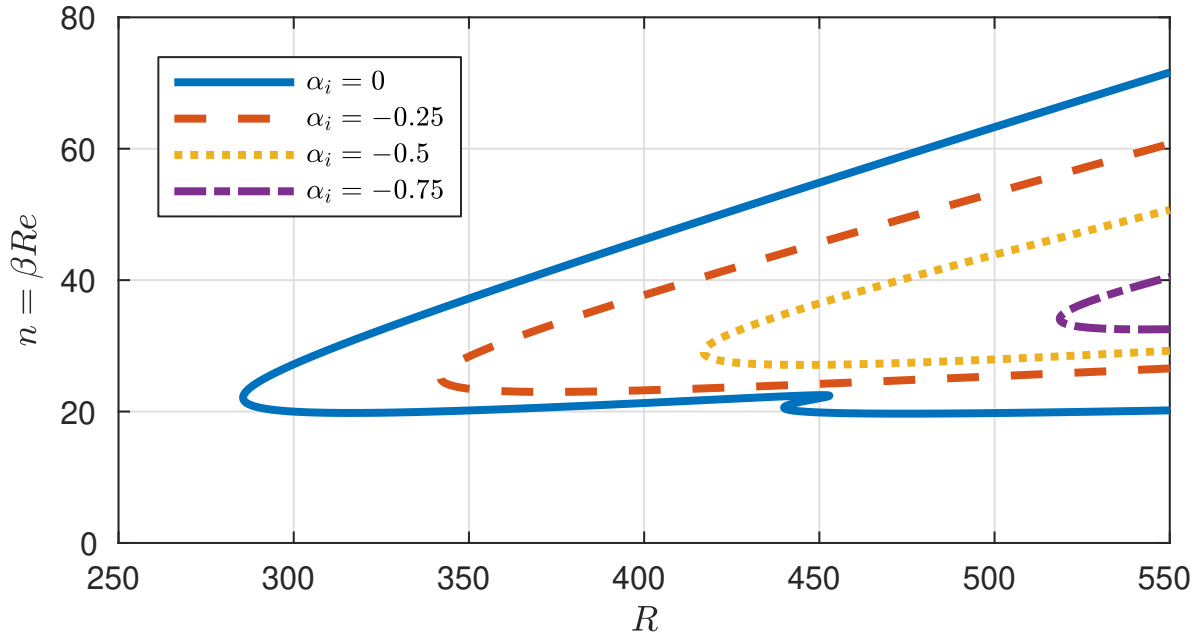

Figure 2.13: Azimuthal wavenumber contours for stationary disturbances, with the neutral curve $\alpha_i = 0$ (—) and $\alpha_i = -0.25$ (- - -), $\alpha_i = -0.5$ ($\cdots$), $\alpha_i = -0.75$ ($\circ$–).

To aid with validation of the new formulation, data from Appelquist [3] was made available to the author and a small discrepancy between the two neutral curves was noticed in the particularly sensitive area around the onset parameters for the type II instability, as seen in figure 2.14.

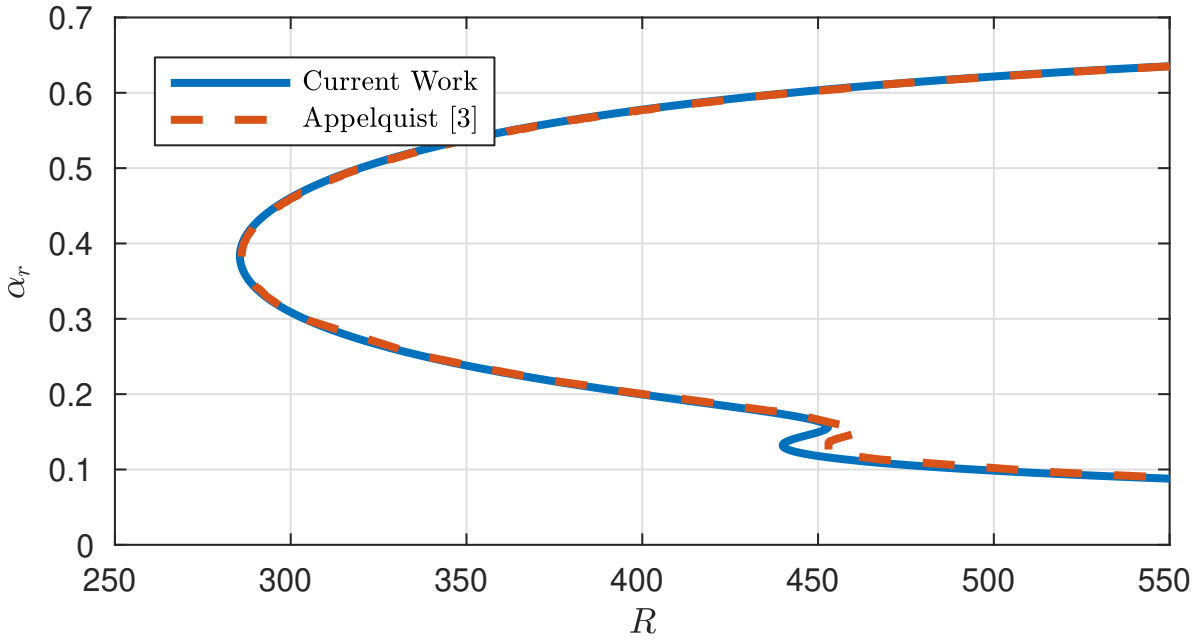

Figure 2.14: Comparison between radial neutral curves for stationary disturbances from Appelquist [3] (- - -) and current work (—).

Initially, it was believed that this discrepancy was due to the difference in formulations and the inclusion of the extra non-parallel terms but in fact it can be accounted for by examining the difference in the spatial growth rates, α_i, from the data sets of Appelquist [3] and the current work. Figure 2.15 shows these frequencies. Clearly, the frequencies from Appelquist [3] are much larger in magnitude than those calculated here and by definition, on the neutral curve we should have $\alpha_i = 0$. The tolerance for convergence of α_i is set during the numerical arclength continuation procedure to be 10^{-8} but increasing this tolerance to around 10^{-3} shows that we can recover Appelquist's [3] curve almost exactly, as in figure 2.16.

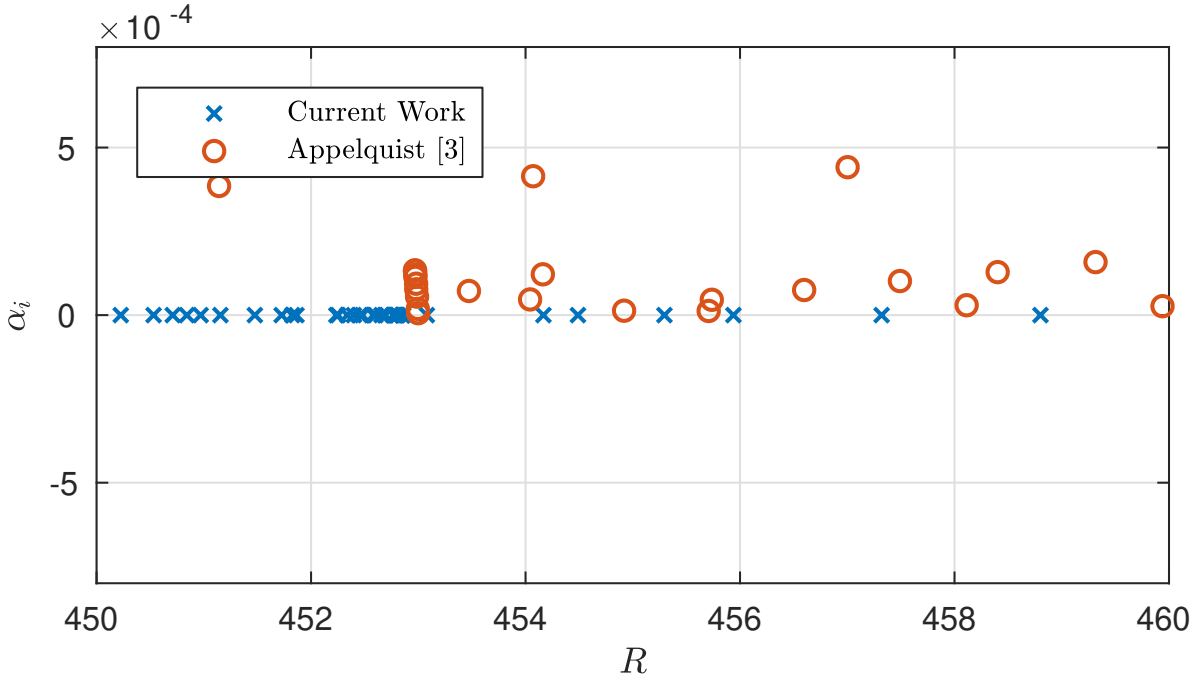

Figure 2.15: Spatial growth rates near the onset of the type II instability. Comparison between Appelquist [3] (○) and current work (×).

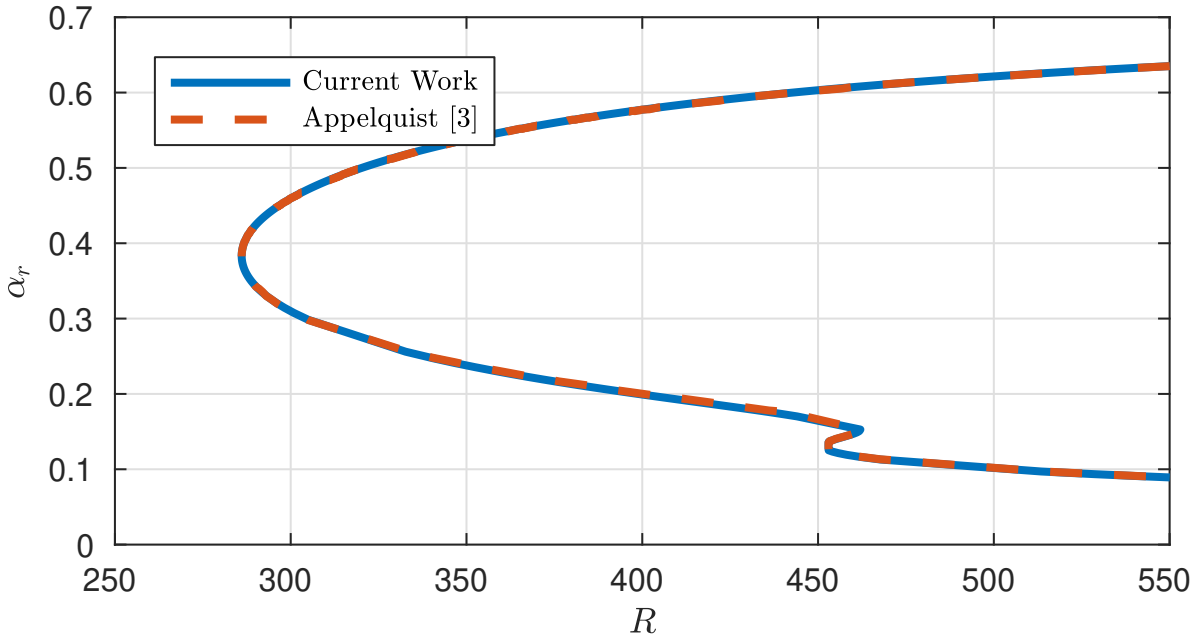

Figure 2.16: Comparison between radial neutral curves for stationary disturbances from Appelquist [3] (- - -) and current work (—) when tolerance is increased to investigate sensitive area around type II onset.

2.2.3 Absolute Instability in the Steady Rotating Disk Boundary Layer

This section will very briefly illustrate the apparent existence of a local absolute instability in the rotating disk boundary layer. In order to distinguish between convectively and absolutely unstable disturbances, we must study the time evolution of an impulsive excitation of the disk surface. An impulse centred at r_e and $t = 0$ for a particular azimuthal wavenumber β can take the form of a boundary condition on the wall-normal component w such that

$$w(0; r, \theta, t) = \delta(r - r_e)\delta(t)e^{i\beta R\theta} \tag{2.55}$$

where δ denotes the Dirac delta function. For this particular azimuthal wavenumber β, the response to the impulsive forcing (2.55) is given in terms of a Green's function such that

$$\mathcal{D}(i\frac{\partial}{\partial t}, -i\frac{\partial}{\partial r}; \beta, Re)G(r, t) = \delta(r - r_e)\delta(t) \tag{2.56}$$

where $\mathcal{D}$ is the dispersion relation (2.35). In a frame of reference fixed by the perturbation, we can quantify this response into the following conditions for absolute and convective instability:

- $G(t \to \infty, r) = 0 \implies$ convective instability
- $G(t \to \infty, r) = \infty \implies$ absolute instability

Without entering into the extensive analytic detail which can be found in Lingwood [47] & Lingwood [43], we will briefly explain the method for finding absolute instability and detail the critical parameters for its onset.

Absolute instabilities can be identified numerically by following the paths of two solution branches in the α-plane. A so-called *pinch point* occurs when waves propagating in opposite directions coalesce, producing a *branch-point singularity* in the ω-plane. Certain criteria must be satisfied in order for branch-point singularities in the dispersion relation to correspond to an absolute instability, and these conditions are encapsulated in the Briggs [15] criterion. If the two solution branches originate in distinct halves of the α-plane when ω_i is large and positive and if coalescence occurs before $\omega_i = 0$ then an absolute instability is present. For example, if this pinch point occurs at some temporal

wavenumber ω_0 then at the pinch point we must have

$$\frac{\partial \omega_0}{\partial \alpha} = 0 \tag{2.57}$$

and by Briggs' criterion, the flow is absolutely unstable if $\mathfrak{I}(\omega_0) > 0$.

Figure 2.17 shows these pinch points for some values of ω_i chosen for comparison with Lingwood [47]. The lower branch can be identified as what is known as the type III mode, discovered by Mack [49] and mentioned in section 2.1.4. Before Lingwood's [43] discovery of this absolute instability, little attention had been paid to this mode, since it has relatively large positive values of α_i and so is heavily damped. However, the coalescence between this and the type I mode is crucial for the onset of absolute instability. Lingwood [47] states that above a critical Reynolds number of $R = 507.3$,[1] and azimuthal wavenumber $\beta \approx 0.126$ (or $n = 68$), these pinch points have $\mathfrak{I}(\omega_0) > 0$ as required by the absolute instability criterion. A finite range of β values were found by Lingwood [43] to define the absolutely unstable region, but in figure 2.17, the value of $\beta = 0.126$ has been chosen simply to demonstrate the existence of absolute instability. These plots can be compared with similar ones in Cooper and Carpenter [19] and also in Lingwood [47]. While this analysis appears to predict an absolute instability in the flow configuration, it is important to note the global subtleties in the radial homogenisation procedure, which are first noted by Davies and Carpenter [27]. A brief overview of the global stability properties of the flow is given in chapter 4 and detailed discussions of the global behaviour are given in many references such as Davies and Carpenter [27], Davies et al. [28], Thomas and Davies [72], Healey [40], Thomas and Davies [74], Appelquist et al. [4, 6]. The true behaviour of this absolute instability is as yet unresolved and is still the focus of a great deal of ongoing work by the aforementioned authors, as can be seen in Thomas and Davies [75].

We will refer back to this absolute instability at several points throughout the forthcoming report and as mentioned, it will be particularly important when discussing global stability in chapter 4. However, for the time being the reader should simply be aware of its existence and the implications for the local analysis.

[1] Stated as $R = 510.625$ in Lingwood [47] but subsequently corrected.

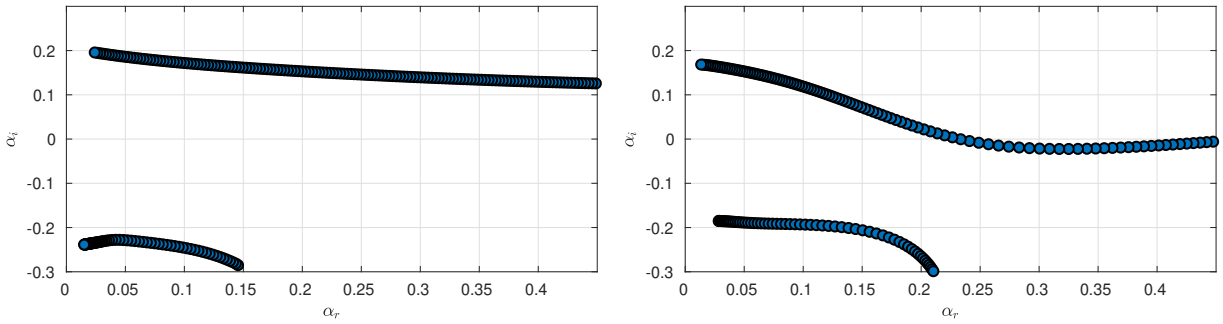

(a) $\omega_i = 0.01$

(b) $\omega_i = 0.004$

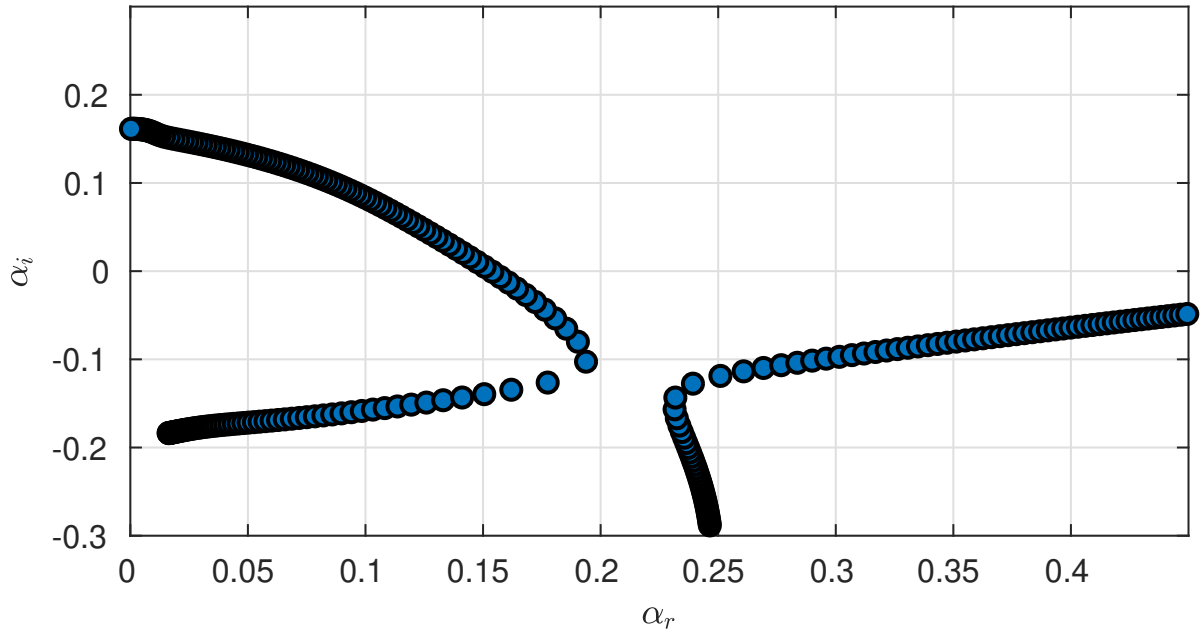

(c) $\omega_i = 0.000289$

Figure 2.17: Coalescence of type I and type III spatial branches for azimuthal mode number $\beta = 0.126$ and Reynolds number $R = 530$. A pinch point can be seen to occur for $\omega_i \approx 0.000289 > 0$. Note that the two solution branches originate from the upper and lower parts of the complex α plane, as is required for a pinch point to be associated with absolute instability by Briggs' criterion.

2.2.4 Numerical Methods for Linear Stability - Monochromatic Direct Numerical Simulations

As discussed in the introduction to section 2.2, there are three approaches which we will take to analyse the stability of the boundary layer. This section describes the second of these three, namely the alteration induced by retaining the time dependence in the stability equations and only decomposing the perturbation variables as

$$\mathbf{u} = \hat{\mathbf{u}}(z,t)e^{i(\alpha r+\beta R\theta)}, \quad \xi = \hat{\xi}(z,t)e^{i(\alpha r+\beta R\theta)} \tag{2.58}$$

Substituting into (2.36) and applying the parallel flow approximation replacing r by R leaves the set of time-dependent ODEs

$$\frac{\partial \xi_r}{\partial t} + i\beta N_z - \frac{\partial N_\theta}{\partial z} - \frac{2}{R}(\xi_\theta + i\alpha w) = \frac{1}{R}\left[\left(\hat{\nabla}^2 - \frac{1}{r^2}\right)\xi_r - \frac{2i\beta}{R}\xi_\theta\right] \tag{2.59a}$$

$$\frac{\partial \xi_\theta}{\partial t} + \frac{\partial N_r}{\partial z} - \frac{\partial N_z}{\partial r} + \frac{2}{R}(\xi_r - i\beta w) = \frac{1}{R}\left[\left(\hat{\nabla}^2 - \frac{1}{r^2}\right)\xi_\theta + \frac{2i\beta}{R}\xi_r\right] \tag{2.59b}$$

$$\hat{\nabla}^2 w = \frac{1}{r}\left(\frac{\partial \xi_r}{\partial \theta} - \frac{\partial (r\xi_\theta)}{\partial r}\right) \tag{2.59c}$$

where

$$\hat{\nabla}^2 = -\alpha^2 + \frac{i\alpha}{R} - \beta^2 + \frac{\partial^2}{\partial z^2} \tag{2.60}$$

The convective terms $\mathbf{N}$, and the boundary and integral conditions may still be described by (2.51) and (2.45) respectively while the secondary variables (2.37) become

$$u_r = -\int_z^\infty (\xi_\theta + i\alpha w)\, dz \tag{2.61a}$$

$$u_\theta = \int_z^\infty (\xi_r - i\beta w)\, dz \tag{2.61b}$$

$$\xi_z = \int_z^\infty \left(\frac{\xi_r}{R} + i\alpha\xi_r + i\beta\xi_\theta\right) dz \tag{2.61c}$$

The flow is disturbed for a given azimuthal mode number $n = \beta R$ by a temporally localised impulsive forcing of the form

$$\eta(\theta,t) = b(t)e^{i\beta R\theta} \tag{2.62}$$

where b defines the time-dependent amplitude, given by

$$b(t) = (1 - e^{-\sigma t^2})e^{-\sigma t^2} \tag{2.63}$$

The first term of b acts as a continuous Heaviside function to scale the forcing up from zero and σ is a parameter which dictates the timescale over which this takes place. Figure

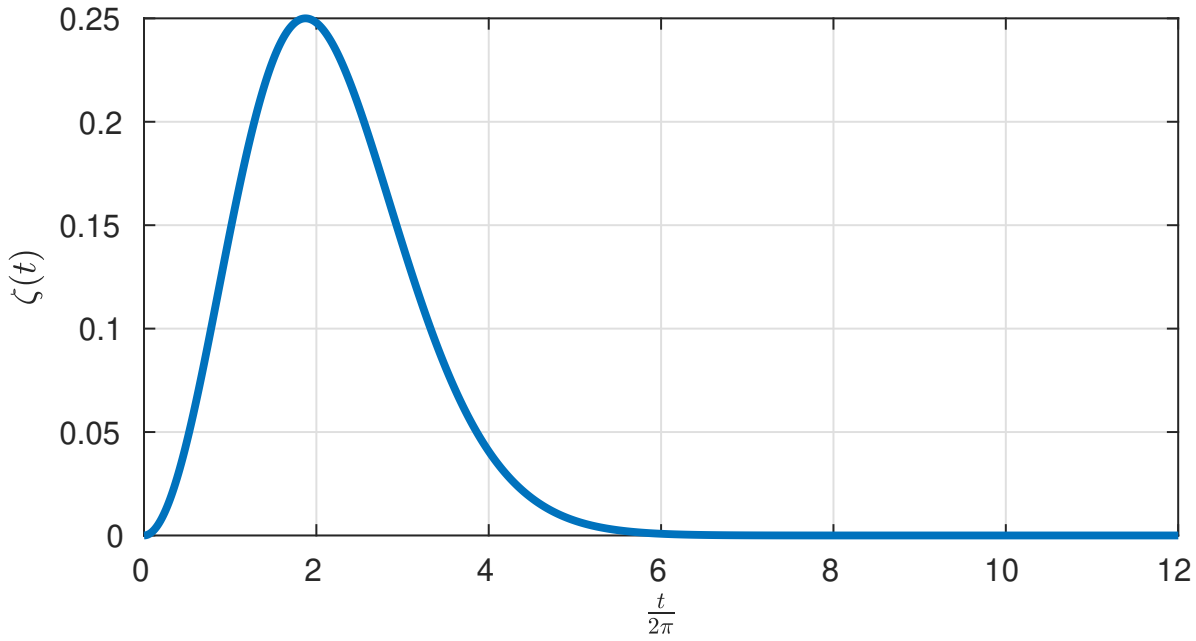

Figure 2.18: Typical temporal development of impulsive excitation.

2.18 shows the temporal evolution of this impulse at the forcing location for some σ. The solution method employed is similar to that described in section 2.1.1 for the solution of the time-dependent base flow fields and involves a spectral scheme in the wall-normal direction with a predictor-corrector scheme for the temporal integration. The spectral expansions in the wall-normal direction are given in terms of Chebyshev polynomials as described in full in section 2.2 and are identical to the ones used for the linear normal mode stability analysis described there. We state them here for completeness however, as there is a subtle difference involving the azimuthal mode number worth mentioning. As explained in the previous section, the *primary* perturbation variables $\{\xi_r, \xi_\theta, w\}$ are expanded in terms of odd Chebyshev polynomials and mapping the physical coordinate $z \in [0, \infty)$ to the computational coordinate $\eta \in (0, 1]$ by the usual mapping (1.40) leads to an expansion of the form

$$f(r, \theta, \eta, t) = \left(\sum_{k=1}^{N} f_k(r, t) T_{2k-1}(\eta) \right) e^{in\theta} \tag{2.64}$$

which has been restricted to an individual azimuthal wavenumber $n = \beta R$.

There are many similarities between the time-dependent simulation and the eigenvalue problem presented in section 2.2, and much of what has already been discussed will be relevant here. The important difference is the inclusion of temporal integration, which is

achieved by the backward three-level scheme of section 2.1.1, namely

$$\left(\frac{\partial f}{\partial t}\right)^l = \frac{1}{2\Delta t}\left(3f^l - 4f^{l-1} + f^{l-2}\right) \tag{2.65}$$

where we have used the notation

$$f^l = f\Big|_{t=l\Delta t}$$

Similarly to section 2.1.1, the convective terms contained in $\mathbf{N}$, as well as the Coriolis terms are treated explicitly via a predictor-corrector method in the temporal integration, while the remaining viscous terms including the second z-derivative term are treated implicitly. The predictor step for the convective terms is given by

$$\begin{aligned}(\mathbf{N}^l)_p &= 2\mathbf{N}^{l-1} - \mathbf{N}^{l-2} \\ &= 2(\boldsymbol{\Xi}^B \times \mathbf{u}^{l-1} + \boldsymbol{\xi}^{l-1} \times \mathbf{U}^B) - (\boldsymbol{\Xi}^B \times \mathbf{u}^{l-2} + \boldsymbol{\xi}^{l-2} \times \mathbf{U}^B)\end{aligned}$$

while the corrector step is defined by

$$(\mathbf{N}^l)_c = (\mathbf{N}^l)_p = \boldsymbol{\Xi}^B \times (\mathbf{u}^l)_p + (\boldsymbol{\xi}^l)_p \times \mathbf{U}^B$$

where $(\mathbf{u}^l)_p$ and $(\boldsymbol{\xi}^l)_p$ are the disturbance velocity and vorticity fields determined from the predictor stage. The products involving the base flow quantities $\mathbf{U}^B$ and $\boldsymbol{\Xi}^B$ are treated with a pseudo-spectral scheme which uses a Fast Fourier Transform to convert between Chebyshev coefficients and collocation values for the multiplications.

Validation Against Eigenvalue Solution Procedure

Figure 2.19 shows the temporal development of $\xi_\theta(z = 0)$, excited by an impulsive forcing of the form (2.62) for $R = 500$, $n = 32$ and $\alpha = 0.3$. These parameters were chosen as an example, so that the system would be unstable by the eigenvalue analysis of section 2.2.1.

In order to get viable data against which we may compare our eigenvalue solutions, we must decompose a perturbation variable f as

$$f = \hat{f}(z)e^{i(\alpha r + \beta R\theta - \omega t)} \tag{2.66}$$

so that the dominant temporal growth rate and frequency ω can be computed from the simulation data by means of the formula

$$\omega = \frac{i}{A}\frac{\partial A}{\partial t} \tag{2.67}$$

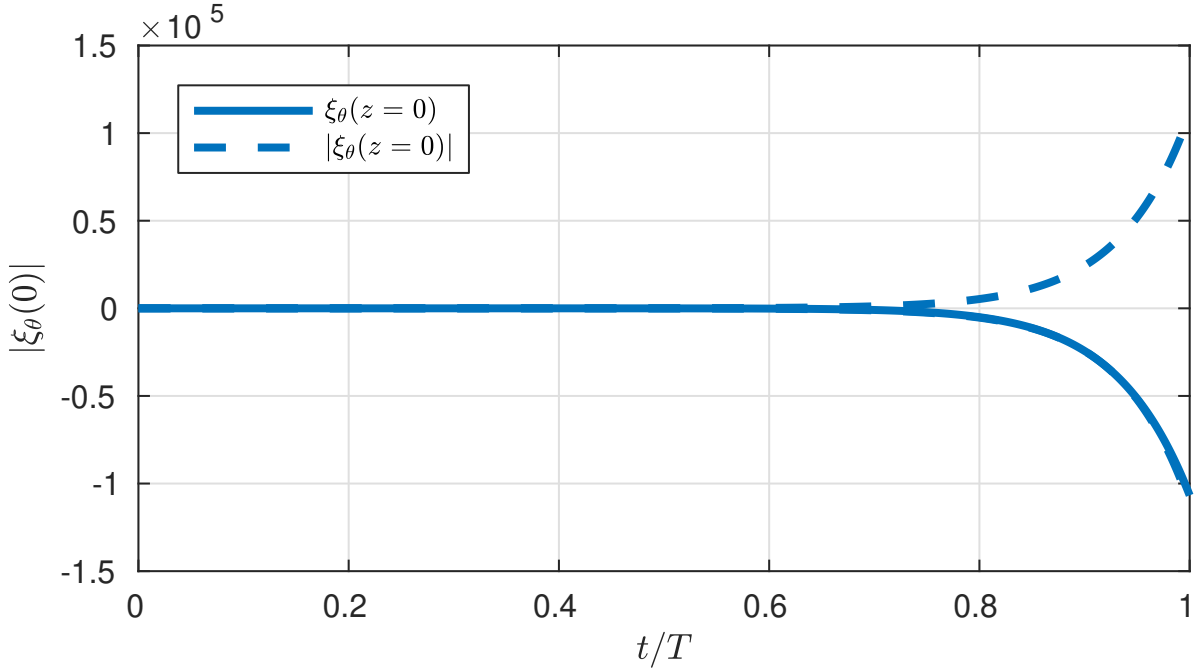

Figure 2.19: Temporal response (—) to impulsive disturbance of $\xi_\theta(z=0)$ for $R=500$, $n=32$ and $\alpha=0.3$ including wavepacket envelopes (- - -). T denotes the disk rotation period.

where A is the amplitude of some flow variable. The disturbance variable which was selected for the results presented below was the azimuthal vorticity component evaluated at the disk surface but other specifications for the disturbance amplitude could likewise be used. Provided that ω is found not to vary too rapidly in time, it can be interpreted as the complex frequency displayed by the disturbance at a particular instant of time. Figure 2.20 shows the convergence of the temporal growth rate calculated by (2.67) to the genuine eigenvalue calculated by the dispersion relation (2.54).

Figure 2.21 shows comparisons between the complex frequencies ω calculated from the eigenvalue dispersion relation (2.54) and the simulation data for varying R. The simulation was conducted until a steady growth rate was achieved and all transient behaviour had passed out of the domain of interest. Throughout the following discussions, we will refer to this time after which the growth rates are constant as T_∞, which is identified by

$$\omega(T_\infty) \approx \lim_{t\to\infty}\left(\frac{i}{A}\frac{\partial A}{\partial t}\right) \tag{2.68}$$

Typically, T_∞ is chosen to be between two and four periods of disk rotation.

Before proceeding with our discussion of the analysis, it is important at this stage to note a distinct difference between this *impulse response* and that presented in chapter

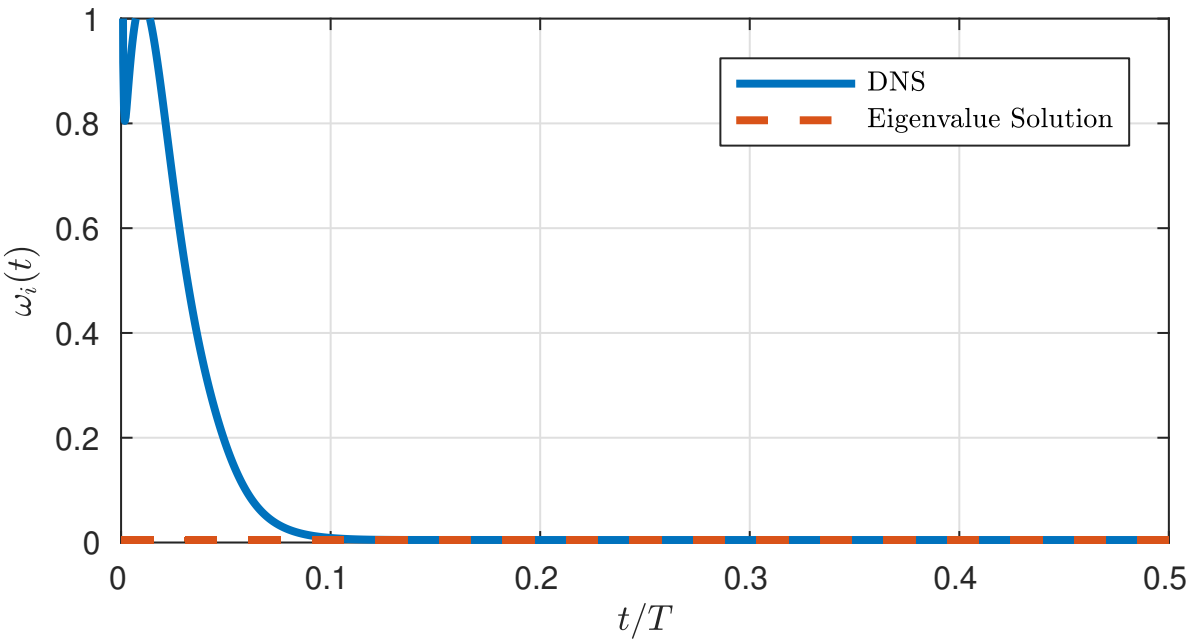

Figure 2.20: Convergence of growth rates from monochromatic DNS calculated by (2.67) (—) to genuine eigenvalue calculated by the dispersion relation (2.54) (- - -) as $t \to T_\infty$ for $R = 500$, $n = 32$ and $\alpha = 0.3$. T denotes the disk rotation period.

4 and the works on the global stability of this configuration associated to Davies and Carpenter [27], Lingwood [43] and [6]. Here, we are, in effect, setting up an initial condition $f(z, t_0)e^{i\alpha r}e^{in\theta}$ and following the development in the space of normal modes with a prescribed radial dependence. Therefore, this impulse is localised in time but not in space with regard to the radius; an important distinction to that of chapter 4.

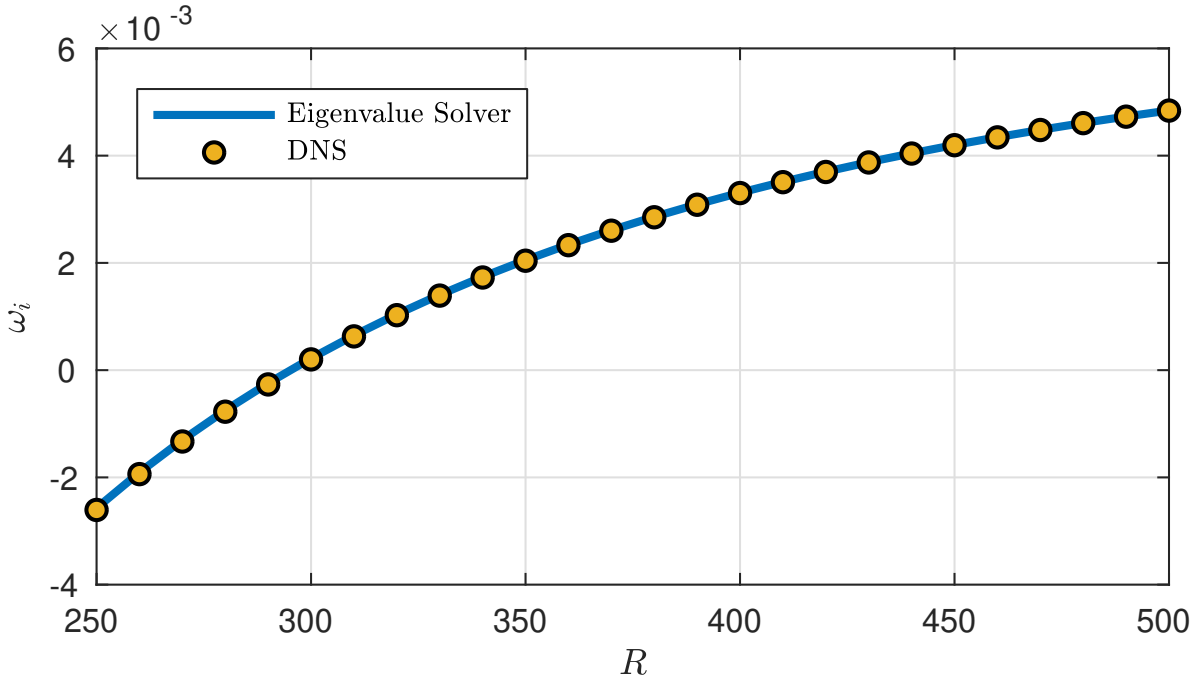

Figure 2.21: Comparison between eigenvalues calculated by the dispersion relation (·) (2.54) and growth rates from monochromatic DNS (—) calculated by (2.67) for $n = 32$ and $\alpha = 0.3$. The simulations were conducted until the growth rates have settled to the dominant value where $t \geq T_\infty$.

2.2.5 Numerical Methods for Linear Stability - Direct Numerical Simulations with Radial Dependence

Finally, we discuss the third method mentioned in section 2.2, which retains the radial dependence in the DNS. This numerical method is described in detail in Davies and Carpenter [26] although in reality the schemes have since evolved to attempt to alleviate numerical instabilities.

The main alteration here over section 2.2.4 is the lack of a normal-mode approximation in the radial direction, leading to the need to calculate r-derivatives of the perturbation variables. The finite difference discretisations for the first and second radial derivatives are standard and described at length in Fasel et al. [33]. All that it is pertinent to mention here is that the schemes used here have been chosen to be non-compact and centred. The more precise details of the schemes are relegated to appendix B.3.2 and the reader is referred there or to Fasel et al. [33] for more details. The inner and outer radial boundaries are both placed well away from the area of interest and a discussion of inflow and outflow conditions is given in B.3.1. Wavelike or null outflow conditions may be used, as described in Davies et al. [28] although in practise, we usually ensure that the simulations are terminated before any significant disturbance reaches the location of the radially outward computational boundary.

Validation Against Eigenvalue Solution Procedure

Following Davies and Carpenter [26], in order to have simulation data comparable to the local eigenvalue results, we excite a periodic disturbance on the disk surface by introducing a forcing of the form

$$\eta(r,\theta,t) = a(r-r_e)b(t)e^{in\theta} \tag{2.69}$$

to give a localised Gaussian pulse centred at position r_e, where λ specifies the radial extent of the forcing.

The time-dependent amplitude (2.63) may be adapted so as to give a time-periodic excitation, for instance by setting

$$b(\tau) = h(\tau)e^{-i\omega_0 t} \tag{2.70}$$

where ω_0 is a prescribed temporal frequency and $h(\tau) = (1-e^{-\sigma\tau})$ is the continuous Heaviside function used to scale the forcing up from zero. Disturbances which are stationary

with respect to the surface may be considered by setting ω_0 equal to zero.

Locally defined spatial wavenumbers α may be computed from the simulation data by means of the formula

$$\alpha = -\frac{i}{A}\frac{\partial A}{\partial r} \tag{2.71}$$

where A is the amplitude of some flow variable. Similarly to section 2.2.4, the disturbance variable which was selected for the results presented below was the azimuthal vorticity component evaluated at the disk surface but other specifications for the disturbance amplitude could likewise be used. Provided that α is found not to vary too rapidly in space, it can be interpreted as the complex wavenumber displayed by the disturbance at a particular radial position and instant of time.

Figure 2.22 shows the radial evolution of a disturbance generated by stationary forcing for $R = 500$ and $n = 32$. These parameter choices ensure that the configuration is unstable according to the eigenvalue analysis. For this figure, the position of maximum forcing is located at $r_e = 500$, although this is somewhat arbitrary since we have applied the parallel flow approximation, replacing r by R in the equations and hence treating all radial locations as equivalent. As already alluded to, this homogenisation of the radial direction is, strictly speaking, unphysical and further discussion of this is given in chapter 4. Similarly to section 2.2.4, the simulations were conducted until a steady growth rate was achieved and all transient behaviour had passed out of the domain of interest so that T_∞ can be identified with

$$\alpha(T_\infty) \approx \lim_{t\to\infty}\left(-\frac{i}{A}\frac{\partial A}{\partial r}\right) \tag{2.72}$$

Typically, T_∞ is chosen to be between two and four periods of disk rotation. Davies and Carpenter [26] state that the variation of the primary variables may be fully resolved using a Chebyshev expansion involving $N = 48$ polynomials and a radial resolution of about $\Delta r \approx 1$. Each of the following simulation plots was produced using $N = 48$, a radial resolution of $\Delta r = 1.25$ and a time discretisation of $\Delta t = 0.625$. In all of the simulations, the computational domain extends well beyond the limits suggested by the figures in order to ensure no computational edge effects creep into affect the results.

Figure 2.23 shows radial growth rates for azimuthal mode number $n = 32$ and maximum wall displacement located at $r = 350$ for a stationary disturbance, with the true radial inhomogeneity incorporated. Away from radial locations near the greatest wall deformation, the results from the DNS and the eigenvalue dispersion relation (2.53) agree

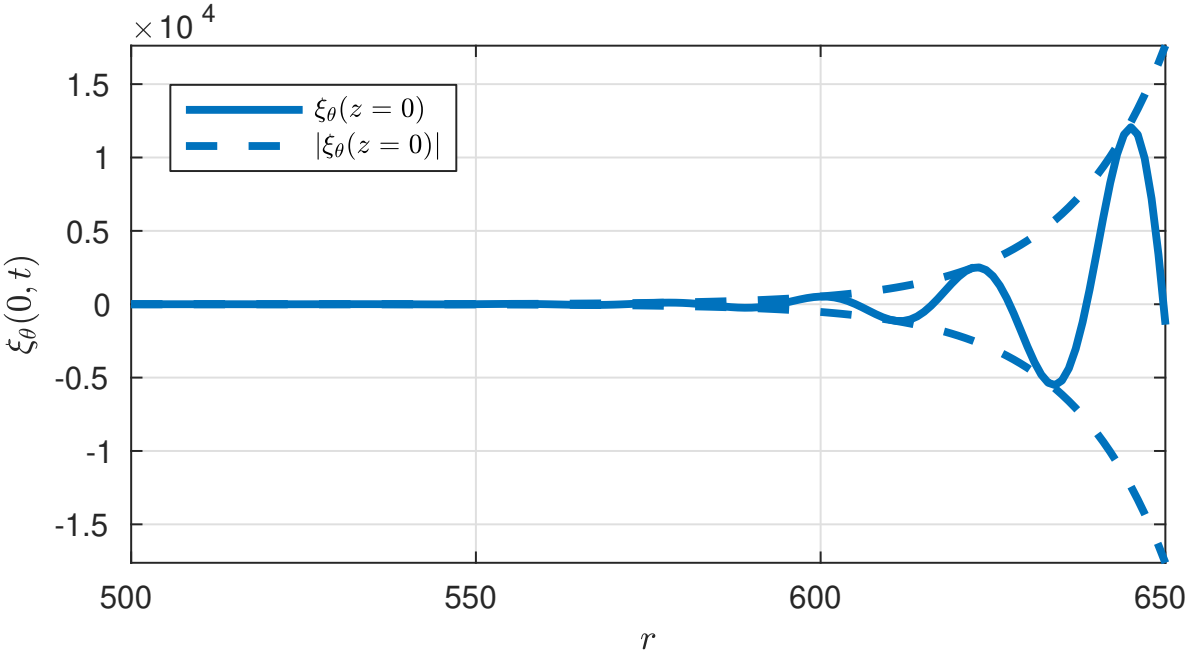

Figure 2.22: Radial evolution of $\xi_\theta(z=0,\tau>T_\infty)$ for $R=500$ and $n=32$ (—) along with wavetrain envelope (- - -).

well with each other, providing confidence in the newly developed solution procedure for the eigenvalue analysis. The oscillations in the curve near the maximum forcing at $r=350$ are due to near-field effects and the fact that in these locations the disturbances do not have a well-defined radial wavenumber that can be computed using equation (2.71) for $t>T_\infty$.

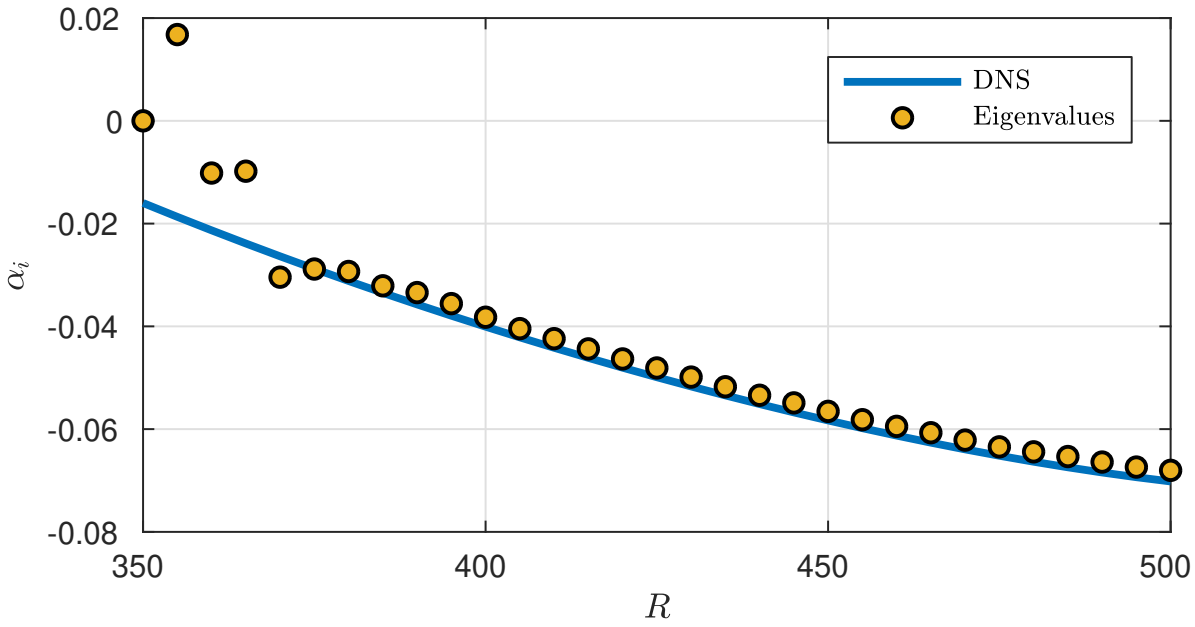

Figure 2.23: Plots of α_r and α_i for a stationary disturbance with azimuthal wavenumber $n = 32$, showing comparisons between DNS ($\cdot$) and local results (—).

Chapter 3

Local Stability of the Periodically Modulated Rotating Disk Boundary Layer using a Velocity-Vorticity Formulation

This forthcoming exposition details the extension of the methods of chapter 2 to the flow configuration that has been the main focus of the work conducted throughout this thesis. We will, as an introduction to the chapter and in the interest of clarity, briefly review the notation and key concepts introduced previously.

Consider a disk of infinite extent rotating with a periodically modulated angular velocity beneath an otherwise stationary fluid. The resulting flow has radial, azimuthal and vertical components and admits the exact similarity solution to the Navier-Stokes equations, as explained in section 2.1.1. The motion of the disk surface is described by the rotation rate

$$\Omega^*(t^*) = \Omega_0^* + \epsilon\phi^* \cos(\phi^* t^*) \tag{3.1}$$

where Ω_0^* may be thought of as analogous to the constant rotation rate in the steady case, while ϵ and ϕ^* denote the angular displacement and angular velocity of the modulation respectively. We use spatial and temporal scalings

$$\delta_k^* = \sqrt{\frac{\nu^*}{\Omega_0^*}}, \qquad \tau = \frac{r_L^*}{\delta_k^*}\Omega_0^* t^* \tag{3.2}$$

and a local velocity scaling is obtained by using the circumferential disk velocity $r_L^*\Omega_0^*$

at some dimensional reference radius r_L^*. This local scaling gives a Reynolds number R, associated with the steady rotation of the disk as

$$R = \frac{r_L^* \Omega_0^* \delta_k^*}{\nu^*} = \frac{r_L^*}{\delta_k^*} = r_L \tag{3.3}$$

where we identify r_L as a local, non-dimensional radial position. As in section 2.1.1, we also define a Reynolds number, R_s associated with the Stokes layer, given by

$$R_s = \frac{r_L^* \epsilon \phi_0^* \delta_s^*}{\nu^*} = r_L \epsilon \sqrt{\frac{\phi^*}{\Omega_0^*}} = \epsilon \sqrt{\varphi} R \tag{3.4}$$

where we have defined $\varphi = \sqrt{\frac{\phi^*}{\Omega_0^*}}$. The resulting three-dimensional base flow may be expressed as the solution to the system

$$\frac{\partial F}{\partial \tau} = \frac{1}{R}\left(F^2 - G^2 + H\frac{\partial F}{\partial z} - \frac{\partial^2 F}{\partial z^2}\right) \tag{3.5a}$$

$$\frac{\partial G}{\partial \tau} = \frac{1}{R}\left(2FG + H\frac{\partial G}{\partial z} - \frac{\partial^2 G}{\partial z^2}\right) \tag{3.5b}$$

$$\frac{\partial H}{\partial z} = -2F \tag{3.5c}$$

with boundary conditions

$$F(0,\tau) = H(0,\tau) = 0, \quad G(0,\tau) = 1 + U_w \cos\left(\frac{\varphi}{R}\tau\right) \tag{3.6a}$$

$$F \to 0, \quad G \to 0 \quad \text{as} \quad z \to \infty \tag{3.6b}$$

where $U_w := \frac{R_s\sqrt{\varphi}}{R}$. With a laminar flow control motivation in mind, we constrain the variation in the wall velocity to be relatively small with respect to the rotation rate, and so we impose the condition $U_w < 0.2$ for the remainder of this work. In turn, for sufficiently high φ and R in the region of interest, this condition keeps the Reynolds number associated with the Stokes layer, Rs, to be small compared with the Reynolds number associated with instability onset in the semi-infinite Stokes layer of Blennerhassett and Bassom [11].

The motivation for the addition of a periodically modulated rotation rate is discussed in section 1.1.1 and originates with Thomas et al. [76], who show that inducing a small amount of oscillation into an otherwise steady flow can have stabilising effects. The introduction of this modulation creates a time-modulated unidirectional flow, and Thomas et al. [76] detail their stabilising effects using a Stokes layer added to plane Poiseuille and Hagen-Poiseuille flows. They complement the work of Kelly and Cheers [42] and

Von Kerczek [81] who studied modulation of plane Couette flow and also found stabilisation. Thomas et al. [76] found that the steady flow was stabilised for certain frequencies of the oscillation but destabilised for others. Wise and Ricco [82] also show that turbulent drag reduction may be achieved using oscillation of flat plates and rotating disks. The work presented in this report will be of a more mathematically fundamental nature than that described in Wise and Ricco [82], and will attempt to explain the underlying concepts of the stabilisation achieved by this modulation.

The investigation into the local stability properties of the modulated system can be executed in several ways, and we will describe the different possible methods and attempt to unify the results to give a detailed understanding of the effects of this modulation on stability. The following procedure encompasses three distinct investigatory approaches. Linearised direct numerical simulations using the vorticity-based methods of previous sections are complemented by a local in time linear stability analysis, which is made possible by imposing an artificial frozen base-flow approximation. This localised analysis is deployed together with a more exact global treatment based upon Floquet theory, which avoids the need for any simplification of the temporal dependency of the base-flow. Before moving on to the time-dependent simulations, we begin the discussion with Floquet theory, and with laminar flow control techniques and suppression of crossflow vortices on swept wings foremost in mind, we will focus on disturbances which are stationary with respect to the disk surface.

3.1 Eigenvalue Analysis via Floquet Theory

Similarly to the Stokes layer scenario discussed in section 1.4.4, an understanding of the disturbance structures may be gleaned by a consideration of Floquet theory. We will use the same temporal and spatial scalings as in section 2.1.1, which, with the boundary layer thickness $\delta_k^* = \sqrt{\frac{\nu^*}{\Omega_0^*}}$, gives rise to the spatial and temporal scalings

$$z = \frac{z^*}{\delta_k^*} \quad \tau = \frac{r_L^*}{\delta_k^*}\Omega_0^* t^*$$

To consider the development of small disturbances to the unsteady base flow $\mathbf{U}^B$, we perturb as for the Stokes layer in section 1.4.4 and write

$$\mathbf{u}(\mathbf{x},\tau) = \mathbf{U}^B(z,\tau) + \epsilon\mathbf{u}'(\mathbf{x},\tau), \quad \xi(\mathbf{x},\tau) = \Lambda(z,\tau) + \epsilon\xi'(\mathbf{x},\tau)$$

Following the method developed by Hall [39], while making use of the theorems and ideas discussed in section 1.4.4, we take the Floquet mode solution

$$f(r,\theta,z,\tau) = \hat{f}(z,\tau)e^{\mu\tau}e^{i(\alpha r+\beta R\theta)} + c.c. \tag{3.7}$$

where $\hat{f}(z,\tau)$ is a time-periodic function with the same period as that of the modulation and all exponential growth of $\hat{f}(z,\tau)$ incorporated into the Floquet exponent $e^{\mu\tau}$. In this case, since the period of modulation, given by the boundary condition on the azimuthal velocity component, is $T = \frac{\varphi}{2\pi R}$, we have that $\hat{f}(z,\tau)$ is periodic with period T. The *c.c.* denotes the complex conjugate, which is added to ensure that the disturbance is real. As for the Stokes case, the quantities of interest here will be μ, as its real part specifies the temporal growth of the disturbance, and α, whose imaginary part gives the spatial growth rate.

Substituting into the perturbation equations (2.36), linearising as usual as neglecting the non-parallel $\mathcal{O}\left(\frac{1}{R^2}\right)$ terms as for the steady case gives

$$\frac{\partial\xi_r}{\partial\tau} + \mu\xi_r + i\beta N_z - \frac{\partial N_\theta}{\partial z} - \frac{2}{R}(\xi_\theta + i\alpha w) = \frac{1}{R}\left(-\alpha^2 - \beta^2 + \frac{\partial^2}{\partial z^2}\right)\xi_r \tag{3.8a}$$

$$\frac{\partial\xi_\theta}{\partial\tau} + \mu\xi_\theta + \frac{\partial N_r}{\partial z} - \frac{\partial N_z}{\partial r} + \frac{2}{R}(\xi_r - i\beta w) = \frac{1}{R}\left(-\alpha^2 - \beta^2 + \frac{\partial^2}{\partial z^2}\right)\xi_\theta \tag{3.8b}$$

$$\left(\hat{\nabla}^2 + \frac{\partial^2}{\partial z^2}\right)w = i\beta\xi_r - i\alpha\xi_\theta - \frac{\xi_\theta}{R} \tag{3.8c}$$

which is similar to equations (2.44) aside for the replacement of the terms multiplied by $-i\omega$ with the Floquet temporal derivative structure $\frac{\partial}{\partial\tau} + \mu$.

As discussed for the Stokes layer in section 1.4.4, the method of Hall [39] involves the decomposition of the perturbation variables into harmonics such that

$$\hat{f}(z,\tau) = \sum_{m=-\infty}^{\infty} f_m(z)e^{im\tilde{\tau}} \tag{3.9}$$

where $\tilde{\tau} = \frac{\varphi}{R}\tau$ and the factor $\frac{\varphi}{R}$ is introduced to ensure the harmonics have the same period as $\hat{f}(z,\tau)$. A representation for the time dependent part of the base flow is also required in a similar form, and this is given by

$$\mathbf{U}^B = \mathbf{U}^S(z) + \mathbf{U}^M(z,\tilde{\tau}) \tag{3.10a}$$

$$= \mathbf{U}^S(z) + \sum_{k=-\infty}^{\infty} \mathbf{u}_k(z)e^{ik\tilde{\tau}} \tag{3.10b}$$

where $\mathbf{U}^S(z)$ is the steady state base flow solution. In practise, we can calculate the Fourier coefficients $\mathbf{u}_k(z)$ by applying a fast Fourier transform on the known values

$$\mathbf{U}^M(z,\tilde{\tau}) := \mathbf{U}^B(z,\tilde{\tau}) - \mathbf{U}^S(z) \tag{3.11}$$

$$= \sum_{k=-\infty}^{\infty} \mathbf{u}_k(z) e^{ik\tilde{\tau}} \tag{3.12}$$

Validation of this method of calculating the base flow contribution to the system is provided by use of the analytic Stokes solution of section 2.1.2. Provided the Stokes layer solution is an appropriate approximation for the parameters in question, we can simply set $\mathbf{u}_1(z) = \bar{\mathbf{u}}_{-1}(z) = e^{-(1+i)z}$, with $\mathbf{u}_k(z) = 0$ $(k \neq 1)$ and proceed to solve.

The system (3.8) is solved by a similar method to that of the Stokes layer. In the case for the steady rotating disk discussed in section 2.2.1, we had a problem of the form

$$\begin{aligned} -i\omega\xi_r + \mathcal{L}_r\{\xi_r, \xi_\theta, w\} &= 0 \\ -i\omega\xi_\theta + \mathcal{L}_\theta\{\xi_r, \xi_\theta, w\} &= 0 \\ \mathcal{L}_w\{\xi_r, \xi_\theta, w\} &= 0 \end{aligned}$$

where $\mathcal{L}_{\{r,\theta,w\}}$ represents all of the terms which are not included in the temporal derivative. The alteration that the inclusion of the Floquet normal mode structure introduces can thus be written similarly as

$$\sum_{m=-\infty}^{\infty} \left(im\left(\frac{\varphi}{R}\right)\xi_{r,m} + \mu\xi_{r,m} + i\beta \sum_{k=-\infty}^{\infty} N^z_{m+k} - \frac{\partial}{\partial z}\sum_{k=-\infty}^{\infty} N^\theta_{m+k} + \mathcal{L}_r\{\xi_{r,m}, \xi_{\theta,m}, w_m\} \right) e^{im\tilde{\tau}} = 0$$

$$\sum_{m=-\infty}^{\infty} \left(im\left(\frac{\varphi}{R}\right)\xi_{\theta,m} + \mu\xi_{\theta,m} + \frac{\partial}{\partial r}\sum_{k=-\infty}^{\infty} N^z_{m+k} + \frac{\partial}{\partial z}\sum_{k=-\infty}^{\infty} N^r_{m+k} + \mathcal{L}_\theta\{\xi_{r,m}, \xi_{\theta,m}, w_m\} \right) e^{im\tilde{\tau}} = 0$$

$$\sum_{m=-\infty}^{\infty} \mathcal{L}_w\{\xi_{r,m}, \xi_{\theta,m}, w_m\} e^{im\tilde{\tau}} = 0$$

where we have defined $\mathbf{N}_k$ to be the unsteady contributions to the convective terms.

Comparing coefficients of $e^{im\tilde{\tau}}$ gives an infinite system of ordinary differential equations which can be truncated and solved for the eigenvalues using MATLAB's *eigs* package. Essentially, this problem reduces to a system of dispersion relations of the form

$$\sum_{m=-\infty}^{\infty} \mathcal{D}_m\{\mu, \alpha\ R, n\} e^{im\tilde{\tau}} = 0 \tag{3.13}$$

and as for the steady case, there are two distinct types of analysis which can be conducted, namely *temporal* and *spatial*. The *temporal* approach consists of specifying $\alpha \in \mathbb{R}$ and

calculating μ from (3.13) while the *spatial* approach specifies $\mu \in \mathbb{R}$ and calculates α from (3.13). At the time of writing, no literature which deals with the spatial implementation of Floquet theory could be found and from a physical viewpoint, its interpretation is in need of some clarification. For the majority of results presented below, unless otherwise stated, we have fixed the Reynolds number associated with the disk rotation at $R = 500$ and the azimuthal mode number at $n = 32$, so as to be sure that instability would be present in the steady, unmodulated scenario. As has been alluded to previously, the base flow may be fully specified by the variation of three parameters, namely (R, U_w, φ) defined by

$$R = r_L, \qquad U_w = \frac{R_s\sqrt{\varphi}}{R}, \qquad \varphi = \sqrt{\frac{\phi^*}{\Omega_0^*}} \tag{3.14}$$

where r_L and R_s are defined by equations (3.3)-(3.4) and ϕ^*, Ω_0^* denote the dimensional modulation frequency and unmodulated disk rotation rate respectively.

As for the steady case, the spatial analysis of the dispersion relation (3.13) introduces two more parameters (n, μ). The restriction to the analysis of disturbances which are stationary with respect to the constant rotation rate is achieved by setting $\mu = 0$, which we will do for all spatial analyses unless specifically otherwise stated.

There are several complications involved in the numerical computation of these quantities, so prior to our presentation and discussion of the results, it is pertinent to provide an overview of these at this stage.

3.1.1 Discussion of Numerical Computation

Temporal vs. Spatial - Computational Times

In general terms, the most physically relevant quantities extractable from (3.13) will be the spatial growth rates, and we will focus on these for much of the discussion in this section. However, since the solution procedure is computationally more feasible in the temporal setting, we consider this first. While presumably not immediately obvious to the reader, the increase in computational feasibility is as a result of the difference in order of the polynomial eigenvalue problem (3.13). The temporal analysis, where μ is calculated, is a linear generalised eigenvalue problem, whereas a spatial analysis would see the eigenvalue α appear to second order, thereby increasing the complexity of the problem considerably. This issue was clearly also present in sections 2.2.1, although we

paid it little attention since it did not have a great effect on the computational time. The added complexity in this problem due to the coupled system of differential equations required to solve the dispersion relation changes this considerably, and we first present a brief discussion of the eigenvalue routines and associated computational times.

The three relevant eigenvalue routines available in MATLAB are *eig*, *polyeig* and *eigs*. The routines *eig* and *eigs* are capable of solving linear generalised eigenvalue problems of the form

$$\mathbf{A}\phi = \lambda \mathbf{B}\phi \tag{3.15}$$

while *polyeig* is optimised to solve polynomial eigenvalue problems of the form

$$\lambda^n \mathbf{A}_n + \lambda^{n-1}\mathbf{A}_{n-1} + \cdots + \lambda \mathbf{A}_1 + \mathbf{A}_0 = 0 \tag{3.16}$$

While *polyeig* performs reasonably well for relatively small matrix operators, it prohibitively struggles for the large matrix operators we are attempting to deal with in this problem. The linear routine *eigs* has an additional flag which allows a user to instruct the routine to find the N closest eigenvalues in absolute value to a given initial guess, although the current version of *polyeig* unfortunately has no such flag and requires a full calculation of every numerical eigenvalue in the solution. Therefore, for many of the results presented for the spatial analysis in later sections, we use the local iteration method (1.48) to calculate the eigenvalues, while conducting regular checks using the global solver to ensure convergence to the correct eigenvalue at all times. Table 3.1 illustrates the computational difficulties encountered using when using *polyeig* for a typical set of rotation and modulation parameters, and compares the spatial and temporal cases. In each case for the linear solver, the MATLAB routine *eigs* was provided with the steady eigenvalue as an initial guess, and instructed to return the 5 closest eigenvalues in absolute value. In each case, the order of the Chebyshev discretisation is taken to be $N_C = 64$ and five terms in the Fourier expansion of the base flow (3.10) were taken, which we label $N_B = 2$. This selection allowed for $\max_{z\in[0,\infty)} |u_{N_B}(z)| < 1\text{e}{-10}$ in all cases. The simulations were performed for a typical set of rotation and modulation parameters, namely $R = 500$, $n = 32$, $U_w = 0.2$ and $\varphi = 10$. In the temporal analysis, we have set $\alpha = 0.3$ and in the spatial analysis, we have set $\mu = 0$.

Number of Harmonics, N_F	Computational Time (s)	
	Linear (*eigs*)	Quadratic (*polyeig*)
2	6.72	247.82
4	40.08	1358.60
6	80.14	3494.68
10	175.29	N/A

Table 3.1: Comparison between computational times for the solution of the temporal (linear) and spatial (quadratic) eigenvalue problems arising from the dispersion relation (3.13). Simulations were performed for a typical set of rotation and modulation parameters, namely $R = 500$, $n = 32$, $U_w = 0.2$ and $\varphi = 10$. In the temporal analysis, we have set $\alpha = 0.3$ and in the spatial analysis we have set $\mu = 0$. This was performed with Matlab version 2017a on a workstation with an Intel Core i5-3470T CPU at 2.90GHz.

Number of Harmonics in Floquet Solution

Section 1.4.4 presented a discussion of the stability properties of the quintessential purely oscillatory flow that is generated when a flat plate oscillates in the plane beneath a semi-infinite expanse of fluid, namely the Stokes layer, and provided an overview of the solution procedure. Table 1.2 shows the number of harmonics required in the truncation of the infinite system of differential equations that determine the dispersion relation (3.13). Throughout this work, we will refer to this computational truncation parameter as N_F, and identify it in the following sense

$$\sum_{m=-\infty}^{\infty} \mathcal{D}_m\{\mu, \alpha\ R, n\} e^{im\tilde{\tau}} = 0 \quad \rightarrow \quad \sum_{m=-N_F}^{N_F} \mathcal{D}_m\{\mu, \alpha\ R, n\} e^{im\tilde{\tau}} = 0 \tag{3.17}$$

In order to achieve eigenvalue convergence for the Stokes layer in section 1.4.4 we required $N_F \gtrsim 0.8\alpha R$, which for the Reynolds numbers close to critical is typically in the region of $N_F \approx 200$. It should not be expected that the same number would be required here, since the modulation constitutes a small modification to a steady rotation rate and we do not have the same separation of temporal scales that we do in the Stokes case.

In fact, as detailed in table 3.2, in almost all cases, $N_F \approx 4$ is sufficient to achieve convergence. In practise, when carrying out the calculations, two routines were performed and compared with differing N_F to ensure convergence is always achieved on each run.

Variation of μ with Number of Harmonics N_F					
R	α	U_w	φ	N_F	μ
500	0.3	0.2	5	1	0.005289 + 0.009825i
				2	0.005289 + 0.019824i
				3	0.005289 + 0.029824i
				4	0.004229 - 0.011160i
				5	0.004229 - 0.011160i
500	0.3	0.2	10	1	0.004779 + 0.019120i
				2	0.004206 - 0.020812i
				3	0.004206 - 0.000811i
				4	0.004206 - 0.000811i
				5	0.004206 - 0.000811i
500	0.3	0.2	15	1	0.004779 + 0.0291144i
				2	0.004497 - 0.000840i
				3	0.004497 - 0.000840i
				4	0.004497 - 0.000840i
				5	0.004497 - 0.000840i

Table 3.2: Variation in the temporal eigenvalue μ calculated from the dispersion relation (3.13) for varying numbers of harmonics N_F. For all cases, the azimuthal mode number n was set to $n = 32$.

Number of Terms in Base Flow Expansion

The final parameter to be addressed in this section is the number of terms taken in the Fourier expansion of the base flow. Since the Stokes layer discussed in section 1.4.4 can be represented exactly as a finite combination of Fourier modes, as displayed in equation (1.71), this parameter does not exist in that case. However, since we cannot readily express our base flow exactly with a finite combination such as this, we must introduce a further truncation parameter N_B which we identify with

$$\mathbf{U}^M(z,t) = \sum_{k=-\infty}^{\infty} \mathbf{u}_k(z) e^{ik\tilde{\tau}} \quad \rightarrow \quad \mathbf{U}^M(z,t) \approx \sum_{k=-N_B}^{N_B} \mathbf{u}_k(z) e^{ik\tilde{\tau}} \tag{3.18}$$

As explained in section 2.1.2 when discussing the high frequency, small amplitude limiting behaviour, the dominant behaviour comes in at first order, the expectation is that N_B should be fairly small to achieve convergence. This is indeed the case, as detailed in table 3.3, and in all cases $N_B \approx 2$ was sufficient for well-resolved results. In practise, when carrying out the calculations, two routines were performed and compared with differing N_B to ensure convergence is always achieved on each run.

Variation of μ with Number of Harmonics N_B					
R	α	U_w	φ	N_B	μ
500	0.3	0.2	5	1	0.004229 - 0.011160i
				2	0.004229 - 0.011160i
				3	0.004229 - 0.011160i
500	0.3	0.2	10	1	0.004207 - 0.000812i
				2	0.004206 - 0.000812i
				3	0.004206 - 0.000812i
500	0.3	0.2	15	1	0.004779 + 0.0291144i
				2	0.004497 - 0.000840
				3	0.004497 - 0.000840i

Table 3.3: Variation in the temporal eigenvalue μ calculated from the dispersion relation (3.13) for varying numbers of terms, N_B, in the Fourier expansion of the base flow. For all cases, the azimuthal mode number n was set to $n = 32$.

3.1.2 Temporal Analysis

We begin the presentation of the modifications introduced by the periodically modulated rotation rate by examining the temporal setting, where we specify the radial wavenumber α as real and use the dispersion relation (3.13) to calculate the eigenvalues μ. In general, μ will be complex, with the real part μ_r corresponding to the disturbance growth rate and the imaginary part μ_i its frequency.

We will consider the configuration to be *stabilised* in the temporal setting if

$$\mu_r^M < \mu_r^S \tag{3.19}$$

where μ_r^S and μ_r^M denote the steady and modulated growth rates respectively. Given the discussions presented in section 3.1.1, the numbers of harmonics and terms in the Fourier expansions of the base flow were chosen to ensure convergence of the eigenvalues in each case. This was achieved in practise by comparing the relative errors between two distinct orders of approximation and ensuring that the output was negligible. For the vast majority of cases presented, a choice of $N_F = 4$ and $N_B = 2$, in addition to a Chebyshev discretisation order of $N = 64$ was sufficient to ensure convergence.

Figure 3.1 shows the temporal eigenvalue spectrum for $R = 500$, $n = 32$, $\alpha = 0.3$, $U_w = 0.2$ and $\varphi = 10$. The corresponding steady eigenvalue $\mu_S = -i\omega_S$ is indicated on the diagram, which clearly shows a shift towards 0, or temporal stabilisation, in the real part of μ in the modulated case.

The parameter choices of $U_w = 0.2$ and $\varphi = 10$ were chosen partly with the aid of hindsight to provide an illustrative example of the stabilisation, but also to lie within a physically significant range for the applications to laminar flow control. As alluded to in the opening of this chapter, we can identify U_w as a modulation amplitude which, under the scalings, becomes a percentage deviation from the steady state. $U_w = 0$ would correspond to the steady case, while $U_w = 0.1$ would constitute a swing of 10% back-and-forth from the steady rotation rate in one modulation period. The quantity φ may be interpreted as a non-dimensional frequency, and is identified with the number of oscillations about the steady state in one disk rotation period. As will be the case with all results presented in this report, the amplitude parameter will be constrained to be small, so as to provide a valid comparison against the steady case and an application to laminar flow control. It is important to note, however, that this small U_w assumption is not an inherent feature of our solution procedure, and $U_w > 0.2$ is easily achievable with the same method.

This demonstrates our first glimpse thus far of the stabilising behaviour achieved by the addition of the modulated rotation rate. As we progress through the following sections we will provide further examination of this behaviour, and attempt to explain some of the underlying physical processes behind it. While figure 3.1 shows only an isolated parameter case, figure 3.2 shows the difference in temporal growth rates $\mu_r^S - \mu_r^M$ for $R = 500$, $n = 32$, $\alpha = 0.3$ with varying φ and $U_w \in \{0.1, 0.2\}$.

Intriguingly, we see a peak stabilisation around $\varphi \approx 8$, while very low frequencies

and very high frequencies contribute little effect to the system. Potential explanations for this phenomena will be given in later sections, although it should be noted that the explanations will be conjecture, and that the true reasoning behind this behaviour is unknown at this time. These figures demonstrate that the stabilisation achieved by the addition of the modulated rotation rate is more robust than being restricted to an isolated parameter set.

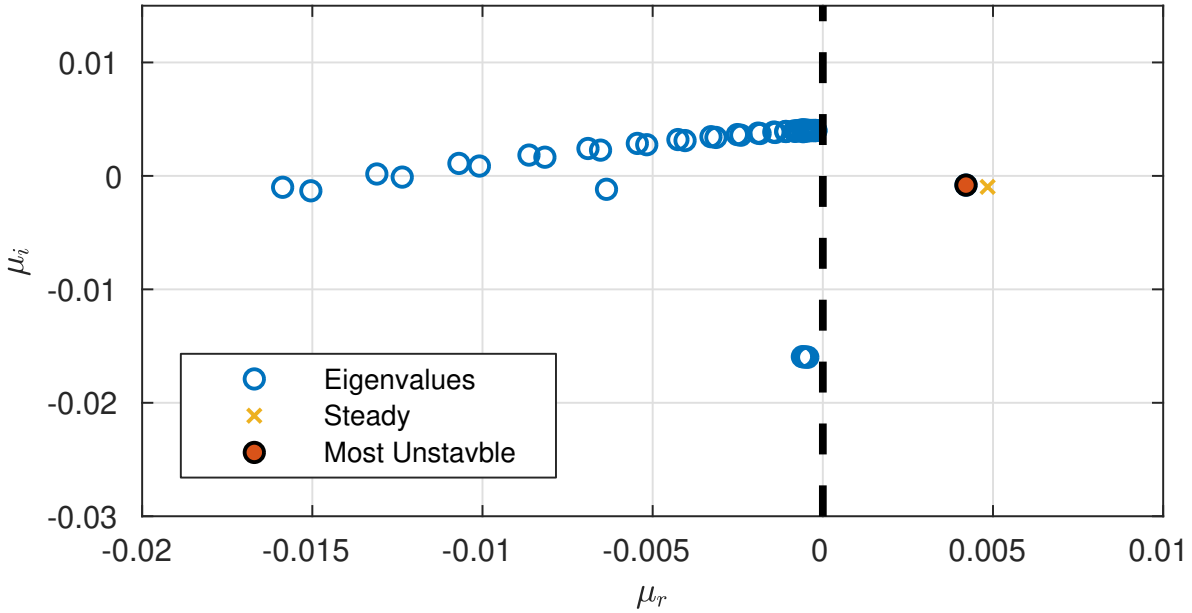

Figure 3.1: Temporal eigenvalue spectrum for $\alpha = 0.3$ with $U_w = 0.2$ and $\varphi = 10$. The steady eigenvalue is shown as ($\times$), while the filled in circle corresponds to the most unstable eigenvalue in the modulated case

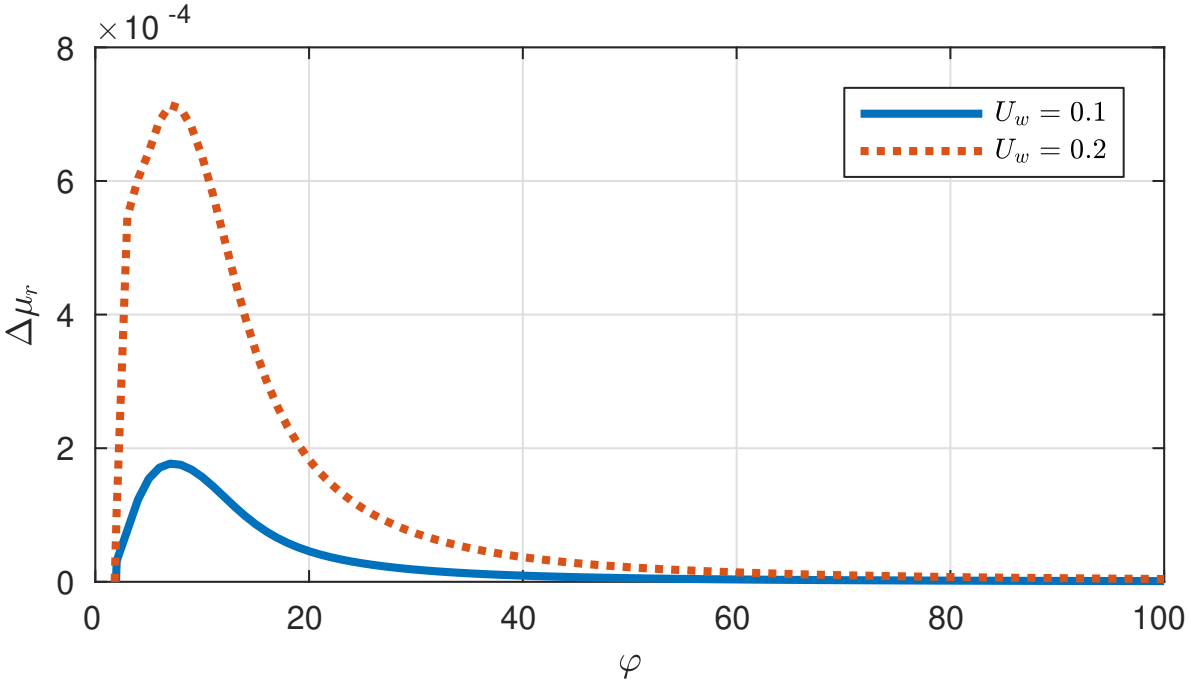

Figure 3.2: Variation in temporal growth rates for the most unstable mode, with $R = 500$, $n = 32$, $\alpha = 0.3$, $U_w = 0.1$ (—), $U_w = 0.2$ ($\cdots$) and varying $\varphi \in (0, 100]$. $\Delta\mu_r := \mu_r^S - \mu_r^M$ denotes the difference in the growth rate between steady and modulated cases with positive $\Delta\mu_r$ indicating a weaker growth rate.

3.1.3 Spatial Analysis

As explained in the previous section, a global spatial analysis is computationally expensive and thus the following results will, in the most part, correspond to calculations carried out using a local iteration procedure first discussed as equation (1.48). This amounts to using an initial guess for the eigenvalue and using the cubically convergent method described in Bridges and Morris [14] to iterate towards α. We can iteratively improve this guess by the formula

$$\alpha_{k+1} = \alpha_k - \frac{2f(\alpha_k)}{f(\alpha_k)^2 - f_1(\alpha_k)} \tag{3.20}$$

where

$$f(\alpha_k) = \mathrm{Tr}[\mathcal{D}^{-1}(\alpha_k)\mathcal{D}'(\alpha_k)]$$
$$f_1(\alpha_k) = \mathrm{Tr}\{\mathcal{D}^{-1}(\alpha_k)\mathcal{D}''(\alpha_k) - [\mathcal{D}^{-1}(\alpha_k)\mathcal{D}'(\alpha_k)]^2\}$$

and $\mathcal{D}(\alpha)$ refers to the system of differential equations (3.13) which determine the dispersion relation while $\mathcal{D}'(\alpha)$ and $\mathcal{D}''(\alpha)$ are the derivatives of $\mathcal{D}$ with respect to α.

The exception to this locally computed method is figure 3.3, which shows a typical *global* α-eigenvalue spectrum for stationary disturbances with $U_w \in \{0.1, 0.2\}$ and $\varphi \in \{10, 25\}$. The corresponding steady, $U_w = 0$, eigenvalue α_S is indicated, with the diagrams clearly showing a shift towards 0, or stabilisation, of the imaginary part of α in the modulated cases. Unlike for the steady configuration, the physical interpretation of the reduction in this radial growth rate is in need of clarification as this study presents the first implementation of Floquet theory in the spatial setting to the best of the author's knowledge. It is anticipated that the analyses and interpretations of the radial growth rate in the steady case will persist in the modulated scenario but a rigorous mathematical justification of this is not presented here.

Figure 3.4 shows the difference in spatial growth rates $\alpha_i^S - \alpha_i^M$ for stationary disturbances with $U_w \in \{0.1, 0.2\}$ and $\varphi \in (0, 100]$. Similarly to the temporal case shown in figure 3.2, we see a peak stabilisation around $\varphi \approx 8$, while very low very high frequencies contribute little effect to the system. This alludes to an *optimal* range of frequencies φ for maximum stabilisation in the system.

Heretofore, we have only considered isolated data points in R and n, chosen as exemplar parameters to demonstrate the stabilising effects of modulation on the radial growth rates α_i. Figures 3.5 and 3.6 show the radial and azimuthal neutral curves respectively

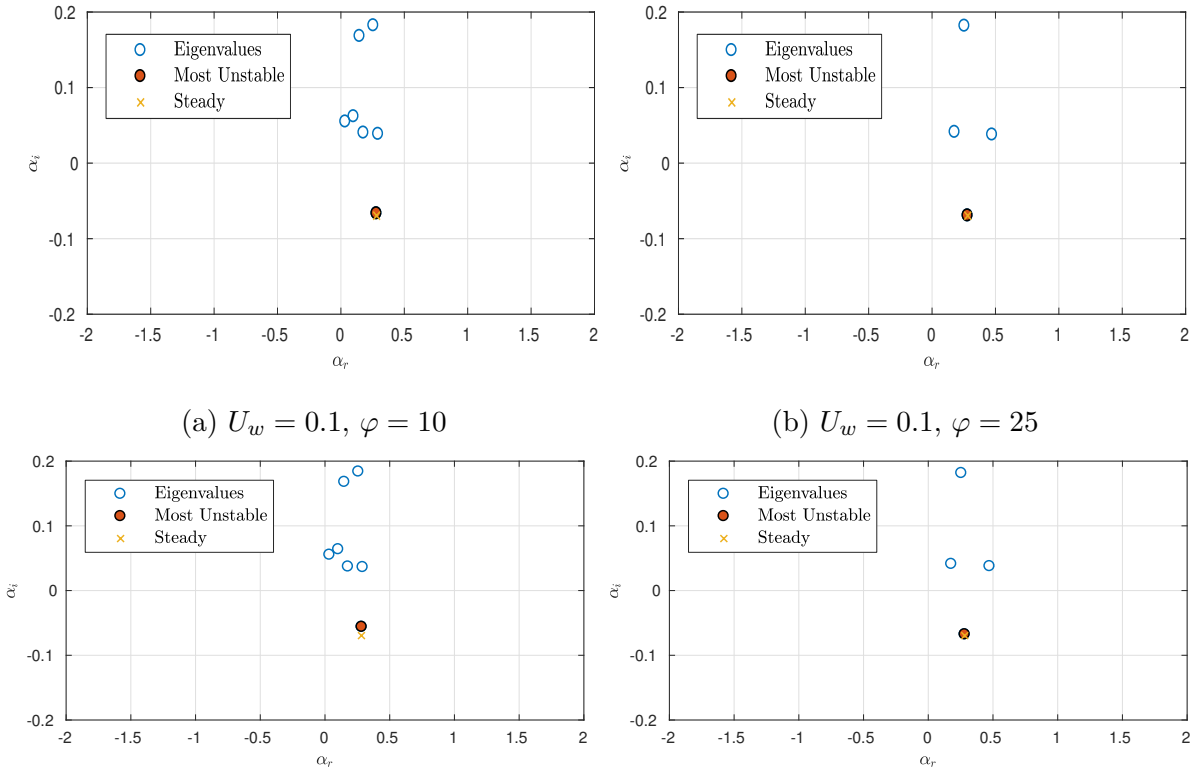

(a) $U_w = 0.1$, $\varphi = 10$

(b) $U_w = 0.1$, $\varphi = 25$

(c) $U_w = 0.2$, $\varphi = 10$

(d) $U_w = 0.2$, $\varphi = 25$

Figure 3.3: Radial wavenumber spectrum for stationary disturbances with $R = 500$, $n = 32$ and varying φ and U_w. The steady eigenvalue is shown as ($\times$), while the filled in circle corresponds to the most unstable eigenvalue in the modulated case.

for stationary disturbances with $U_w = 0.2$ and $\varphi = 20$. This demonstrates that the stabilising behaviour is not an isolated occurrence for a particular parameter set and shows the stabilisation across a large range of R and n. Figure 3.7 shows the variation in the critical Reynolds number R_c for Type I disturbances with $U_w = 0.2$ across a range of φ.

Interestingly, and contrary to other methods of stabilisation studied by other authors such as radially isotropic and anisotropic surface roughness (see Cooper et al. [21], Garrett et al. [36]) or surface compliance (see Cooper and Carpenter [19, 20]), the type II mode seems also to be stabilised by the addition of modulation, at least for the stationary disturbances considered here. Further investigation of the effect of the modulation on non-stationary disturbances is reserved for future work, as is a comprehensive study of the behaviour of the type II mode in the various configurations.

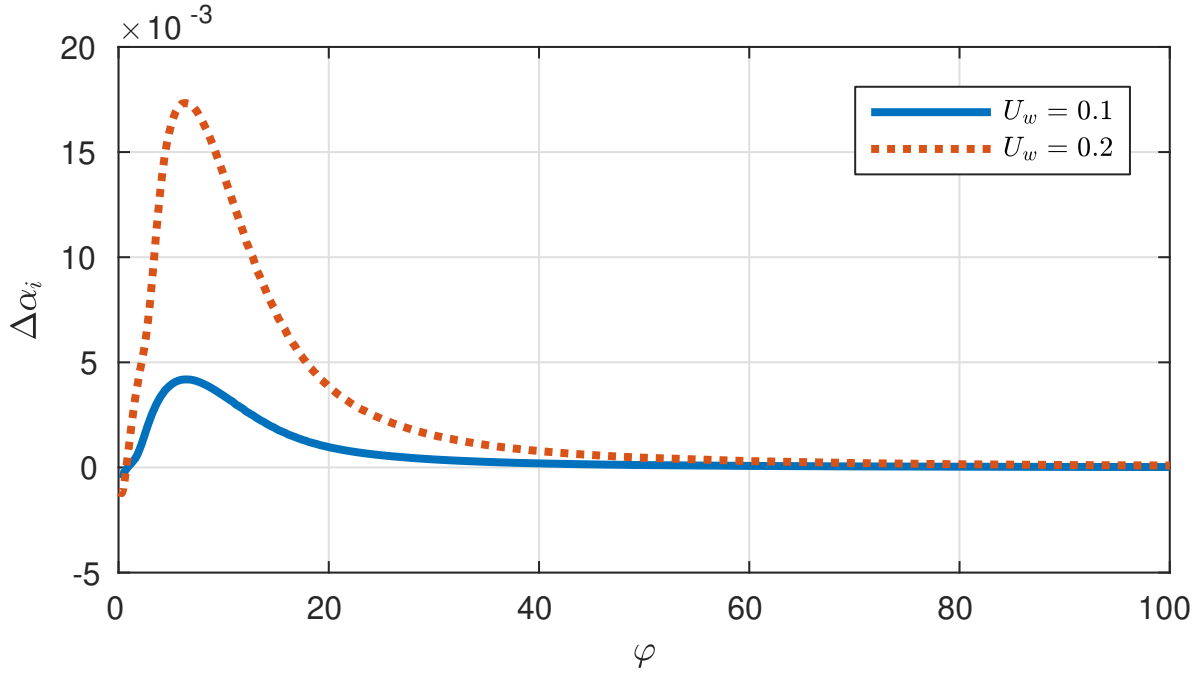

Figure 3.4: Variation in radial growth rates for most unstable mode calculated from (3.13) for stationary disturbances, with $U_w = 0.1$ (—), $U_w = 0.2$ ($\cdots$) and varying $\varphi \in (0, 100]$. $\Delta\alpha_i$ denotes the difference in the growth rate between steady and modulated cases with positive $\Delta\alpha_i$ indicating a weaker growth rate.

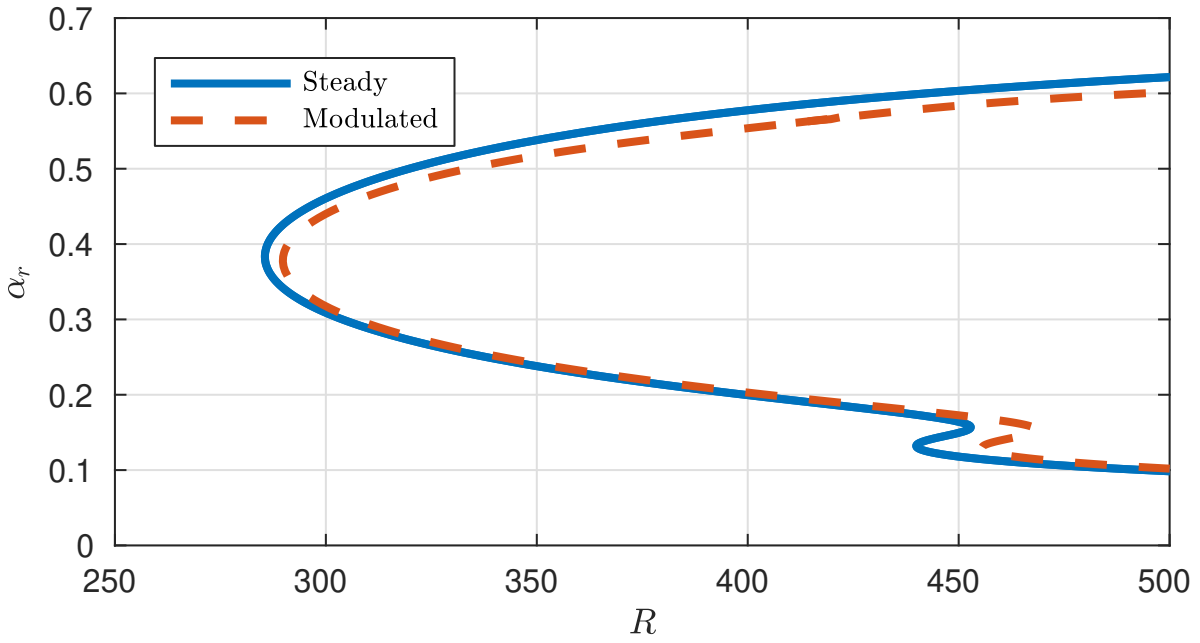

Figure 3.5: Radial neutral curves for stationary disturbances, comparing the steady case (—) with the modulated scenario when $U_w = 0.2$ and $\varphi = 20$ ($\cdots$).

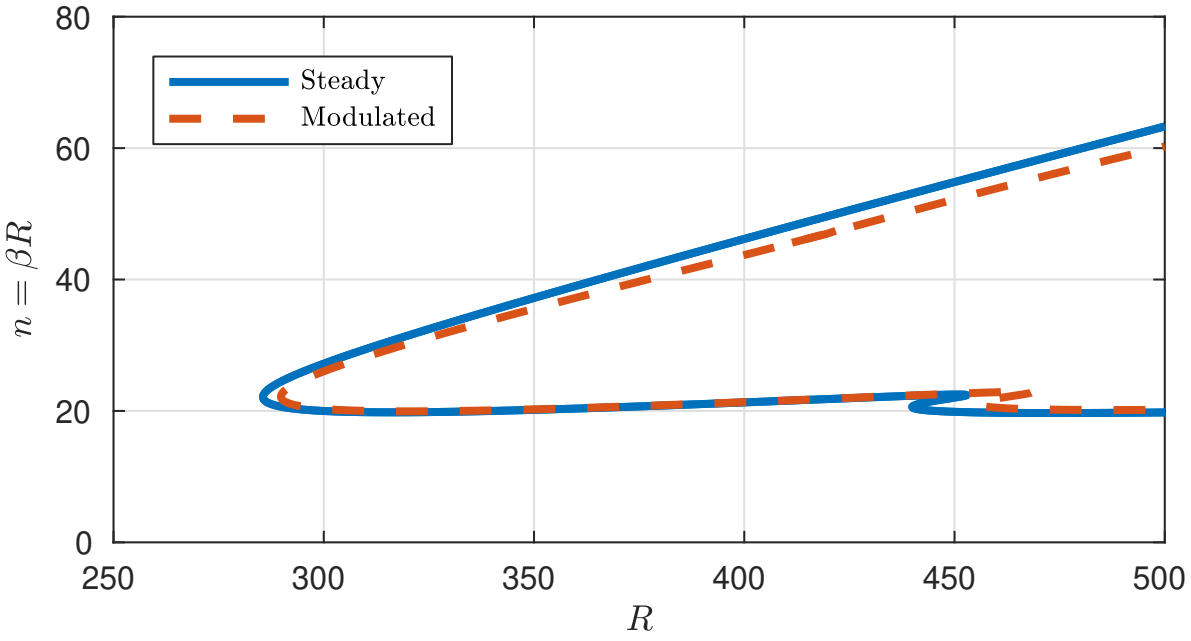

Figure 3.6: Azimuthal neutral curves for stationary disturbances, comparing the steady case (—) with the modulated scenario when $U_w = 0.2$ and $\varphi = 20$ ($\cdots$).

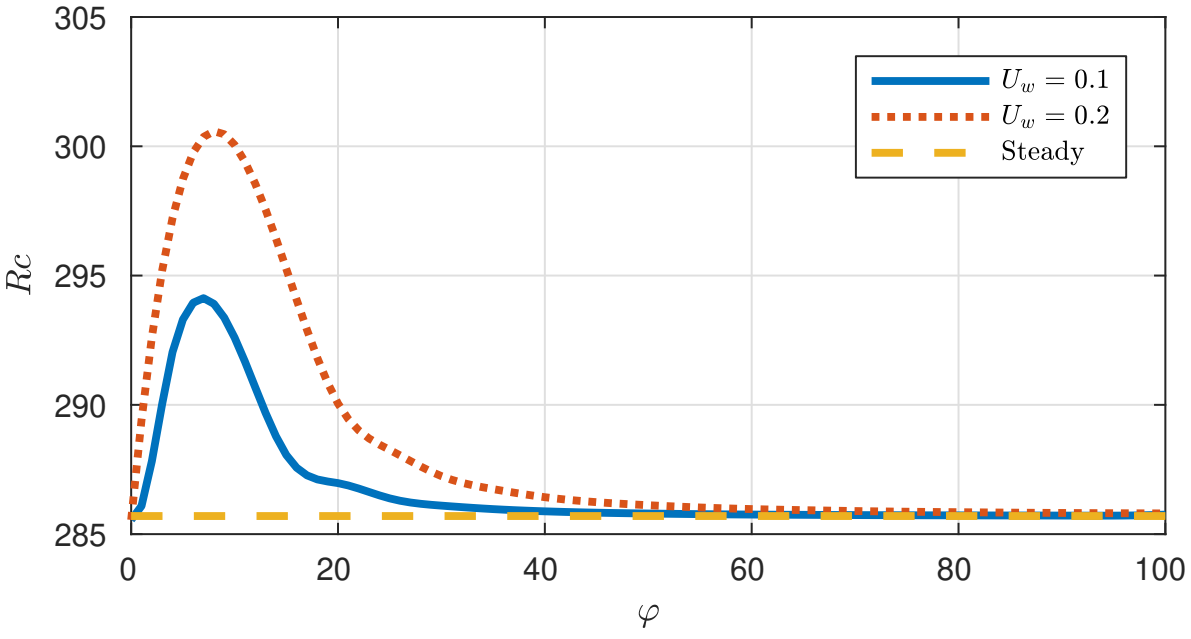

Figure 3.7: Variation in the critical Reynolds number R_c for stationary type I disturbances with varying φ and $U_w = 0.1$ (—), $U_w = 0.2$ ($\cdots$). The critical Reynolds number for onset of instability in the steady case ($R_c \approx 285.55$) is shown as (- - -).

3.1.4 Discussion

Sections 3.1.2 and 3.1.3 have detailed our first encounters with the stabilisation of the rotating disk boundary layer by the addition of a modulated rotation rate, and we have presented and discussed several results which appear to demonstrate a significant stabilisation in both temporal and spatial analyses. We have demonstrated that there is an intriguing range of somewhat *optimal* stabilisation in terms of the non-dimensional modulation frequency parameter φ and that the stabilisation persists across a range of Reynolds numbers, azimuthal mode numbers and modulation parameters.

Similar behaviour is demonstrated by other authors such as Cooper et al. [21], Garrett et al. [36] when discussing radially isotropic and anisotropic surface roughness or by Cooper and Carpenter [19, 20] when studying surface compliance, although a distinct difference and advantage of the method presented here is that there is no modelling of the surface of the disk involved at any point. We do not discard first order effects as the modelling of Cooper et al. [21] and Garrett et al. [36] does, and over a period of modulation, the base flow has a zero average deviation from the steady state, further details and explanations of which are given in section 2.1.3.

The following sections discuss two further methods for analysing the linear stability of stationary disturbances in the modulated rotating disk boundary layer, which will act as validation for the Floquet theory analysis and provide further interesting results in their own right. We proceed first with an instantaneous frozen profile analysis before progressing to an examination of fixed radial wavenumber monochromatic direct numerical simulations. This chapter concludes with an energy analysis intended to illuminate the fine details of the stabilising behaviour and results relating to direct numerical simulations of stationary forcing with the full radial dependence of the mean flow included.

3.2 Quasi-Steady Stability Theory and the Frozen-flow Approximation

As discussed in section 1.4.4 when considering the semi-infinite Stokes layer, an instantaneous stability investigation may be conducted by *freezing* the base flow at a specific time instant and treating it as if it were steady. This allows for the time to be treated as a parameter, and suggests a normal-mode type solution of the form

$$f(r,\theta,z,\tau) = \hat{f}(z;\tau)e^{i\left(\alpha r+\beta R\theta-\int_\tau \omega\right)} \tag{3.21}$$

where $\hat{f}$ is a function which is slowly varying in time. This assumption allows us to neglect the temporal derivative $\frac{\partial \hat{f}}{\partial \tau} \approx 0$ and derive a set of perturbation equations similar to those in section 2.2.1 given by

$$-i\omega\xi_r + i\beta N_z(\tau) - \frac{\partial N_\theta(\tau)}{\partial z} - \frac{2}{R}\left(\xi_\theta + i\alpha w\right) = \frac{1}{R}\left(-\alpha^2-\beta^2+\frac{\partial^2}{\partial z^2}\right)\xi_r \tag{3.22a}$$

$$-i\omega\xi_\theta + \frac{\partial N_r(\tau)}{\partial z} - \frac{\partial N_z(\tau)}{\partial r} + \frac{2}{R}\left(\xi_r - i\beta w\right) = \frac{1}{R}\left(-\alpha^2-\beta^2+\frac{\partial^2}{\partial z^2}\right)\xi_\theta \tag{3.22b}$$

$$\left(\hat{\nabla}^2+\frac{\partial^2}{\partial z^2}\right)w = i\beta\xi_r - i\alpha\xi_\theta - \frac{\xi_\theta}{R} \tag{3.22c}$$

In this system, the base flow $\mathbf{U}_B$ and thus $\mathbf{N}$, is replaced with the frozen base flow at the given time instant. This system is complemented by the definition of the secondary variables (2.37) and the boundary conditions (2.45) of section 2.2.1 to fully specify eigenvalue dispersion relations for each τ of the form

$$\mathcal{D}(\omega,\alpha,\beta,Re;\tau) = 0 \tag{3.23}$$

Section 1.4.4 and Ramage [59] give detailed descriptions of the subtleties and difficulties in using this approximation to specify the disturbance evolution properties of the semi-infinite Stokes layer, indicating that any predictions or conclusions drawn from this analysis must be treated with caution. However, some insight may be gained by a careful treatment of this method and in section 3.3 we will utilise this approximation to discuss the energy balance of the perturbed flow in the modulated rotation rate scenario.

The τ-parameter dependent dispersion relation (3.23) is solved in an identical manner to the steady equations (2.44) for each frozen base flow field $\mathbf{U}_B(z;\tau)$, where each time-instant is treated as if it were steady and τ is taken as a parameter. Similarly to the

steady case, we may solve this dispersion relation (3.23) for either α or ω while specifying the other in a spatial or temporal setting. In keeping with the methodology of section 3.1, for the results below, we have fixed the Reynolds number associated with the disk rotation at $R = 500$ and the azimuthal mode number at $n = 32$, so as to be sure that instability would be present in the steady, unmodulated scenario. Throughout the following sections, the temporal growth rates and frequencies ω are non-dimensionalised so that the period of disk rotation is 2π. Certain authors and results in the literature may use a time-scale such that the locally defined growth rates are a factor R larger, leading the disk rotation period to be $2\pi R$. Since the perturbation quantities are periodic with the period of the modulation, which we will denote $T_\varphi = \frac{\tau\varphi}{2\pi R}$ here.

3.2.1 Temporal Analysis

As for the Floquet analysis, we begin our discussion in the temporal setting, and figure 3.8 shows the variation of $\mu = -i\omega$ in the Argand plane over a period of modulation for $\alpha = 0.3$, $U_w = 0.2$ and $\varphi = 10$. These parameters were chosen as exemplary, with the particular intention of lying near to the peak of the optimal stabilisation in terms of the non-dimensional frequency φ shown in figure 3.2. The corresponding steady and Floquet eigenvalues are also shown on figure 3.8. A reduction in the real part is consistent with stabilising behaviour, as $\mathfrak{R}(\mu)$ denotes the temporal growth rate here. Figure 3.9 shows the time histories of the real and imaginary parts of μ over one modulation period together with the corresponding steady and Floquet counterparts which are necessarily constant across the period. An important distinction between these results and those of Luo and Wu [48] for the semi-infinite Stokes layer should be noted, namely that the eigenvalues of this configuration are indeed periodic, and do not exhibit the *head and tail* behaviour described in Luo and Wu [48].

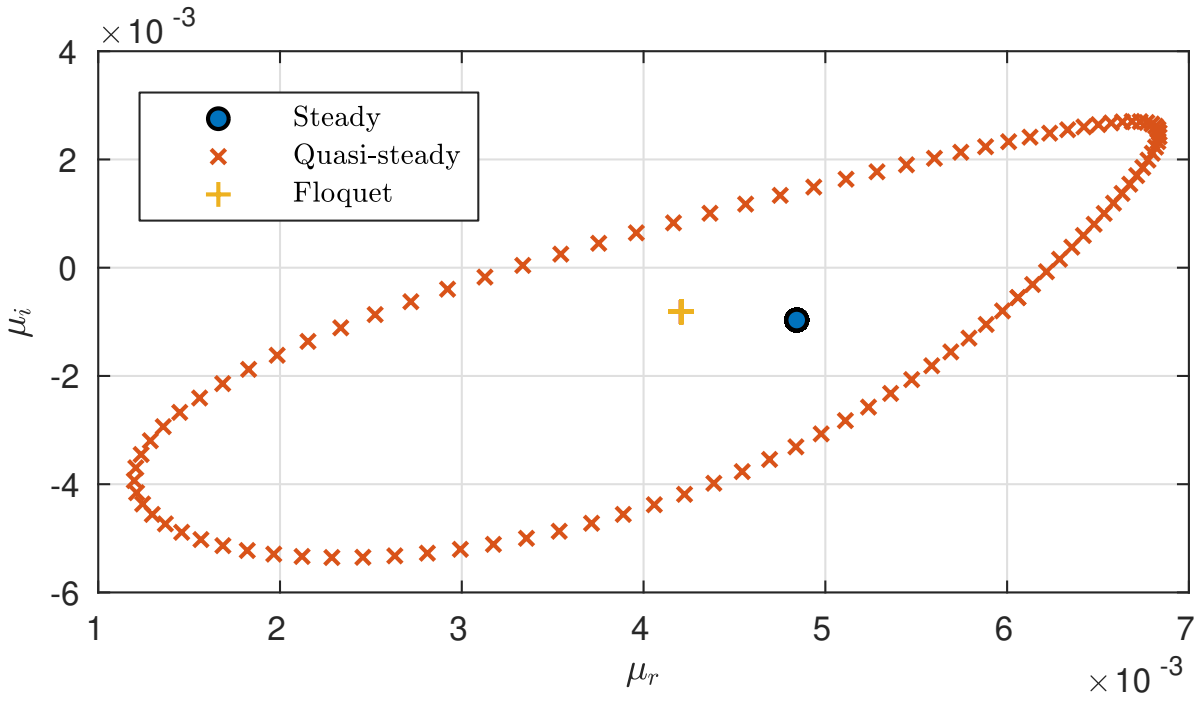

Figure 3.8: Temporal evolution of $\mu = -i\omega$ across a period of modulation in the Argand plane for disturbances with $R = 500$, $n = 32$, $\alpha = 0.3$, $U_w = 0.2$ and $\varphi = 10$. The temporally periodic quantity μ is shown as ($\times$) along with the Floquet ($+$) and steady (o) eigenvalues.

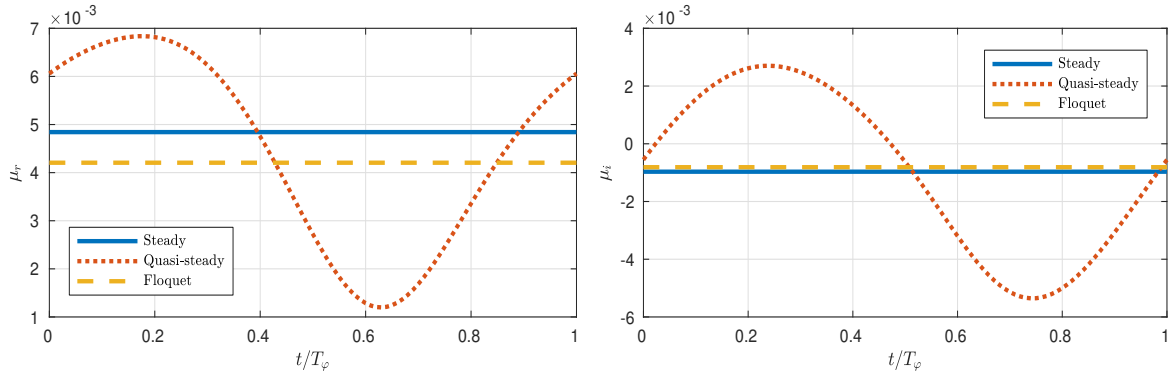

(a) μ_r (b) μ_i

Figure 3.9: Evolution of temporal eigenvalue μ across a period of modulation for disturbances with $R = 500$, $n = 32$, $\alpha = 0.3$, $U_w = 0.2$ and $\varphi = 10$. The temporally periodic quantities $\mathfrak{R}(\mu)$ and $\mathfrak{I}(\mu)$ are shown as ($\cdots$) along with the Floquet (- - -) and steady (—) eigenvalues.

3.2.2 Spatial Analysis

Similarly to the results presented when discussing the Floquet approach in section 3.1, we will consider stationary ($\omega = 0$) disturbances with typical parameter values $R = 500$ and $n = 32$. As throughout the rest of this and previous sections, these parameters are chosen as exemplary, with the particular intention of lying near to the peak of the optimal stabilisation in terms of the non-dimensional frequency φ shown in figure 3.2.

A reduction in the imaginary part of α is consistent with stabilising behaviour, as $\Im(\alpha)$ denotes the spatial growth rate here. Figure 3.11 shows the time histories of the real and imaginary parts of μ over one modulation period together with the corresponding steady and Floquet counterparts which are necessarily constant across the period. Since the quasi-steady eigenvalues calculated from (3.23) are periodic and do not exhibit the *head and tail* behaviour described in Luo and Wu [48], it is expected that the Floquet eigenvalue should be identifiable with an average of the instantaneous eigenvalue across a period of modulation. We can thus expect

$$\alpha_F \sim \frac{1}{T_\varphi} \int_0^{T_\varphi} \alpha(\tau) d\tau \tag{3.24}$$

where μ_F is the Floquet eigenvalue calculated using (3.13) and $T_\varphi = \frac{t\varphi}{2\pi R}$ is the modulation period. This quantity is also shown on figures 3.10 and 3.11 for comparison purposes where it can be seen that the two quantities match well.

While providing validation for the Floquet analysis, this method provides an alternative approach for calculating the spatial growth rates in a substantially more computationally feasible manner. There is no requirement to work with the particularly large matrices present in the Floquet theory and the computation is only limited by the number of temporal locations required to sample the data. In effect, this method is of comparable computational feasibility to the steady case and is advantageous over the Floquet analysis for this reason. However, great care must be taken on using this approach in isolation, as it is not rigorously guaranteed that equation (3.24) holds in all cases.

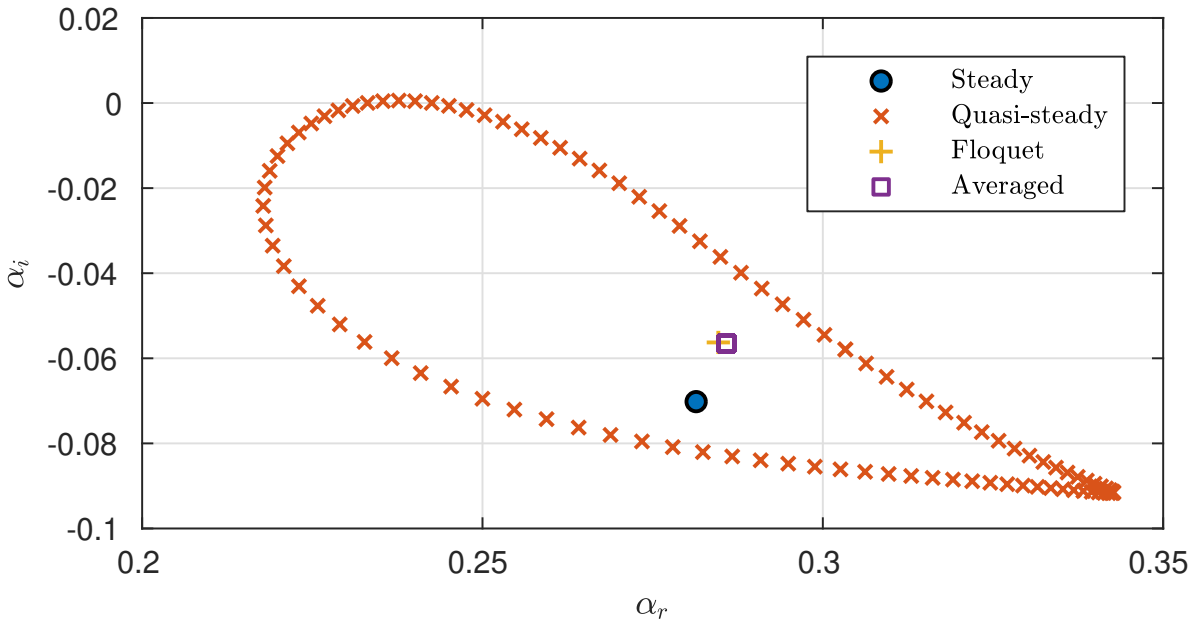

Figure 3.10: Temporal evolution of α across a period of modulation in the Argand plane for stationary disturbances with $R = 500$, $n = 32$, $U_w = 0.2$ and $\varphi = 10$. The temporally periodic quantity μ is shown as ($\times$) along with the Floquet (+), steady (o) and period-averaged ($\square$) eigenvalues.

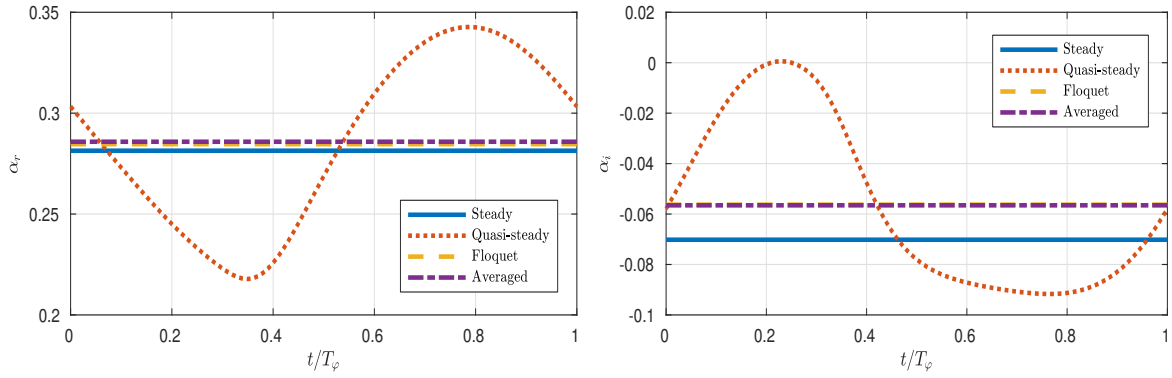

(a) α_r (b) α_i

Figure 3.11: Evolution of spatial eigenvalue α across a period of modulation for stationary disturbances with $R = 500$, $n = 32$, $U_w = 0.2$ and $\varphi = 10$. The temporally periodic quantities $\Re(\alpha)$ and $\Im(\alpha)$ are shown as ($\cdots$) along with the Floquet (- - -), steady (—) and period-averaged (o —) eigenvalues.

3.3 Energy Analysis

This section will explore an energy balance approach which will enable the assessment of the relative influences of the various energy transfer mechanisms affecting the stability properties of the disturbances. Similar approaches have been used by several authors in previous studies, with Cooper and Carpenter [19] intending to measure how the introduction of wall compliance modified the energy balance and Cooper et al. [21], Garrett et al. [36] investigating radially iso- and anisotropic surface roughness. The aim of the forthcoming section will be to conduct a similar analysis, and following these previous studies, we begin by deriving an integral energy equation to analyse the fundamental physical mechanisms behind the apparent stabilising effects of periodic modulation on the stability of the boundary layer.

The energy equation is obtained by multiplying the velocity transport equations by u_r, u_θ and w respectively, and subsequently summing to give an equation for the kinetic energy, $K := \frac{1}{2}\left(u_r^2 + u_\theta^2 + w^2\right)$ given by

$$\begin{aligned}\left[\frac{\partial K}{\partial t} + U\frac{\partial K}{\partial r} + \frac{V}{r}\frac{\partial K}{\partial \theta} + W\frac{\partial K}{\partial z}\right] &= -u_r w U' - u_\theta w V' - w^2 W' - u_r^2\frac{\partial U}{\partial r} - \frac{U u_\theta^2}{r} \\ &\quad - \left[\frac{\partial}{\partial r}(u_r p) + \frac{1}{r}\frac{\partial}{\partial r}(u_\theta p) + \frac{\partial}{\partial z}(wp) + \frac{u_r p}{r}\right] \\ &\quad + \left[\frac{\partial}{\partial x_i}(u_j \sigma_{ij}) - \sigma ij\frac{\partial u_j}{\partial x_i}\right] + \mathcal{O}\left(\frac{1}{R^2}\right)\end{aligned}$$

where $j \in \{r, \theta, z\}$, the $'$ signifies $\frac{\partial}{\partial z}$, repeated indices represent summation and σ_{ij} is an anti-symmetric tensor representing the viscous stress terms, namely

$$\sigma_{ij} = \frac{1}{R}\left(\frac{\partial u_i}{\partial x_j} - \frac{\partial u_j}{\partial x_i}\right) \tag{3.25}$$

We have neglected the $\mathcal{O}\left(\frac{1}{R^2}\right)$ for consistency with the eigenvalue analysis, and can further simplify the equations by averaging over a single azimuthal mode number n, thus removing the $\frac{\partial}{\partial \theta}$ terms, while clearly by definition, $\sigma_{ii} = 0$. Collecting some $\frac{\partial}{\partial r}$ terms on the left

hand side and integrating across the boundary layer gives

$$\int_0^\infty \left[\frac{\partial \overline{K}}{\partial t} + \underbrace{U\frac{\partial \overline{K}}{\partial r}}_{\text{A}} + \underbrace{\frac{\partial}{\partial r}(\overline{u_r p})}_{\text{B}} - \underbrace{\frac{\partial}{\partial r}(\overline{u_\theta \sigma_{12}} - \overline{w\sigma_{13}})}_{\text{C}}\right] dz$$

$$= \int_0^\infty \left(-\overline{u_r w U'} - \overline{u_\theta w V'} - \overline{w^2 W'}\right) dz \qquad \text{(I)}$$

$$- \int_0^\infty \left(\overline{\sigma_{12}\frac{\partial u_\theta}{\partial r}} + \overline{\sigma_{13}\frac{\partial w}{\partial r}} + \overline{\sigma_{31}\frac{\partial u_r}{\partial z}} + \overline{\sigma_{32}\frac{\partial u_\theta}{\partial z}}\right) \qquad \text{(II)}$$

$$- \int_0^\infty \left(\frac{\overline{u_r p}}{r}\right) dz + (wp)_w \qquad \text{(III)}$$

$$- \left(u_r\sigma_{31} + u_\theta\sigma_{32}\right)_w \qquad \text{(IV)}$$

$$- \int_0^\infty \left(W\frac{\partial \overline{K}}{\partial z} + \frac{\partial U}{\partial r}\overline{u_r^2} + \frac{U}{r}\overline{u_\theta^2}\right) dz \qquad \text{(V)}$$

where the subscript $_w$ denotes a variable evaluated at the wall, $z = 0$ and $\overline{ab} = ab^* + a^*b$ a quantity averaged across a perturbation period. The terms in the energy equation are calculated using the eigenvalues and eigenfunctions from the dispersion relation (3.13) given R, n and ω, while the pressure is obtained from the primary and secondary variables via the relation

$$p = \int_z^\infty \left[\frac{\partial w}{\partial t} + \frac{i\alpha}{R}Fw + \frac{1}{R}\left(i\alpha\xi_\theta + \frac{1}{R}\xi_\theta\right)\right] dz + \frac{1}{R}Hw \qquad (3.27)$$

as in Davies and Carpenter [26].

As described in Cooper et al. [21], each term has a physical interpretation in terms of its contributions to the energy of the system. On the left hand side, the term (A) gives the average kinetic energy convected by the radial mean flow, while (B) gives the work done by the perturbation pressure. (C) denotes the work done by viscous stresses across some internal boundary in the fluid and for the majority of results presented below is negligible in comparison to the others. On the right hand side we have the Reynolds stress energy production term (I), the viscous dissipation energy removal term (II), pressure work terms (III) contributions from work done on the wall by viscous stresses (IV) and terms arising from streamline curvature effects and the three-dimensionality of the mean flow (V). The energy balance may be carried out for any eigenmode, and positive terms may be identified with energy production while negative ones remove energy from the system. A mode is amplified, giving $\alpha_i < 0$ in a spatial analysis, when energy production outweighs the energy dissipation in the system. Calculation of each term in the energy equation allows for the identification of where the effects of the modulation are the greatest.

The following section will provide an analysis of the steady case, and produce results analogous to those in Cooper et al. [21] for validation purposes. Following this analysis, we describe the process applied to the modulated scenario and detail the modifications to the energy balance found therein.

3.3.1 Energy Balance for the Steady Rotating Disk Boundary Layer

In the steady case, we are able to further eliminate the $\frac{\partial}{\partial t}$ terms by averaging across a single perturbation period and as in Cooper et al. [21], we normalise the energy equation by the integrated mechanical energy flux which contributes the left hand side. Applying the same nomenclature for each term as Cooper et al. [21], we write

$$-2\alpha_i = \underbrace{(P_1 + P_2 + P_3)}_{\text{(I)}} + \underbrace{D}_{\text{(II)}} + \underbrace{(PW_1 + PW_2)}_{\text{(III)}} + \underbrace{(S_1 + S_2 + S_3)}_{\text{(IV)}} + \underbrace{(G_1 + G_2 + G_3)}_{\text{(V)}} \tag{3.28}$$

The energy balance may be carried out for any eigenvalue α, and figures 3.12 and 3.13 are given for validation against similar figures in Cooper et al. [21], showing variation in the Type I and II energy production and viscous dissipation terms, P_2 and $-D$, with azimuthal mode number n for stationary disturbances with $R = 400$. In all cases tested, the energy functions as calculated by our novel numerical methods described throughout this thesis agree well with those in the literature of Cooper et al. [21] and Garrett et al. [36].

Figure 3.14 shows that the energy balance in the system is essentially between the two terms detailed in figures 3.12 and 3.13, with the rest of the terms in (3.28) contributing negligibly to the overall balance. The terms that are not shown, namely S_1, S_2, S_3 and PW_2, are identically zero in this situation due to the boundary conditions. The following section will analyse whether this balance remains the case in the modulated scenario, and give an overview of the modifications to the energy terms when the modulation is added.

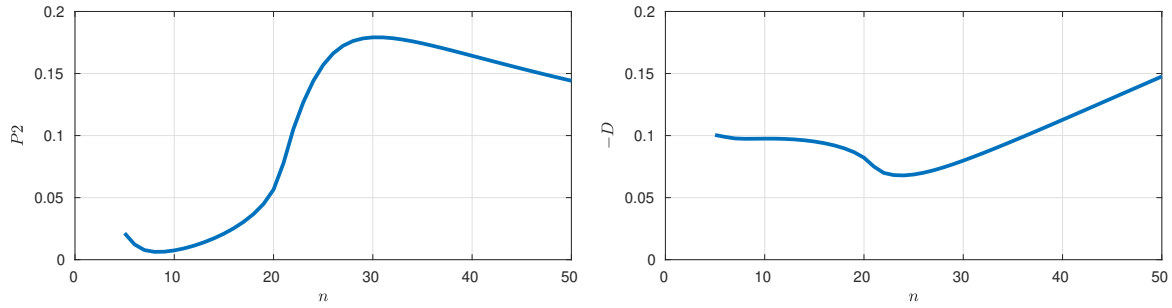

(a) $P2$ (b) $-D$

Figure 3.12: Variation in the Type I energy production and viscous dissipation terms P_2 and $-D$ with azimuthal mode number n for stationary disturbances with $R = 400$. A clear peak in energy production can be seen around $n \approx 28$, consistent with the location of maximum disturbance amplification described in Cooper et al. [21].

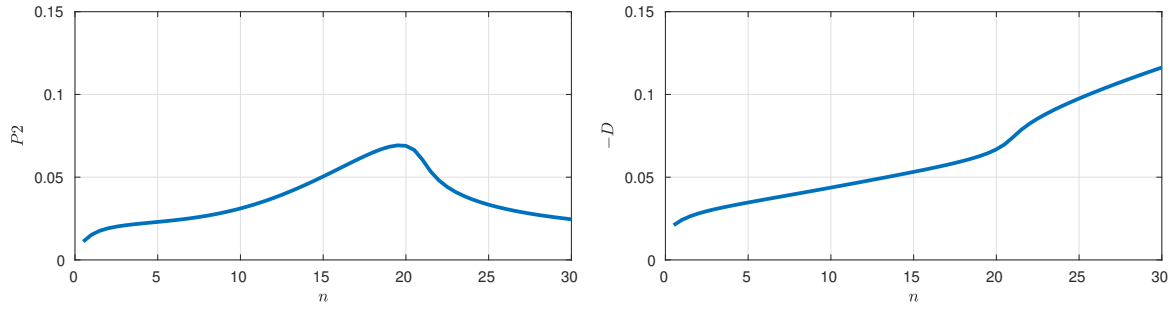

(a) Energy production term $P2$ (b) Viscous dissipation term $-D$

Figure 3.13: Variation in the Type II energy production and viscous dissipation terms P_2 and $-D$ with azimuthal mode number n for stationary disturbances with $R = 400$. A clear peak in energy production can be seen around $n \approx 19$, consistent with the location of maximum disturbance amplification described in Cooper et al. [21].

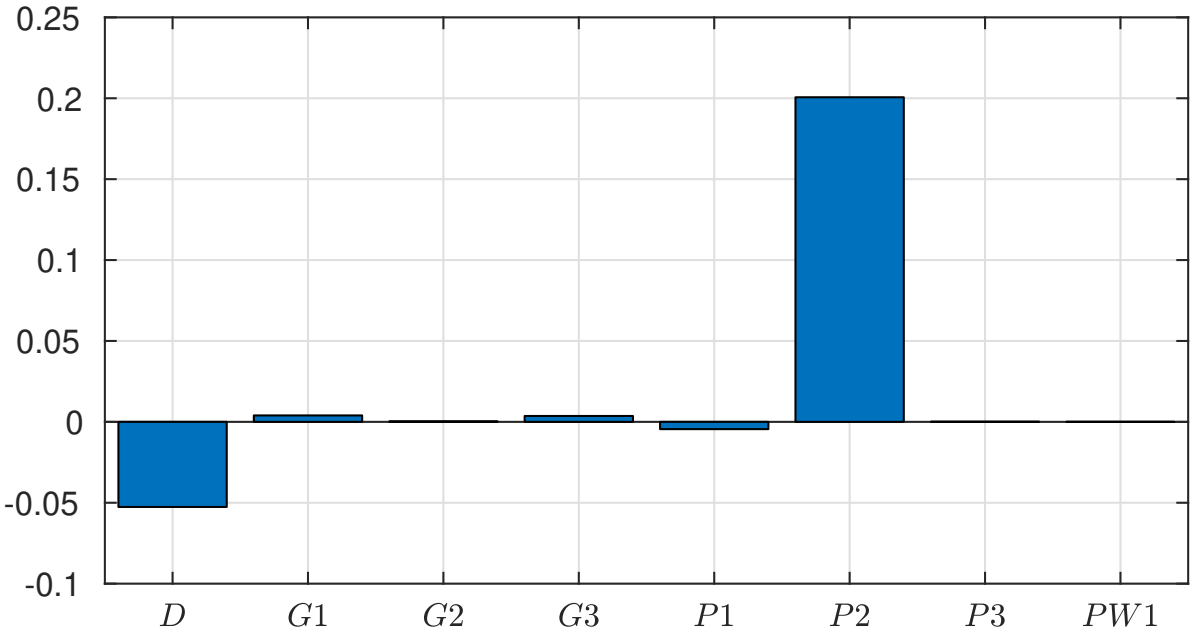

Figure 3.14: Balance of terms in the energy analysis for stationary disturbances with $R = 500$ and $n = 32$ in the steady rotating disk boundary layer. This figure shows that the balance is essentially between the energy production term $P2$ and the viscous dissipation term $-D$, consistent with that found in Cooper et al. [21]. The other terms contribute negligibly to the system.

3.3.2 Energy Balance for the Rotating Disk Boundary Layer with a Periodically Modulated Rotation Rate

The modulated rotation rate comes into the system by way of a temporally periodic modification of the disk rotation rate, as described by equation (2.3) and in detail throughout this thesis. Therefore, with the full time-dependent structure of the modulated rotation rate incorporated, we are no longer able to eliminate the $\frac{\partial}{\partial t}$ terms as we did for the steady case, and thus may only write

$$-2\alpha_i(t) = -\frac{\partial K}{\partial t} + \underbrace{(P_1+P_2+P_3)(t)}_{\text{(I)}} + \underbrace{D(t)}_{\text{(II)}} + \underbrace{(PW_1+PW_2)(t)}_{\text{(III)}} + \underbrace{(S_1+S_2+S_3)(t)}_{\text{(IV)}} + \underbrace{(G_1+G_2+G_3)(t)}_{\text{(V)}} \quad (3.29)$$

where each variable, including the mechanical energy flux by which the equations are normalised, is time-dependent and in particular periodic with the same period as the modulation. We will deal with this in a similar fashion to that of section 3.2, where we effectively freeze the flow at each time-step and march through the period as if t were a parameter. This allows us to get an idea of how the energy changes across a period of modulation, and provides insight into how the modulation affects the balance in the system. Since the energy terms in (3.29) are periodic with the period of the modulation, which we will denote $T_\varphi = \frac{t\varphi}{2\pi R}$ here, we may average the variation across T_φ to give an appropriate quantity to be compared against the steady case.

Figure 3.15 shows the evolution of the temporal growth rate α_i for $R = 500$, $n = 32$, $U_w = 0.2$ and $\varphi = 10$ across two periods of modulation T_φ, along with the quantity $\frac{-1}{T_\varphi}\int_0^{T_\varphi} \alpha_i$ averaged across the modulation period. The stabilisation, as should be expected for this parameter set by the analyses of section 3.1, is clear by the reduction in magnitude of $-\alpha_i$ by the modulation. Figure 3.16 shows the evolution of the energy production and viscous dissipation terms, P_2 and $-D$, across a period of the flow modulation for the same parameter set, along with the quantities $\frac{1}{T_\varphi}\int_0^{T_\varphi} P$ and $\frac{-1}{T_\varphi}\int_0^{T_\varphi} D$ averaged across the modulation period. Clearly, the averaged energy production term is smaller than the steady equivalent and likewise the averaged dissipation term is larger than its steady counterpart. This is similar to results given by Cooper and Carpenter [19], Cooper et al. [21] and Garrett et al. [36] when studying wall compliance and surface roughness and alludes to potentials for further analysis of the exact mechanisms for this via a care-

ful study of the contributions to each term. Figure 3.17 shows the full energy balance for this parameter set, comparing the modulated scenario against the steady case, and demonstrates that the main contributions to the system are still the energy production and viscous dissipation terms when modulation is added. The other terms contribute negligibly to the system, as in the steady case.

While this discussion does not give a robust explanation of the stabilising behaviour, it may be utilised to pinpoint the important terms in the equations which contribute to it. A more thorough examination of the energy production and viscous dissipation terms could be used to shed light on the exact mechanism for the stabilisation, but such an analysis is reserved for future work.

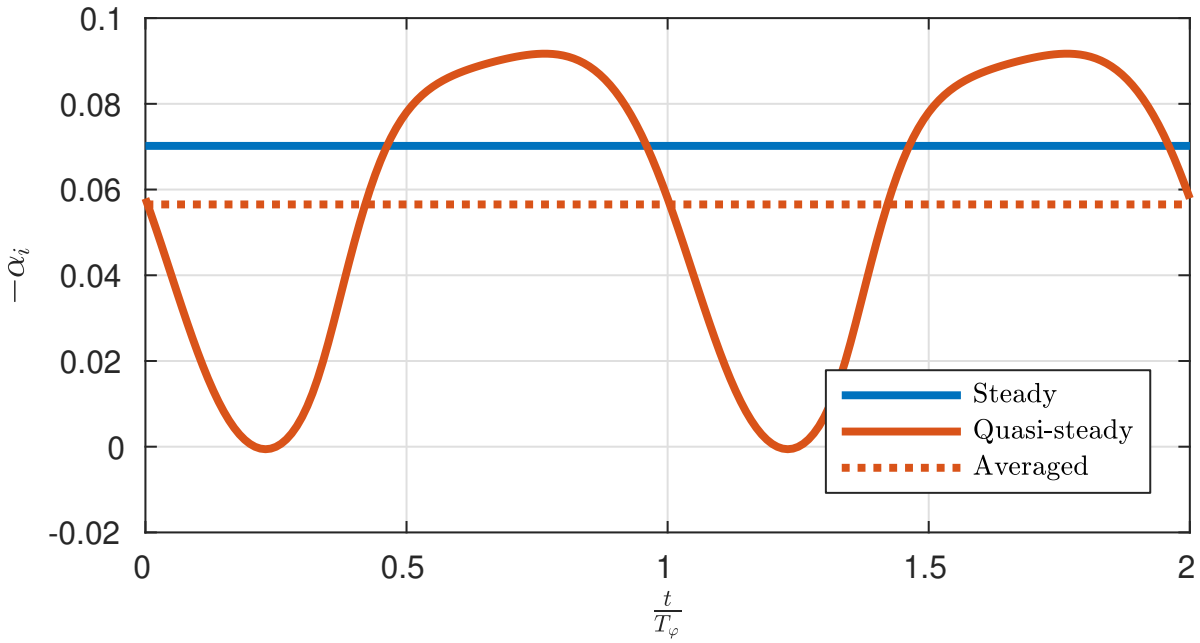

Figure 3.15: Variation in the spatial growth rate $-\alpha_i$ across a period for stationary disturbances with with $R = 500$, $n = 32$, $U_w = 0.2$ and $\varphi = 10$ (—), compared with the steady case ($\cdots$) and quantity $\frac{-1}{T_\varphi}\int_0^{T_\varphi} \alpha_i$ (- - -) averaged across the modulation period T_φ.

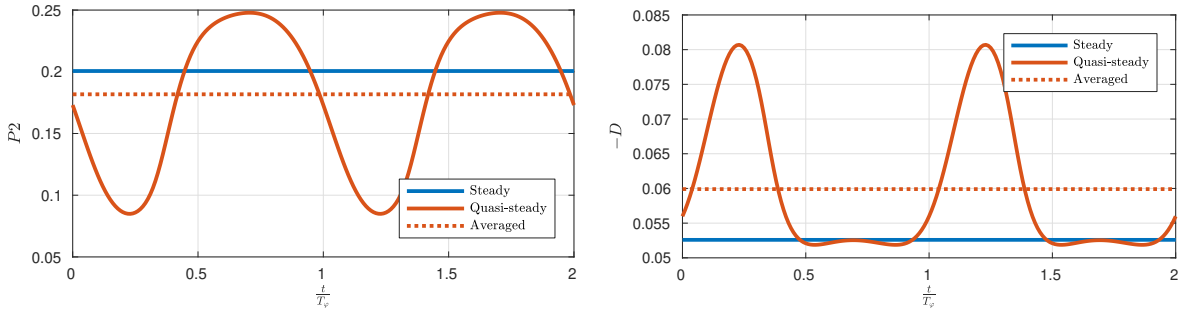

(a) Energy production term $P2$ (b) Viscous dissipation term $-D$

Figure 3.16: Variation in the energy production and viscous dissipation terms P_2 and $-D$ across a period for stationary disturbances with with $R = 500$, $n = 32$, $U_w = 0.2$ and $\varphi = 10$ (—), compared with the steady case (- - -) and quantities $\frac{1}{T_\varphi}\int_0^{T_\varphi} P$ and $\frac{-1}{T_\varphi}\int_0^{T_\varphi} D$ ($\cdots$) averaged across the modulation period T_φ.

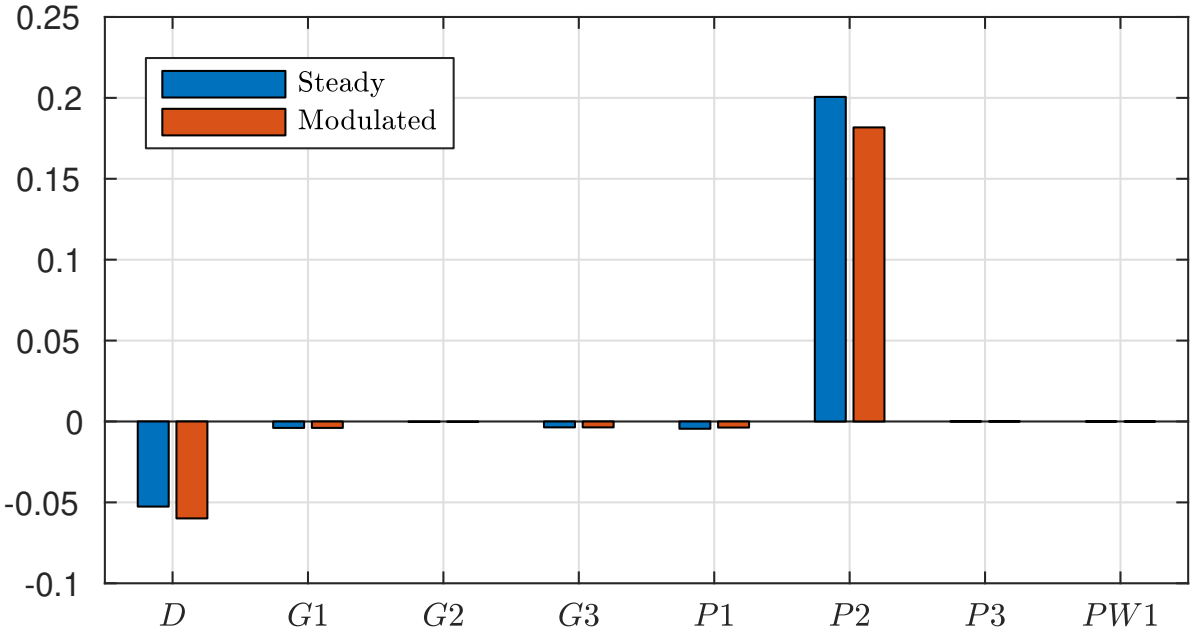

Figure 3.17: Balance of terms in the energy analysis for stationary disturbances with $R = 500$ and $n = 32$. The steady case is compared against the modulated scenario with $U_w = 0.2$ and $\varphi = 10$. This figure shows the reduction in the energy production term $P2$ and expansion in the viscous dissipation term D produced by the modulation and that the balance is still essentially between these terms, as for the steady case. The other terms contribute negligibly to the system.

3.4 Monochromatic Direct Numerical Simulations

The following section describes a further method of analysis which we will use for validation against the Floquet theory and to provide an alternative approach to calculating temporal growth rates. A similar idea was discussed in section 2.2.4 when considering the steady rotating disk boundary layer. This will be the analysis of monochromatic disturbances, and the solution method is essentially identical to that described in section 2.2.4. The primary difference is the fact that the base flow is now time-dependent, and therefore updated at each time-step in the calculation. As in section 2.2.4, we apply a temporally impulsive, but not radially localised, disturbance of the form

$$\eta(\theta, t) = b(t)e^{i\beta R\theta} \tag{3.30}$$

where b defines the time-dependent amplitude, given by

$$b(t) = (1 - e^{-\sigma t^2})e^{-\sigma t^2} \tag{3.31}$$

The first term of b acts as a continuous Heaviside function to scale the forcing up from zero and σ is a parameter which dictates the timescale over which this takes place. We decompose the perturbation quantities as

$$\mathbf{u} = \hat{\mathbf{u}}(z, t)e^{i(\alpha r + \beta R\theta)}, \quad \xi = \hat{\xi}(z, t)e^{i(\alpha r + \beta R\theta)} \tag{3.32}$$

which gives the system

$$\frac{\partial \xi_r}{\partial t} + i\beta N_z - \frac{\partial N_\theta}{\partial z} - \frac{2}{R}(\xi_\theta + i\alpha w) = \frac{1}{R}\left[\left(\hat{\nabla}^2 - \frac{1}{r^2}\right)\xi_r - \frac{2i\beta}{R}\xi_\theta\right] \tag{3.33a}$$

$$\frac{\partial \xi_\theta}{\partial t} + \frac{\partial N_r}{\partial z} - \frac{\partial N_z}{\partial r} + \frac{2}{R}(\xi_r - i\beta w) = \frac{1}{R}\left[\left(\hat{\nabla}^2 - \frac{1}{r^2}\right)\xi_\theta + \frac{2i\beta}{R}\xi_r\right] \tag{3.33b}$$

$$\hat{\nabla}^2 w = \frac{1}{r}\left(\frac{\partial \xi_r}{\partial \theta} - \frac{\partial (r\xi_\theta)}{\partial r}\right) \tag{3.33c}$$

with

$$\hat{\nabla}^2 = -\alpha^2 + \frac{i\alpha}{R} - \beta^2 + \frac{\partial^2}{\partial z^2} \tag{3.34}$$

where the convective quantities $\mathbf{N}$, given by (2.51), are time-dependent in line with the time-dependent base flow $\mathbf{U}_B$. We solve the system using the identical predictor-corrector scheme described in section 2.2.4.

3.4.1 Results and Comparison with Floquet Analysis

In order to obtain results which are comparable to the Floquet Analysis of section 3.1, we must invoke a similar normal mode hypothesis and assume we can write a perturbation variable f as

$$f(r,\theta,z,\tau) = \hat{f}(z,\tau)e^{\mu\tau}e^{i(\alpha r+\beta R\theta)} \tag{3.35}$$

where $\hat{f}(z,\tau)$ is a time-periodic function with the same period as that of the modulation and all exponential growth of $\hat{f}(z,\tau)$ is incorporated into the Floquet exponent $e^{\mu\tau}$. Thus, following similar ideas in Thomas et al. [76], we can calculate the dominant eigenvalue μ directly from the simulation data by

$$\mu \approx \frac{1}{T}\log\left(\frac{\hat{p}(z=0,\tau_0+T)}{\hat{p}(z=0,\tau_0)}\right) \tag{3.36}$$

for some starting value τ_0. With this operation, we are effectively calculating numerically estimated asymptotic values, for large τ, and implicitly assuming that there is a most unstable mode that dominates the behaviour. The growth rates calculated via this method may then be identified with the temporal Floquet eigenvalues discussed in section 3.1.2, thereby adding confidence to the reliability of the results presented in that section.

As for previous sections, the following results are shown for $R = 500$ and $n = 32$ so that an instability would exist in the corresponding steady scenario. Figure 3.18 shows the temporal development of $\xi_\theta(z=0)$, excited by an impulsive forcing of the form (2.62) for typical parameters $\alpha = 0.3$, $U_w = 0.2$ and $\varphi = 10$, compared against the steady, $U_w = 0$, case with the same parameters. The reduction in the growth rate for this parameter set is such that we have used the natural logarithm of the absolute value of the disturbance wavetrain to illustrate the stabilisation. A clear dampening effect can be seen in the modulated case, as would be expected by the corresponding reduction in growth rate as calculated by the Floquet analysis.

Figure 3.19 shows the temporal growth rates for a range of φ, together with a comparison of the results against those of the Floquet analysis. This diagram clearly shows the temporal stabilisation achieved by adding the modulation, and its increasing effect for $\phi \approx 10$. The agreement between the two distinct methods of growth rate calculation is apparent, with the very slight discrepancy attributed to the inevitable errors that are involved in estimating asymptotic values using results obtained for a finite simulation length.

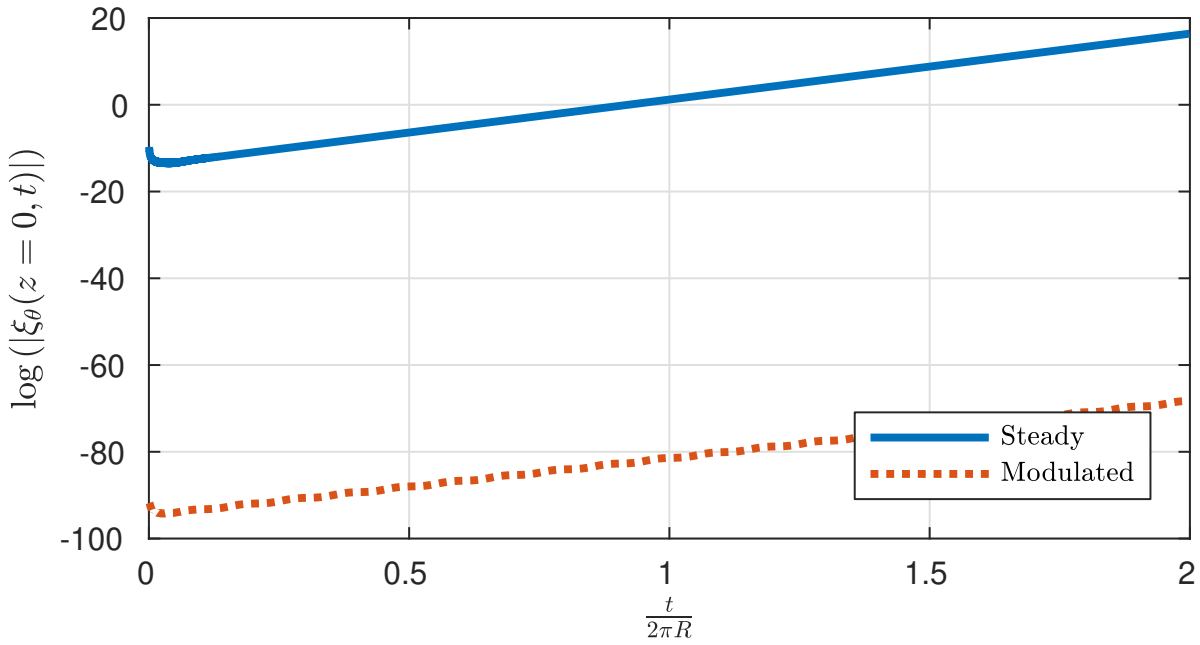

Figure 3.18: Log plot of the temporal response to impulsive disturbance of $\xi_\theta(z = 0)$ for $\alpha = 0.3$, $U_w = 0.2$ and $\varphi = 10$ (- - -), together with the corresponding solutions for the steady case (—). A clear reduction in the temporal growth rate is visible for the modulated case.

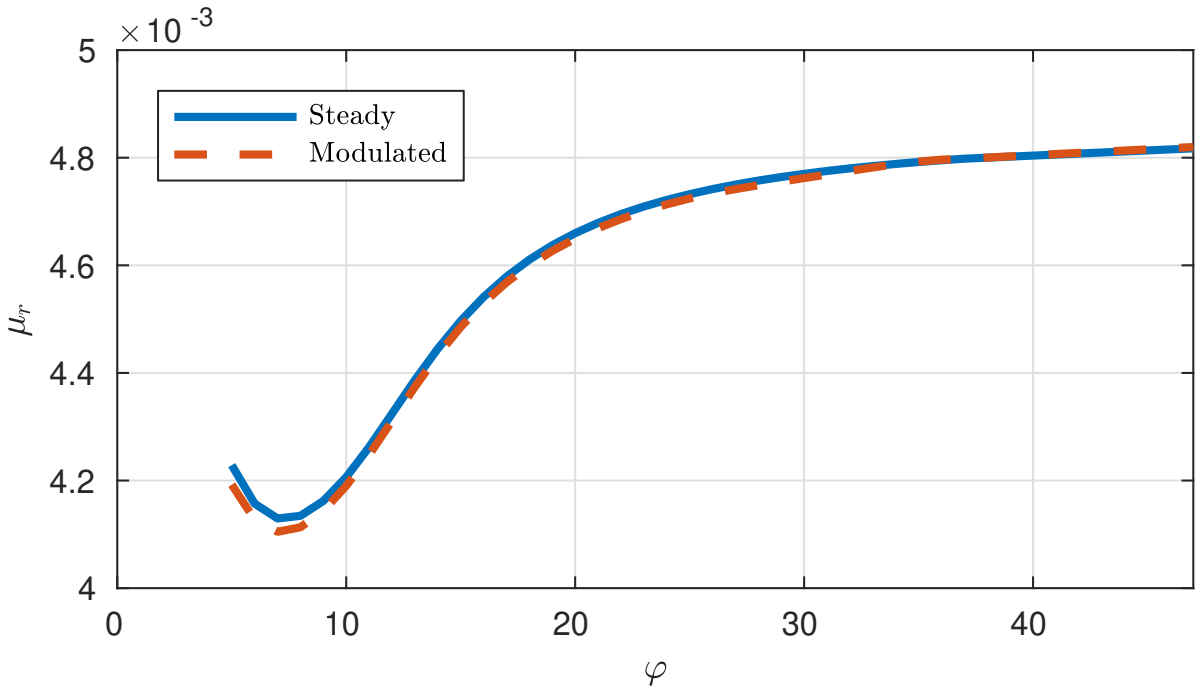

Figure 3.19: Temporal growth rates μ_r for $\alpha = 0.3$, $U_w = 0.2$ and varying φ. Comparison shown between monochromatic simulations (- - -) and Floquet analysis (—)

3.5 Direct Numerical Simulations of Stationary Forcing with a Radial Dependence

Similarly to the analysis of the equivalent forcing method for the steady case presented in section 2.2.5, we may incorporate a radial dependence into our simulations and include the full r-derivatives of the perturbation variables. This analysis will provide independent validation of the spatial Floquet analysis conducted in section 3.1 and lend confidence to the methods presented there. Concentrating our exposition on stationary forcing as in section 3.1, we look to excite disturbances in the flow by prescribing radially localised motion around some location r_e of the form

$$\zeta(r, \theta, \tau) = a(r - r_e)b(\tau)e^{in\theta} \tag{3.37}$$

for some azimuthal mode number n. We can pin down the radial variation of the forcing by employing the parallel-flow approximation and choose

$$a(r) = e^{-\lambda r^2} \tag{3.38}$$

to give a localised Gaussian pulse, where λ specifies the radial extent of the forcing. The time-dependent amplitude may be chosen so as to give a time-periodic excitation, for instance by setting

$$b(\tau) = h(\tau)e^{-i\omega_0 t} \tag{3.39}$$

here ω_0 is a prescribed temporal frequency and $h(\tau) = (1 - e^{-\sigma\tau})$ acts like a continuous Heaviside function to scale the forcing up from zero. In the steady case, disturbances which are stationary with respect to the surface can be considered by setting ω_0 equal to zero. There is a concern that since the modulation is time-dependent, this naïve approach could potentially introduce modes at different frequencies, thereby giving spurious results. However, after thorough validation, the subsequent evolution transpired to be independent of the form of stationary forcing employed, and rigorous checks were carried out to ensure the frequency of forcing introduced was consistent with that of a stationary disturbance analogous to the steady case.

3.5.1 Results and Comparison against Floquet Analysis

The general idea behind the solution method described in section 2.2.5 is preserved here, with the modification introduced by the modulation incorporated by simply altering the

mean flow at each time-step. This is achieved in practise by solving equations (2.10) in tandem with the time-marching procedure of the DNS and using the resulting mean flow when calculating the convective terms (2.38). Computational efficiency can be enhanced by utilising the periodicity of the mean flow and only computing the mean flow profiles once over a modulation period, then replicating these values throughout the simulation. For the majority of the results presented in this section, the primary variables may be fully resolved using a Chebyshev expansion involving $N = 64$ polynomials and a radial resolution of about $\Delta r \approx 1$. Each of the following simulation plots was produced using $N = 64$ and a radial resolution of $\Delta r = 1.25$. In all of the simulations, the computational domain extends well beyond the limits suggested by the figures in order to ensure no computational edge effects creep into affect the results. The temporal discretisation is such that there are no less than 100 time-steps in one period of modulation. For small $\varphi \lesssim 15$, it was necessary to use up to 1000 time-steps per modulation period to fully resolve the disturbance quantities under consideration. No formal mathematical analysis of the exact number required was undertaken during this work, and convergence was determined empirically from comparisons between differing values of temporal discretisation.

The following figures show the radial evolution of a disturbance generated by stationary forcing for $R = 500$ and $n = 32$. These parameter choices ensure that the steady disk configuration is unstable, and similarly to previous sections, provide us with a base to compare modulation effects against. The position of maximum forcing is located at $r = R = 500$, again somewhat arbitrary since the parallel flow approximation treats all radial locations as equivalent. Similarly to section 2.2.4, the simulations were conducted until a steady growth rate was achieved and all transient behaviour had passed out of the domain of interest so that T_∞ can be identified with

$$\alpha(T_\infty) \approx \lim_{t\to\infty} \left(-\frac{i}{A}\frac{\partial A}{\partial r} \right) \tag{3.40}$$

Typically, T_∞ is chosen to be between two and four periods of disk rotation. Further discussions of the inflow and outflow criteria are given in Thomas [71] and briefly in appendix B.3.1.

Figure 3.20 shows this evolution for $U_w = 0.2$ and $\varphi = 10$ on a log plot showing the differences in the growth rates in each case. These parameters are chosen to give an indication of the type of behaviour observed in the simulations and relatively small amplitude oscillations. An initial inspection would suggest that the modulation heavily

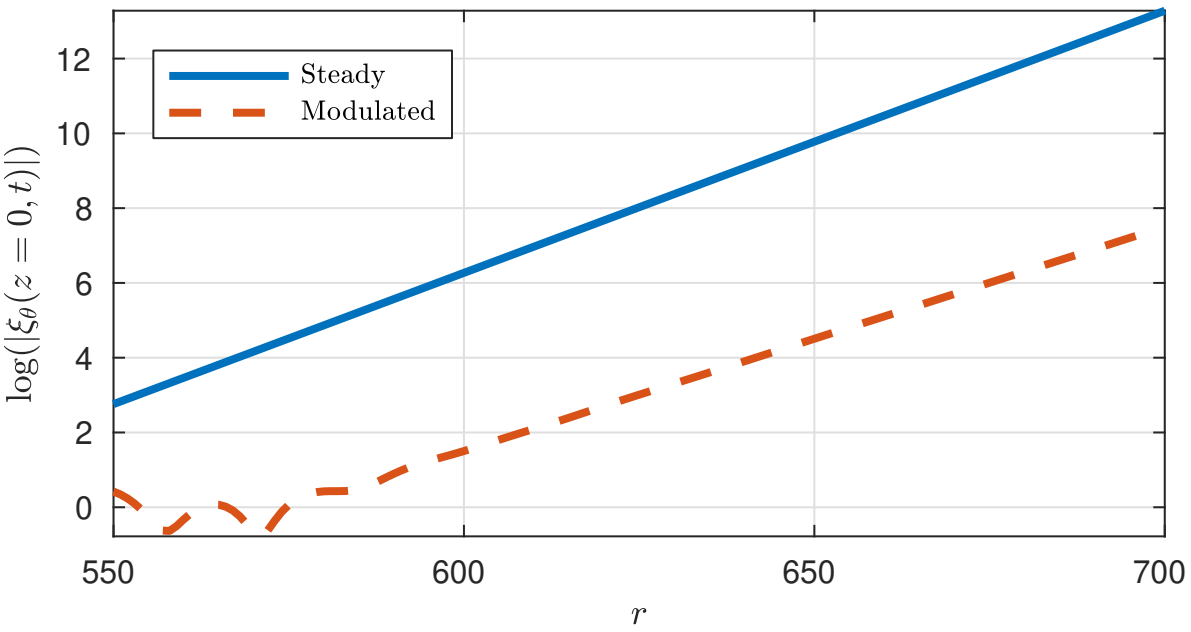

Figure 3.20: Radial evolution of a disturbance generated by stationary forcing for $R = 500$, $n = 32$, $Uw = 0.2$ and $\varphi = 10$. The simulations were conducted until the growth rates has settled to the dominant value where $t \geq T_\infty$.

dampens the radial growth rates of the disturbance, indicating a stabilising effect. This effect may be quantified by calculating, retrospectively, the radial growth rates using the normal mode approximation. As dictated by linear stability theory and the normal mode hypothesis, after a sufficient amount of time and sufficiently far away from the point of maximal forcing, we would expect the radial growth rates to be the same at each radial position and be prescribed by a single wavenumber α which may be calculated directly from the simulation data. If, since we are considering parallel flow in the radial direction, we decompose our perturbation variables as

$$A = \hat{A}(z,t)e^{i(\alpha r + n\theta)}$$

then we can identify the complex wavenumber displayed by the disturbance at a particular radial position and instant of time with

$$\alpha \approx \frac{1}{A}\frac{\partial A}{\partial r} \tag{3.41}$$

In this case, we take A to be $\xi_\theta(z = 0, t > T_\infty)$ for some T_∞ such that the disturbance at fixed r has reached a steady state, provided $\frac{1}{A}\frac{\partial A}{\partial r}$ is found not to vary too rapidly in space. For the purposes of this investigation, we choose to study the azimuthal component of

vorticity at the wall, although other selections could equally be made without adverse effects on the results. For the same parameters as in figure 3.20, figure 3.21 gives the temporal evolution of the wavenumbers α_s and α_m corresponding to the unmodulated and modulated scenarios respectively, and shows a steady growth rate being achieved after around 25 periods of modulation, or 2.5 disk rotations under this non-dimensionalisation. The imaginary parts of the wavenumbers, $\mathfrak{I}(\alpha_s)$ and $\mathfrak{I}(\alpha_m)$ are the quantities of interest here as these give the expressions for the radial growth rates. Clearly we have

$$\mathfrak{I}(\alpha_s) > \mathfrak{I}(\alpha_m) \tag{3.42}$$

which confirms our conclusions of stabilisation from figure 3.20.

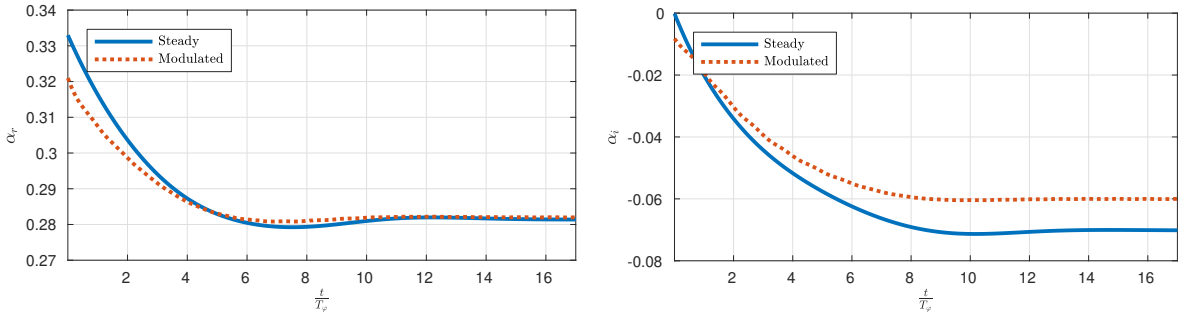

(a) α_r (b) α_i

Figure 3.21: Temporal evolution of real and imaginary parts of $\frac{1}{A}\frac{\partial A}{\partial r}$ for $R = 500$, $n = 32$, $U_w = 0.2$ and $\varphi = 10$, with comparison between steady (—) and modulated cases (- - -). Stabilisation in terms of growth rate (α_i) reduction is clear.

This apparent stabilisation seems not to be an isolated case in terms of the parameters shown, and figure 3.22 shows a plot of various modulation frequencies φ against the growth rates $\mathfrak{I}(\alpha_m)$ for $R = 500$ and $n = 32$, with $U_w \in \{0.1, 0.2\}$. Validation of these results is provided by calculation of α from the Floquet dispersion relation (3.13) while specifying $\mu = 0$. The results of these calculations are also shown in figure 3.22 which agree well with the simulation data. The agreement between the two distinct methods of growth rate calculation is apparent, with any discernible discrepancy attributed to the inevitable errors that are involved in estimating asymptotic values using results obtained for a finite simulation length. For values of $\varphi \lesssim 6$, the computational time required for the growth rates to settle to a constant, namely T_∞, increased greatly. For very small values of φ it was not possible to fully resolve the growth rates using the simulations to the required

accuracy in a reasonable time-frame. It is, as yet, unclear to the author whether there is a physical process preventing the settling of these quantities for such values of φ or whether the phenomenon is numerical. Such an analysis is beyond the scope of this project and is thus reserved for future work.

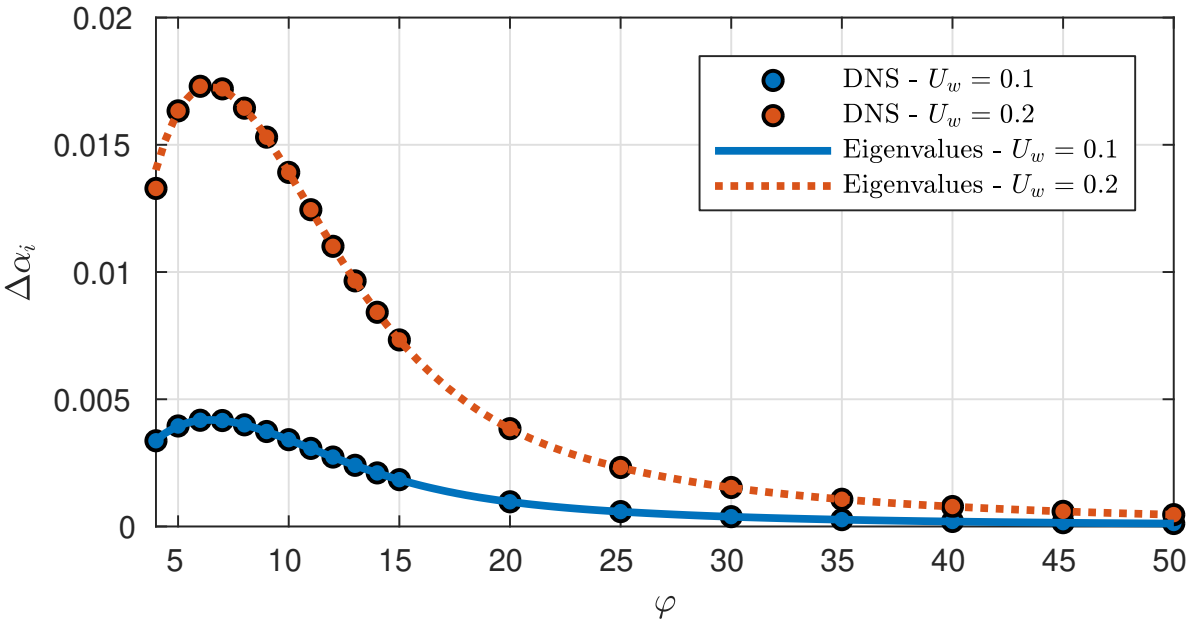

Figure 3.22: Variation of $\Im(\alpha_m)$ with φ, for $R = 500$ and $n = 32$. Data from the Floquet dispersion relation for $U_w = 0.1$ (—) and $U_w = 0.2$ ($\cdots$) is compared against growth rates calculated from the simulations ($\circ$). Values of $\varphi \leq 3$ are intentionally omitted due to the restrictive computational time required for t to pass T_∞ in these cases.

3.6 Discussion

Throughout the preceding sections, we have detailed four distinct approaches to calculating the linear stability properties of a rotating disk boundary layer with a modulated rotation rate. The approaches have involved an application of Floquet theory in the temporal and spatial settings along with quasi-steady frozen profile analyses, monochromatic direct numerical simulations to calculate temporal growth rates and simulations with a radial dependence capable of calculating spatial growth rates. Consistency in the results between each method has been demonstrated in all cases, lending strength to the confidence in our approaches. Each method constitutes an essentially alternative way of presenting the same result, and have been illustrated to give validation to the others. Each

approach also presents both advantages and disadvantages in terms of computational cost and mathematical rigour and the choice of solution method in any future study should depend on the parameter set in question.

The main result of this chapter is to have demonstrated that the addition of a modulated rotation rate stabilises the boundary layer formed above a rotating disk to disturbances which have a fixed temporal frequency and spatial wavenumber. In particular, we demonstrated that the spatial growth rates may be reduced when modulation is incorporated for disturbances which are stationary with respect to the motion of the disk surface. This stabilisation has been shown for isolated parameter cases in the sense of the Reynolds number and azimuthal mode number and across a range of parameters in the sense of critical values for instability onset. Several results were presented which demonstrated fairly strong stabilising behaviour for even small amplitude modulations. There is also an indication of a somewhat *optimal region* of the non-dimensional frequency term φ where the strongest stabilisation is present.

The underlying physical mechanisms for such behaviour are as yet unclear, although an analysis of the energy balance of the disturbance was described in an attempt to illustrate the finer details of the stabilising behaviour shown by the addition of the modulation. Certain terms in the energy balance equations were identified as being dominant, and comparisons were made against similar studies by Cooper et al. [21] and Garrett et al. [36] during their investigations of surface roughness and by Cooper and Carpenter [19] during their investigations of wall compliance. Similar behaviour to these alternative stabilising mechanisms was identified for the periodically modulated boundary layer, indicating the potential for parallels between each configuration and the requirement for a substantial future study to ascertain the exact nature of the stabilisation.

Chapter 4

Global Behaviour and Absolute Instabilities in Periodically Modulated Rotating Disk Boundary Layers

Chapters 1, 2 and 3 have thus far only considered the analysis of locally defined dispersion relations and results from radially simplified direct numerical simulations. These give only limited insight into the true behaviour exhibited by the rotating disk boundary layer and in reality, rotating flows can exhibit rich, complex disturbance structures including absolute instability and turbulence. Heretofore, we have, in all cases, described disturbance properties from the standpoint of either a temporal analysis or a spatial one. Genuine behaviour, however, develops both spatially and temporally and some sense may be made of this by considering the spatio-temporal analysis that was briefly discussed in section 2.2.3. This may be studied by an analysis of the flow response to a radially localised impulsive forcing, as will be performed in this chapter.

During our discussions in section 2.2.3, we remarked on an analysis conducted by Lingwood [43] which appeared to show the existence of a local absolute instability in the rotating disk boundary layer. Lingwood's [43] analysis utilises the so-called parallel flow approximation which amounts to neglecting the radial dependence of the basic state, with which it is useful to refamiliarise ourselves with at this stage. Section 2.1.5 first introduced

the concept of this homogenising technique, where we defined the base velocity field as

$$\mathbf{U}(r,z) = \left(\frac{r}{R}F(z), \frac{r}{R}G(z), \frac{1}{R}H(z)\right) \tag{4.1}$$

with F, G and H being the solutions to the Kármán ODEs given by equation 2.12. The parallel flow approximation amounts in this case, as discussed in more detail in section 2.1.5, to the replacement of r by R in the equations, thereby allowing the radial evolution of the perturbation to be separable into normal mode form. Using this approximation, Lingwood [43] demonstrates the existence of the absolute instability using Brigg's criterion. While we will not reproduce the analytical methods used in this study, we will present numerical simulation results for the steady rotating disk configuration which are consistent with Lingwood's [43] and were first discussed in Davies and Carpenter [26]. These results, outlined in the first part of this chapter, utilise the same parallel flow approximation as in Lingwood [43] and thereby allow for the homogenisation of the radial direction. As background to the study we first present the steady case before discussing the modifications to the behaviour introduced by the periodic modulation.

The removal of the parallel flow approximation and thereby the radial homogenisation was first studied by Davies and Carpenter [27] who discovered that the locally defined absolute instability described in Lingwood [43] does not trigger a linearly unstable global mode and convective behaviour dominates at all radii and azimuthal mode numbers, at least within the ranges discussed in Lingwood [43]. A further explanation of the subtleties involved in this approximation and the current state of research in this area is provided later in section 4.3 where simulation results are given to illustrate the behaviour. We discuss the steady inhomogeneous configuration as an introduction to the presentation of the results pertaining to the modulated rotation rate.

4.1 Radially Homogeneous Steady Case

For completeness, and in an attempt to provide a base from which to elaborate, we detail several important results regarding the stability of the steady rotating disk boundary layer, and will use these to illustrate the local absolute instability which is present in this configuration. Similarly to section 2.2.5, we excite the impulsive disturbance by means of prescribed wall motion which takes the form

$$\eta(r,\theta,t) = a(r-r_e)b(t)e^{in\theta} \tag{4.2}$$

where a describes the radial variation centred at the location r_e and the function b defines the time-dependent amplitude. Since the simulations of this section are radially homogeneous, the forcing location is somewhat arbitrary since it is the Reynolds number which dictates the behaviour. The notation r_e is retained however, to allow for direct comparisons between the homogeneous and inhomogeneous simulations conducted in section 4.3. The radial distributions of the impulsive disturbance (4.2) take the form

$$a(r) = e^{-\lambda r^2}$$

and the impulsive excitation for b takes the form

$$b(t) = (1 - e^{-\sigma t^2})e^{-\sigma t^2}$$

where σ is a parameter chosen such that $\frac{1}{\sqrt{\sigma}}$ gives the timescale of the forcing up from zero amplitude at $t = 0$.

Davies and Carpenter [26] state that the variation of the primary variables may be fully resolved using a Chebyshev expansion involving $N = 48$ polynomials and a radial resolution of about $\Delta r \approx 1$. Each of the following simulation plots was produced using $N = 48$, a radial resolution of $\Delta r = 1.25$ and a time discretisation of $\Delta t = 0.625$. In all of the simulations, the computational domain extends well beyond the limits suggested by the figures in order to ensure no computational edge effects creep into affect the results.

4.1.1 Convective Instability

Figure 4.1 shows the temporal development of the azimuthal component of the vorticity $\xi_\theta(z = 0, t)$ for a disturbance with azimuthal mode number $n = 32$ triggered by an impulse with Reynolds number $R = 350$. It is clear that the disturbance decays rapidly at $r = r_e$ and subsequently, for $r > r_e$, there is an initial period of inactivity before the disturbance takes hold, followed by a decay as would be expected for this convectively unstable configuration.

The radially localised impulsive forcing is located at $r = R = 500$. The radial position of the forcing is arbitrary in the homogenised flow configuration as it it the Reynolds number which dictates the flow behaviour, and the figure shows the temporal development at four radial locations, namely $r = R$, $r = R + 25$, $r = R + 50$ and $r = R + 100$. The temporal axis is scaled by the disk rotation period $2\pi R$.

Figure 4.2 shows the spatio-temporal contour plots of $|\xi_\theta(z=0,t)|$ for a convectively unstable configuration with $R = 350$ and $n = 32$. It is possible to identify both the leading and trailing edges of a disturbance wavepacket, from which it is clearly determined that both ends of the wavepacket propagate outwards. This is characteristic of convective instability, as would be expected for this parameter choice.

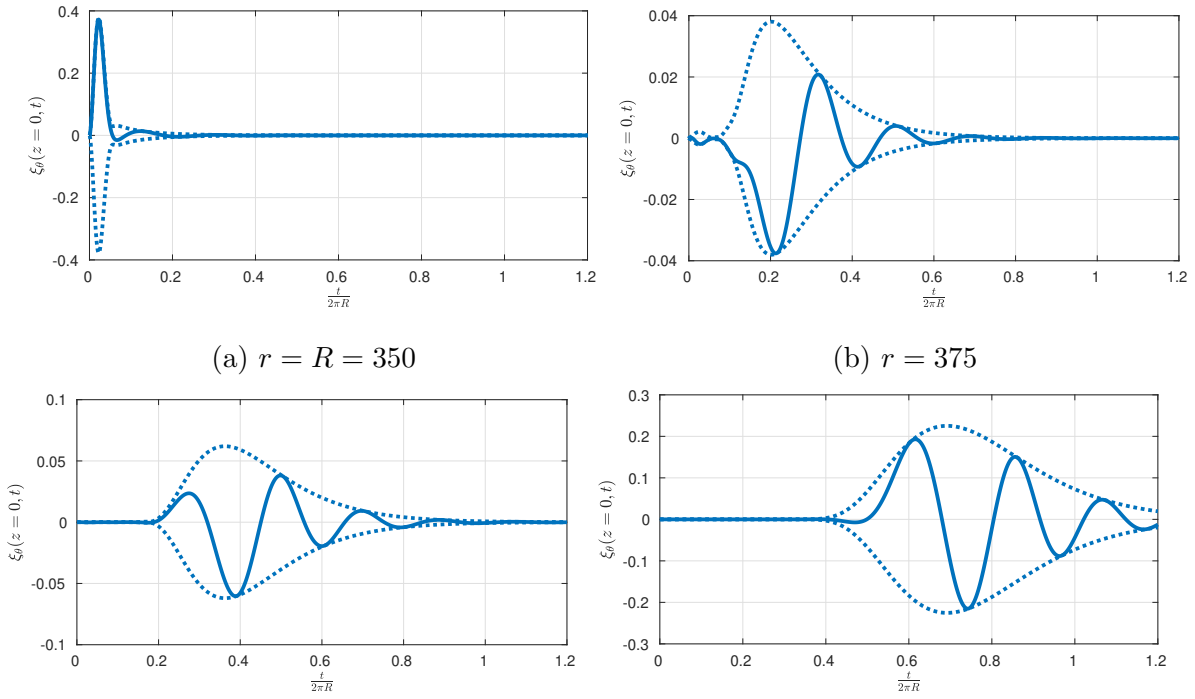

(a) $r = R = 350$ (b) $r = 375$

(c) $r = 400$ (d) $r = 450$

Figure 4.1: Temporal evolution of $\xi_\theta(z = 0, t)$ (—) for a disturbance with $n = 32$ and an impulse excited with Reynolds number $R = 350$ in the steady configuration. The wavepacket envelopes $|\xi_\theta(z = 0, t)|$ are also shown (- - -). The temporal axis is scaled by the disk rotation period $2\pi R$.

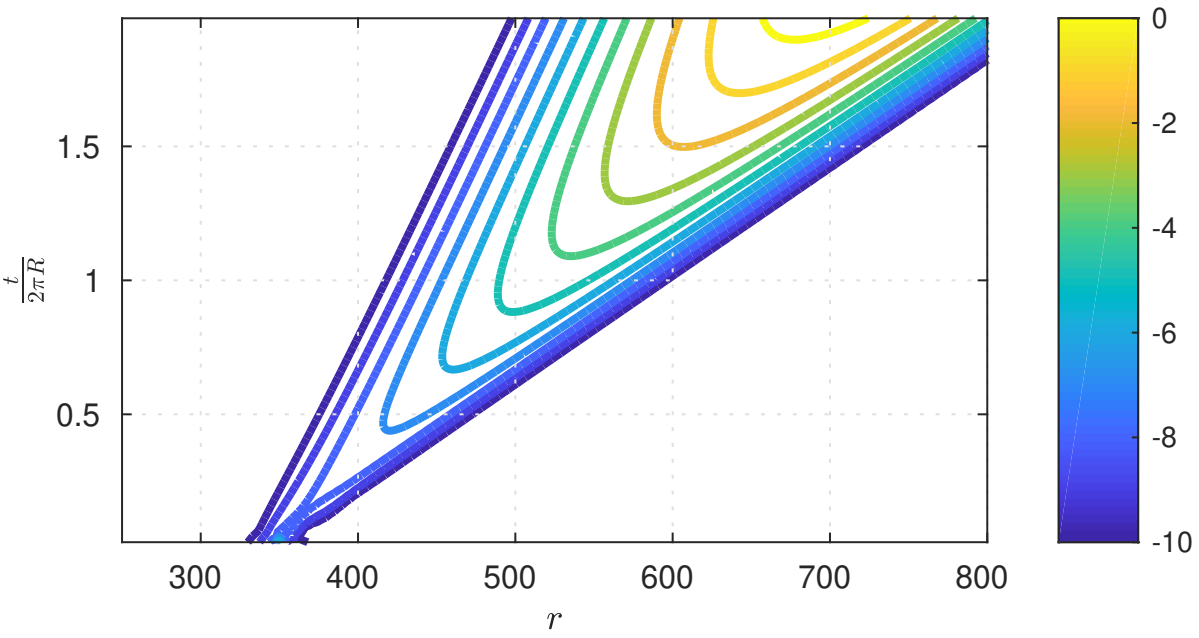

Figure 4.2: Spatio-temporal development of $|\xi_\theta(z = 0, t)|$ for an impulsively excited disturbance with Reynolds number $R = 350$ and azimuthal mode number $n = 32$. The temporal axis is scaled by the disk rotation period $2\pi R$. Contours are drawn using a logarithmic scale, with levels separated by factors of two.

4.1.2 Absolute Instability

The critical values for the onset of absolute instability as stated in Lingwood [44] are given by $(R, n) \approx (507, 68)$. Figure 4.3 shows the temporal evolution of a wavepacket in response to radially localised impulsive forcing located at $r = R = 525$ with prescribed azimuthal wavenumber of $n = 68$. The figure shows the temporal development at four radial locations, namely $r = R$, $r = R + 25$, $r = R + 50$ and $r = R + 100$ and the temporal axis is scaled by the disk rotation period $2\pi R$. Since $R > 507$ and $n = 68$, this is within the absolutely unstable region according to Lingwood [43], as illustrated by the exponential growth in time of the wavepacket seen at all radial locations at all times.

Figure 4.4 show the spatio-temporal development of the disturbance and from the contours we can see that over the time interval considered, the trailing edge of the disturbance propagates along the inward radial direction, confirming the existence of the local absolute instability.

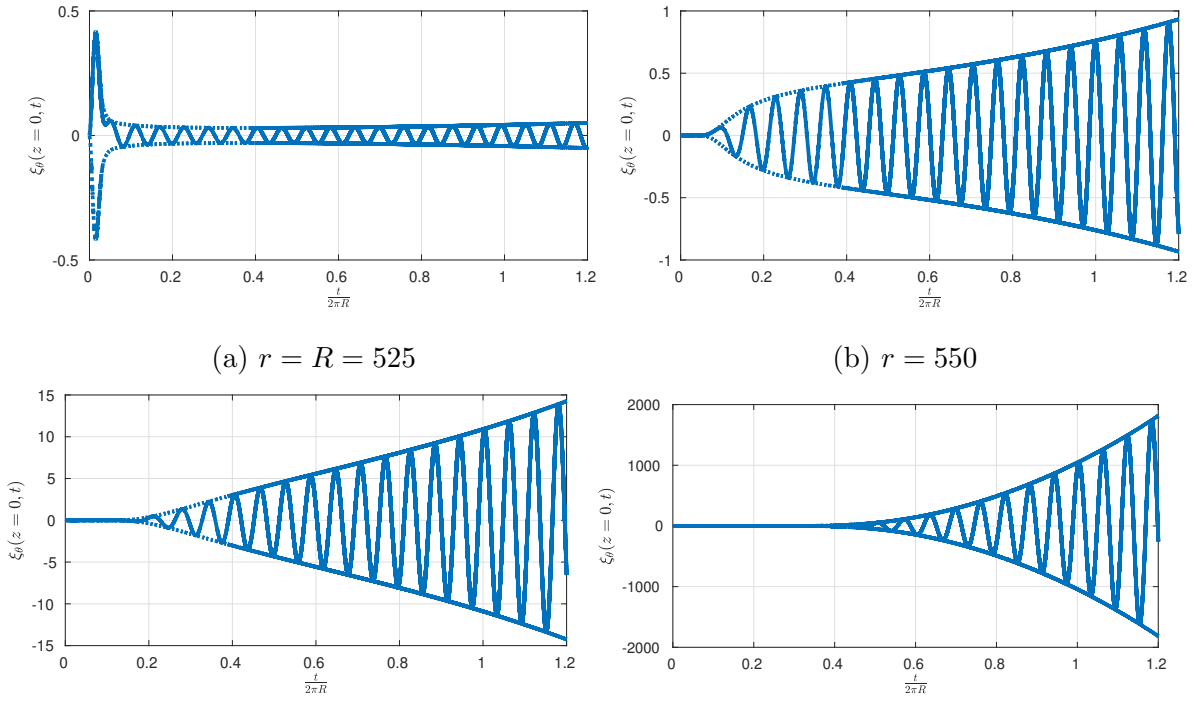

(a) $r = R = 525$ (b) $r = 550$

(c) $r = 575$ (d) $r = 625$

Figure 4.3: Temporal evolution of $\xi_\theta(z = 0, t)$ (—) for a disturbance with $n = 68$ and an impulse excited with Reynolds number $R = 525$ in the steady configuration. The wavepacket envelopes $|\xi_\theta(z = 0, t)|$ are also shown (- - -). The temporal axis is scaled by the disk rotation period $2\pi R$.

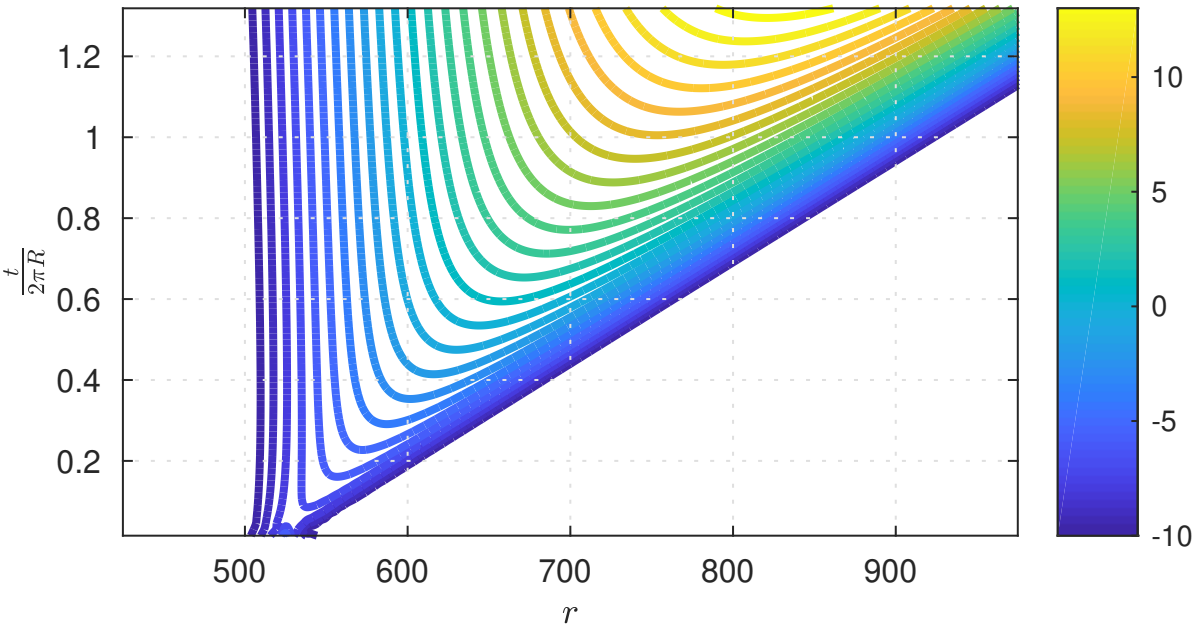

Figure 4.4: Spatio-temporal development of $|\xi_\theta(z = 0, t)|$ for an impulsively excited disturbance with Reynolds number $R = 350$ and azimuthal mode number $n = 32$. The temporal axis is scaled by the disk rotation period $2\pi R$. Contours are drawn using a logarithmic scale, with levels separated by factors of two.

4.2 Radially Homogeneous Periodically Modulated Case

The goal of this following section will be to provide a demonstration of the response of the periodically modulated rotating disk boundary layer to radially localised impulsive forcing, and contrast this behaviour to the steady case. We will, for the time being, employ the same parallel flow approximation discussed in section 4.1 and homogenise the radial direction by replacing r by R in the governing equations for the base flow and perturbations. The impulsive forcing in all cases is taken to be equivalent in amplitude to that of the steady case, the form of which is given by equation (4.2). We begin our presentation with a typical configuration which is convectively unstable in the steady case, before exploring a parameter set which would exhibit absolutely unstable behaviour without the added modulation.

Similarly to Davies and Carpenter [26], the variation of the primary variables in the modulated case may be fully resolved using a Chebyshev expansion involving $N = 48$ polynomials and a radial resolution of about $\Delta r \approx 1$. Each of the following simulation plots was produced using $N = 48$, a radial resolution of $\Delta r = 1.25$ and a time discretisation of $\Delta t = 0.625$. In all of the simulations, the computational domain extends well beyond the limits suggested by the figures in order to ensure no computational edge effects creep into affect the results.

4.2.1 Convective Instability

Figure 4.5 shows the temporal development of the azimuthal component of the vorticity $|\xi_\theta(z = 0, t)|$ for a disturbance with azimuthal mode number $n = 32$ triggered by an impulse with Reynolds number $R = 500$ at varying radial locations for $U_w = 0.2$ and various values of φ.

The impulsive forcing is taken to be equivalent in amplitude across all parameter choices, with the position of maximum forcing located at $r = R = 500$. The radial position of the forcing is arbitrary in the homogenised flow configuration as it it the Reynolds number which dictates the flow behaviour, and the figure shows the temporal development at four radial locations, namely $r = R$, $r = R + 25$, $r = R + 50$ and $r = R + 100$. The temporal axis is scaled by the disk rotation period $2\pi R$.

Clearly, sufficiently far from the centre of excitation, the addition of a modulated rotation rate has a dampening effect on the disturbance evolution, leading to significant stabilisation in terms of suppression of the wavepacket maximum for a certain parameter range. While this isolated parameter set has been chosen for illustrative purposes, similar behaviour was observed in the preliminary work to this study across a wide range of Reynolds and azimuthal mode numbers. Intriguingly, we see a stronger reduction in the wavepacket maximum for $\varphi = 8$ than for $\varphi = 12$, consistent with the idea of a somewhat *optimal* stabilisation parameter range first remarked upon in section 3.1.3, figure 3.4.

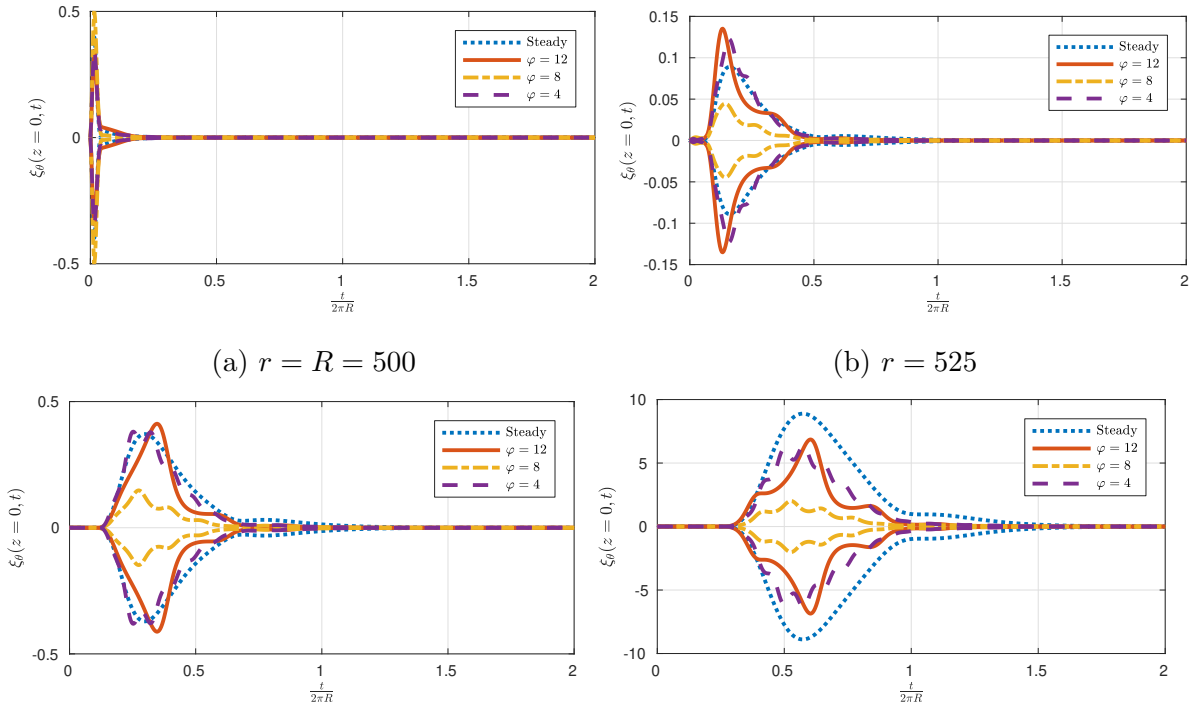

(a) $r = R = 500$ (b) $r = 525$

(c) $r = 550$ (d) $r = 600$

Figure 4.5: Temporal evolution of wavepackets $|\xi_\theta(z = 0, t)|$. The disturbance is excited with an azimuthal mode number $n = 32$ and Reynolds number $R = 500$ for $U_w = 0.2$ and $\varphi = 4$ (- - -), $\varphi = 8$ (∘−), $\varphi = 12$ (—). The steady case is shown as $(\cdots)$ and the temporal axis is scaled by the disk rotation period $2\pi R$.

4.2.2 Absolute Instability

To demonstrate the modifications to the behaviour of the disturbance evolution subject to an impulsive forcing in an absolutely unstable configuration, we consider $R = 525$ and $n = 68$. Figure 4.6 shows the temporal development of the azimuthal component

of the vorticity $|\xi_\theta(z=0,t)|$ for a disturbance excited with these parameters along with $U_w = 0.2$ and various φ.

Similarly to the convective case, the impulsive forcing is taken to be equivalent in amplitude across all parameter choices, with the position of maximum forcing located at $r = R = 525$. The figure shows the temporal development at four radial locations, namely $r = R$, $r = R + 25$, $r = R + 50$ and $r = R + 100$ and the temporal axis is scaled by the disk rotation period $2\pi R$.

Again, clear stabilisation may be seen for the modulated simulations, in the sense that the wavepacket maximum is smaller across the range of r. Of particular interest is the apparent suppression of the characteristic behaviour indicating absolute instability. Figure 4.7 shows the spatio-temporal development of the disturbance in a similar manner to figure 4.4, which no longer exhibits contours indicative of absolute instability, implying that this is also stabilised by the modulation. Furthermore, as may be seen by the range of values shown on the colourbar accompanying figures 4.7 and 4.4, the wavepacket maximum is a factor 2^4 smaller in the modulated case, indicating a particularly strong stabilisation for this parameter set.

Given the apparent strength of this stabilisation in this case, it is pertinent to present similar indicative figures (4.8-4.9) for very low values of modulation parameter $U_w = 0.01$ and $U_w = 0.05$. It appears, from this parameter set at least, that the stabilisation of the global behaviour is particularly strong and while a thorough parametric investigation of has not been conducted through the process of this work, such a study would make for a particularly interesting avenue for future investigation.

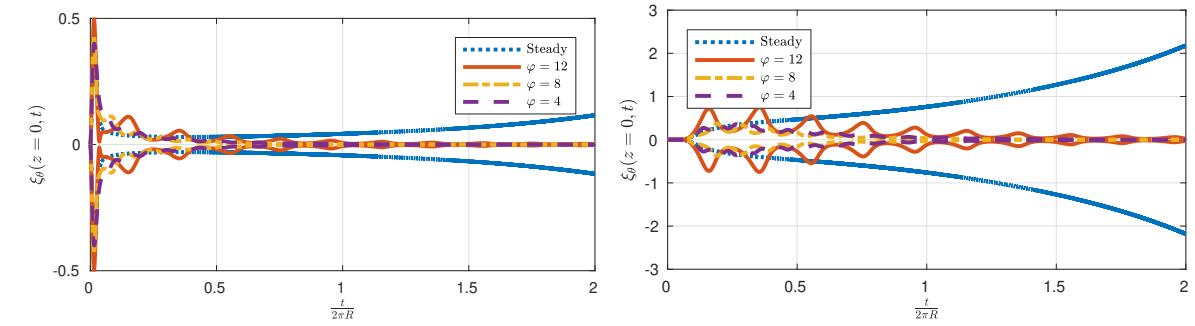

(a) $r = R = 525$ (b) $r = 550$

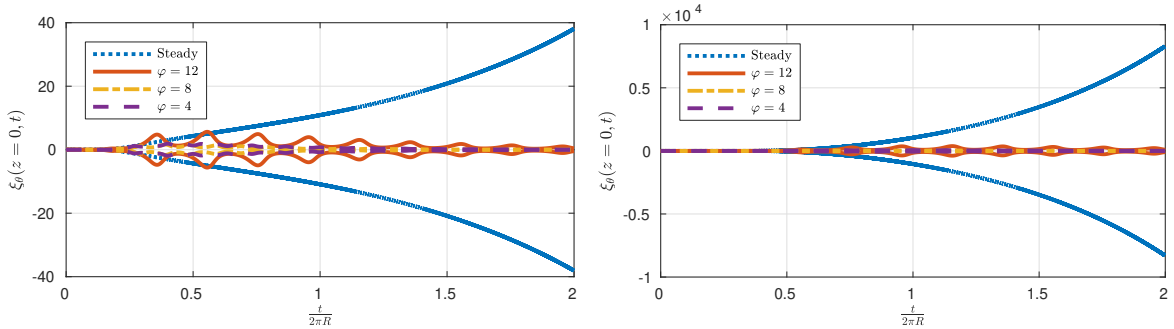

(c) $r = 575$ (d) $r = 625$

Figure 4.6: Temporal evolution of wavepackets $|\xi_\theta(z = 0, t)|$. The disturbance is excited with an azimuthal mode number $n = 68$ and Reynolds number $R = 525$ for $U_w = 0.2$ and $\varphi = 4$ (- - -), $\varphi = 8$ (∘−), $\varphi = 12$ (—). The steady case is shown as (—) and the temporal axis is scaled by the disk rotation period $2\pi R$.

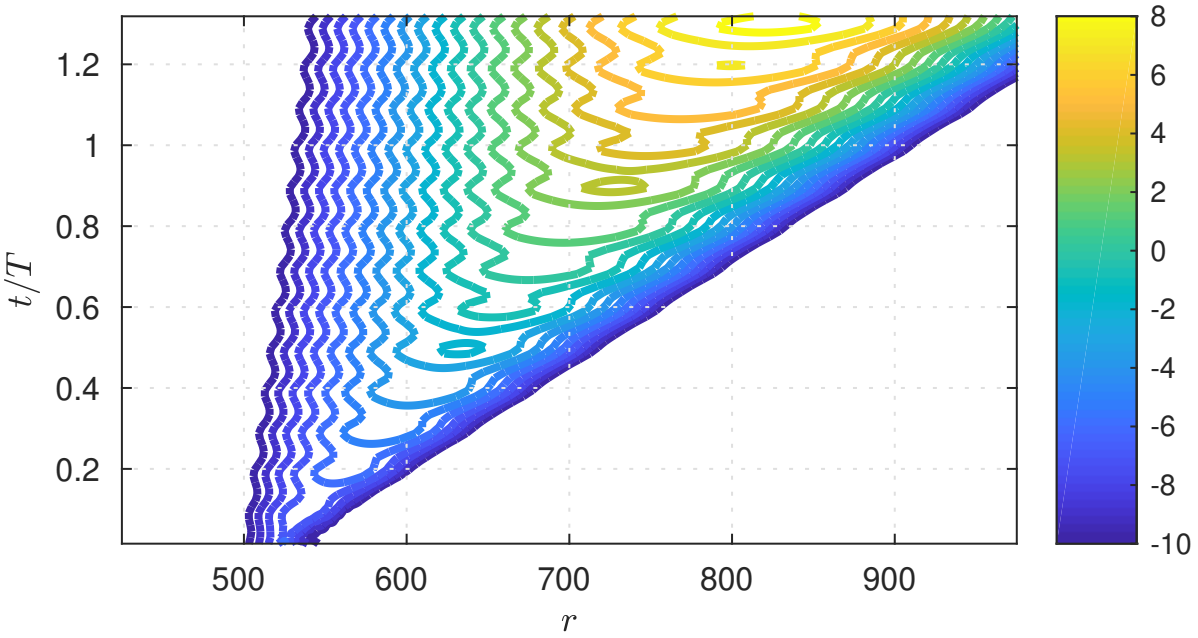

Figure 4.7: Spatio-temporal development of $|\xi_\theta(z=0,t)|$ for an impulsively excited disturbance with Reynolds number $R = 525$ and azimuthal mode number $n = 68$, for $U_w = 0.2$ and $\varphi = 10$. The temporal axis is scaled by the disk rotation period $2\pi R$. Contours are drawn using a logarithmic scale, with levels separated by factors of two.

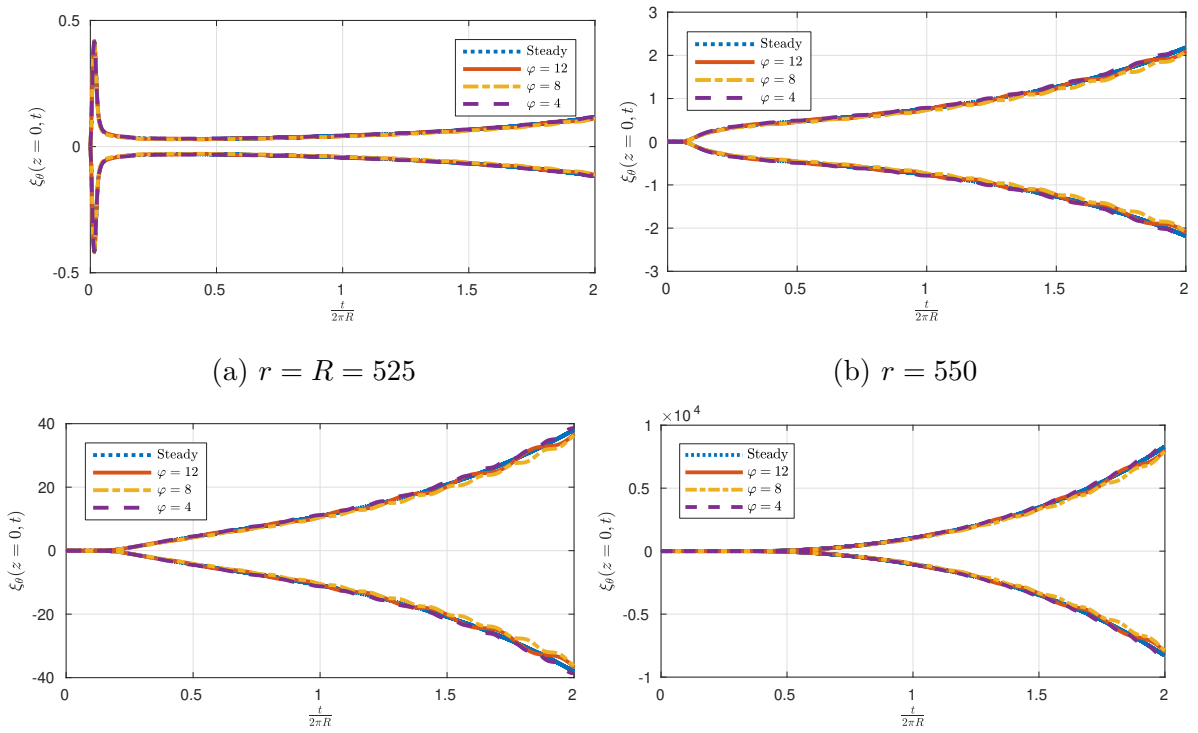

(a) $r = R = 525$ (b) $r = 550$

(c) $r = 575$ (d) $r = 625$

Figure 4.8: Temporal evolution of wavepackets $|\xi_\theta(z = 0, t)|$. The disturbance is excited with an azimuthal mode number $n = 68$ and Reynolds number $R = 525$ for $U_w = 0.01$ and $\varphi = 4$ (- - -), $\varphi = 8$ ($\circ-$), $\varphi = 12$ (—). The steady case is shown as (—) and the temporal axis is scaled by the disk rotation period $2\pi R$.

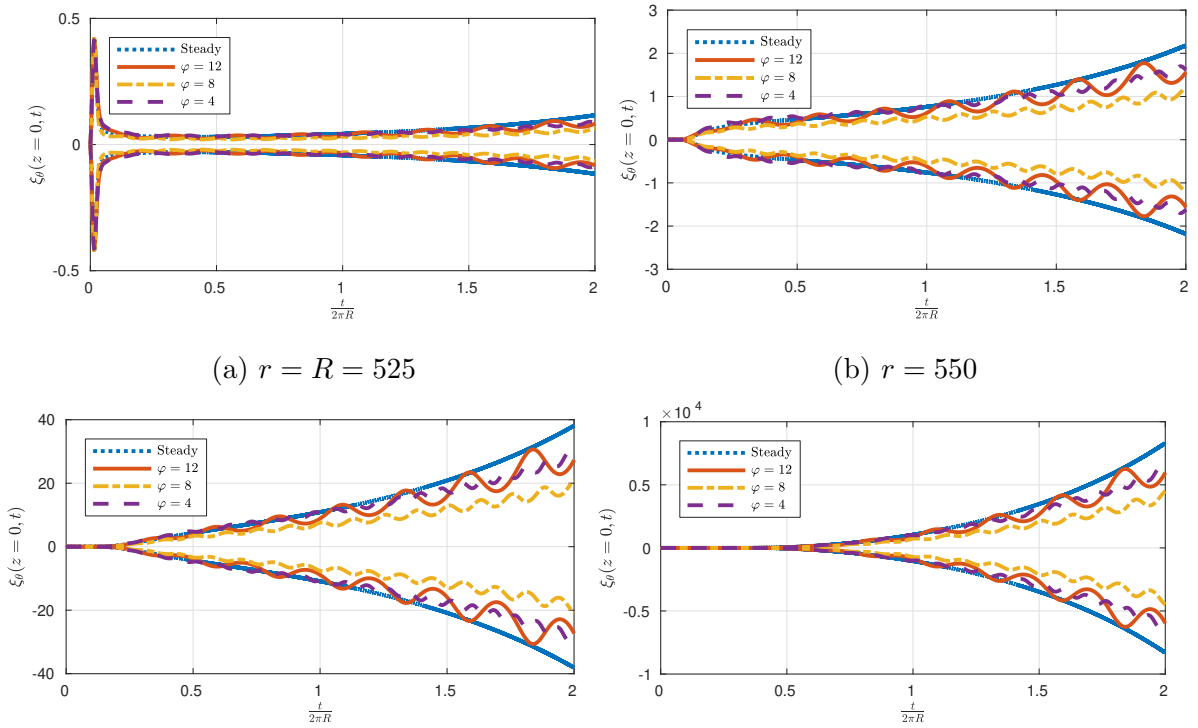

(a) $r = R = 525$ (b) $r = 550$

(c) $r = 575$ (d) $r = 625$

Figure 4.9: Temporal evolution of wavepackets $|\xi_\theta(z = 0, t)|$. The disturbance is excited with an azimuthal mode number $n = 68$ and Reynolds number $R = 525$ for $U_w = 0.05$ and $\varphi = 4$ (- - -), $\varphi = 8$ (∘−), $\varphi = 12$ (—). The steady case is shown as (—) and the temporal axis is scaled by the disk rotation period $2\pi R$.

4.3 Global Stability of the Periodically Modulated Rotating Disk Boundary Layer

In the local stability analyses of chapters 2-3, we applied the so-called parallel flow approximation and simplified the mean flow by taking it to be homogeneous along the radial direction. Additionally, we have remarked several times throughout this thesis that this process is somehow unphysical and should be treated with caution. If we allow the mean flow to vary with the radius, then the separability of the solution into normal mode form is destroyed for the radial direction and the r-derivatives must be retained to specify the disturbance structure. For the radially inhomogeneous flow, Davies and Carpenter [27] discovered that the absolute instability predicted by the local analysis does not in fact give rise to any global linear instability. Instead, convective behaviour dominates the flow at all Reynolds numbers, even those taken well within the region of absolute instability. This was the first numerical global study of the flow and was contrary to what many other authors believed at the time. Experimental studies since undertaken by Othman and Corke [56] have confirmed this conclusion, and provided the disturbance amplitudes can be forced to remain small enough to avoid non-linearity, convective transient behaviour wins out at all Reynolds numbers. An exposition of the global behaviour is given in Davies and Carpenter [27], later explained by Davies et al. [28] and Thomas and Davies [72], and has been referred to in many studies since, for example during the investigation of secondary instabilities by Pier [57] and the influence of an axial magnetic field by Thomas and Davies [74]. Healey [40] also investigated the effect of a finite disk radius using the Ginzburg-Landau equation. The most recent studies have been undertaken by Appelquist et al. [4, 5, 6] and have investigated non-linear behaviour and the influence of a finite radius disk on the global stability by means of full direct numerical simulations. A fairly recent review by Lingwood and Alfredsson [46] gives a detailed overview of the up-to-date state of the field which it would be superfluous to repeat.

To illustrate the concept of global stability, it is useful to consider an example. Figure 4.10 shows the response to an impulsive disturbance centred at $r = 520$ with azimuthal mode number $n = 68$ in both the radially homogeneous and inhomogeneous cases.

These parameters were chosen so as to be inside the absolutely unstable region described by Lingwood [43]. It can be seen that while the initial growth is similar in both

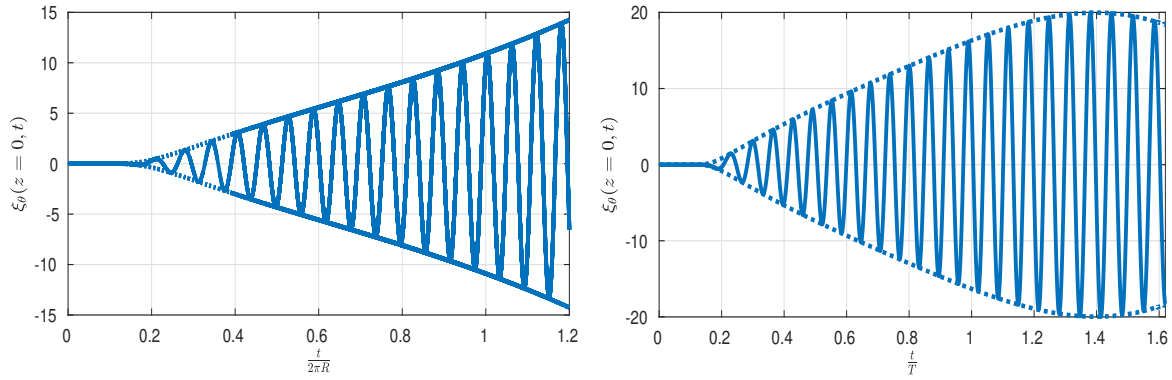

(a) Homogeneous

(b) Inhomogeneous

Figure 4.10: Comparison between temporal evolution of $\xi_\theta(z = 0, t)$ (—) for a disturbance with azimuthal mode number $n = 68$ and an impulse excited by radially localised impulsive forcing centred at $r_e = 520$ in both the homogeneous and inhomogeneous configurations. The wavepacket envelopes $|\xi_\theta(z = 0, t)|$ are also shown (- - -). In the inhomogeneous configuration, the temporal axis is scaled by the disk rotation period $T = 2\pi r_i$ where r_i is the interior of the computational boundary, and by $2\pi R$ in the homogeneous case.

the homogeneous and inhomogeneous cases, after around $t/T \approx 1.3$, the magnitudes of this flow variable in the inhomogeneous case start to decrease. This behaviour is not what had been anticipated on the basis of the absolute instability predicted from the local theory, where it had been expected that for these parameters, the magnitude should increase without bound at all fixed radial locations. It was thus inferred by Thomas and Davies [72] that once the radial inhomogeneity of the base flow is incorporated, the flow is linearly globally stable. This phenomenon was also shown to be reproducible using a linearised Ginzburg-Landau equation with spatially varying coefficients, as detailed in Thomas [71], Davies et al. [28] and Thomas and Davies [72]. The expectation that the non-parallel corrections should not have had any effect on the absolute instability properties arose from Lingwood's [43] inviscid analysis which demonstrated that the absolute instability persisted in an appropriate inviscid limit. This suggested that the absolute instability should be robust even when it is embedded in the non-parallel flow, since non-parallel corrections ought to eventually become insignificant at large enough radii. However, as explained in Davies et al. [28], there is a subtlety to the localised viscous stability analysis, as well as to its inviscid counterpart, in the time scalings used for the non-dimensionalisation of the

time variation and the corresponding disturbance frequencies. In the local analysis, where the absolute instability is present, the time scale is constructed from the ratio between the constant boundary-layer thickness of the mean flow and the circumferential speed of the disk surface, which increases linearly with the radius. But there is also a global time scale, independent of the radius, that is defined by simply taking the inverse of the constant angular rotation rate of the disk. Thus if ω_l and ω_g represent the local and global non-dimensional temporal frequencies corresponding to the same physical frequency, then we have the relation

$$\omega_g = \omega_l R$$

which corresponds to ω_l = const. in the inviscid analysis. We can thus see that the fixed local frequency characterising the absolute instability actually corresponds, in the inhomogeneous flow, to a collection of radially varying globally non-dimensionalised frequencies. It was this subtlety that, as explained by Davies et al. [28], was shown to cause the inhomogeneity to be globally stabilising, contrary to intuition.

In the homogeneous simulations of section 4.1, the disk rotation period T was set to be $2\pi R$ where R specifies the Reynolds number of the forcing location which is locally equivalent to the radius. Similarly, the azimuthal wavenumber β was set to be $\beta = 68/R$. In the forthcoming results for the inhomogeneous simulations, since the disturbance is evolving in a genuine radially inhomogeneous flow, the disk rotation period T is set to be $2\pi r_i$ where r_i is the radius of the inner computational boundary and the azimuthal wavenumber β is set to be $\beta = 68/r_i$. This allows for direct comparisons between the homogeneous and inhomogeneous configurations, as has been done in Davies and Carpenter [27], Davies et al. [28], Thomas and Davies [73] and Thomas [71].

4.3.1 Steady Case

Similarly to section 4.1, we excite the impulsive disturbance by means of prescribed wall motion which takes the form of equation (4.2). The important difference with this radially inhomogeneous configuration is that the forcing location is no longer arbitrary, and the radial extent of the computational domain is not approximated by the replacement of r by R in this case.

Figure 4.11 shows the temporal development of the azimuthal component of the vorticity $\xi_\theta(z = 0, t)$ for a disturbance with azimuthal mode number $n = 68$ triggered by

an impulse at $r_e = 510$. According to the local analysis of Lingwood [43], this parameter choice should be within the absolutely unstable range and the temporal evolutions should, therefore, grow at all spatial locations at all times. This is not the case, as first demonstrated by Davies and Carpenter [27], and the disturbances show a clear decay in finite time after an initial period of growth. This is indicative of a convectively unstable disturbance, consistent with the results presented in Davies and Carpenter [27].

As illustration of the behaviour exhibited by this steady configuration, figure 4.2 shows the spatio-temporal contour plots of $|\xi_\theta(z = 0, t)|$ for the same parameter set of $n = 68$ and $r_e = 510$. The temporal axis is scaled by the disk rotation period T, set to be $2\pi r_i$ where r_i is the radius of the inner computational boundary. Similarly, the azimuthal wavenumber β is fixed as $\beta = 68/r_i$. It is possible to identify the turn towards convectively unstable behaviour around $t/T \approx 1.3$ of the disturbance wavepacket, from which it is clearly determined that both ends of the wavepacket propagate outwards. This is characteristic of convective instability, not absolute instability as would have been predicted by Lingwood's [43] local analysis.

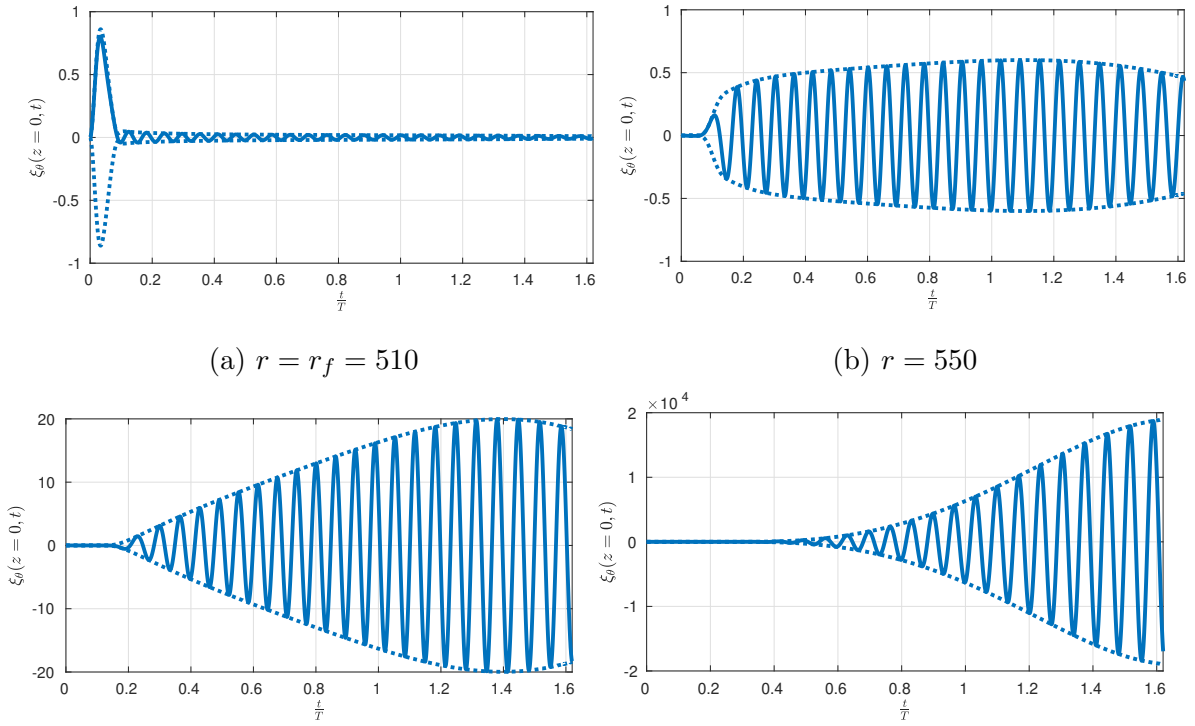

(a) $r = r_f = 510$

(b) $r = 550$

(c) $r = 575$

(d) $r = 600$

Figure 4.11: Temporal evolution of $\xi_\theta(z = 0, t)$ (—) for a disturbance with azimuthal mode number $n = 68$ and an impulse excited by radially localised impulsive forcing centred at $r_e = 510$ in the steady configuration. The wavepacket envelopes $|\xi_\theta(z = 0, t)|$ are also shown (- - -). The temporal axis is scaled by the disk rotation period $T = 2\pi r_i$ where r_i is the interior of the computational boundary.

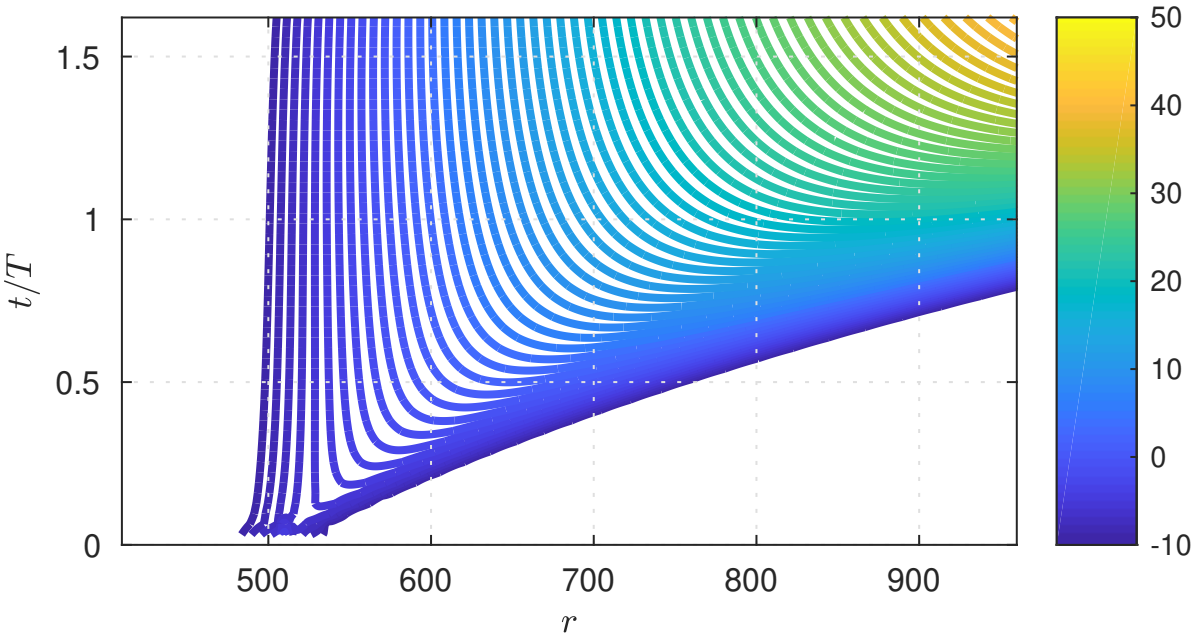

Figure 4.12: Spatio-temporal development of $|\xi_\theta(z = 0, t)|$ for azimuthal mode number $n = 68$ and radially localised impulsive forcing centred at $r_e = 510$. The temporal axis is scaled by the disk rotation period $T = 2\pi r_i$ where r_i is the interior of the computational boundary. Contours are drawn using a logarithmic scale, with levels separated by factors of two. The trailing edge can be seen to turn around $\frac{t}{T} \approx 1.3$, indicating convective behaviour as discussed in Davies and Carpenter [27].

4.3.2 Periodically Modulated Case

Figure 4.5 shows the temporal development in the periodically modulated boundary layer of the azimuthal component of the vorticity $|\xi_\theta(z=0,t)|$ for a disturbance with azimuthal mode number $n = 68$ triggered by an impulsive forcing centred at $r_e = 510$ at varying radial locations for $U_w = 0.2$ and various values of φ.

The impulsive forcing is taken to be equivalent in amplitude across all parameter choices, with the position of maximum forcing located at $r = r_e = 510$. The radial position of the forcing is no longer arbitrary in the inhomogeneous flow configuration. The figure shows the temporal development at four radial locations, namely $r = r_e$, $r = r_e + 25$, $r = r_e + 50$ and $r = r_e + 100$. The temporal axis is scaled by the disk rotation period $2\pi r_i$ where r_i is the interior of the computational boundary.

Clearly, sufficiently far from the centre of excitation, the addition of a modulated rotation rate has a dampening effect on the disturbance evolution, leading to significant stabilisation in terms of suppression of the wavepacket maximum for a certain parameter range. While this isolated parameter set has been chosen for illustrative purposes, similar behaviour was observed in the preliminary work to this study across a wide range of Reynolds and azimuthal mode numbers. Intriguingly, we see a stronger reduction in the wavepacket maximum for $\varphi = 8$ than for $\varphi = 12$, consistent with the idea of a somewhat *optimal* stabilisation parameter range first remarked upon in figure 3.4, section 3.1.3.

Additionally, the radially outward movement of the trailing edge is clearly much stronger for the modulated case than for the unmodulated scenario, indicating a strong stabilisation to impulsive forcing for the parameter choices considered in this study.

Similarly to the radially homogeneous case, given the apparent strength of this stabilisation, it is pertinent to present similar indicative figures (4.15-4.16) for very low values of modulation parameter $U_w = 0.01$ and $U_w = 0.05$. It appears, from this parameter set at least, that the stabilisation of the global behaviour is particularly strong and while a thorough parametric investigation of has not been conducted through the process of this work, such a study would make for a particularly interesting avenue for future investigation.

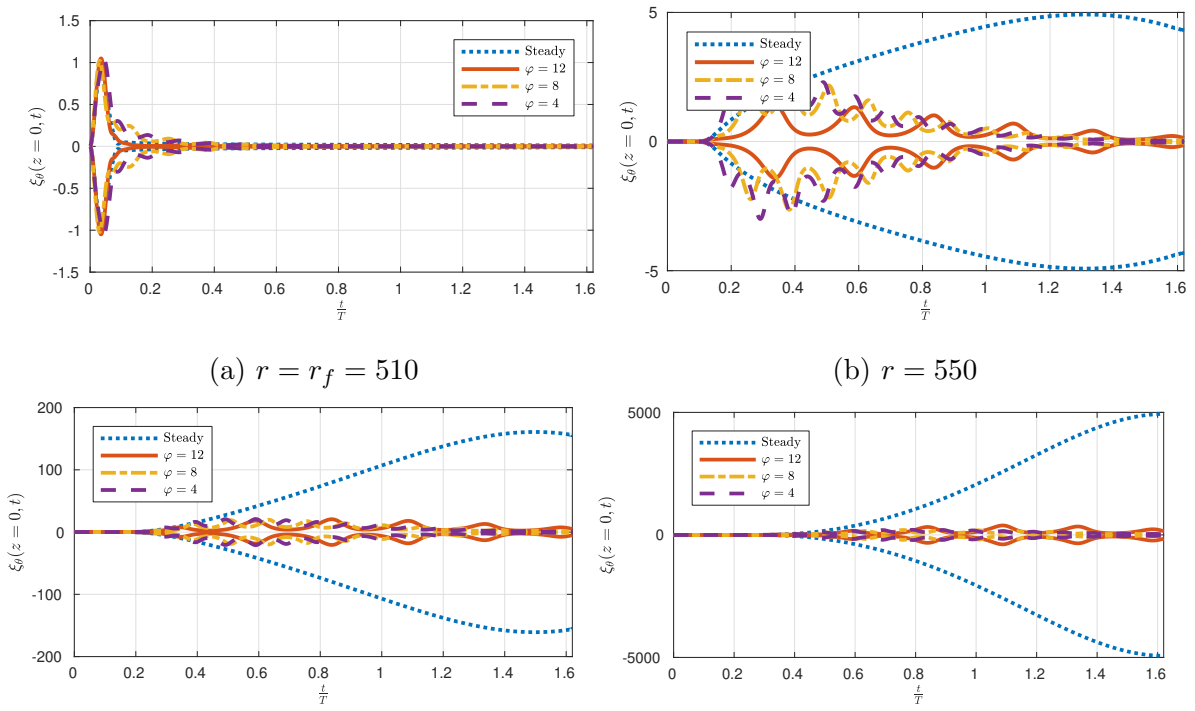

(a) $r = r_f = 510$ (b) $r = 550$

(c) $r = 575$ (d) $r = 600$

Figure 4.13: Temporal evolution of wavepackets $|\xi_\theta(z = 0, t)|$. The disturbance is excited with an azimuthal mode number $n = 68$ and impulse centred at $r_e = 510$ for $U_w = 0.2$ and $\varphi = 4$ (- - -), $\varphi = 8$ ($\circ$–), $\varphi = 12$ (—). The steady case is shown as (—) and the temporal axis is scaled by the disk rotation period $T = 2\pi r_i$ where r_i is the interior of the computational boundary.

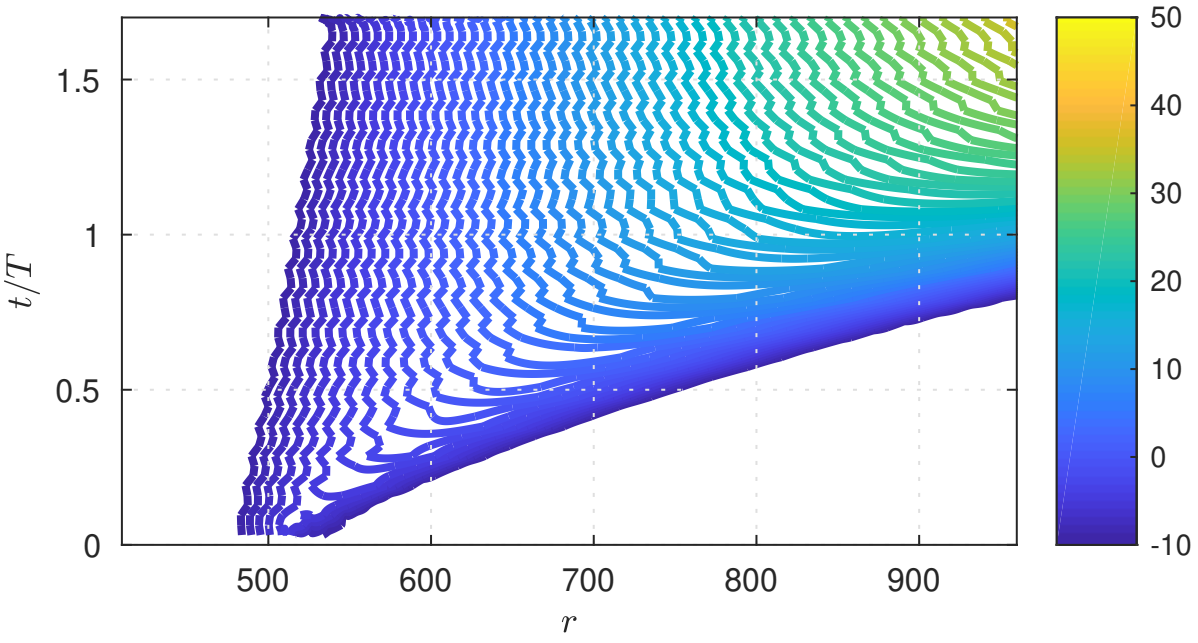

Figure 4.14: Spatio-temporal development of $|\xi_\theta(z=0,t)|$ for azimuthal mode number $n = 68$ and radially localised impulsive forcing centred at $r_e = 510$ with $U_w = 0.2$ and $\varphi = 10$. The temporal axis is scaled by the disk rotation period $T = 2\pi r_i$ where r_i is the interior of the computational boundary. Contours are drawn using a logarithmic scale, with levels separated by factors of two. The radially outward propagation of trailing edge is much clearer than in the steady case, indicating stabilisation.

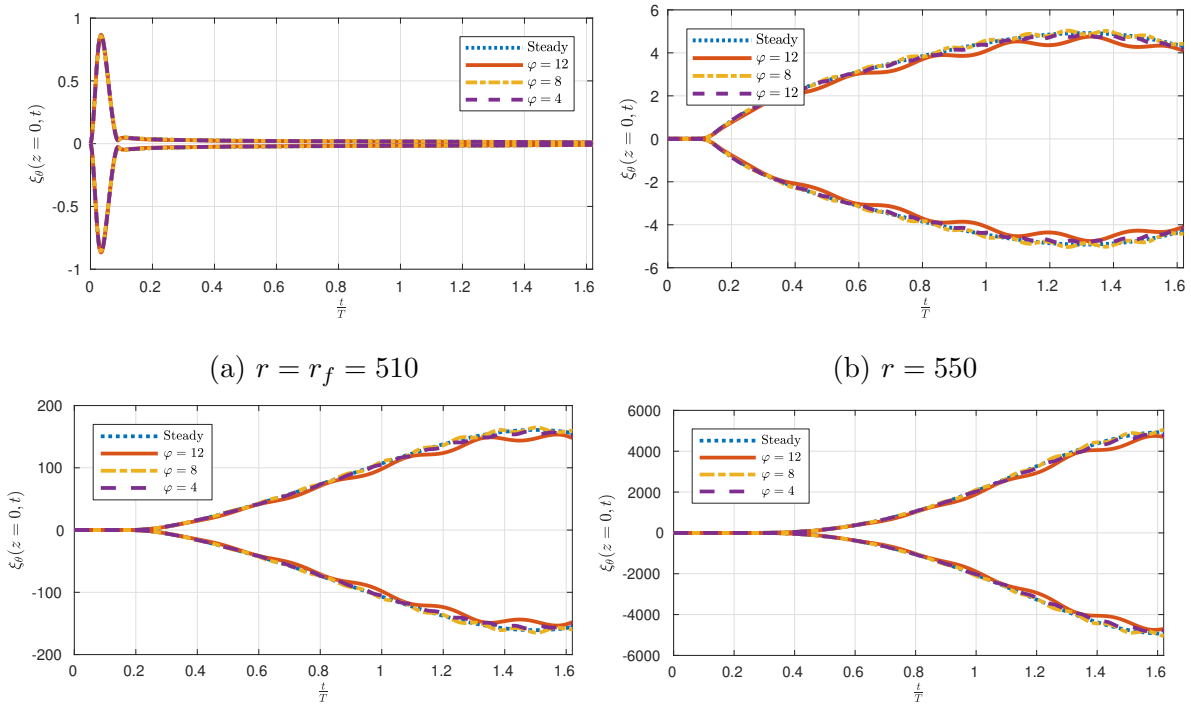

(a) $r = r_f = 510$

(b) $r = 550$

(c) $r = 575$

(d) $r = 600$

Figure 4.15: Temporal evolution of wavepackets $|\xi_\theta(z = 0, t)|$. The disturbance is excited with an azimuthal mode number $n = 68$ and impulse centred at $r_e = 510$ for $U_w = 0.01$ and $\varphi = 4$ (- - -), $\varphi = 8$ ($\circ-$), $\varphi = 12$ (—). The steady case is shown as (—) and the temporal axis is scaled by the disk rotation period $T = 2\pi r_i$ where r_i is the interior of the computational boundary.

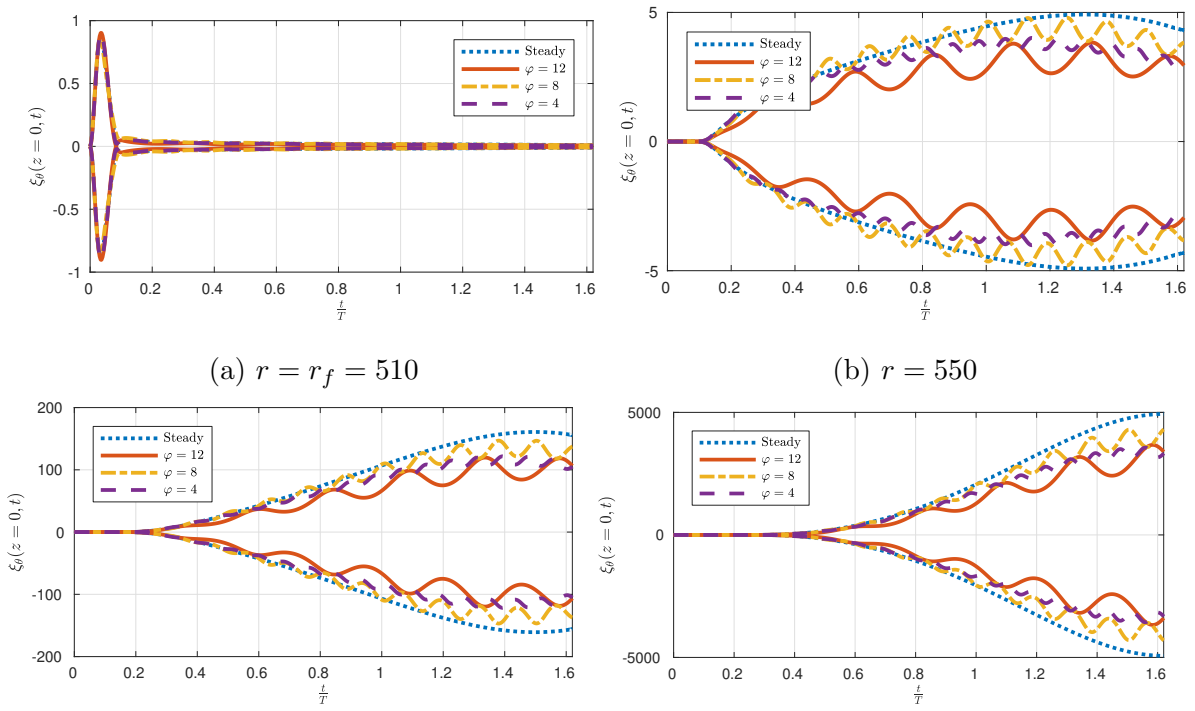

(a) $r = r_f = 510$ (b) $r = 550$

(c) $r = 575$ (d) $r = 600$

Figure 4.16: Temporal evolution of wavepackets $|\xi_\theta(z = 0, t)|$. The disturbance is excited with an azimuthal mode number $n = 68$ and impulse centred at $r_e = 510$ for $U_w = 0.05$ and $\varphi = 4$ (- - -), $\varphi = 8$ (∘−), $\varphi = 12$ (—). The steady case is shown as (—) and the temporal axis is scaled by the disk rotation period $T = 2\pi r_i$ where r_i is the interior of the computational boundary.

4.4 Discussion

This chapter has detailed the study of radially localised impulsive forcing in both the steady and periodically modulated rotating disk boundary layers. Split into two sections, we examined the behaviour of disturbances in both radially homogenised and inhomogeneous configurations and presented results showing the differences in behaviour between the steady and modulated cases. Similarly to that shown in chapter 3, stabilising behaviour was demonstrated by the simulations across a range of modulation parameters and Reynolds numbers. For a certain absolutely unstable configuration in the homogenised flow, it was also shown that the modulation suppresses the absolute instability and converts the behaviour to convective for even very small amplitude modulations. Similarly, in the inhomogeneous configuration, we demonstrated that small amplitude modulations have a significant dampening effect on the wavepacket evolution across a range of modulation frequencies.

Since this spatio-temporal analysis is, in general, more indicative of physical, experimental behaviour than the fixed-frequency forcing of chapter 3, it may provide confidence that the stabilisation shown by the addition of the modulated rotation rate is more robust than being isolated to stationary or fixed wavenumber disturbances. Impulsive excitation has been used throughout this chapter, thereby creating disturbances that take the form of wavepackets, initially containing a wide range of frequencies, and the form of the perturbations in our simulations is not specified in any way. Just like in a physical experiment, the perturbations are initially excited by a radially localised displacement of the disk surface with the subsequent evolution of the disturbance governed purely by the perturbation equations. Therefore, we may have confidence that any results presented here should be ratifiable by experimental data. However, it should be noted that these global studies were not the main focus of the work carried out during this thesis, and thorough parametric testing and experimental confirmation is reserved for future studies.

Chapter 5

Future Directions

The following sections provide an insight into the author's intentions for future directions, and will introduce an interesting inter-disciplinary application to the work conducted throughout this thesis. We begin the discussion with purely torsional oscillations and a calculation of the base state in this configuration, before progressing through a further exploration of the Floquet stability theory to some fundamental techniques in electrochemistry. We conclude the discussion of future directions with alternative stabilising methods such as designed surface roughness and some parallels to our work contained therein.

5.1 The Torsionally Oscillating Disk Boundary Layer

The previous chapters have dealt primarily with a disk of infinite extent rotating with an unsteady rotation rate and we have discussed the stabilising effects of a periodically modulated rotation rate on the local stability of the boundary layer. We now turn our attention to a slightly different configuration, and consider the case where the disk performs torsional oscillations around the azimuth, which is an important configuration in several electrochemical engineering processes such as chemical deposition, hydrodynamic voltammetry and electroplating, see Cummings et al. [22, 23], Ahn et al. [1, 2]. To the best of my knowledge, there has been very little mathematical study of this flow, and only a few analytical studies exist which calculate the basic state in various configurations. Rosenblat [63] was the first to study this problem, and Benney [9] subsequently improved on the results. Since then, there have been several studies on variants of the

configuration, including Secomb and Rosenblat [67], Reddy et al. [60] and Srivastava [69] who study various non-Newtonian effects and dual-disk configurations. It seems, however, that there has been no formal exploration of the hydrodynamic stability of such a flow, and we thus proceed to present an introductory examination.

We begin by considering a disk of infinite extent, torsionally oscillating in the plane $z = 0$ about the axis $r = 0$. Let the oscillations have angular displacement ϵ and frequency ϕ^* so that the disk moves with angular velocity $\epsilon\phi^* \cos(\phi^* t^*)$. Thus, the base flow $\mathbf{U}_B = (U^*, V^*, W^*)$ obeys the usual Navier-Stokes equations in a cylindrical polar coordinate system with boundary conditions

$$U^*(0) = W^*(0) = 0, \;\; V^*(0) = r^* \epsilon \phi^* \cos(\phi^* t^*)$$
$$U^* \to 0, \quad V^* \to 0 \;\; \text{as} \;\; z^* \to \infty$$

When discussing the periodically modulated rotation rate in chapter 2, we noted two length scales on which the flow evolves, namely

$$\delta_k^* = \sqrt{\frac{\nu^*}{\Omega_0^*}}, \qquad \delta_s^* = \sqrt{\frac{\nu^*}{\phi^*}} \tag{5.1}$$

where Ω_0^* was the underlying steady rotation rate and ϕ^* the frequency of modulation. In that case, we selected the Kármán scale δ_k^* for the non-dimensionalisation. In this scenario, we do not have a mean rotation rate and so must choose the Stokes length scale $\delta_s^* = \sqrt{\frac{\nu^*}{\phi^*}}$ which leads to the natural selection for the temporal scale of

$$\tau_s = \phi^* t^* \tag{5.2}$$

Following Rosenblat [63], we can take a similar solution to von Kármán [80] for the steady case, and scale the velocities as

$$F(z,t) = \frac{U^*(r,z,t)}{\epsilon\phi^* r^*}, \quad G(z,t) = \frac{V^*(r,z,t)}{\epsilon\phi^* r^*}, \quad H(z,t) = \frac{W^*(r,z,t)}{\epsilon\phi^* \delta^*} \tag{5.3}$$

giving the system of equations for the base flow as

$$\frac{\partial F}{\partial \tau} = \epsilon \left(G^2 - F^2 - H\frac{\partial F}{\partial z} \right) + \frac{\partial^2 F}{\partial z^2} \tag{5.4a}$$
$$\frac{\partial G}{\partial \tau} = \epsilon \left(-2FG - H\frac{\partial G}{\partial z} \right) + \frac{\partial^2 G}{\partial z^2} \tag{5.4b}$$
$$\frac{\partial H}{\partial z} = -2F \tag{5.4c}$$

with boundary conditions

$$F(0,\tau) = H(0,\tau) = 0, \quad G(0,\tau) = \cos(\tau)$$
$$F \to 0, \quad G \to 0 \quad \text{as} \quad z \to \infty$$

This system is solved in an identical way to that of the periodically modulated disk in section 2.1.1, so the reader is referred to the explanation presented there for further details. Figure 5.1 shows the typical evolution of the velocity flow components over one period of oscillation for $\epsilon = 0.25$. In addition, figures 5.2, 5.3 and 5.4 show the time history of the base flow profiles at selected locations $z = 0$ (-), $z = 0.1$ (- - -) and $z = 0.25$ ($\cdots$) over one period of oscillation.

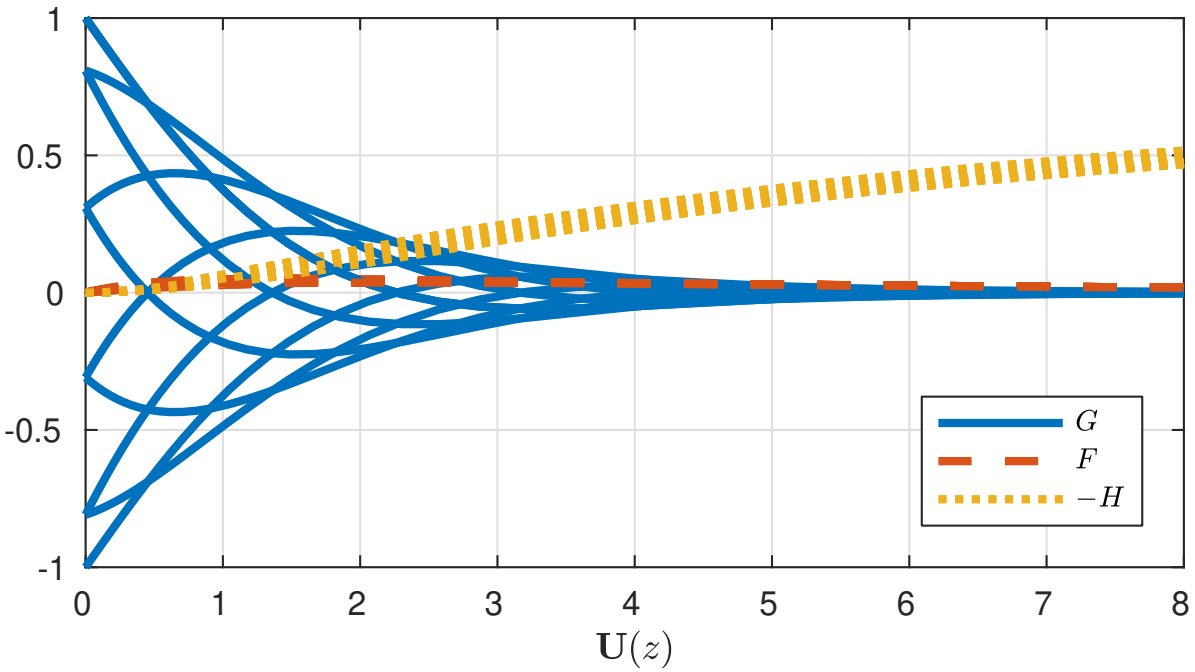

Figure 5.1: Torsional oscillation velocity profiles F (- - -), G (—), $-H$ ($\cdots$) with $\epsilon = 0.25$.

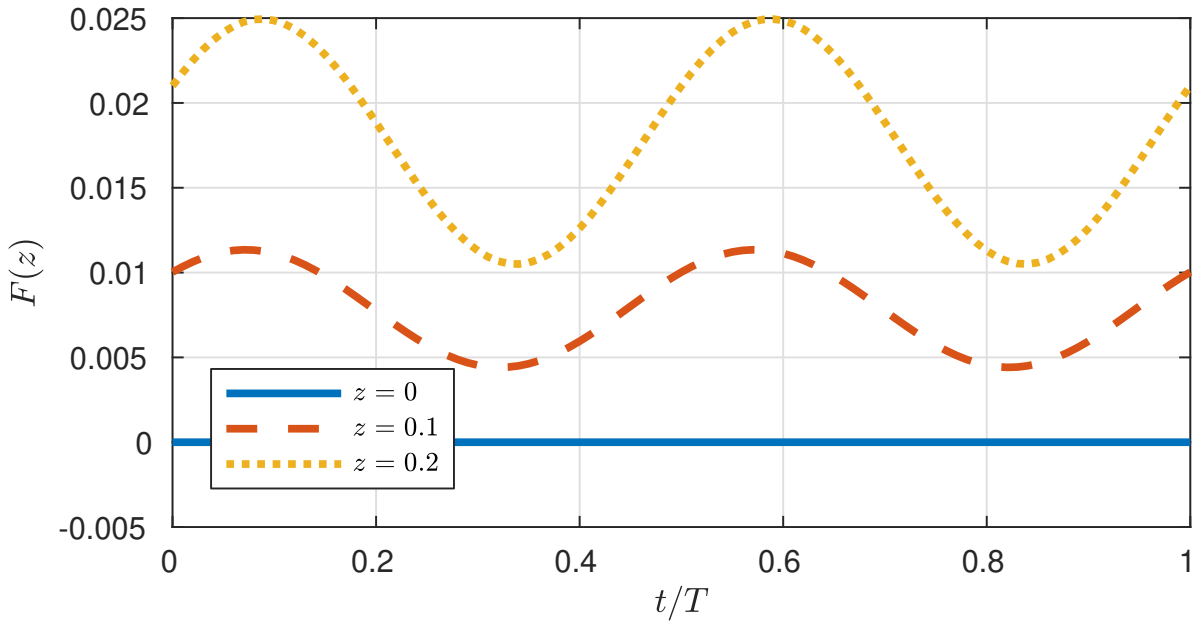

Figure 5.2: Time history of radial velocity at selected locations $z = 0$ (-), $z = 0.1$ (- - -) and $z = 0.25$ ($\cdots$) over one period of oscillation with $\epsilon = 0.25$.

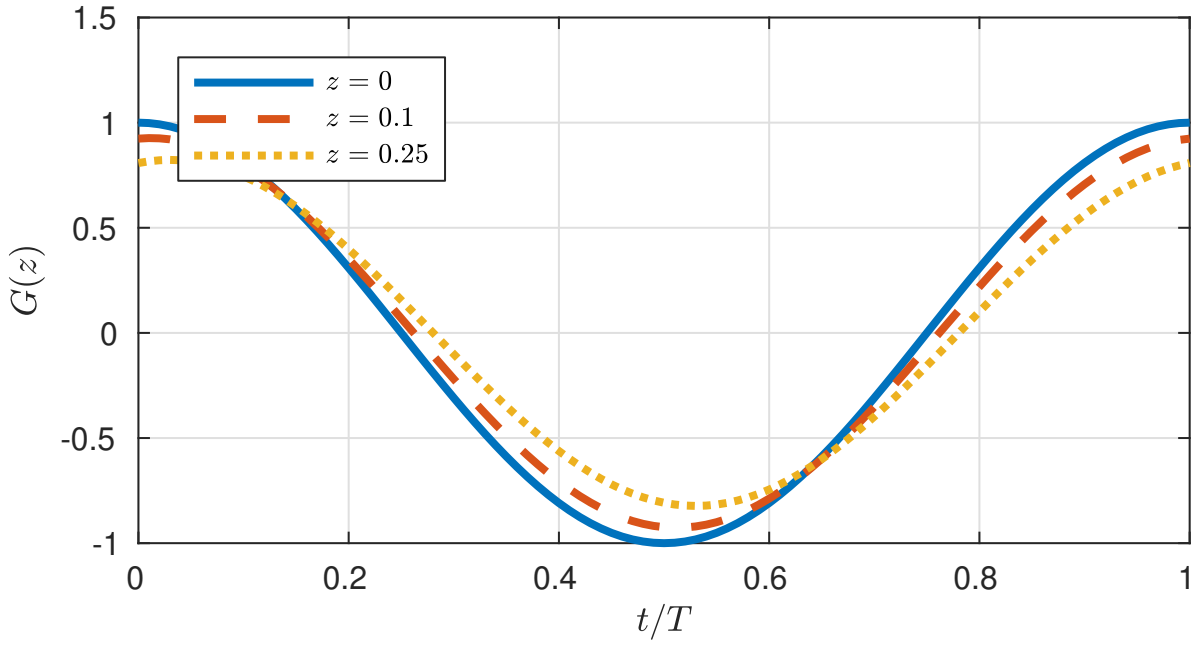

Figure 5.3: Time history of azimuthal velocity at selected locations $z = 0$ (-), $z = 0.1$ (- - -) and $z = 0.25$ ($\cdots$) over one period of oscillation with $\epsilon = 0.25$.

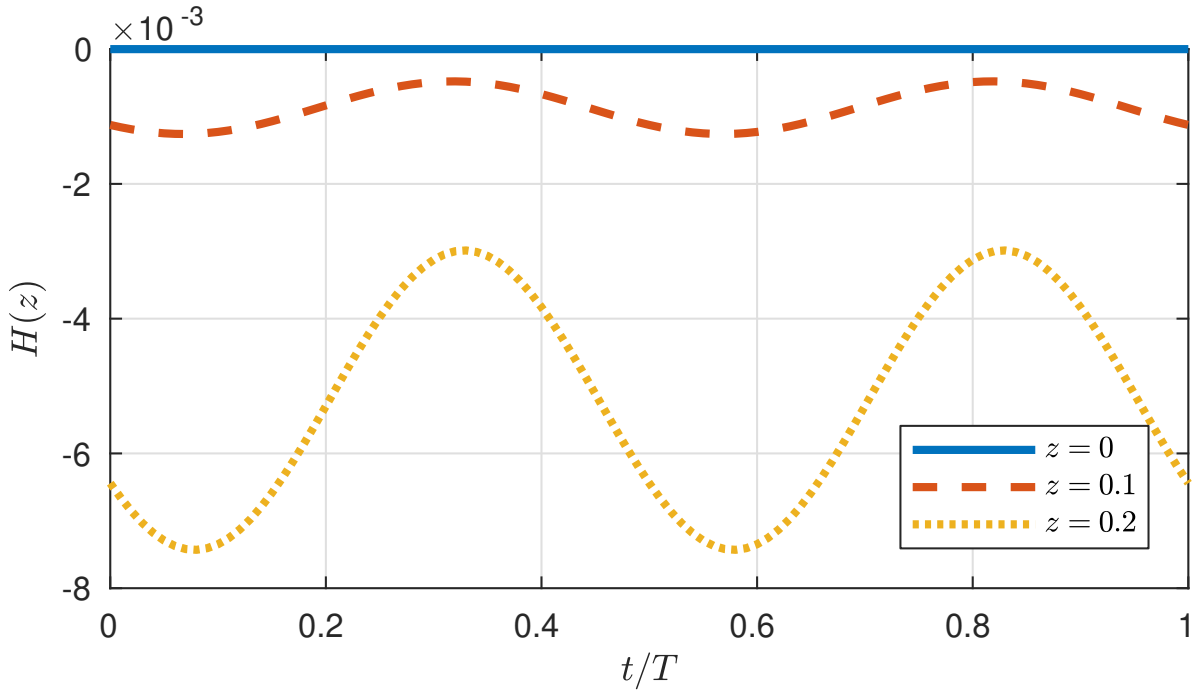

Figure 5.4: Time history of vertical velocity at selected locations $z = 0$ (-), $z = 0.1$ (- - -) and $z = 0.25$ ($\cdots$) over one period of oscillation with $\epsilon = 0.25$.

5.1.1 Local Linear Stability of the Torsionally Oscillating Disk Boundary Layer

We proceed here to develop the methodology required to analyse the stability of the oscillatory flow configuration discussed in the previous section, and begin by deriving an appropriate Reynolds number based on the Stokes length scale δ_s^* and the local velocity scale $r_L^*\epsilon\phi^*$ where r_L is a local radial position. This gives

$$R = \frac{r^*\epsilon\phi^*\delta_s^*}{\nu^*} = \epsilon r_L \tag{5.5}$$

for $r_L = \frac{r_L^*}{\delta_s^*}$ the non-dimensional radial position. Thus we can fully specify the motion by supplying the two non-dimensional parameters (R, ϵ). The base flow can be represented similarly to the steady case as

$$\mathbf{U}_B = \left(\frac{\epsilon r}{R}F, \frac{\epsilon r}{R}G, \frac{\epsilon}{R}H\right) \tag{5.6}$$

This gives a similar velocity-vorticity formulation to that for the rotating disk in chapter 2,

$$\frac{1}{R}\frac{\partial\xi_r}{\partial t} + \frac{1}{r}\frac{\partial N_z}{\partial\theta} - \frac{\partial N_\theta}{\partial z} = \frac{1}{R}\left[\left(\nabla^2 - \frac{1}{r^2}\right)\xi_r - \frac{2}{r^2}\frac{\partial\xi_\theta}{\partial\theta}\right] \tag{5.7a}$$

$$\frac{1}{R}\frac{\partial\xi_\theta}{\partial t} + \frac{\partial N_r}{\partial z} - \frac{\partial N_z}{\partial r} = \frac{1}{R}\left[\left(\nabla^2 - \frac{1}{r^2}\right)\xi_\theta + \frac{2}{r^2}\frac{\partial\xi_r}{\partial\theta}\right] \tag{5.7b}$$

$$\nabla^2 w = \frac{1}{r}\left(\frac{\partial\xi_r}{\partial\theta} - \frac{\partial(r\xi_\theta)}{\partial r}\right) \tag{5.7c}$$

where $\mathbf{N}$ is given by (2.38) and the $\frac{1}{R}$ factor in the temporal derivative term arises from the temporal scale of choice. The secondary variables (u_r, u_θ, ξ_z) can be represented in terms of the primary variables in an identical way to chapter 2, given by (2.37). The notable lack of the Coriolis terms in (5.7) is a consequence of working in a non-rotating laboratory frame, in contrast to the methods presented in chapter 2. Since we do not have a mean rotation rate in this scenario, the concept of a rotating frame of reference is illogical and thus, for the remainder of this section, we will work only in the non-rotating frame.

As in chapter 3, we have several methods at our disposal for analysing the stability of these time-dependent flow configurations. We could use a combination of eigenvalue analyses from Floquet theory and *frozen flow* approximations, in conjunction with more global treatments from both monochromatic simulations and simulations with the full radial dependence incorporated. Since this exposition is intended to be merely an indication

to future directions, we present only the formulation of the Floquet analysis, and leave any corresponding results to future work. The methods of Floquet analysis are virtually identical to those already presented in chapter 2 and so in the interest of concision, we will only reiterate the main points here and the interested reader is directed there for a more thorough explanation.

Floquet Theory

As in chapter 3, the Floquet stability analysis may be undertaken by introducing small disturbances to the unsteady base flow $\mathbf{U}^B$ and writing

$$\mathbf{u}(\mathbf{x},\tau) = \mathbf{U}^B(z,\tau) + \epsilon\mathbf{u}'(\mathbf{x},\tau), \quad \xi(\mathbf{x},\tau) = \Lambda(z,\tau) + \epsilon\xi'(\mathbf{x},\tau)$$

Again following chapter 3 and in particular the method developed by Hall [39], we assume a Floquet-mode approximation of the form

$$f(r,\theta,z,\tau) = \hat{f}(z,\tau)e^{\mu\tau}e^{i(\alpha r+\beta R\theta)} + c.c. \tag{5.8}$$

where $\hat{f}(z,\tau)$ is a time-periodic function with the same period as that of the modulation and all exponential growth of $\hat{f}(z,\tau)$ is incorporated into the Floquet exponent $e^{\mu\tau}$. The *c.c.* denotes the complex conjugate, which is added to ensure that the disturbance is real. The quantities of interest here will be μ, as its real part specifies the temporal growth of the disturbance, and α, whose imaginary part gives the spatial growth rate. The βR term is introduced into the normal-mode solution so as to maintain the structure of the steady rotating disk. Whether or not the value $n = \beta R$ retains its experimental importance is as yet unclear, and any radial homogenisation, parallel flow approximation or replacement of R by ϵR should be treated with extreme caution. At the time of writing, no exploration of the effects of the radial homogenisation has been conducted, and such a study is reserved for future work.

Substitution of (5.8) into (5.7), along with linearisation and neglect of the non-parallel $\mathcal{O}\left(\frac{1}{R^2}\right)$ terms gives

$$\frac{1}{R}\frac{\partial\xi_r}{\partial\tau} + \mu\xi_r + \frac{i\beta R}{\epsilon r}N_z - \frac{\partial N_\theta}{\partial z} = \frac{1}{R}\left(-\alpha^2 - \left(\frac{\beta R}{\epsilon r}\right)^2 + \frac{\partial^2}{\partial z^2}\right)\xi_r \tag{5.9a}$$

$$\frac{1}{R}\frac{\partial\xi_\theta}{\partial\tau} + \mu\xi_\theta + \frac{\partial N_r}{\partial z} - \frac{\partial N_z}{\partial r} = \frac{1}{R}\left(-\alpha^2 - \left(\frac{\beta R}{\epsilon r}\right)^2 + \frac{\partial^2}{\partial z^2}\right)\xi_\theta \tag{5.9b}$$

$$\left(\hat{\nabla}^2 + \frac{\partial^2}{\partial z^2}\right)w = \frac{i\beta R}{\epsilon r}\xi_r - i\alpha\xi_\theta - \frac{\xi_\theta}{r} \tag{5.9c}$$

Similarly to chapter 2, using the method of Hall [39], we decompose the perturbation variables and base flow velocity fields into harmonics so that

$$\hat{f}(z,\tau) = \sum_{n=-\infty}^{\infty} f_n(z) e^{in\tau} \tag{5.10}$$

and

$$\mathbf{U}^B = \sum_{k=-\infty}^{\infty} \mathbf{u}_k(z) e^{ik\tau} \tag{5.11a}$$

The Fourier coefficients $\mathbf{u}_k(z)$ are calculated from the time-dependent solution data via a fast Fourier transform, as in chapter 2.

The parallel flow approximation and radial homogenisation in this scenario amounts to replacing ϵr by R in (5.9) as per the local definition of R. Due to the subtleties in the global behaviour discussed in chapter 4 for the rotating disk, this approximation would necessarily require rigorous justification in any future studies carried out on this flow configuration. For the purposes of the following presentation, we will assume that this is a valid approximation to make, and present the derivations of the corresponding stability equations. We make no attempt here to justify this step, and leave the reader simply with a remark that the implications of such an approximation are unknown at this time. Therefore, applying the parallel flow approximation and replacing ϵr by R, the secondary variable ξ_θ and the convective terms $\mathbf{N}$ become

$$N_r = F'w - \frac{2\epsilon}{R} G u_\theta + \frac{\epsilon}{R} H \xi_\theta - G\xi_z \tag{5.12a}$$

$$N_\theta = G'w + \frac{2\epsilon}{R} G u_r - \frac{\epsilon}{R} H \xi_r + F\xi_z \tag{5.12b}$$

$$N_z = G\xi_r - G'u_\theta - F'u_r - F\xi_\theta \tag{5.12c}$$

$$\frac{\partial N_z}{\partial r} = i\alpha(G\xi_r - G'u_\theta - F'u_r - F\xi_\theta) + \frac{1}{R}\left(G\xi_r - G'u_\theta - F'u_r - F\xi_\theta\right) \tag{5.12d}$$

and

$$\xi_z = \int_0^\infty \left(\frac{\epsilon}{R}\xi_r + i\alpha\xi_r + i\beta\xi_\theta \right) dz \tag{5.13}$$

while u_r and u_θ are still given by (2.50). Subsequently, this problem reduces to a set of $2K+1$ dispersion relations of the form

$$\sum_{m=-K}^{K} \mathcal{D}_m\{\mu, \alpha\ R, \beta\} e^{im\tau} = 0 \tag{5.14}$$

where K is a truncation parameter, chosen so that the eigenvalues calculated are independent of the choice of K. It is anticipated that the number of harmonics necessary to

fully resolve the eigenvalue solutions would be of the order of that for the Stokes layer, namely $\mathcal{O}(\alpha R)$, which may cause computational difficulties on implementation of this method. As for the periodically modulated case, there are two distinct types of analysis which can be conducted, namely *temporal* and *spatial*. The *temporal* approach consists of specifying $\alpha \in \mathbb{R}$ and calculating μ from (3.13) while the *spatial* approach specifies $\mu \in \mathbb{R}$ and calculates α from (3.13). As yet, no such study has been conducted, and is reserved for future work.

5.1.2 Hydrodynamic Voltammetry at Rocking Disk Electrodes

The primary motivation for the modulation of the rotation rate in the rotating disk boundary layer was that of methods for laminar flow control on swept wings. We utilised the commonly applied approximation that the rotating disk exhibits similar instability mechanisms to the flow over a swept wing, and applied constraints based on this application. These constraints amounted to a small deviation in the rotation rate from the steady case, and as such no mind was paid to any configurations with large oscillatory parts. Moving away from this application allows us the freedom to explore the other end of the spectrum and in particular torsional oscillations. Mathematical curiosity is a valid motivation for the study of such a system, as it is a fundamental flow configuration for which no previous hydrodynamic stability studies have been conducted. Indeed, it is arguably the simplest three-dimensional oscillatory flow configuration and its study is in natural progression from that of the two-dimensional Stokes layer. However, during the course of this work, an explicit application of such a configuration was discovered in the field of electrochemical engineering. This application is as a result of Cummings et. al.'s [22] modification to the more classically studied *rotating disk electrode*, for which we will provide an introductory overview.

Voltammetry is the name given to a class of methods used in analytical chemistry and various industrial processes. In voltammetry, information about an analyte is obtained by measuring the current at a working electrode as the potential is varied in a controlled way. This current can be easily influenced or disturbed by convective behaviour of ions in the solution, and any fluctuations in the current measured at the electrode can have detrimental effects on the reproducibility and reliability of results. Thus, the solution movement is critical to the experiment, and mass transfer at the electrode surface is often

controlled by forced convection of the analyte. There are several methods commonly used for such a forced convection, the most important of which for our applications is that of the *rotating disk electrode*.

The steady-state laminar flow properties of the rotating disk electrode are widely known in the chemical engineering literature, see [24, 35, 16, 61], and Lingwood [43] references Chin and Litt [18] for their study of the instability properties of the steady system from an electrochemical engineering perspective. The modification to the rotating electrode proposed by Cummings et al. [22, 23] and Ahn et al. [1, 2] utilises a *rocking* motion for the disk instead, which the relevant authors claim is a novel but easier experimental setup which gives comparable results. However, the hydrodynamic stability properties of such a system are as yet mathematically poorly understood, and Marken et. al.[1] have only empirically determined the steady state solution and turbulence breakdown properties. Therefore, a fundamental mathematical study of the configuration, in tandem with experimental data from the chemical engineering research, must be conducted to properly understand the stability and transition properties. Such a study has great relevance to both fields, would be the first systematic mathematical study of this three-dimensional fundamental configuration and would enable the chemical engineering applications to proceed in an optimal way, providing *a priori* assumptions about the flow configuration.

5.2 The Rotating Disk Boundary Layer with Surface Roughness

As alluded to in section 3.1, other stabilising techniques for the steady rotating disk boundary layer have been studied by many authors such as designed surface roughness, see Garrett et al. [36], Cooper et al. [21] and wall compliance, see Cooper and Carpenter [19, 20]. Both of these techniques show stabilisation of the type I instability for stationary disturbances, and Garrett et al. [36] use this as an advertisement for further study of laminar flow control techniques using designed surface roughness on swept wings. In all of these aforementioned studies, some form of modelling is carried out whether it be of the surface or of the flow. This modelling results in an averaging procedure which essentially removes first-order effects and potentially interesting contributions therein.

[1] personal communication

The temporally periodic configuration discussed in the main body of this thesis requires no such modelling, and as such retains the full range of information from the basic state.

Garrett et al. [36] and Cooper et al. [21] describe theoretical results investigating effects of distributed surface roughness on the convective stability of the rotating disk boundary layer using two distinct approaches to the modelling of the disk surface. It has now been firmly established that contrary to the classic belief, the interaction of boundary layer flow with the *right sort of roughness*, as discussed by Carpenter [17], can result in energetically beneficial, drag-reducing effects.

The two approaches considered by Garrett et al. [36] are the so-called MW and YHP models, attributed to Miklavčič and Wang [52] and Yoon et al. [84], and consist of different ways of modelling the surface. The MW model for roughness replaces the usual no-slip boundary conditions with partial-slip conditions at the disk surface. As described in Garrett et al. [36], this is achieved by introducing slip factors in Newton's law of viscosity for the azimuthal and radial velocity component. Selecting different slip factors for each component enables modelling roughness distributed in the radial and azimuthal directions. The authors refer to the case where both slip factors are equal as isotropic roughness, whereas different values for the slip factors represent anisotropic roughness.

The YHP approach models roughness by directly imposing a particular surface profile as a function of the radial position and, since it assumes rotational symmetry, can only model anisotropic roughness. A major advantage of the YHP approach over the MW model is that a specific geometric roughness height can be defined explicitly in terms of the amplitude and the wavelength of the surface profile.

The following sections will outline the methods of Garrett et al. [36] and present results reproduced using the methods of chapter 2 which are consistent with the previous literature. We begin our discussion with an overview of the MW model before giving a brief account of the YHP model and some insights for future directions. These following sections are not intended to be novel, but will serve as a useful overview of this currently highly active field of research and allude to potentials for future collaborative work.

5.2.1 The Partial Slip Model (MW)

In 1921, von Kármán formulated the exact similarity solution to the Navier-Stokes equations for the steady laminar flow over a rotating disk of infinite radius and section 2.1.1

gave a detailed presentation of the solution methods we have employed in this work. A brief recap of the fundamental equations will be given here in the interest of concision, but the reader is referred to section 2.1.1 for further details. Following von Kármán and the nomenclature employed throughout this thesis, let U^*, V^* and W^* denote the dimensional radial, azimuthal and axial similarity velocities respectively and r^* and z^* denote the dimensional radial position and wall-normal height. Let also ν^* denote the kinematic viscosity and Ω_0^* the angular velocity of the disk. For the results presented in this section, in contrast to the majority of this thesis, Ω_0^* will be taken to be constant.

Under von Kármán's [80] similarity scaling, we normalise the velocity fields on a local scale $r^*\Omega_0^*$ and the lengths on the boundary layer thickness $\delta^* = \sqrt{\frac{\nu^*}{\Omega^*}}$ to get

$$F(z) = \frac{U^*}{r^*\Omega_0^*}, \quad G(z) = \frac{V^*}{r^*\Omega_0^*}, \quad H(z) = \frac{W^*}{\delta^*\Omega_0^*} \tag{5.15}$$

which gives the system of ordinary differential equations governing the base flow as

$$F^2 - G^2 + F'H - F'' = 0 \tag{5.16a}$$

$$2FG + G'H - G'' = 0 \tag{5.16b}$$

$$H' = -2F \tag{5.16c}$$

This local scaling gives a Reynolds number R, associated with the steady rotation of the disk as

$$R = \frac{r_L^*\Omega_0^*\delta^*}{\nu^*} = \frac{r_L^*}{\delta^*} = r_L \tag{5.17}$$

where we identify r_L as a local, non-dimensional radial position. The partial slip model for roughness is imposed by a boundary condition alteration of the radial and azimuthal components of the base flow to give

$$F(0) = \lambda F'(0), \quad G(0) = \epsilon G'(0) \quad H(0) = 0 \tag{5.18a}$$

$$F(\zeta) \to 0, \quad G(\zeta) \to -1 \quad \text{as} \quad \zeta \to 0 \tag{5.18b}$$

Non-zero λ corresponds to radially isotropic roughness while non-zero ϵ corresponds to radially anisotropic roughness. Taking $\lambda = \epsilon = 0$ recovers the smooth case. Since we will primarily be using this method to compare and contrast against the YHP approach which models anisotropic roughness, we will set $\lambda = 0$ for the remainder of this section.

As explained in section 2.1.1, this system can be solved with a relatively straightforward application of MATLAB's *bvp4c* solver, and evaluated at the Chebyshev collocation

points required for the solution procedure. It is worth noting that out-of-the-box, *bvp4c* has issues with directly solving the equation on a large physical domain. In fact, it is numerically unstable over $[0, a]$ for $a > 12$. This was avoided by introducing an iterative scheme which used the solution over $[0, K]$ as an initial guess for the solution over $[0, K+1]$ and proceeded for $K \geq 1$. Figure 5.5 shows the base flow profiles for varying degrees of anisotropic roughness, achieved by alteration of the parameter ϵ in (5.18). These diagrams agree with those presented by Garrett et al. [36].

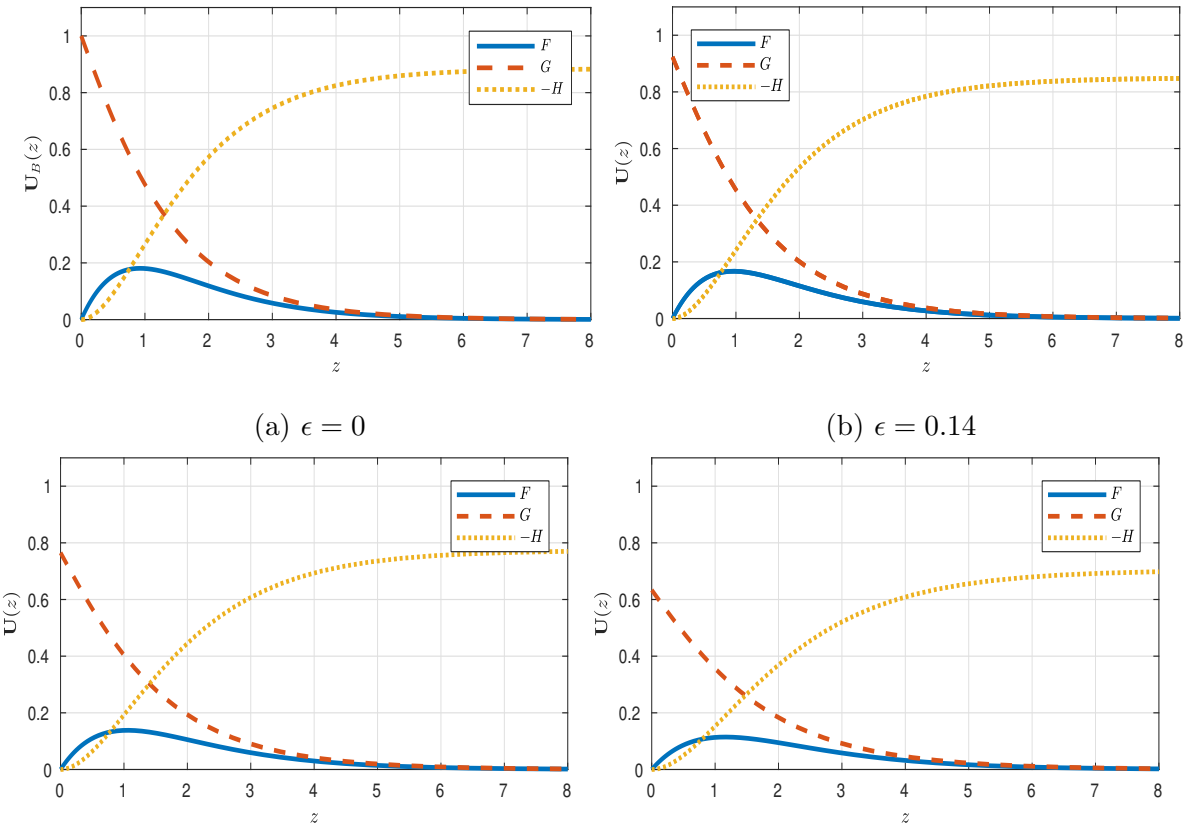

(a) $\epsilon = 0$ (b) $\epsilon = 0.14$

(c) $\epsilon = 0.57$ (d) $\epsilon = 1.18$

Figure 5.5: Radial (—), azimuthal (- - -) and vertical ($\cdots$) base flow profiles for the rotating disk boundary layer with radially anisotropic surface roughness, imposed by the partial slip MW model. Various values of ϵ are shown, corresponding to varying degrees of anisotropic roughness.

5.2.2 The Surface Geometry Model (YHP)

As discussed in Garrett et al. [36], after scaling lengths on the boundary layer thickness $\delta^* = \sqrt{\frac{\nu^*}{\Omega^*}}$ and velocities on the local scale $r^*\Omega^*$ where Ω^* is the disk rotation rate, we define a non-dimensional surface roughness function as

$$s(r) = \Lambda \cos\left(\frac{2\pi r}{\gamma}\right) \tag{5.19}$$

This particular form of $s(r)$ gives rise to two non-dimensional control parameters, namely Λ and γ, which may be interpreted as the height and pitch of the roughness respectively. The authors subsequently define an aspect ratio *roughness parameter*

$$a := \frac{\Lambda}{\gamma} \tag{5.20}$$

as a single parameter describing the surface. Both parameters Λ and γ are expressed in units of boundary layer thickness as a consequence of the spatial scalings and the standard von Kármán system are recovered by imposing $a = 0$.

The base flow equations analogous to the von Kármán ODEs (2.12) may be described by first applying a coordinate transformation $\zeta = z - s(r)$ to give the usual base flow quantities $\mathbf{U}_B = (U, V, W)$ by the transformed variables

$$\begin{aligned} u(r, \hat{\zeta}) &= U(r, z) \\ v(r, \hat{\zeta}) &= V(r, z) \\ w(r, \hat{\zeta}) &= -s'(r)U(r, z) + W(r, z) \end{aligned}$$

Scaling the radial dependence in an analogous way to von Kármán and applying the boundary layer approximation by setting $R^{-1} = r_L^{-1} \ll 1$ with $\zeta = R\hat{\zeta}$, we get

$$\begin{aligned} f(r, \zeta) &= \frac{1}{r}u(r, \zeta) \\ g(r, \zeta) &= \frac{1}{r}v(r, \zeta) \\ h(r, \zeta) &= w(r, \zeta) \end{aligned}$$

which results in a system of equations which determine the base flow given by

$$2f + r\frac{\partial f}{\partial r} + \frac{\partial h}{\partial \zeta} = 0 \tag{5.23a}$$

$$rf\frac{\partial f}{\partial r} + h\frac{\partial f}{\partial \zeta} + \left(1 + r\frac{s's''}{1 + s'^2}\right) = \left(1 + s'^2\right)\frac{\partial^2 f}{\partial \zeta^2} + \frac{(1+g)^2}{1+s'^2} \tag{5.23b}$$

$$rf\frac{\partial g}{\partial r} + h\frac{\partial g}{\partial \zeta} = \left(1 + s'^2\right)\frac{\partial^2 g}{\partial \zeta^2} - 2f(1+g) \tag{5.23c}$$

This system is complemented by the boundary conditions

$$f(r,0) = g(r,0) = h(r,0) = 0 \tag{5.24a}$$

$$f(r,\zeta) \to 0, \quad g(r,\zeta) \to -1 \quad \text{as} \quad \zeta \to 0 \tag{5.24b}$$

which represent the no-slip and far-field decay conditions at all radial positions in the rotating reference frame. Note that the usual von Kármán equations (2.12) are recovered if $s(r) = 0$, as would be expected.

A notable difference in terms of the base flow equations between the MW and YHP models is that the YHP method results in a system of partial, rather than ordinary differential equations. Garrett et al. [36] solve these equations (5.23) using the NAG routine D03PEF, although we use MATLAB's *bvp5c* here. The solvers use an initial solution given by

$$f(r,\zeta) \sim rF(\zeta), \quad g \sim rG(\zeta), \quad h \sim H(\zeta) \tag{5.25}$$

at $r = 0$ to find the velocity profiles at the next increment of r and step forward. This initial condition is the result of the assumption that the von Kármán equations (5.16) should be recovered as $r \to 0$. Garrett et al. [36] argue that the flow field arising from the solution to (5.23) vary at two distinct spatial scales in the radial direction, namely a scale associated with γ and the similarity scale with r, as per von Kármán. They proceed to state that since they choose $\gamma \lesssim O(10^{-1})$, it is a reasonable approximation to take a spatial average of the flow field over any complete cycle in r, thereby leading to a modified von Kármán mean flow $(\hat{f}(z), \hat{g}(z), \hat{h}(z))$. This method has the distinct advantage of allowing previous normal-mode analyses to be achieved without much modification, although the physical interpretation of such an averaging procedure is unclear and should be explored further. It is this further exploration that we will discuss during the following exposition, and allude to potentials for using the numerical simulation techniques of chapter 4 to calculate the flow response to genuine surface roughness. Figure 5.6 shows the base flow profiles for varying degrees of anisotropic roughness, achieved by alteration of the parameter a in (5.20). These diagrams agree with those presented by Garrett et al. [36].

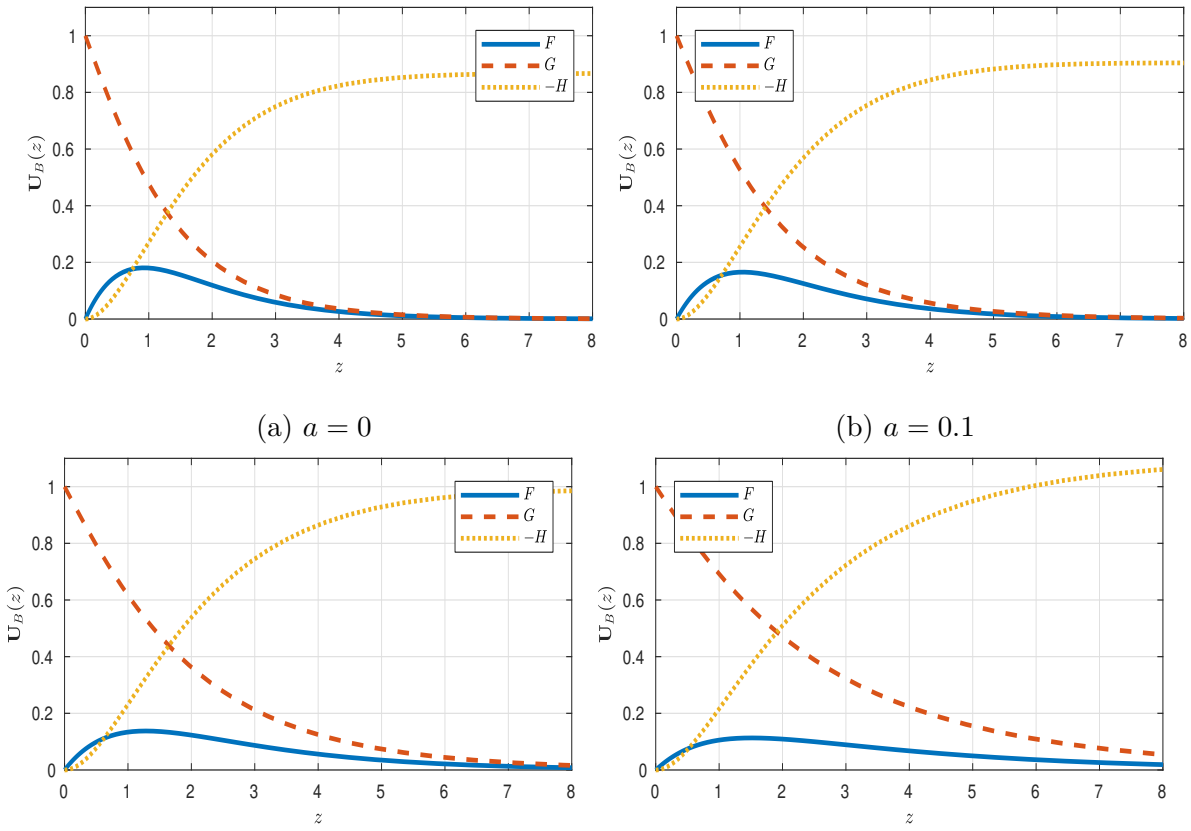

(a) $a = 0$ (b) $a = 0.1$

(c) $a = 0.2$ (d) $a = 0.3$

Figure 5.6: Averaged radial (—), azimuthal (- - -) and vertical ($\cdots$) base flow profiles for the rotating disk boundary layer with radially anisotropic surface roughness, imposed by the surface geometry YHP model. Various values of a are shown, corresponding to varying degrees of anisotropic roughness. The quantity a is defined by equation (5.20).

5.2.3 Future Directions for Surface Roughness

We conclude this chapter with a brief discussion of the potentials for future work analysing the stabilisation of the rotating disk boundary layer via imposed surface roughness. Both approaches taken by Cooper et al. [21] and Garrett et al. [36] and discussed in the preceding sections involve a model for the surface roughness that culminates in either a potentially unphysical averaging process or a procedure that inherently neglects first order effects in the system. The numerical methods proposed to deal with the modulated rotation rate introduced in chapters 2 - 4 require no such modelling, and may therefore allow first order effects to be considered more cleanly. In terms of the spatial averaging procedure involved in the YHP model, while required to ensure separability in the radial direction and enable a normal mode analysis, such an averaging is not required if the inhomogeneous simulations discussed in section 4.3 are used instead. As described in section 5.2.2, the YHP model involves a spatial average of the flow field over any complete cycle in r, thereby leading to a modified von Kármán mean flow $(\hat{f}(z), \hat{g}(z), \hat{h}(z))$ which may be fed into the existing normal mode analyses as a modified base flow. The simulations of section 4.3, by construction, allow for a radial dependence to be incorporated directly into the base flow, leaving the full radial structure given by the results of equations (5.23) to be retained throughout the simulations.

Furthermore it is the author's belief, which we stress at this time is untested conjecture, that the simulations may be used to directly impose radially anisotropic surface roughness without any modification to the base flow or inherent periodic modelling of the surface. Since the simulations are based on Chebyshev spectral methods in the wall-normal direction, it is practical and feasible to impose boundary conditions at any vertical location in space, in a similar manner to that described in the appendices of Davies and Carpenter [26]. This would allow for a base flow and the subsequent evolution of any perturbations to be calculated explicitly by the simulations for arbitrary roughness, provided the roughness extended only along one radial direction and was not azimuthally localised. Such a study would confirm or otherwise the modelling procedures of Cooper et al. [21] and Garrett et al. [36] and potentially provide a physically truer demonstration of the modifications to the stability properties introduced by surface roughness.

Chapter 6

Conclusions

The main result of this thesis is to have demonstrated, in various configurations, that the addition of a modulated rotation rate stabilises the boundary layer formed above a rotating disk. We have also discussed and described novel solution methods for conducting linear stability analyses of steady and temporally periodic two and three dimensional boundary layers, which were presented in the context of application to several canonical flow configurations. Chapter 1 described the solution methods for the two dimensional Blasius boundary layer and the Stokes boundary layer formed above an oscillating flat plate. Chapter 2 introduced a three dimensional boundary layer over a disk rotating at a steady rate and presented results validating the novel numerical method against previous work in the literature. Chapters 3 and 4 discussed the effects of the modulated rotation rate on the stability properties for both stationary disturbances and those resulting from a radially localised impulsive forcing. Chapter 5 alluded to potential avenues for future study, including techniques in electrochemistry and the effects of surface roughness. The solution method employed utilised a velocity-vorticity formulation, first seen in Davies and Carpenter [26], and while we only presented the three dimensional results for a cylindrical polar coordinate system, the corresponding methodology for a Cartesian coordinate system should be evident.

A key advantage of this approach over traditional primitive variable methods for the rotating disk problem is that under the velocity-vorticity formulation of Davies and Carpenter [26], the perturbation equations reduce to three coupled second order equations, as opposed to six of first order. The perturbation equations comprise of three primary variables; the perturbations to the wall-normal velocity component and the two vorticity

components in the plane of the wall and three secondary variables; the perturbations to the remaining velocity and vorticity components. The implementation of the Chebyshev-tau method of Bridges and Morris [14] in tandem with the velocity-vorticity formulation provides a convenient framework for the linear stability analysis of many flow configurations, and we have presented a format for dealing with the secondary variables and boundary integral constraints in a novel way.

Our solution method employs a Chebyshev discretisation in the wall-normal direction, and utilises the Chebyshev-tau method to form systems of integral eigenvalue dispersion relations which are solved by the MATLAB polynomial eigenvalue solver package *polyeig*. The boundary conditions and integral constraints placed on the primary variables are incorporated into the system by replacing the rows of the matrices that would otherwise correspond to the arbitrary constants of integration, and the secondary variables are calculated directly from the primary variables by means of matrix multiplications which correspond to the integral operators from the application of the Chebyshev-tau method.

Validation has been presented for our solution method against the literature for the steady rotating disk boundary layer and the semi-infinite Stokes layer above an oscillating flat plate. As a preliminary investigation, validation for a two dimensional steady configuration has also been undertaken against the Blasius boundary layer (see [65]), with good agreement being found in all cases.

Chapter 3 presents illustrative results for a novel flow configuration, and explores the stabilising properties of the addition of a modulated rotation rate to the steady rotating disk boundary layer in the case of disturbances which are stationary with respect to the disk motion. This configuration is three dimensional and temporally periodic, and the sections detail the first mathematical application of Floquet theory to the stability of three dimensional temporally periodic boundary layers. We demonstrated several parametric studies of the influence of modulation frequency and angular displacement on the stabilisation, and validated results using four independent methods; a Floquet dispersion relation, quasi-steady frozen profile analyses, monochromatic direct numerical simulations and simulations which retain the radial dependence of the flow. Each independent solution method was shown to be consistent with the others. Following the presentation of simulation results, an attempt was made to shed further light on the findings using an energy analysis. This analysis showed a strong correlation between reduction in one of

the energy production terms and the stabilisation behaviour, indicating an area for future exploration as to the cause of the behaviour. It is worth noting that the reductions in the energy production term can be substantially larger than other stabilisation techniques reported in the literature (such as [20, 19, 21, 36]), indicating a much stronger stabilisation mechanism for our configuration in certain parameter cases. It would, however, be erroneous to claim that we have understood the true nature of the stabilisation following this work, and further study must be undertaken before concluding as such.

Chapter 4 presents an exploration of the local absolute instability present in the rotating disk boundary layer, and a discussion of the effects of the modulated rotation rate on the global behaviour incorporating radial inhomogeneity. This chapter looks at the evolution of a disturbance in the boundary layer following a localised impulsive forcing at some fixed radial location, and compares results in the modulated scenario to the steady-state literature (see [27, 28, 72, 74, 3, 4, 5]). There has been limited previous work on stabilisation techniques for impulsive forcing in the rotating disk boundary layer, and this exploration constitutes one of the first such studies. Many other authors, such as Cooper and Carpenter [20], Cooper et al. [21], Garrett et al. [36] examine only stationary or fixed-frequency disturbances and do not incorporate the full spatio-temporal disturbance structure into their analyses of stabilisation techniques. Cooper and Carpenter [19] explore the effects of wall compliance on the absolute instability in the flow, but this reference pre-dates the Davies and Carpenter [27] study on the global behaviour. Therefore, the author is presently unaware of any studies which incorporate the radial inhomogeneity and global disturbance structure into an analysis of stabilisation techniques. Such an analysis was conducted in the latter stages of chapter 4, where a strong stabilisation was shown in both radially homogeneous and inhomogeneous cases for impulsive forcing with periodic modulation of the rotation rate. For certain parameter cases, the local absolute instability present in the radially homogeneous configuration was stabilised, as shown by the spatio-temporal contours in figure 4.7. A full parametric study, and analytical explanation of this absolute instability was not presented, and such an analysis is left for future work. However, from the brief preliminary explorations conducted as part of the background to this thesis, it is anticipated that similar behaviour to the stationary forcing will be discovered, in that the range of $\varphi \approx 10$ will contribute the strongest stabilisation while modulations with $\varphi >> 20$ will have little effect.

The final chapter of this thesis described some potentials for future directions beginning with torsional oscillations and applications to certain electrochemical processes. These avenues for further study were briefly introduced to give a flavour for the potential applications of our new methods and to indicate the necessity for a fundamental study of the stability properties of the torsionally oscillating disk; a configuration which is arguably the canonical three-dimensional oscillatory boundary layer and to date has not been studied from a stability framework. Finally, the chapter concluded with an overview of the effects of designed surface roughness on the stability properties of the steady rotating disk boundary layer and some parallels between this configuration and the one with a modulated rotation rate. Two models, see ([21], [36]) were discussed briefly, as a precursor to future studies involving the numerical methods described throughout this report. Future work on such a configuration could involve arbitrarily distributed surface roughness, with the numerical simulations of chapter 4 being utilised to calculate the base flow and subsequent disturbance development.

Bibliography

[1] S. D. Ahn, P. E. Frith, A. C. Fisher, A. M. Bond, and F. Marken. Mass transport and modulation effects in rocking dual-semi-disc electrode voltammetry. *Journal of Electroanalytical Chemistry*, 722-723:78–82, 2014. ISSN 1572-6657. doi: https://doi.org/10.1016/j.jelechem.2014.02.018.

[2] S. D. Ahn, K. Somasundaram, H. V. Nguyen, E. Birgersson, J. Yang Lee, X. Gao, A. C. Fisher, P. E. Frith, and F. Marken. Hydrodynamic voltammetry at a rocking disc electrode: Theory versus experiment. *Electrochimica Acta*, 188:837–844, 2016. ISSN 0013-4686. doi: https://doi.org/10.1016/j.electacta.2015.11.143.

[3] E. Appelquist. *Direct numerical simulations of the rotating-disk boundary-layer flow*. PhD thesis, KTH Royal Institute of Technology, 2014.

[4] E. Appelquist, P. Schlatter, P. H. Alfredsson, and R. J. Lingwood. Global linear instability of the rotating-disk flow investigated through simulations. *Journal of Fluid Mechanics*, 765:612–631, 2 2015. ISSN 1469-7645. doi: 10.1017/jfm.2015.2.

[5] E. Appelquist, S. Imayama, P. H. Alfredsson, P. Schlatter, and R.J. Lingwood. Linear disturbances in the rotating-disk flow: A comparison between results from simulations, experiments and theory. *European Journal of Mechanics - B/Fluids*, 55, Part 1: 170–181, 2016. ISSN 0997-7546. doi: http://dx.doi.org/10.1016/j.euromechflu.2015.09.010.

[6] E. Appelquist, P. Schlatter, P. H. Alfredsson, and R. J. Lingwood. Transition to turbulence in the rotating-disk boundary-layer flow with stationary vortices. *Journal of Fluid Mechanics*, 836:43–71, 2018. doi: 10.1017/jfm.2017.771.

[7] P. Balakumar and M. R. Malik. Traveling disturbances in rotating-disk flow. *Theoretical and Computational Fluid Dynamics*, 2(3):125–137, 1990. ISSN 0935-4964.

[8] A. J. Bard and L. R. Faulkner. *Electrochemical Methods: Fundamentals and Applications*. John Wiley and Sons, 2000. ISBN 9780470452530.

[9] D. J. Benney. The flow induced by a disk oscillating in its own plane. *Journal of Fluid Mechanics*, 18(3):385–391, 1964. doi: 10.1017/S0022112064000283.

[10] P. J. Blennerhassett and A. P. Bassom. The linear stability of high-frequency oscillatory flow in a channel. *Journal of Fluid Mechanics*, 556:1–25, 2006.

[11] P. J. Blennerhassett and Andrew P. Bassom. The linear stability of flat stokes layers. *Journal of Fluid Mechanics*, 464:393–410, 2002.

[12] John P. Boyd. Spectral methods in fluid dynamics. *SIAM Review*, 30(4):666–668, 1988. doi: 10.1137/1030157.

[13] J.P. Boyd. *Chebyshev and Fourier Spectral Methods: Second Revised Edition*. Dover Books on Mathematics. Dover Publications, 2001. ISBN 9780486411835.

[14] T. J. Bridges and P. J. Morris. Differential eigenvalue problems in which the parameter appears nonlinearly. *Journal of Computational Physics*, 55:437–460, 1984.

[15] R. J. Briggs. *Electron-stream Interaction with Plasmas*. Cambridge: MIT, 1964.

[16] S. Bruckenstein and B. Miller. Unraveling reactions with rotating electrodes. *Accounts of Chemical Research*, 10(2):54–61, 1977. doi: 10.1021/ar50110a004.

[17] P. Carpenter. The right sort of roughness. *Nature*, 388:713–714, 1997. doi: 10.1038/41870.

[18] D. T. Chin and M. Litt. An electrochemical study of flow instability on a rotating disk. *Journal of Fluid Mechanics*, 54:613–625, 1972. doi: 10.1017/S0022112072000904.

[19] A. J. Cooper and P. W. Carpenter. The stability of rotating-disc boundary-layer flow over a compliant wall. part 2. absolute instability. *Journal of Fluid Mechanics*, 350:261–270, 11 1997.

[20] A. J. Cooper and P. W. Carpenter. The stability of rotating-disc boundary-layer flow over a compliant wall. part 1. type i and ii instabilities. *Journal of Fluid Mechanics*, 350:231–259, 1997. doi: 10.1017/S0022112097006976.

[21] A. J. Cooper, J. H. Harris, S. J. Garrett, M. Özkan, and P. J. Thomas. The effect of anisotropic and isotropic roughness on the convective stability of the rotating disk boundary layer. *Physics of Fluids*, 27(1):1–16, 2015.

[22] C. Y. Cummings, P. E. Frith, G. Zoppi, I. Forbes, K. D. Rogers, D. W. Lane, and F. Marken. Rocking disc electro-deposition of copper films on mo/mose2 substrates. *Thin Solid Films*, 519(21):7458 – 7463, 2011. ISSN 0040-6090. doi: https://doi.org/10.1016/j.tsf.2010.12.107. Proceedings of the EMRS 2010 Spring Meeting Symposium M: Thin Film Chalcogenide Photovoltaic Materials.

[23] C. Y. Cummings, G. Zoppi, I. Forbes, D. Colombara, L. M. Peter, and F. Marken. Rocking disc electro-deposition of cuin alloys, selenisation, and pinhole effect minimisation in cise solar absorber layers. *Electrochimica Acta*, 79:141 – 147, 2012. ISSN 0013-4686. doi: https://doi.org/10.1016/j.electacta.2012.06.095.

[24] F. Dalton. Ecs classics: Historical origins of the rotating ring-disk electrode. *The Electrochemical Society Interface*, 25(3):50–59, 2016. doi: 10.1149/2.F03163if.

[25] J. Daou. Manchester university stability theory. `http://www.maths.manchester.ac.uk/~jd/MATH45132/MATH45132.html`, 2016.

[26] C. Davies and P. W. Carpenter. A novel velocity-vorticity formulation of the navier-stokes equations with applications to boundary layer disturbance evolution. *Journal of Computational Physics*, 172(1):119 – 165, 2001.

[27] C. Davies and P. W. Carpenter. Global behaviour corresponding to the absolute instability of the rotating-disc boundary layer. *Journal of Fluid Mechanics*, Vol.48: 287–329, June 2003.

[28] C. Davies, C. Thomas, and P.W. Carpenter. Global stability of the rotating-disk boundary layer. *Journal of Engineering Mathematics*, 57(3):219–236, 2007. ISSN 0022-0833. doi: 10.1007/s10665-006-9112-8.

[29] S. H. Davis. The stability of time-periodic flows. *Annual Review of Fluid Mechanics*, 8(1):57–74, 1976.

[30] M. R. Dhanak, A. Kumar, and C. L. Streett. *Effect of Suction on the Stability of Flow on a Rotating Disk*, pages 151–167. Springer New York, New York, NY, 1992. ISBN 978-1-4612-2956-8. doi: 10.1007/978-1-4612-2956-8_16.

[31] K. I. Dickson, C. T. Kelley, I. C. F. Ipsen, and I. G. Kevrekidis. Condition estimates for pseudo-arclength continuation. *SIAM Journal on Numerical Analysis*, 45(1):263–276, 2007.

[32] P.G. Drazin. *Introduction to Hydrodynamic Stability*. Cambridge Texts in Applied Mathematics. Cambridge University Press, 2002. ISBN 9780521009652.

[33] H. F. Fasel, U. Rist, and U. Konzelmann. Numerical investigation of the three-dimensional development in boundary-layer transition. *AIAA Journal*, 28(1):29–37, 2015/05/23 1990. doi: 10.2514/3.10349.

[34] R. Feynman. Turbulence theory gets a bit choppy. `http://www.usatoday.com/tech/science/columnist/vergano/2006-09-10-turbulence-x.htm`, 2006.

[35] A. Frumkin, L. Nekrasov, B. Levich, and Ju. Ivanov. Die anwendung der rotierenden scheibenelektrode mit einem ringe zur untersuchung von zwischenprodukten elektrochemischer reaktionen. *Journal of Electroanalytical Chemistry (1959)*, 1(1):84 – 90, 1959. ISSN 0368-1874. doi: https://doi.org/10.1016/0022-0728(59)80012-7.

[36] S. J. Garrett, A. J. Cooper, J. H. Harris, M. Özkan, A. Segalini, and P. J. Thomas. On the stability of von Kármán rotating-disk boundary layers with radial anisotropic surface roughness. *Physics of Fluids*, 28(1), 2016.

[37] M. Gaster. On the generation of spatially growing waves in a boundary layer. *Journal of Fluid Mechanics*, 22:433–441, 7 1965. ISSN 1469-7645. doi: 10.1017/S0022112065000873.

[38] N. Gregory, J. T. Stuart, and W. S. Walker. On the stability of three-dimensional boundary layers with application to the flow due to a rotating disk. *Philosophical Transactions of the Royal Society of London A: Mathematical, Physical and Engineering Sciences*, 248(943):155–199, 1955. doi: 10.1098/rsta.1955.0013.

[39] P. Hall. The linear stability of flat stokes layers. *Proceedings of the Royal Society of London. A. Mathematical and Physical Sciences*, 359(1697):151–166, 02 1978.

[40] J. J. Healey. Model for unstable global modes in the rotating-disk boundary layer. *Journal of Fluid Mechanics*, 663:148–159, 11 2010. ISSN 1469-7645. doi: 10.1017/S0022112010003836.

[41] D.W. Jordan and P. Smith. *Nonlinear Ordinary Differential Equations: An Introduction to Dynamical Systems*. Oxford applied and engineering mathematics. Oxford University Press, 1999. ISBN 9780198565628.

[42] R. E. Kelly and Alison M. Cheers. On the stability of oscillating plane couette flow. *The Quarterly Journal of Mechanics and Applied Mathematics*, 23(1):127–136, 1970. doi: 10.1093/qjmam/23.1.127.

[43] R. J. Lingwood. Absolute instability of the boundary layer on a rotating disk. *Journal of Fluid Mechanics*, 299:17–33, 9 1995.

[44] R. J. Lingwood. On the effects of suction and injection on the absolute instability of the rotating-disk boundary layer. *Physics of Fluids (1994-present)*, 9(5):1317–1328, 1997. doi: http://dx.doi.org/10.1063/1.869246.

[45] R. J. Lingwood. On the impulse response for swept boundary-layer flows. *Journal of Fluid Mechanics*, 344:317–334, 1997. doi: 10.1017/S0022112097006149.

[46] R. J. Lingwood and P. H. Alfredsson. Instabilities of the von kármán boundary layer. *Applied Mechanics Reviews*, 67(3), 05 2015.

[47] R.J. Lingwood. *Stability and transition of the boundary layer on a rotating disk*. PhD thesis, Cambridge University, 1995.

[48] J. Luo and X. Wu. On the linear instability of a finite stokes layer: Instantaneous versus floquet modes. *Physics of Fluids*, 22(5):054106, 2010. doi: http://dx.doi.org/10.1063/1.3422004.

[49] L. M. Mack. Linear stability theory and the problem of supersonic boundary- layer transition. *AIAA Journal*, 13(3):278–289, 2015/05/23 1975. doi: 10.2514/3.49693.

[50] M. R. Malik. The neutral curve for stationary disturbances in rotating-disk flow. *Journal of Fluid Mechanics*, 164:275–287, 3 1986.

[51] M. R. Malik and P. Balakumar. Non-parallel stability of rotating disk flow using pse. In M.Y. Hussaini, A. Kumar, and C.L. Streett, editors, *Instability, Transition, and Turbulence*, ICASE NASA LaRC Series, pages 168–180. Springer New York, 1992.

[52] M. Miklavčič and C. Y. Wang. The flow due to a rough rotating disk. *Zeitschrift für angewandte Mathematik und Physik ZAMP*, 55(2):235–246, Mar 2004. ISSN 1420-9039. doi: 10.1007/s00033-003-2096-6.

[53] The Numerical Algorithms Group (NAG). The nag fortran library. `www.nag.com`, n.d.

[54] Netlib. Fftpack, n.d.

[55] William M'F. Orr. The stability or instability of the steady motions of a perfect liquid and of a viscous liquid. part i: A perfect liquid. *Proceedings of the Royal Irish Academy. Section A: Mathematical and Physical Sciences*, 27:9–68, 01 1907. doi: 10.2307/20490590.

[56] H. Othman and T. C. Corke. Experimental investigation of absolute instability of a rotating-disk boundary layer. *Journal of Fluid Mechanics*, 565:63–94, 10 2006. ISSN 1469-7645. doi: 10.1017/S0022112006001546.

[57] B. Pier. Finite-amplitude crossflow vortices, secondary instability and transition in the rotating-disk boundary layer. *Journal of Fluid Mechanics*, 487:315–343, 6 2003. ISSN 1469-7645. doi: 10.1017/S0022112003004981.

[58] L. Prandtl. Bemerkungen über die entstehung der turbulenz. *ZAMM - Journal of Applied Mathematics and Mechanics / Zeitschrift für Angewandte Mathematik und Mechanik*, 1(6):431–436, 1921. ISSN 1521-4001. doi: 10.1002/zamm.19210010602.

[59] A. Ramage. *Linear disturbance evolution in the semi-infinite Stokes layer and related flows*. PhD thesis, Cardiff University, 2017.

[60] G. Bhaskar Reddy, S. Sreenadh, R. Hemadri Reddy, and A. Kavitha. Flow of a jeffrey fluid between torsionally oscillating disks. *Ain Shams Engineering Journal*, 6(1):355 – 362, 2015. ISSN 2090-4479. doi: https://doi.org/10.1016/j.asej.2014.09.004.

[61] Pine Research. Rotating electrode theory. https://www.pineresearch.com/shop/knowledgebase/pine-rotating-electrode-theory/#rotating_disk_electrode_rde_theory, 2016.

[62] O. Reynolds. An experimental investigation of the circumstances which determine whether the motion of water shall be direct or sinuous, and of the law of resistance in parallel channels. *Philosophical Transactions of the Royal Society of London*, 174: 935–982, 01 1883. doi: 10.2307/109431.

[63] S. Rosenblat. Torsional oscillations of a plane in a viscous fluid. *Journal of Fluid Mechanics*, 6(2):206–220, 1959. doi: 10.1017/S002211205900057X.

[64] Oleg S. Ryzhov and E. D. Terent'ev. Streamwise absolute instability of a three-dimensional boundary layer at high reynolds numbers. *Journal of Fluid Mechanics*, 373:111–153, 1998. doi: 10.1017/S0022112098002456.

[65] P. J. Schmid and D. S. Henningson. *Stability and transition in shear flows*. Applied mathematical sciences. Springer, New York, 2001. ISBN 0-387-98985-4.

[66] D. T. Schwartz, T. J. Rehg, P. Stroeve, and B. G. Higgins. Fluctuating flow with mass transfer induced by a rotating disk electrode with a superimposed time periodic modulation. *Physics of Fluids A: Fluid Dynamics*, 2(2):167–177, 1990. doi: 10.1063/1.857766.

[67] T. W. Secomb and S. Rosenblat. Torsional oscillations of a non-newtonian fluid with a free surface. *Journal of Fluid Mechanics*, 93(pt 4):767–780, 1 1979. ISSN 0022-1120.

[68] A. Sommerfeld. Ein beitrag zur hydrodynamischen erklärung der turbulenten flüssigkeitsbewegungen. *Proc. 4th Intl. Congr. Math.*, III:116–124, 1908.

[69] A. C. Srivastava. Torsional oscillations of an infinite plate in second-order fluids. *Journal of Fluid Mechanics*, 17(2):171–181, 1963. doi: 10.1017/S0022112063001221.

[70] M. J. Taylor and N. Peake. The long-time behaviour of incompressible swept-wing boundary layers subject to impulsive forcing. *Journal of Fluid Mechanics*, 355: 359–381, 1998. doi: 10.1017/S002211209700788X.

[71] C. Thomas. *Numerical simulations of disturbance development in rotating boundary layers.* PhD thesis, Cardiff University, 2007.

[72] C. Thomas and C. Davies. The effects of mass transfer on the global stability of the rotating-disk boundary layer. *Journal of Fluid Mechanics*, 663:401–433, 2010.

[73] C. Thomas and C. Davies. Global stability of the rotating-disc boundary layer with an axial magnetic field. *Journal of Fluid Mechanics*, 724:510–526, 6 2013. ISSN 1469-7645. doi: 10.1017/jfm.2013.162.

[74] C. Thomas and C. Davies. Global stability of the rotating-disc boundary layer with an axial magnetic field. *Journal of Fluid Mechanics*, 724:510–526, 6 2013. ISSN 1469-7645. doi: 10.1017/jfm.2013.162.

[75] C Thomas and C. Davies. On the impulse response and global instability development of the infinite rotating-disc boundary layer. *Submitted to Journal of Fluid Mechanics*, 2018.

[76] C. Thomas, A. P. Bassom, P. J. Blennerhassett, and C. Davies. The linear stability of oscillatory poiseuille flow in channels and pipes. *Proceedings of the Royal Society of London A: Mathematical, Physical and Engineering Sciences*, 2011.

[77] W. Tollmien. Über die entstehung der turbulenz. 1. mitteilung. *Nachrichten von der Gesellschaft der Wissenschaften zu Göttingen, Mathematisch-Physikalische Klasse*, 1929:21–44, 1928.

[78] L. N. Trefethen et al. *Chebfun Version 4.2.* The Chebfun Development Team, 2011. `http://www.chebfun.org/`.

[79] L.N. Trefethen. *Spectral Methods in MATLAB.* Software, Environments, and Tools. Society for Industrial and Applied Mathematics, 2000. ISBN 9780898714654.

[80] T. von Kármán. Uber laminaire und turbulente reibung. *Zeitschrift für angewandte Mathematik und Mechanik*, 1:233–52, 1921.

[81] C. H. Von Kerczek. The instability of oscillatory plane poiseuille flow. *Journal of Fluid Mechanics*, 116:91–114, 3 1982. ISSN 1469-7645. doi: 10.1017/S002211208200038X.

[82] D. J. Wise and P. Ricco. Turbulent drag reduction through oscillating discs. *Journal of Fluid Mechanics*, 746:536–564, 2014. doi: 10.1017/jfm.2014.122.

[83] J. R. Womersley. Method for the calculation of velocity, rate of flow and viscous drag in arteries when the pressure gradient is known. *The Journal of Physiology*, 127(3): 553–563, 1955.

[84] M. S. Yoon, J. M. Hyun, and J. S. Park. Flow and heat transfer over a rotating disk with surface roughness. *International Journal of Heat and Fluid Flow*, 28(2):262 – 267, 2007. ISSN 0142-727X. doi: https://doi.org/10.1016/j.ijheatfluidflow.2006.04.008.

Appendices

Appendix A

Convergence of Eigenvalue Routines

A.1 Blasius Boundary Layer

Section 1.4.3 describes the application of the novel numerical method discussed throughout chapter 1 to a two-dimensional steady flow configuration; the Blasius boundary layer. The perturbation variables are expanded in terms of Chebyshev polynomials as follows

$$f = \sum_{n} f_n T_{2n-1}$$

and truncated at some appropriate level. Convergence tests were carried out to empirically determine the appropriate truncation level when solving the dispersion relation

$$\mathcal{D}(R, \alpha, \omega) = 0 \tag{A.1}$$

in both the temporal (specifying ω as real and solving for α) and spatial (specifying α as real and solving for ω) settings. Tables A.1-A.2 show the convergence of the most unstable mode in the temporal and spatial spectra of the Blasius dispersion relation (A.1).

α	R	N	ω
0.2	500	4	0.034967 - 0.009858i
		12	0.072992 - 0.0032771i
		20	0.073044 - 0.0033146i
		24	0.073039 - 0.0033168i
		48	0.073039 - 0.0033173i
		96	0.073039 - 0.0033172i
		128	0.073039 - 0.0033172i
0.2	10000	4	0.059196 - 0.001624i
		12	0.044011 - 0.0071315i
		20	0.053099 - 0.0092124i
		24	0.049906 - 0.014714i
		48	0.054488 - 0.014431i
		96	0.054489 - 0.014431i
		128	0.054489 - 0.014431i

Table A.1: Convergence with Chebyshev discretisation order N of the most unstable mode in the temporal spectra of the Blasius dispersion relation (A.1).

ω	R	N	α
0.085	500	4	0.25674 - 0.0050924i
		12	0.22695 + 0.0043486i
		20	0.22678 + 0.0045134i
		24	0.22678 + 0.0045133i
		48	0.22677 + 0.0045137i
		96	0.22677 + 0.0045137i
		128	0.22677 + 0.0045137i
0.085	10000	4	0.26979 + 0.036377i
		12	0.2811 - 0.00080097i
		20	0.27628 + 0.0081857i
		24	0.2705 + 0.015632i
		48	0.27381 + 0.012845i
		96	0.27381 + 0.012845i
		128	0.27381 + 0.012845i

Table A.2: Convergence with Chebyshev discretisation order N of the most unstable mode in the spatial spectra of the Blasius dispersion relation (A.1).

A.2 Stokes Boundary Layer

Section 1.4.4 describes the novel numerical method discussed throughout chapter 1, applied using Floquet theory to a two-dimensional temporally periodic flow configuration; the Stokes oscillatory boundary layer. The perturbation variables are expanded in terms of Chebyshev polynomials as follows

$$f = \sum_n f_n T_{2n-1}$$

and truncated at some appropriate level. Convergence tests were carried out to empirically determine the appropriate truncation level when solving the system of equations that make up the dispersion relation

$$\mathcal{L}_k(\alpha, R)\hat{f}_k = -\mu \mathbf{I}_2 \hat{f}_k \tag{A.2}$$

in the temporal (specifying μ as real and solving for α) setting. There are two discretisation orders in this problem that should be considered when assuring convergence, namely those of the Chebyshev discretisation and the number of harmonics. Table 1.2 in the main text illustrates the convergence with the number of harmonics while table A.3 shows the convergence with Chebyshev discretisation order N of the most unstable mode in the temporal spectra of the Stokes dispersion relation (A.2). The spatial analysis was not possible in this setting due to memory constraints and the number of harmonics required.

α	R	N	μ_r
0.3	700	4	0.97922
		12	-0.052847
		20	-0.044284
		24	-0.045992
		48	-0.045159
		96	-0.045016
		128	-0.045016
0.3	800	4	1.1681
		12	-0.052528
		20	0.11162
		24	0.1487
		48	0.081821
		96	0.081745
		128	0.081745

Table A.3: Convergence with Chebyshev discretisation order N of the most unstable mode in the temporal spectra of the Stokes dispersion relation (A.2). In each case, the number of harmonics was chosen so as to be greater than the number required by Blennerhassett and Bassom [11] for convergence.

A.3 Steady Rotating Disk Boundary Layer

Section 2.2.1 describes the application of the novel numerical method discussed throughout chapter 2 to a three-dimensional steady flow configuration; the rotating disk boundary

layer. The perturbation variables are expanded in terms of Chebyshev polynomials as follows

$$f = \sum_n f_n T_{2n-1}$$

and truncated at some appropriate level. Convergence tests were carried out to empirically determine the appropriate truncation level when solving the dispersion relation

$$\mathcal{D}(R, \alpha, n, \omega) = 0 \tag{A.3}$$

for the temporal (specifying ω and n as real and solving for α) setting and for stationary ($\omega = 0$) disturbances with fixed n in the spatial setting. Tables A.4-A.5 show the convergence of the most unstable mode of the steady rotating disk dispersion relation (A.3).

α	n	R	N	ω
0.3	32	350	4	-0.060424 + 0.0040383i
			12	-0.014563 + 0.011932i
			20	-0.013946 + 0.0030149i
			24	-0.013171 + 0.0022687i
			48	-0.013364 + 0.0020526i
			96	-0.013364 + 0.0020526i
			128	-0.013364 + 0.0020526i
0.2-0.12i	32	400	4	-0.042808 + 0.0090325i
			12	-0.011335 - 0.00091879i
			20	-0.010526 - 0.0029679i
			24	-0.010689 - 0.0032092i
			48	-0.01068 - 0.0032368i
			96	-0.010682 - 0.003239i
			128	-0.010682 - 0.003239i
0.3	68	500	4	-0.053142 + 0.064032i
			12	-0.044739 + 0.018807i
			20	-0.035369 + 0.0046288i
			24	-0.033816 + 0.0046894i
			48	-0.03341 + 0.0046586i
			96	-0.03341 + 0.0046586i
			128	-0.03341 + 0.0046586i

Table A.4: Convergence with Chebyshev discretisation order N of the most unstable mode in the temporal spectra of the steady rotating disk dispersion relation (A.3).

ω	n	R	N	α
0	32	350	4	0.041031 - 0.1251i
			12	0.21696 + 0.036043i
			20	0.42371 + 0.10186i
			24	0.45287 - 0.023098
			48	0.46309 - 0.015994i
			96	0.46309 - 0.015993i
			128	0.46309 - 0.015993i
0	68	550	4	0.040614 - 0.1425i
			12	0.21541 + 0.073515i
			20	0.39671 + 0.073663i
			24	0.59856 + 0.021235i
			48	0.60954 - 0.008059i
			96	0.60955 - 0.0080429i
			128	0.60955 - 0.0080429i
-0.01023	32	300	4	0.039256 - 0.12277i
			12	0.19899 + 0.053982i
			20	0.27861 + 0.28042i
			24	0.43467 - 0.007954i
			48	0.44191 - 0.0020801i
			96	0.44191 - 0.0020794i
			128	0.44191 - 0.0020794i

Table A.5: Convergence with Chebyshev discretisation order N of the most unstable mode in the spatial spectra for stationary disturbances in the steady rotating disk dispersion relation (A.3).

A.4 Periodically Modulated Rotating Disk Boundary Layer

Section 3.1 describes the novel numerical method discussed throughout chapter 3, applied using Floquet theory to the three dimensional periodically modulated rotating disk boundary layer on which the bulk of this thesis is based. The perturbation variables are expanded in terms of Chebyshev polynomials as follows

$$f = \sum_{n} f_n T_{2n-1}$$

and truncated at some appropriate level N_C. Convergence tests were carried out to empirically determine the appropriate truncation level when solving the system of equations that make up the dispersion relation

$$\sum_{m=-\infty}^{\infty} \mathcal{D}_m\{\mu, \alpha\ R, n\} e^{im\tilde{\tau}} = 0 \tag{A.4}$$

for the temporal (specifying ω and n as real and solving for α) setting and for stationary ($\omega = 0$) disturbances with fixed n in the spatial setting.

There are three discretisation orders in this problem that should be considered when assuring convergence, two of which are the Chebyshev discretisation order, N_C, and the number of harmonics, N_F. The third discretisation order to be taken into account is the number of terms taken in the Fourier expansion of the base flow $\mathbf{U}^M(z, \tilde{\tau})$

$$\mathbf{U}^M(z, \tilde{\tau}) := \mathbf{U}^B(z, \tilde{\tau}) - \mathbf{U}^S(z) \tag{A.5}$$

$$= \sum_{k=-N_B}^{N_B} \mathbf{u}_k(z) e^{ik\tilde{\tau}} \tag{A.6}$$

as given by equation (3.11) in the main text. Tables 3.2-3.3 in the main text illustrate the convergence with the number of harmonics and terms in the base flow expansion while table A.6 shows the convergence with Chebyshev discretisation order N of the most unstable mode in the temporal spectra of the periodically modulated rotating disk dispersion relation (A.4). The results for the spatial analysis are similar and so are not presented here in the interest of concision.

R	α	U_w	φ	N_C	μ
500	0.3	0.2	5	48	0.004229 - 0.011160i
				64	0.004229 - 0.011160i
				96	0.004229 - 0.011160i
				128	0.004229 - 0.011160i
500	0.3	0.2	10	48	0.004206 - 0.020812i
				64	0.004206 - 0.020812i
				96	0.004206 - 0.000811i
				128	0.004206 - 0.000811i
500	0.3	0.2	15	48	0.004497 - 0.000840i
				64	0.004497 - 0.000840i
				96	0.004497 - 0.000840i
				128	0.004497 - 0.000840i

Table A.6: Convergence with Chebyshev discretisation order N_C of the most unstable mode in the temporal spectra for stationary disturbances in the periodically modulated rotating disk dispersion relation (A.4).

Appendix B

Algorithms and Numerical Schemes

B.1 Numerical Solution of the Base Flow Equations

We will begin our discussion with the numerical solution procedure for the periodically modulated rotating disk base flow equations (2.20a), and will build to describing the algorithm used for the full simulations with radial dependence procedure described in section 3.5. From equations (2.20a), we have

$$\left(\frac{3}{2\Delta\tau}\iint - \iint \mathcal{D}^2\right) F^{l+1} d\eta = \frac{2}{\Delta\tau}\iint F^{l} d\eta - \frac{1}{2\Delta\tau}\iint F^{l-1} d\eta + \iint \mathcal{R}_F^l d\eta$$
$$\left(\frac{3}{2\Delta\tau}\iint - \iint \mathcal{D}^2\right) G^{l+1} d\eta = \frac{2}{\Delta\tau}\iint G^{l} d\eta - \frac{1}{2\Delta\tau}\iint G^{l-1} d\eta + \iint \mathcal{R}_G^l d\eta$$

subject to the boundary conditions

$$F(1,\tau) = H(1,\tau) = 0, \quad G(1,\tau) = 1 + \frac{R_s\sqrt{\varphi}}{R}\cos\left(\frac{\varphi}{R}\tau\right)$$
$$F \to 0, \quad G \to 0 \quad \text{as} \quad \eta \to 0$$

as described in section 3.5. We can write this for simplicity as

$$F^{l+1} = \mathcal{L}^{-1}\left(\mathcal{P}_1 F^l - \mathcal{P}_2 F^{l-1} + \mathcal{R}_F^l\right) \tag{B.1a}$$
$$G^{l+1} = \mathcal{L}^{-1}\left(\mathcal{P}_1 G^l - \mathcal{P}_2 G^{l-1} + \mathcal{R}_G^l\right) \tag{B.1b}$$

and solved with a predictor-corrector algorithm, using an algorithm akin to the following diagram:

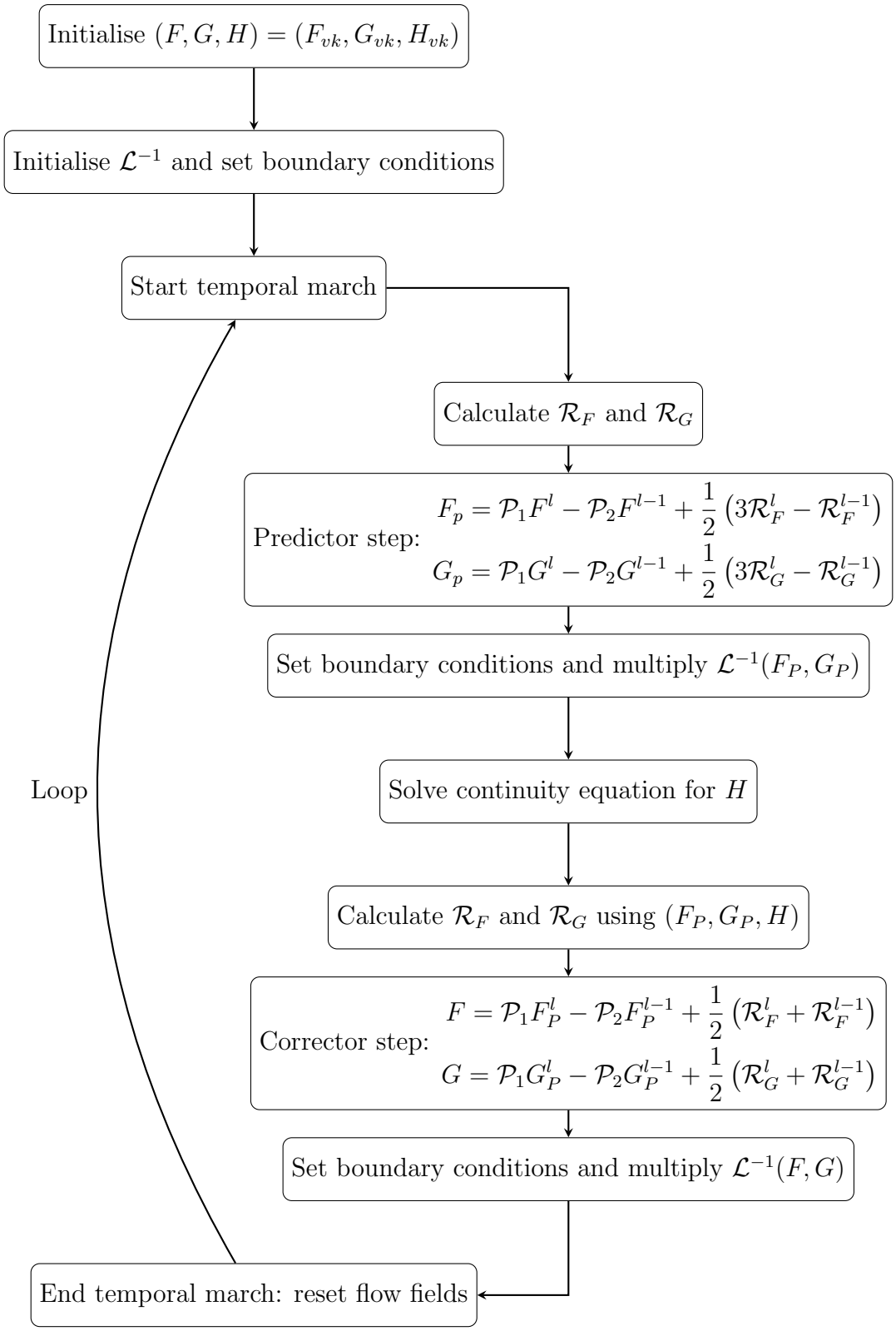
Initialise $(F, G, H) = (F_{vk}, G_{vk}, H_{vk})$
Initialise $\mathcal{L}^{-1}$ and set boundary conditions
Start temporal march
Calculate $\mathcal{R}_F$ and $\mathcal{R}_G$
Predictor step:
$F_p = \mathcal{P}_1 F^l - \mathcal{P}_2 F^{l-1} + \frac{1}{2}\left(3\mathcal{R}_F^l - \mathcal{R}_F^{l-1}\right)$
$G_p = \mathcal{P}_1 G^l - \mathcal{P}_2 G^{l-1} + \frac{1}{2}\left(3\mathcal{R}_G^l - \mathcal{R}_G^{l-1}\right)$
Set boundary conditions and multiply $\mathcal{L}^{-1}(F_P, G_P)$
Solve continuity equation for H
Calculate $\mathcal{R}_F$ and $\mathcal{R}_G$ using (F_P, G_P, H)
Corrector step:
$F = \mathcal{P}_1 F_P^l - \mathcal{P}_2 F_P^{l-1} + \frac{1}{2}\left(\mathcal{R}_F^l + \mathcal{R}_F^{l-1}\right)$
$G = \mathcal{P}_1 G_P^l - \mathcal{P}_2 G_P^{l-1} + \frac{1}{2}\left(\mathcal{R}_G^l + \mathcal{R}_G^{l-1}\right)$
Set boundary conditions and multiply $\mathcal{L}^{-1}(F, G)$
End temporal march: reset flow fields
Loop

B.2 Monochromatic Numerical Simulations

The algorithm for the solution of the equations which appear in section 2.2.4 when conducting monochromatic direct numerical simulations is very similar to that presented in section B.1, although we will outline it here for clarity. The equations (2.59) are given by

$$\frac{\partial \xi_r}{\partial t} + i\beta N_z - \frac{\partial N_\theta}{\partial z} - \frac{2}{R}\left(\xi_\theta + i\alpha w\right) = \frac{1}{R}\left[\left(\hat{\nabla}^2 - \frac{1}{r^2}\right)\xi_r - \frac{2i\beta}{R}\xi_\theta\right]$$
$$\frac{\partial \xi_\theta}{\partial t} + \frac{\partial N_r}{\partial z} - \frac{\partial N_z}{\partial r} + \frac{2}{R}\left(\xi_r - i\beta w\right) = \frac{1}{R}\left[\left(\hat{\nabla}^2 - \frac{1}{r^2}\right)\xi_\theta + \frac{2i\beta}{R}\xi_r\right]$$
$$\hat{\nabla}^2 w = \frac{1}{r}\left(\frac{\partial \xi_r}{\partial \theta} - \frac{\partial (r\xi_\theta)}{\partial r}\right)$$

which we integrate and rearrange to get

$$\left(\frac{3}{2\Delta\tau}\iint - \frac{1}{2R}\iint \mathcal{D}^2\right)\xi_r^{l+1} d\eta = \frac{2}{\Delta\tau}\iint \xi_r^l d\eta - \frac{1}{2\Delta\tau}\iint \xi_r^{l-1} d\eta + \iint \mathcal{R}_r^l d\eta$$
$$\left(\frac{3}{2\Delta\tau}\iint - \frac{1}{2R}\iint \mathcal{D}^2\right)\xi_\theta^{l+1} d\eta = \frac{2}{\Delta\tau}\iint \xi_\theta^l d\eta - \frac{1}{2\Delta\tau}\iint \xi_\theta^{l-1} d\eta + \iint \mathcal{R}_\theta^l d\eta$$

where

$$\mathcal{R}_r^l = \frac{2}{R}\left(\xi_\theta^l + i\alpha w^l\right) + \frac{\partial N_\theta^l}{\partial z} - i\beta N_z^l + \frac{1}{R}\left[\left(-\alpha^2 + \frac{i\alpha}{R} - \beta^2 + \frac{1}{2}\frac{\partial^2}{\partial z^2} - \frac{1}{R^2}\right)\xi_r^l - \frac{2i\beta}{R}\xi_\theta^l\right]$$
$$\mathcal{R}_\theta^l = -\frac{2}{R}\left(\xi_r^l - i\beta w^l\right) + \frac{\partial N_z^l}{\partial r} - \frac{\partial N_r^l}{\partial z} + \frac{1}{R}\left[\left(-\alpha^2 + \frac{i\alpha}{R} - \beta^2 + \frac{1}{2}\frac{\partial^2}{\partial z^2} - \frac{1}{R^2}\right)\xi_\theta^l + \frac{2i\beta}{R}\xi_r^l\right]$$

together with the continuity equation

$$\left(-\alpha^2 + \frac{i\alpha}{R} - \beta^2 + \frac{\partial^2}{\partial z^2}\right) w^l = i\beta\xi_\theta^l - i\alpha\xi_r^l - \frac{\xi_r^l}{R}$$

As with section B.1, we may write this succinctly as

$$\xi_r^{l+1} = \mathcal{L}^{-1}\left(\mathcal{P}_1\xi_r^l - \mathcal{P}_2\xi_r^{l-1} + \mathcal{R}_r^l\right)$$
$$\xi_\theta^{l+1} = \mathcal{L}^{-1}\left(\mathcal{P}_1\xi_\theta^l - \mathcal{P}_2\xi_\theta^{l-1} + \mathcal{R}_\theta^l\right)$$

which gives a similar equation set to (B.1). The algorithm may be explained by the following diagram:

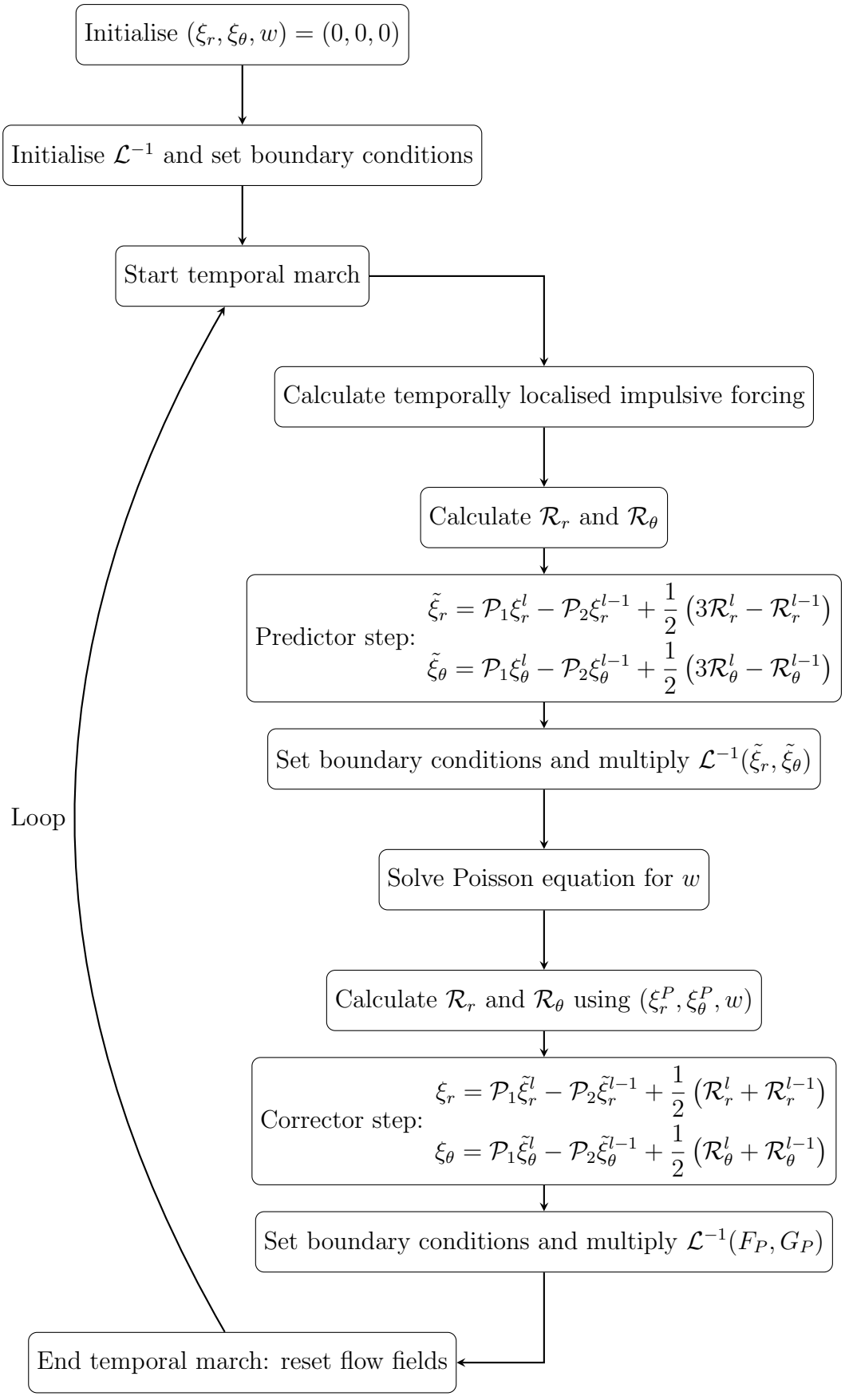
Initialise $(\xi_r, \xi_\theta, w) = (0, 0, 0)$
Initialise $\mathcal{L}^{-1}$ and set boundary conditions
Start temporal march
Calculate temporally localised impulsive forcing
Calculate $\mathcal{R}_r$ and $\mathcal{R}_\theta$
Predictor step:
$\tilde{\xi}_r = \mathcal{P}_1\xi_r^l - \mathcal{P}_2\xi_r^{l-1} + \frac{1}{2}\left(3\mathcal{R}_r^l - \mathcal{R}_r^{l-1}\right)$
$\tilde{\xi}_\theta = \mathcal{P}_1\xi_\theta^l - \mathcal{P}_2\xi_\theta^{l-1} + \frac{1}{2}\left(3\mathcal{R}_\theta^l - \mathcal{R}_\theta^{l-1}\right)$
Set boundary conditions and multiply $\mathcal{L}^{-1}(\tilde{\xi}_r, \tilde{\xi}_\theta)$
Solve Poisson equation for w
Calculate $\mathcal{R}_r$ and $\mathcal{R}_\theta$ using $(\xi_r^P, \xi_\theta^P, w)$
Corrector step:
$\xi_r = \mathcal{P}_1\tilde{\xi}_r^l - \mathcal{P}_2\tilde{\xi}_r^{l-1} + \frac{1}{2}\left(\mathcal{R}_r^l + \mathcal{R}_r^{l-1}\right)$
$\xi_\theta = \mathcal{P}_1\tilde{\xi}_\theta^l - \mathcal{P}_2\tilde{\xi}_\theta^{l-1} + \frac{1}{2}\left(\mathcal{R}_\theta^l + \mathcal{R}_\theta^{l-1}\right)$
Set boundary conditions and multiply $\mathcal{L}^{-1}(F_P, G_P)$
End temporal march: reset flow fields
Loop

B.3 Numerical Simulations with Radial Dependence

The algorithm for the simulations which include the radial dependence of the perturbations is similar to that described in section B.2, although has the distinct difference that there are radial derivatives to be calculated and a radial domain to be taken into account. This leads to the need for radial inflow and outflow conditions to be imposed in the algorithm and highly accurate finite difference schemes to calculate the radial derivatives. The solution to the Poisson equation also becomes trickier with this modification as it cannot now be simply solved by a matrix inversion across the boundary layer. The inflow and outflow conditions are described in section B.3.1 while the finite difference schemes are described in B.3.2. Finally, this section concludes with a discussion of the Poisson solver routine in section B.3.3. The equations to be solved are given by (2.36) but are stated here again for completeness:

$$\frac{\partial \xi_r}{\partial t} + \frac{1}{r}\frac{\partial N_z}{\partial \theta} - \frac{\partial N_\theta}{\partial z} - \frac{2}{R}\left(\xi_\theta + \frac{\partial w}{\partial r}\right) = \frac{1}{R}\left[\left(\nabla^2 - \frac{1}{r^2}\right)\xi_r - \frac{2}{r^2}\frac{\partial \xi_\theta}{\partial \theta}\right] \tag{B.2a}$$

$$\frac{\partial \xi_\theta}{\partial t} + \frac{\partial N_r}{\partial z} - \frac{\partial N_z}{\partial r} + \frac{2}{R}\left(\xi_r - \frac{1}{r}\frac{\partial w}{\partial \theta}\right) = \frac{1}{R}\left[\left(\nabla^2 - \frac{1}{r^2}\right)\xi_\theta + \frac{2}{r^2}\frac{\partial \xi_r}{\partial \theta}\right] \tag{B.2b}$$

$$\nabla^2 w = \frac{1}{r}\left(\frac{\partial \xi_r}{\partial \theta} - \frac{\partial (r\xi_\theta)}{\partial r}\right) \tag{B.2c}$$

where

$$\mathbf{N} = (N_r, N_\theta, N_z) = (\nabla \times \mathbf{U}_B) \times \mathbf{u} + \boldsymbol{\xi} \times \mathbf{U}_B$$

and

$$\nabla^2 = \frac{\partial^2}{\partial r^2} + \frac{1}{r}\frac{\partial}{\partial r} + \frac{1}{r^2}\frac{\partial^2}{\partial \theta^2} + \frac{\partial^2}{\partial z^2}$$

$$\nabla \times \mathbf{U}^B = \left(\frac{1}{r}\frac{\partial U_z^B}{\partial \theta} - \frac{\partial U_\theta^B}{\partial z}\right)\mathbf{e}_r + \left(\frac{\partial U_r^B}{\partial z} - \frac{\partial U_z^B}{\partial r}\right)\mathbf{e}_\theta + \frac{1}{r}\left[\frac{\partial}{\partial r}\left(rU_\theta^B\right) - \frac{\partial U_r^B}{\partial \theta}\right]\mathbf{e}_z$$

are the usual Laplacian and curl operators in cylindrical polar coordinates.

B.3.1 Inflow and Outflow Conditions

A thorough examination of the inflow and outflow conditions required in the steady rotating disk configuration has been undertaken for this problem by several authors including Davies and Carpenter [27] and Thomas [71]. Following these authors, all perturbation quantities are set to zero at the inflow boundary, which is placed sufficiently far away from

the domain of interest to not influence the results. The outflow condition is somewhat trickier, and for the purposes of the current investigation we impose a wavelike condition on the second derivative of the normal velocity, similar to Fasel et al. [33], namely

$$\frac{\partial^2 w}{\partial w^2} = -\alpha^2 w$$

for some radial wavenumber α. In any case, the outflow boundary is placed sufficiently far away from the initial forcing so as not to impact the results. These conditions have been explored by Davies and Carpenter [27] and Thomas [71] in detail, so we proceed with confidence in their application to the current problem in question.

B.3.2 Finite Difference Discretisation Schemes

The finite difference schemes used in the radial direction to calculate r-derivatives of the perturbation quantities are similar to those found in Fasel et al. [33] and are described below for completeness. As discussed in the main text, the schemes are centered and non-compact.

First Derivative

$$\left(\frac{\partial f}{\partial r}\right)\Big|_{\{j=2\}} = \frac{f^{j+1} - f^{j-1}}{2\Delta r}$$

$$\left(\frac{\partial f}{\partial r}\right)\Big|_{\{j=N\}} = \frac{11f^{j} - 18f^{j-1} + 9f^{j-2} - 2f^{j-3}}{6\Delta r}$$

$$\left(\frac{\partial f}{\partial r}\right)\Big|_{\{j=3,j=N-2\}} = \frac{(f^{j-2} - f^{j+2}) + 8(f^{j+1} - f^{j-1})}{12\Delta r}$$

$$\left(\frac{\partial f}{\partial r}\right)\Big|_{\{j=4,j=N-3\}} = \frac{(f^{j+3} - f^{j-3}) + 9(f^{j-2} - f^{j+2}) + 45(f^{j+1} - f^{j-1})}{60\Delta r}$$

$$\left(\frac{\partial f}{\partial r}\right)\Big|_{\{j=N-1\}} = \frac{12f^{j+1} + 65f^{j} - 120f^{j-1} + 60f^{j-2} - 20f^{j-3} + 3f^{j-4}}{60\Delta r}$$

$$\left(\frac{\partial f}{\partial r}\right)\Big|_{\{j=5,\ldots,N-4\}} = \frac{3(f^{j-4} - f^{j+4}) + 32(f^{j+3} - f^{j-3}) + 168(f^{j-2} - f^{j+2}) + 672(f^{j+1} - f^{j-1})}{840\Delta r}$$

Second Derivative

$$\left(\frac{\partial^2 f}{\partial r^2}\right)\Big|_{\{j=4,\ldots,N-3\}} = \frac{2(f^{j+3}+f^{j-3}) - 27(f^{j+2}+f^{j-2}) + 270(f^{j+1}+f^{j-1}) - 490f^j}{180(\Delta r)^2}$$

$$\left(\frac{\partial^2 f}{\partial r^2}\right)\Big|_{\{j=3,j=N-2\}} = \frac{-(f^{j+2}+f^{j-2}) + 16(f^{j+1}+f^{j-1}) - 30f^j}{12(\Delta r)^2}$$

$$\left(\frac{\partial^2 f}{\partial r^2}\right)\Big|_{\{j=2\}} = \frac{(f^{j+1}+f^{j-1}) - 2f^j}{(\Delta r)^2}$$

$$\left(\frac{\partial^2 f}{\partial r^2}\right)\Big|_{\{j=N-1\}} = \frac{10f^{j+1} - 15f^j - 4f^{j-1} + 14f^{j-2} - 6f^{j-3} + f^{j-4}}{12(\Delta r)^2}$$

$$\left(\frac{\partial^2 f}{\partial r^2}\right)\Big|_{\{j=N\}} = -\alpha^2 f^j$$

B.3.3 Poisson Equation

The solution to the Poisson equation is computed by an iterative solver embedded within the main predictor-corrector algorithm used to compute the solutions to the vorticity transport equations. In particular, on expanding the Poisson equation in (B.2), we have

$$\left(\frac{\partial^2}{\partial r^2} + \frac{1}{r}\frac{\partial}{\partial r} - \frac{n^2}{r^2} + \frac{\partial^2}{\partial z^2}\right) w = \frac{n}{r}\xi_r - \frac{\partial \xi_\theta}{\partial r} - \frac{1}{r}\xi_\theta$$

Clearly, the radial derivatives are computed in practise by the finite difference schemes described in B.3.2. However, to illustrate the method and for notational brevity, we will use a simpler scheme here, namely

$$\left(\frac{\partial f}{\partial r}\right)\Big|_{\{j=2,\ldots,N-1\}} = \frac{f^{j+1} - f^{j-1}}{2\Delta r}$$

$$\left(\frac{\partial f}{\partial r}\right)\Big|_{\{j=N\}} = \frac{f^j - f^{j-1}}{\Delta r}$$

$$\left(\frac{\partial^2 f}{\partial r^2}\right)\Big|_{\{j=2,\ldots,N-1\}} = \frac{f^{j+1} - 2f^j + f^{j-1}}{(\Delta r)^2}$$

$$\left(\frac{\partial^2 f}{\partial r^2}\right)\Big|_{\{j=N\}} = -\alpha^2 f^j$$

At the interior points $j = 2, \ldots, N-1$, we thus write

$$\iint \left(\frac{2}{(\Delta r)^2} + \frac{n^2}{r_j^2} - \frac{\partial^2}{\partial z^2}\right) w^j dz = \iint \left(\frac{w^{j+1} + w^{j-1}}{(\Delta r)^2}\right) dz + \iint \frac{1}{r_j}\left(\frac{w^{j+1} - w^{j-1}}{\Delta r}\right) dz + \iint \left(\frac{\partial \xi_\theta^j}{\partial r} + \frac{1}{r_j}\xi_\theta^j - \frac{n}{r_j}\xi_r^j\right) dz$$

while we have

$$\iint \left(\alpha^2 + \frac{n^2}{r_j^2} - \frac{\partial^2}{\partial z^2}\right) w^j dz = \iint \frac{1}{r_j}\left(\frac{w^j - w^{j-1}}{\Delta r}\right) dz + \iint \left(\frac{\partial \xi_\theta^j}{\partial r} + \frac{1}{r_j}\xi_\theta^j - \frac{n}{r_j}\xi_r^j\right) dz$$

at the outflow boundary $j = N$. The perturbation quantities are set to zero at the inflow boundary which is placed far away from the centre of excitation, as discussed in the opening to this section. This allows us to write the equation succinctly as

$$\mathcal{L}w^j = \mathcal{P}_1 w^{j+1} + \mathcal{P}_2 w^{j-1} + \mathcal{R}^j$$

and use an iterative solver to obtain the solution which may be described as follows: